Université de Montréal

Templating gold nanoparticles on nanofibers using block copolymer thin films

par
Hu Zhu

Département de chimie
Faculté des arts et des sciences

Thèse présentée à la Faculté des études supérieures et postdoctorales
en vue de l'obtention du grade de
Philosophiae Doctor (Ph.D.) en chimie

Septembre 2018

Résumé

Les nanocapteurs à diffusion Raman exaltée par effets de surface (SERS) basés sur les nanofibres sont une des technologies prometteuses pour les études cellulaires. Une approche ascendante de nanofabrication des nanofibres reposant sur l'auto-assemblage électrostatique des nanoparticules d'or (AuNPs) chargées avec un film portant des charges opposées qui recouvre la nanofibre est proposée. Les revêtements courants tels que les monocouches auto-assemblées d'alcoxysilanes et les films d'homopolymère souffrent de l'agrégation des AuNPs et d'inhomogénéités. Des gabarits de film en copolymère à bloc (BCP) ayant des motifs de surface bien définis peuvent guider le dépôt ordonné des réseaux d'AuNPs, mais ont été étudiés presque exclusivement sur des substrats plats. L'objectif principal de cette thèse a été de revêtir les nanofibres avec des BCP dans le but d'obtenir des réseaux d'AuNPs denses et uniformes sur la nanofibre.

Pour y parvenir, des fibres de verre étirées ayant des diamètres allant jusqu'à 100 nm ont été trempées dans des solutions de polystyrène-*bloc*-poly(4-vinylpyridine) (PS-*b*-P4VP) dans le THF à différentes concentrations et taux d'enduction. On a constaté que seul un film de type brosse ayant une épaisseur d'environ 3 nm est obtenu sur la nanofibre. Ce film se forme par adsorption où le bloc P4VP ancre le BCP à la surface polaire de la nanofibre de verre via de multiples liaisons hydrogène alors que le bloc PS est exposé à la solution. L'incubation de la nanofibre recouverte de la brosse dans des colloïdes aqueux d'AuNPs entraîne un dépôt d'AuNPs dense et bien dispersé. En revanche, les films de l'homopolymère, P4VP, et d'un copolymèrestatistique, PS-*s*-P4VP, présentent une certaine agrégation des AuNPs, indiquant un effet de barrière stérique créée par les blocs du PS. Une augmentation de la rugosité de la brosse a été observée après l'immersion dans l'eau, ce qui indique que le dépôt des AuNPs a conduit à un réarrangement local des chaînes du PS pour exposer des portions des chaînes P4VP afin d'attirer les AuNPs. De même, en suivant la cinétique d'adsorption en mesurant l'épaisseur du film sec en fonction du temps d'adsorption, on a constaté que les films saturés avaient une morphologie lisse (obtenue après 2 minutes d'adsorption) et que les films insaturés avaient une morphologie plus

rugueuse; cependant, cette dernière n'a pas modifié les caractéristiques de dépôt des AuNPs.

Pour une meilleure compréhension, les mêmes films PS-*b*-P4VP ont été étudiés sur des surfaces planes. L'effet de la courbure de surface s'est avéré similaire à l'effet de la concentration de la solution de polymère, avec une évolution similaire de la morphologie du film pour une concentration décroissante et un diamètre de fibre décroissant, à savoir d'une morphologie de type micellaire à une morphologie partiellement micellaire et partiellement brosse et, finalement, à une morphologie brosse. Alors que cette dernière conduit à un dépôt d'AuNPs denses et bien dispersées, la morphologie micellaire conduit à des petites grappes d'AuNPs (pour de petites AuNPs). Enfin, il a été démontré que les nanofibres peuvent être recouvertes par des BCPs chargés d'ions en utilisant des techniques de revêtement en goutte. En ce qui concerne les applications de l'optophysiologie SERS, la nanofibre revêtue d'AuNPs denses et bien dispersées grâce au BCP en brosse s'est révélée, par la détection *in vitro* des neurotransmetteurs, plus performante.

Mots-clés: SERS, nanofibres, couches minces, copolymères à blocs, polystyrène-*bloc*-poly(4-vinylpyridine), couches de type brosse, adsorption, trempage, courbure du substrat, nanoparticules d'or, auto-assemblage.

Abstract

Surface enhanced Raman scattering (SERS) nanosensors based on pulled nanofibers are a promising technology for cellular studies. A bottom-up nanofabrication approach towards SERS nanofibers is based on electrostatic self-assembly of charged gold nanoparticles (AuNPs) with a film carrying opposite charges that coats the nanofiber. Common coatings such as self-assembled monolayers of alkoxysilanes and homopolymer films suffer from AuNP aggregation and inhomogeneities. Block copolymer (BCP) film templates having surface patterns can guide the ordered deposition of AuNP arrays, but have been investigated almost exclusively on flat substrates. A major objective of this thesis is to coat nanofibers with BCPs with the aim of achieving uniform AuNP arrays on the nanofiber.

To achieve this, pulled glass fibers with sub-micron tip diameters were dip-coated from polystyrene-*block*-poly(4-vinylpyridine) (PS-*b*-P4VP) solutions in THF of various polymer solution concentrations and dip-coating rates. It was found that only a brush film with a thickness of about 3 nm was obtained on the nanofiber. The brush film forms by adsorption, where the P4VP block anchors the BCP on the polar surface of the glass nanofiber via multiple H-bonds and the PS block dangles into the solution. Incubating the BCP-coated nanofiber in aqueous AuNP colloids leads to the deposition of dense and well-dispersed AuNPs on the nanofibers. In contrast, P4VP homopolymer and PS-*s*-P4VP random copolymer films show significant AuNP aggregation, indicating a steric barrier effect provided by the PS blocks. An increase in roughness of the BCP brush film was shown after immersion in water, indicating that the AuNP deposition results from local PS chain rearrangement to expose portions of the P4VP chains for attracting AuNPs. Similarly, when following the adsorption kinetics by measuring the dry film thickness as a function of adsorption time, it was found that saturated films had a smooth morphology (achieved within two minutes of adsorption) and unsaturated films exhibited a rougher morphology, but this did not change the deposition pattern of the AuNPs.

For greater understanding, the same dip-coated PS-*b*-P4VP films were studied on flat surfaces. The effect of surface curvature (fiber diameter) was found to parallel that of changing polymer solution concentration, as indicated by a similar film morphology evolution between decreasing polymer solution concentration and decreasing fiber diameter. Notably, it changes from a full micellar morphology to a mixed morphology of micelles and the brush layer (dewetting) to a full brush layer. While the featureless brush films led to dense and well dispersed AuNP deposition, the dots led to small AuNP clusters for AuNP diameters of about 10 nm. Finally, it was shown that nanofibers can be coated with gold ion-loaded BCPs using drop-coating techniques. In terms of applications in SERS optophysiology, the BCP brush-coated nanofiber with well dispersed AuNP deposition was shown to give a superior performance, as shown by *in vitro* detection of neurotransmitters.

Keywords: SERS, nanofibers, thin films, block copolymers, polystyrene-*block*-poly(4-vinylpyridine), block copolymer brush layers, block copolymer adsorption, dip-coating, substrate curvature, gold nanoparticles, self-assembly.

Table of contents

List of tables

List of schemes

List of figures

List of symbols and abbreviations

APTES	aminopropyltriethoxysilane
θ	angle
AFM	atomic force microscope
G	bicontinuous gyroids
b	block
BCP	block copolymer
BCML	block copolymer micelle lithography
f'	block volume fraction
S	body-centered-cubic spheres
C	constant
CPS	closely packed spheres
CMC	critical micelle concentration
ε_m	dielectric constant of surrounding medium
D	diffusion coefficient
V	dip-coating velocity
DA	dopamine
EM	electromagnetic
$E_{out}(\nu_L)$	electromagnetic field of the incident excitation on molecules
E_0	electromagnetic field of the incident excitation on nanoparticles
$E_{out}(\nu_S)$	electromagnetic field of the Raman scattered light
N	electron density
E	energy
EF_{SERS}	enhancement factor in surface enhanced Raman scattering
C_{ext}	extinction cross-section of nanoparticles
σ^R	extinction cross-section of Raman scattering
χ'	factor accounting for the shape of nanoparticles
FFT	fast Fourier transform
h	film thickness
FEM	finite element method
FDTD	finite-difference time domain

χ	Flory-Huggins segment-segment interaction parameter
v_L	frequency of laser
v_{aS}	frequency of light in anti-Stokes Raman scattering
v_S	frequency of light in Stokes Raman scattering
v_M	frequency of molecular vibrations
Glu	glutamate
GFP	green fluorescent protein
C	hexagonally packed cylinders
ε_i	imaginary part of dielectric constant
I_L	intensity of laser
P	Kruskal-Wallis one-way analysis of variance
L	lamellae
LLD	Landau-Levich-Derjaguin
LSPR	localized surface plasmon resonance
MeOH	methanol
μ	micron
NPs	nanoparticles
M_n	number-average molecular weight
PBS	phosphate-buffered saline
h	Planck constant
P2VP	poly(2-vinylpyridine)
P4VP	poly(4-vinylpyridine)
PEO	poly(ethylene oxide)
PDMS	polydimethylsiloxane
PI	polyisoprene
PLA	polylactide
C_0	polymer solution concentration
PMMA	polymethylmethacrylate
PS	polystyrene
R	radius of fiber
R	radius of nanoparticle
ε_r	real part of dielectric constant

Rms	root mean square roughness
Ra	roughness
SEM	scanning electron microscope
SAM	self-assembled monolayer
$I_{NRS}(\nu_S)$	signal intensity in normal Raman scattering
$I_{SERS}(\nu_S)$	signal intensity in surface enhanced Raman scattering
P_{RS}	signal power of a Raman line
i	square root of negative one
s	statistical
SERS	surface enhanced Raman scattering
γ	surface tension
T	temperature
THF	tetrahydrofuran
$A(t)$	the adsorbed amount of polymer as a function of time
j_s	the flux of the material
N_{surf}	the number of molecules bound to the enhancing metallic substrate
N_{vol}	the number of molecules in the excitation volume of normal Raman scattering
t	time
TERS	tip-enhanced Raman spectroscopy
N	degree of polymerization
TEM	transmission electron microscope
2D	two-dimensional
UV	ultraviolet
η	viscosity
Vis	visible
λ	wavelength of light
M_w	weight-average molecular weight
WT	White and Tallmadge
HEPES	4-(2-hydroxyethyl)-1-piperazineethanesulfonic acid
4-MBA	4-mecaptobenzoic acid

Acknowledgements

I would like to express my deep gratitude to my supervisors, Professor C. Géraldine Bazuin and Professor Jean-François Masson for their guidance and support throughout my PhD journey. I thank them for their kindness, willingness to help and well-wishing for the success of their students. Their enthusiasm to science and loyalty to accuracy is definitely an inspiration to me. Their scientific advice and insightful discussions have helped me a great deal in learning knowledge and focusing my goals. Their encouragement and reassurance have helped me overcome self-doubt and despair at difficult times of the project. Their attention to my work and encouragement to attending conferences is the source of my growing interest and confidence in science. I will always be grateful to their mentorship and hope to become a supervisor like them.

I would like to extend my thanks to the thesis committee members, Professors Anna Ritcey, Robert E. Prud'homme and Christian Pellerin. Their timely, careful and critical reading of the document has helped eliminate every last bit of stubborn mistakes, exaggerations and unclearness from the thesis. I thank them for many helpful questions and suggestions, of which the water contact angle experiment by Prof. Ritcey is particularly helpful in understanding the block copolymer brush films and has become a compelling part in Chapter 3. It is of great honor to have them as witnesses to my graduation and I truly enjoyed the celebration dinner with them on the January 10, 2019.

I would also like to thank our collaborators, Prof. Joachim P. Spatz for his guidance and kind help during my internship, Prof. Louis-Éric Trudeau and Marie-Josée Bourque and Charles Ducrot from his lab for their contribution to the neuron transmitters work in Chapter 2, Prof. Wei Peng and her students Wenli Cui and Li Yu for their contribution in the simulation work in Chapter 2, Prof. Denis Boudreau for many helpful discussions over Skype, and Prof. Russ Algar for his help with quantum dots.

My thanks also goes to the research agents at the chemistry department at UdeM, Patricia Moraille for the assistance on AFM and Ellipsometry, Samir Elouatic for the assistance on Raman spectroscopy, and Sylvain Essiembre for his frequent kind help in the

lab. All of the SEM data was collected at Prof. Antonio Nanci's lab and I, thus, thank him and his team members, Aurélien Fouillen, Alejandra Rodriguez-Contreras and Rima Wazen. Thanks to Prof. Julian Zhu and his team members, Meng Zhang, Kaojin Wang and Hu Zhang, I got to obtain the data on water contact angle, dynamic light scattering and UV-vis spectroscopy.

A big thank you to all the lab members, past and present, in both Bazuin and Masson groups for your kind friendship. Many of them have worked with me and provided me with help and discussions at different stages of my PhD. Without a particular order, in the Bazuin Group, I want to thank Sébastien Roland, Ximin Chen, Xin Wang, Jaana Vapaavuori, Zhida Wang, Anna Gittsegrad, Katia Borozenko, Mahnaz Kamaliardakani, Josué Grosrenaud, Arthur Vas and Rangon Damaëlle. In the Masson Group, I want to thank Alexandra Aubé, Maxime Couture, Hugo-Pierre Poirier-Richard, Julien Breault-Turcot, Sandy Shuo Zhao, Natalia Bukar, Kristy Mckeating, Daniel Pelechacz, Jérémy Labrecque-Carbonneau, Hélène Yockell-Lelièvre, Marc Vidal, Thibault Brulé, Félix Lussier, Mengdi Lu, Xingjuan Zhao, Marie-Pier Dinel, Geneviève Granger, Simon Forest, Simon Laporte, Long Hong, Haifeng Zhou, Benjamin Charron and Gregory Q. Wallace. In the same spirit, I also want thank Xiaoxiao Wang and Nora Chelfouh in Prof. Pellerin's group and Phuong Nguyen Tri, Stéphanie Boissé, Xuewei Zhang, Liliana Jimmenez, Tien Nguyen Dung and Abbas Ghanbari in Prof. Prud'homme's group.

I would like to record an acknowledgement to the various organizations that had offered me prizes and scholarships. I thank Overseas Study Program of Guangzhou Elite Project for a PhD scholarship, FESP and the Chemistry Department of Université de Montréal for complementary PhD scholarships, a conference travel scholarship and a summer school scholarship, and the Fonds de Recherche du Québec–Nature et Technologies (FRQ-NT) for a three-month internship scholarship.

As always, I wish to thank my parents and sisters for their constant love and support.

Chapter 1

Introduction

Nanotechnology is a revolutionary technology where features of nanoscale size are key to achieve applications such as miniaturized sensors and other advanced technological devices. Nanofabrication, the process to generate nanostructures, is at the heart of nanotechnology. Top-down approaches relying on photo- and electron beam lithography are now facing the resolution dilemma, among other limitations such as being cost ineffective and time consuming, as well as having low throughput. Therefore, bottom-up approaches relying on the efficient and spontaneous self-assembly of molecules into ordered structures with nanometer precision are particularly attractive for nanofabrication. Block copolymers represent an important class of self-assembling systems, since a variety of nanostructures can be obtained from block copolymers by tuning their molecular characteristics.

The work in this thesis revolves around the bottom-up nanofabrication of a unique nanosensor for single-cell studies using block copolymer self-assembly thin film templates. This chapter begins with a brief introduction to the localized surface plasma resonance phenomenon and the surface enhanced Raman scattering effect, which are the basis of the nanosensor. Then, we introduce the nanosensor, including the various probes that have been used as platforms for the nanosensor, the employment of the nanosensors in single-cell studies, and the fabrication of the nanosensor using self-assembly templates other than block copolymer films. In the second part of the introduction, we focus on block copolymer self-assembly and their use as templates. Two types of block copolymer thin films will be addressed; namely, relatively thick block copolymer films spontaneously giving rise to surface patterns based on phase separation and ultrathin block copolymer films in the form of an adsorbed or brush layer.

1.1 Localized surface plasmon resonance (LSPR)

The Lycurgus cup manufactured in the 4th and 5th centuries A.D. shows ruby red color in transmission and green color in reflection (Figure 1.1A).[1] This phenomenon is due to the localized surface plasmon resonance (LSPR) effect associated with the gold and silver nanoparticles contained in the glass. While LSPR was used unknowingly for colour decorations by glass workers in ancient times, it is now widely used knowingly for biosensing applications by scientists living in the modern times of nanotechnology, where analytes cause shifts in the LSPR wavelength (Figure 1.1B).

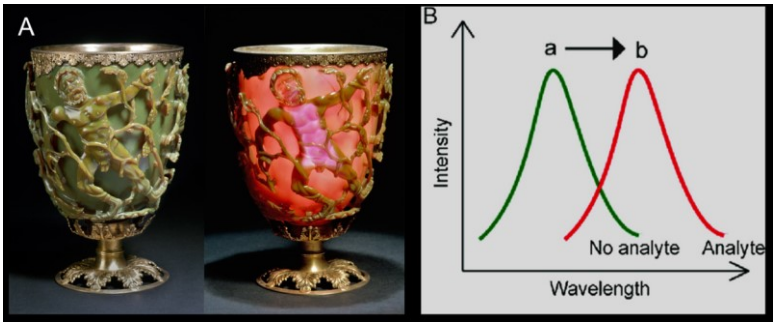

Figure 1.1. A, A Lycurgus cup made in Rome around the 4th century AD, now preserved in the British Museum. The cup contains silver and gold nanoparticles and changes colour from opaque green to translucent red, depending on whether light is reflected or transmitted. B, Shift in peak wavelength of the excitation spectrum of gold nanoparticles, induced by the presence of the analyte that increases the local refractive index, a mechanism now widely used for LSPR sensing. Adapted from the website in Ref. 1.

LSPR is an optical phenomenon exhibited by noble metal nanoparticles (NPs).[2-4] It occurs when the size of the NP (e.g. its radius R) is much smaller than the wavelength of the incident light (λ): $R/\lambda<0.1$.[3] As illustrated in Figure 1.2, when light shines on NPs, the oscillating electric field of light generates a collective oscillation of conduction electrons locally around the surface of the NPs. The oscillation of conduction electrons displaces the electron cloud relative to the nuclei, giving rise to a restoring force by coulombic attraction. As a result, a resonance condition is reached at a specific frequency, leading to the

extinction (absorption and scattering) of light at certain wavelengths. For silver (Ag) and gold (Au) NPs, the surface plasmon resonance frequency falls in the visible region, making them particularly interesting materials for colorimetric sensing applications.[4]

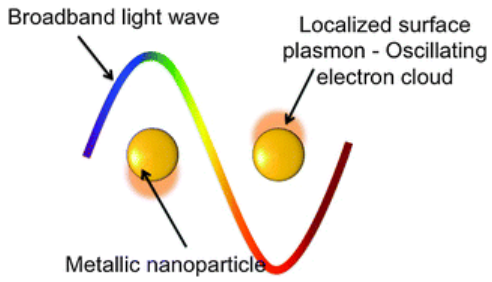

Figure 1.2. Schematic depiction of localized surface plasmons of metal nanospheres. Reproduced with permission from Ref. 2. Copyright (2013), Royal Society of Chemistry.

The LSPR wavelength is not only determined by its material, but it is also dependent on the NP size, shape, and the local dielectric environment. These dependences combine to generate the LSPR spectrum, which can be obtained by using Mie's solution of Maxwell's equation for well separated nanoparticles,[3-4]

$$C_{ext} = \frac{24\pi^2 R^3 \varepsilon_m^{3/2} N}{\lambda \ln(10)} \frac{\varepsilon_i}{(\varepsilon_r + \chi\varepsilon_m)^2 + \varepsilon_i^2} \qquad \textbf{1.1}$$

where C_{ext} is the extinction cross-section, ε_m is the dielectric constant of the surrounding medium, ε_r and ε_i are the real and imaginary parts, respectively, of the complex dielectric constant of the bulk metal ($\varepsilon = \varepsilon_r + i\varepsilon_i$), R is the NP radius and N is the electron density. The factor χ accounts for the shape of the particle, which is assigned a magnitude of two for a spherical particle and can be as large as 20 for particles with high aspect ratios such as nanorods.[3-5]

1.2 Surface enhanced Raman scattering (SERS)

Raman scattering occurs during the inelastic collision of photons with molecules.[6] As illustrated in Figure 1.3, the scattered photon may have the same energy as the excitation photon (Rayleigh scattering). The scattered photon may also gain energy from the molecule (anti-Stokes scattering), or lose it to the molecule (Stokes scattering). In these cases, the scattered photon experiences a change in its frequency, Δv, that is proportional to the energy loss or gain, ΔE, *as* $\Delta v = \Delta E/h$ where h is the Planck constant. This results in the scattered photon frequency, v_S, being shifted relative to the excitation photon frequency, v_L (where L denotes laser). The energy loss or gain gives rise to the characteristic molecular vibrations, hv_M, of the molecule (Stokes: $hv_S = hv_L - hv_M$; anti-Stokes: $hv_{aS} = hv_L + hv_M$;). Therefore, a Raman spectrum comprising several different Raman lines generated by scattering from different molecular vibrations provides a vibrational "fingerprint" of a molecule.

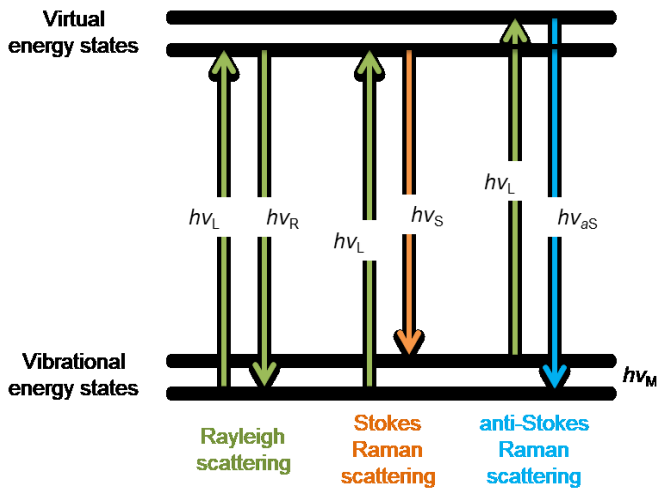

Figure 1.3. Jablonski diagram representing quantum energy transitions at a molecular level for Rayleigh and Raman scattering. In a scattering process, molecules are excited by light to higher virtual energy states; excited molecules then relax and reemit light at the same frequency or shifted frequency, giving rise to Rayleigh and Raman scattering, the latter further including Stokes scattering for energy downshifts and and anti-Stokes scattering for energy upshifts.

The scattering signal power, P_{RS}, of a Raman line depends on the excitation intensity, I_L, and the Raman cross section, σ^R,

$$\mathbf{P_{RS} \sim \sigma^R \cdot I_L} \qquad \mathbf{1.2}$$

However, Raman scattering is a very weak effect, with about 1 in 10^6-10^8 of the incident photons being scattered by the molecules and 1 in 10^3 of the scattered photons being Raman-scattered.[6-8] A typical Raman cross section is between 10^{-30} – 10^{-29} cm^2 per molecule. For comparison, fluorescence spectroscopy exploits effective cross sections between 10^{-17} and 10^{-16} cm^2.[6] Hence, a large number of molecules and/or extremely high laser powers are required to achieve adequate conversion rates from excitation laser photons to Raman photons. Therefore, Raman spectroscopy was considered early-on as a technique for structural analysis, rather than a method for ultra-sensitive trace detection.

In surface enhanced Raman scattering (SERS), however, the Raman signals of molecules are significantly enhanced by placing the molecules in the vicinity of metal nanoparticles.[4] It was first observed by Fleischmann, Hendra and McQuilan in 1974.[9-10] However, the phenomenon was more fully recognized and described by Jeanmaire and Van Duyne,[11] and separately by Albrecht and Creighton in 1977,[12] half a century after the first report on the Raman effect by C. V. Raman in 1928. LSPR of metal nanostructures not only causes the scattering and absorption of light, but it also creates intense local electromagnetic (EM) fields within a few nanometers of the nanostructure surface.[3-4] The EM field is mainly responsible for the enhancement in SERS. The intensity of Raman scattering is proportional to the square of the EM field of the incident excitation, $E_{out}(\nu_L)$, as well as the square of the EM field of the resulting Raman-scattered light, $E_{out}(\nu_S)$. Therefore, the enhancement factor can be calculated by the following equation,[4,13-14]

$$EF_{SERS}(\nu_S) = \frac{\left|E_{out}(\nu_L)^2\right| \left|E_{out}(\nu_S)^2\right|}{E_0^4} \qquad \mathbf{1.3}$$

The enhancement factor can also be calculated from experimental measurements using the following equation,

$$EF_{SERS}(\nu_S) = \frac{[I_{SERS}(\nu_S)/N_{surf}]}{[I_{NRS}(\nu_S)/N_{vol}]} \qquad \textbf{1.4}$$

where $I_{SERS}(\nu_S)$ is the intensity in SERS, $I_{NRS}(\nu_S)$ is the intensity in normal Raman scattering, N_{surf} is the number of molecules bound to the enhancing metallic substrate, and N_{vol} is the number of molecules in the excitation volume of normal Raman scattering.

There are several ways to further increase the EM field, and thus the SERS intensity. The EM field in the gap between two nearby nanoparticles significantly exceeds the EM field on the surface of an isolated particle (Figure 1.4).[3,15] This is because of the coupling of the transient dipoles of the NPs and the coherent interference of their EM fields.[3] These regions are called SERS "hot spots" and are designed and exploited by SERS experts to achieve high enhancements. Hot spots can also be found at sharp points of nanoparticles such as nanostars, arising from the "lightning-rod" effect induced by the higher surface charge density at a sharp point.[15] This observation led to the synthesis of a series of asymmetric nanoparticles. SERS at extremely high enhancement level, mostly using clusters or aggregates of nanoparticles, brings the effective Raman cross section to the same order of magnitude as fluorescence cross sections, and thus enables the measurement of Raman spectra from single molecules.[6]

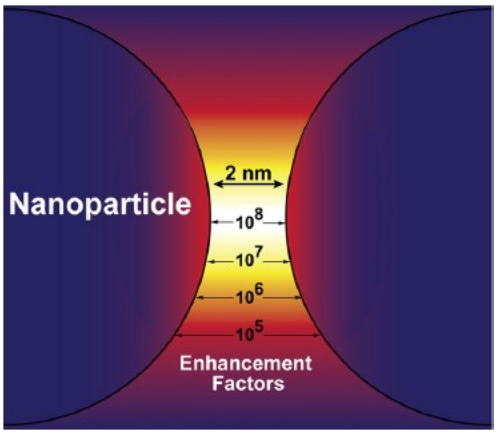

Figure 1.4. Schematic illustration of a "hot spot" for a NP dimer and the rapid change in SERS enhancement factors with respect to relative position. Reproduced with permission from Ref. 3. Copyright (2011), Elsevier.

1.3 SERS nanoprobes for single cell studies

Owing to its high sensitivity, SERS has been utilized to obtain Raman spectral information from complex biosystems rapidly and at high lateral resolution.[16-17] SERS nanopipettes are a recent and exciting application of SERS designed for single-cell studies.[18-28] Many fundamental life processes such as signal transduction, intracellular trafficking, protein degradation and DNA repair occur at the nanometer scale in subcellular compartments. Therefore, it is critical to analyze single living cells. A SERS nanopipette is a desirable tool in this regard because it provides many critical merits: high spatial resolution for detecting chemical details of the heterogeneous compositions of cells, high temporal resolution for monitoring fast cellular dynamics, high sensitivity to detect minute amounts of biochemicals in individual organelles and high specificity to identify targeting biomolecules against complex background signals. It also provides a minimally invasive approach, which is necessary to retain a cell in its native state.

As shown in Figure 1.5, the SERS nanopipette is simply created by immobilizing plasmonic nanoparticles on a tip that is much smaller than cells (tips are tens to hundreds of nanometers in diameter; for comparison, the cross-section of a HeLa cell is more than 20,000 nm). Such miniature sensors allow sensing at subendosomal resolution in a non-destructive fashion.[25-27] Due to the large effective Raman scattering cross section, SERS offers advantages such as short data acquisition times and high sensitivity with minimal sample volumes, all achieved with the use of very low laser powers (high laser power could potentially damage the cells). Furthermore, no labels or other sample pretreatments are required in SERS. Raman provides a fingerprint of molecules and, thus, has the potential for molecule-specific and multiplexed identification of chemical and biological species.[20,22] Bioassays can be used for highly specific SERS sensing in complex cellular environments.[21,29] Correlative sensing between SERS and electrochemical sensing has also been demonstrated.[25] All of these features make SERS on a nanopipette an interesting approach for cell biology, physiology and biophysical studies.

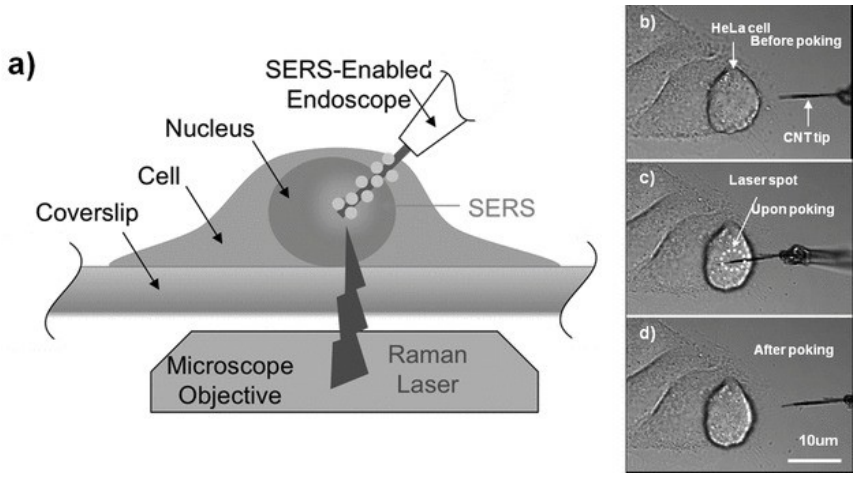

Figure 1.5. Intracellular SERS sensing with a SERS nanopipette. a) Experimental scheme depicting a SERS nanopipette probing the intracellular environment. b-d) Time series showing a HeLa cell b) before the penetration by the SERS nanopipette, c) during SERS analysis after penetration, and d) after the withdrawal of the SERS nanopipette. Reproduced with permission from Ref. 28. Copyright (2011), John Wiley & Sons.

1.3.1 Platforms for constructing SERS nanoprobes

Figure. 1.6 summarizes a collection of nanosized objects that have been employed as platforms for constructing SERS nanopipettes. Glass nanopipettes are a convenient platform for fabricating SERS nanopipettes. They are produced by a laser-based heating and pulling process from glass rods or capillaries of millimeter thickness as well as from optical fibers. They enable the interfacing between a nanostructure and a macroscopic handle and have been used as cellular probes for decades.[30] However, the rigid structure of glass nanopipettes renders them easy to buckle when penetrating a cell. Carbon nanopipettes were therefore developed by Bau and coworkers by using glass pipettes as templates.[31-34] Carbon nanopipettes showed good mechanical and electrical properties in single cell sensing experiments.[31-32,34-35] However, the size of carbon-coated glass nanopipettes is relatively large and their conical shape often causes cell damage. Many researchers have instead employed carbon nanotubes, which can be attached on a glass nanopipette.[25,28,36] Metal nanowires can similarly be attached to a glass nanopipette.[19]

Because metal nanowires are themselves plasmonic nanostructures, no further decoration of nanoparticles is needed in order to make it SERS-active.[19] AFM tips have also been shown to be suitable nanoprobes[37] for cellular studies or for attaching carbon nanotubes.[36]

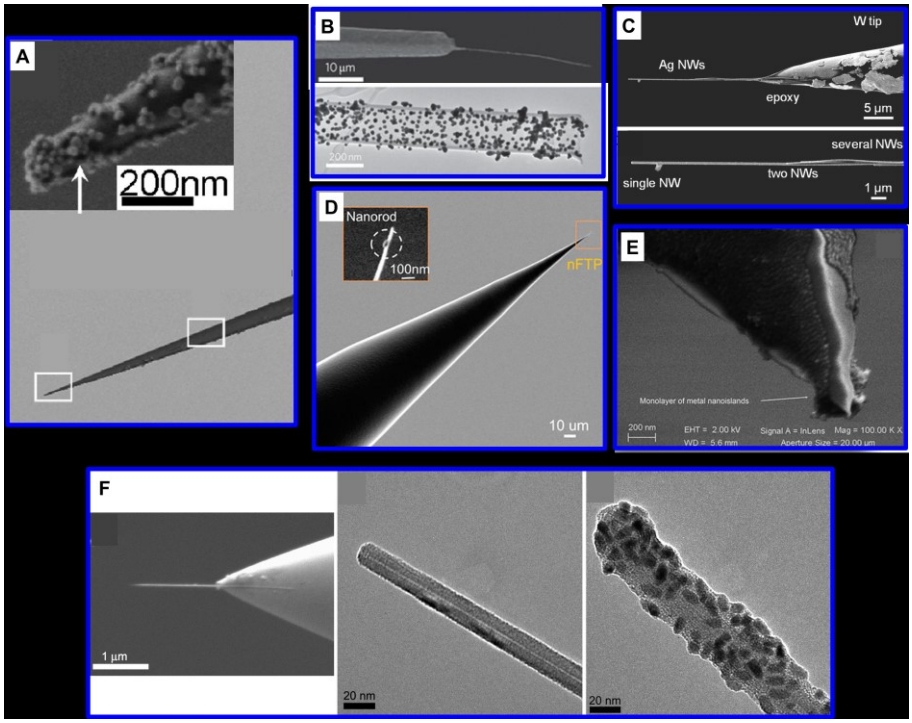

Figure 1.6. Various nanoprobes that have been used as platforms for SERS sensing: A, a glass nanopipette coated with gold nanoparticles. Reproduced with permission from Ref. 23. Copyright (2009), American Chemical Society. B, a gold nanoparticles-coated carbon nanotube attached to a glass nanopipette. Reproduced with permission from Ref. 25. Copyright (2011), Nature Publishing Group. C, a silver nanowire attached to a glass nanopipette. Reproduced with permission from Ref. 19. Copyright (201), John Wiley & Sons. D, a single silver nanorod deposited on a glass nanopipette. Reproduced with permission from Ref. 35. Copyright (2016), American Chemical Society. E, an AFM tip coated with gold nanoparticles. Reproduced with permission from Ref. 36. Copyright (2016), Nature Publishing Group. F, a carbon nanotube coated with quantum dots attached to an AFM tip. Reproduced with permission from Ref. 36. Copyright (2007), United States National Academy of Sciences.

1.3.2 Detection using SERS nanoprobes

SERS nanopipettes can probe heterogeneous content at different specific locations inside living cells. For example, by inserting a SERS nanopipette into the nucleus or the cytoplasm of a single living cell, Vitol *et al.* obtained two distinct SERS spectra with high signal intensities at the two different locations (Figure 1.7a).[23] A dynamic behavior was observed over time by the SERS nanopipette, which allowed the authors to measure time-resolved SERS spectra to uncover the cellular response to KCl stimulation.[23] The dynamic behavior, plus the high temporal resolution of SERS, was also exploited in the Masson group to monitor the extracellular metabolites of a single Madin-Darby canine kidney (MDCKII) epithelial cell.[20] The SERS nanopipette demonstrated the capability of simultaneous detection of multiple metabolites, such as pyruvate, lactate, ATP, and urea, through a bar-coding data analysis process, and the potential for mapping the concentration gradient of the metabolites near cells was demonstrated (Figure 1.7b).[20] Because SERS nanopipettes could only detect molecules that are close to the surface of nanoparticles, the above-mentioned examples rely on weak and nonspecific interactions between molecules and nanoparticles. However, immunoassay capability can be imparted to the SERS nanopipette for the specific capture and detection of targeted molecules.[21] Using the SERS immunoassay sketched in Figure 1.7c, Masson *et al*. have demonstrated the specific detection of IgG by the SERS nanopipette (Figure 1.7d).[21] Such a configuration also benefited from using Raman reporter molecules with their strong and distinct Raman bands as well as from using secondary nanoparticles to further enhance SERS signals.[21] According to some researchers, the future of nanopipette technology is lab-on-a-tip, where a nanopipette can perform several tasks at the same time. Singhal *et al.* reported a multifunctional SERS nanopiette based on carbon nanotubes.[25] In addition to SERS sensing, the electrical conduction of carbon nanotubes allows simultaneous electrophysiological measurements (Figure 1.7e and f) and the hollow nanotube provides channels for fluid transport.

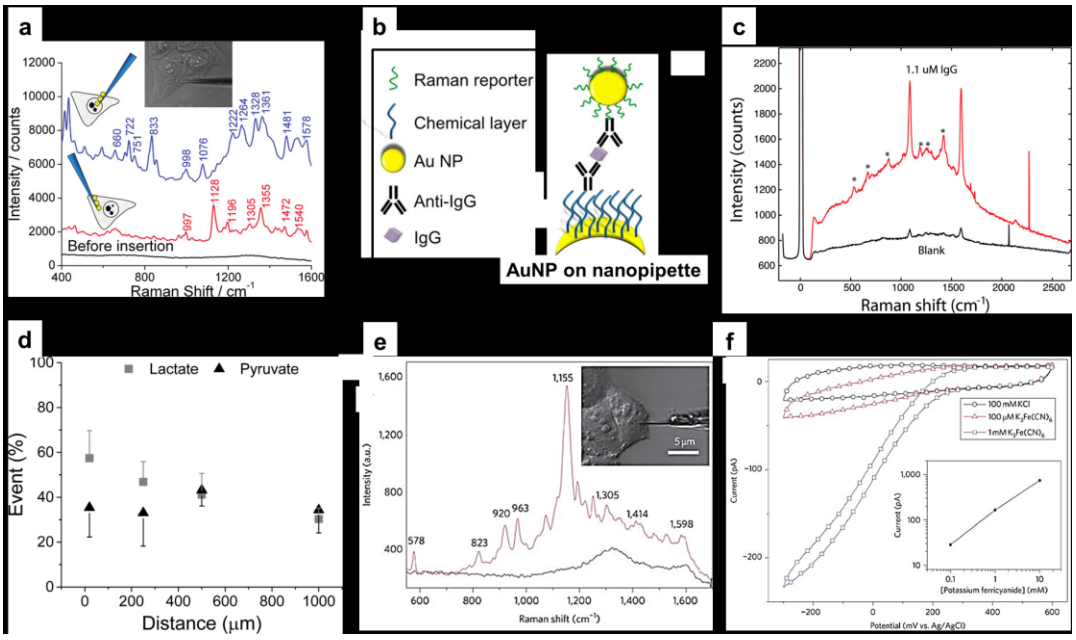

Figure 1.7. a, SERS spectra from the cell nucleus (upper spectrum), cytoplasm (middle spectrum) obtained with the SERS nanopipette, and the blank before insertion. Reproduced with permission from Ref. 23. Copyright (2009), American Chemical Society. b and c, Schematic illustration of the immunoassay on a SERS nanopipette and SERS spectra collected from SERS-nanopipettes in the presence (red) and absence (black) of 1.1 μM IgG. Reproduced with permission from Ref. 21. Copyright (2014), American Chemical Society. d, Plot of relative number of events for lactate and pyruvate near MDCKII cells as a function of nanosensor-cell distance. Reproduced with permission from Ref. 20. Copyright (2016), American Chemical Society. e and f, Simultaneous SERS and electrochemical detection on a SERS nanopipette. Reproduced with permission from Ref. 25. Copyright (2011), Nature Publishing Group.

1.3.3 Fabrication of SERS nanoprobes

1.3.3.1 Aminosilane self-assembled monolayers

As with other SERS substrates, to render the nanoprobes SERS active, it is necessary to coat them with plasmonic nanoparticles. The immobilization is often accomplished through surface modification with functional groups that provide attractive

interactions to nanoparticles. Aminosilane self-assembled monolayers (SAMs) are the most commonly used templates for incorporating nanoparticles to glass and silicon surfaces.[38-42] These bifunctional small molecules can covalently attach to SiO_2 surfaces through silanol bonds with their amine endgroups to attract nanoparticles via electrostatic interactions. Besides silanol bonds, various other interactions, such as hydrogen bonding and electrostatic interactions, exist between aminosilane molecules and the substrate and among aminosilane molecules themselves (Figure 1.8).[43-44] As a result, aminosilane SAMs are multiple layered in nature and often contain loosely attached molecules. In addition, the silanization process is affected by ambient humidity and silane purity, resulting in the formation of oligomers and polymers, which can also react with and attach to the surface.[43] These issues associated with SAMs often lead to irregularities in the AuNPs deposited on them, such as incomplete AuNP coverage and surface AuNP aggregates.[20-21]

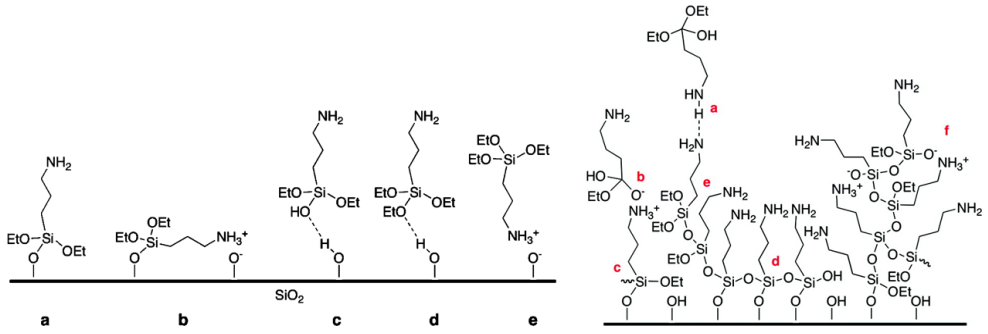

Figure 1.8. Left, different types of interactions between aminosilane molecules and silicon dioxide substrates: (a) a covalently attached aminosilane molecule with its amine group extending away from the interface, (b) the amine group lying on the surface, and (c-e) weakly bonded aminosilane molecules. Right, an aminosilane-derived layer with structural irregularities: individual silane molecules can be incorporated into the layer via (a) hydrogen bonding, (b) electrostatic attraction, (c) covalent bonding, and (d) horizonatal and (e) vertical polymerization with neighbouring silanes; (f) is oligomeric/polymeric silanes attached to the surface. Reproduced with permission from Ref. 44. Copyright (2008), American Chemical Society.

1.3.3.2 Homopolymer templates

Homopolymer films have also been widely used as templates for the deposition of nanoparticles.[45-62] A major advantage in using polymer films is that there are many ways to prepare a homopolymer film on a surface, from simple physical processes such as dip-coating,[45,62] spin-coating,[45] and adsorption[23,49] to chemically bonded coating methods such as end-grafting polymer brushes.[53,57-58] Owing to the high molecular weight of polymers, it is easy to obtain uniform and high coverage films. The electrostatic self-assembly deposition of nanoparticles on polymer films is enabled by functional groups contained in polymer chains. For example, the pyridine groups in poly(vinylpyridine) polymer chains can be protonated to carry positive charges to attract negatively charged nanoparticles[59] and poly(acrylic acid) can carry negative charges under proper pH for positively charged nanoparticles.[59] However, nanoparticles deposited on polymer films typically suffer from different degrees of aggregations.[45-49,53,57-58,60,63] The electrostatic repulsion among nanoparticles tend to prevent nanoparticles from aggregating on the surface. However, this stabilization force is weakened as the substrate dries.[45] On the other hand, polymer films that are capable of attracting charged or metallic nanoparticles necessarily contain many polar groups and are, thus, swollen by, or gain a certain mobility in, aqueous colloidal solutions of these NPs.[45,53,62-63] These combined effects results in the formation of nanoparticle aggregates during the drying of the film.

1.3.3.3 Block copolymer templates

Block copolymer (BCP) thin films can be used to produce highly ordered nanostructures, making them one of the best templates for preparing high-quality SERS chips.[10,64-67] Unlike other film templates introduced above, block copolymer thin films generally show nanopatterns on the film surface due to the block immiscibility leading to a self-assembly phenomenon, as will be described in greater detail in the next section. Using appropriate blocks, these nanopatterns can selectively attract gold nanoparticles and thus the patterns in BCP thin films can be used as scaffolds for the controlled deposition or synthesis of surface NP arrays.[68-70] The high pattern regularity over large areas, high NP density and tunable center-to-center distances on the nanoscale enabled by BCP templates are particularly beneficial for SERS substrates. Therefore, a variety of techniques have been

developed to use self-assembled BCP thin films to produce ordered deposition of nanoparticles,[71-76] as will also be described in the following section. However, so far, most BCP templated SERS substrates have been reported on planar substrates[71-72,77-78] or sometimes curved substrates with low curvature.[79-80] We will explore these templates on highly curved glass nanofibers, in order to make SERS endoscopic probes.

1.4 Block copolymer self-assembly

1.4.1 Microphase separation of diblock copolymers

Linear diblock copolymers are the simplest class of block copolymers. They are composed of two chemically distinct, usually immiscible, polymer chains which are covalently bound together at one end.[81-86] Some examples of diblock copolymers are polystyrene-b-poly(methylmethacrylate) (PS-b-PMMA; most studied system for nanolithography),[87-88] polystyrene-b-poly(4-vinylpyridine) (PS-b-P4VP), most studied system for supramolecular self-assembly and used in this thesis),[89-94] polystyrene-b-poly(ethylene oxide) (PS-b-PEO), polystyrene-b-polylactide (PS-b-PLA),[95-96] polystyrene-b-polyisoprene (PS-b-PI),[97-98] and polystyrene-b-polydimethylsiloxane (PS-b-PDMS, silicon containing block copolymer),[99-100] to name but just a few (Figure 1.9).

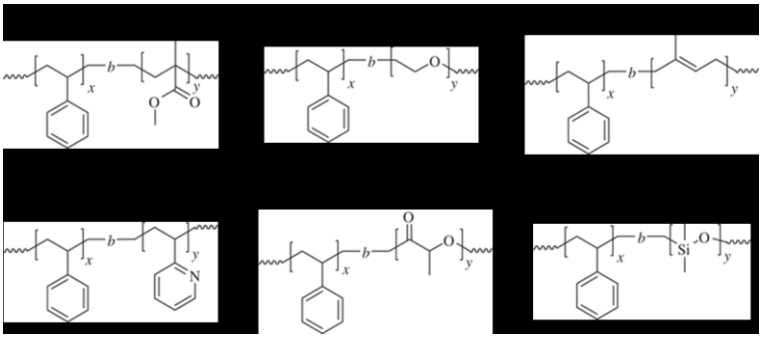

Figure 1.9. Chemical structures of some common diblock copolymers.

Because of block immiscibility and the covalent connection between blocks that does not allow large-scale phase separation, BCPs are subject to what is termed microphase

separation, resulting in the spontaneous formation of various types of ordered nanostructures.[101-102] (The adjective "microphase" is commonly used where nowadays "nanophase" would be used, because at the time of the discovery of the phase behavior of BCPs, micro was considered very small.[102]) Figure 1.10 shows the theoretical thermodynamic phase diagram for diblock copolymers, which depicts the conditions under which various microphase-separated morphologies are obtained, including body-centered-cubic spheres (S, S'), hexagonally packed cylinders (C, C'), bicontinuous gyroids (G), and lamellae (L), as well as a disordered region where the blocks are miscible.[103-106] The characterization of phase equilibria in a BCP melt is determined by two parameters: the block volume fraction f and the product χN, where χ is the Flory-Huggins segment-segment interaction parameter between two blocks and N is the degree of polymerization. The size of the domain is dictated by N and the morphology is dictated by f. The lower limit of the microdomain size is set by the condition (for symmetric BCPs) that χN=10.5, below which the BCP blocks will mix, forming a homogeneous or mixed-phase morphology.

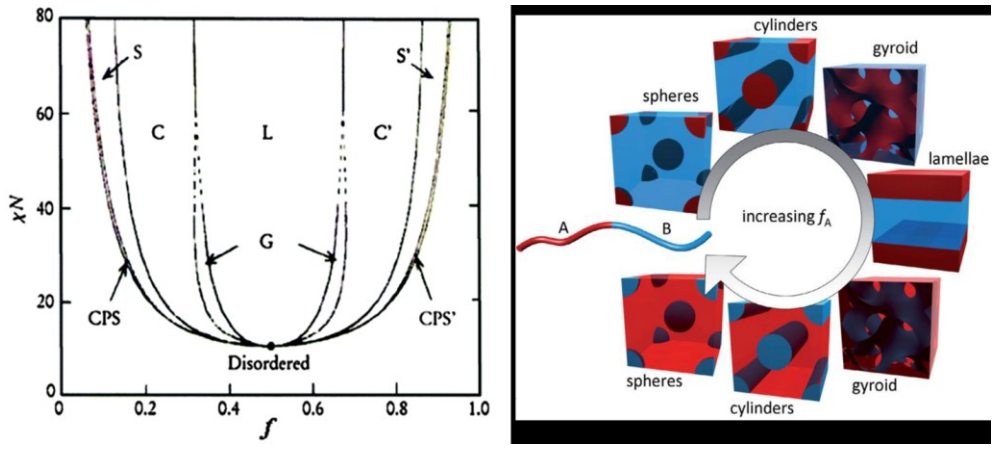

Figure 1.10. Self-consistent mean-field theoretical phase diagram of diblock copolymers at equilibrium in the melt. χN is the segregation parameter and f is the volume fraction of one block. The equilibrium morphologies depend on f: CPS and CPS' = closely packed spheres, S and S' = body-centered-cubic spheres, C and C' = hexagonally packed cylinders, G = bicontinuous gyroids, L = lamellae. Reproduced with permission from Ref. 86. Copyright (2016), John Wiley & Sons.

1.4.2 Block copolymer thin films

Block copolymer thin films are of particular interest because of the possibility of obtaining two-dimensional patterns with very high registry and regularity, providing suitable templates for surface nanopatterning (Figure 1.11, top).[81-85,103,107-114] For example, a pattern of hexagonal dots can be achieved by using sphere-forming BCP thin films or cylinder-forming BCP thin films where the cylinders are aligned vertically relative to the substrate.[115] Cylinders lying parallel to the surface and lamellae standing perpendicular to the surface can be used for producing line patterns.[116] Owing to the nanoscale dimensions of BCP patterns (typically 10–100 nm), BCP thin films are a promising approach for the nanofabrication of next-generation microelectronics.[117-122] Driven by this goal, a great deal of research has been devoted to BCP thin films and their use for achieving nanoparticle arrays or patterns, as summarized by a number of reviews.[83-86,103,108-112,114,123-124] There are two basic nanofabrication strategies based on BCP thin film surface patterning, including the transfer of BCP patterns to underlying substrates by using BCP films as masks for nanolithography (Figure 1.11 bottom)[125-131] and the position-selective deposition of nanoparticles (NPs) on BCP domains,[10,67,132-134] the latter being addressed in detail in the following section.

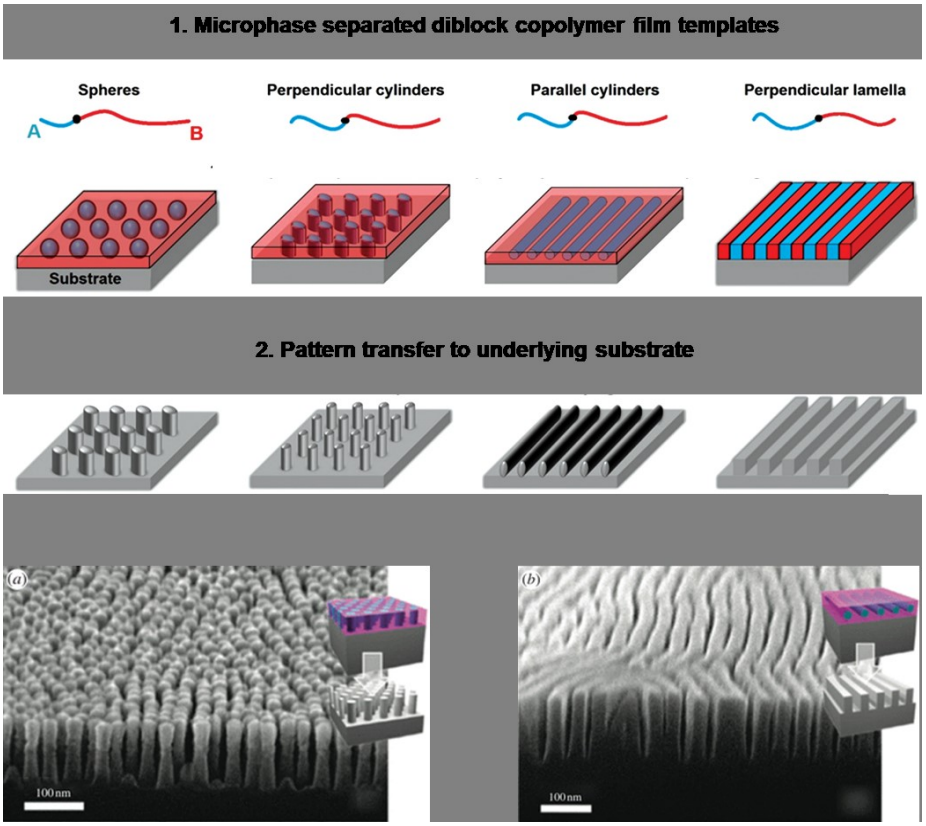

Figure 1.11. Top, Schematic representation of microphase-separated BCP thin film patterns. Reproduced with permission from Ref. 86. Copyright (2016), John Wiley & Sons. Bottom, pattern transfer to the underlying substrate by using BCP films as photolithographic masks. Reproduced with permission from Ref. 116. Copyright (2011), American Chemical Society.

1.4.3 Fabrication of NP arrays using BCP film templates

Four different approaches have been used to fabricate NP arrays via BCP thin films, namely direct deposition of NPs on BCP thin films,[73] back-filling of NPs,[135] on-site synthesis of NPs,[76,136] and preloading of NP precursor into BCP micelles.[71]

1.4.3.1 Guided deposition of NPs on BCP thin films

The first approach involves using BCP thin film surface patterns to guide the ordered deposition of NPs. Its advantage lies in the broad variety of NPs accessible by

colloidal chemistry. Hexagonally arranged nanoparticles can be templated by BCP films that have spherical[137] or vertical cylindrical[73] morphologies and parallel lines of nanoparticles can be templated by BCP films with horizontal cylindrical[138] or vertical lamellar[139] morphologies. Depending on the size match between nanoparticles and the BCP nanodomains, arrays of both single NPs and NP clusters have been reported on BCP thin films.[73-74,137,140]

Yap *et al.* reported the fabrication of gold nanoparticle (AuNP) cluster arrays on Si surfaces using a spin coated polystyrene-b-poly(2-vinylpyridine) film template (Figure 1.12).[137] The film consisted of a monolayer of quasi-hexagonally ordered micelles with P2VP cores and PS coronae. The P2VP domains were positively charged in an acid environment and electrostatically attracted negative citrate capped AuNPs. Because the lateral dimensions of the P2VP domains were many times larger than the AuNPs used, clusters of AuNPs formed on each micelle, leading to the ordered deposition of AuNP cluster arrays. To tune the number of AuNPs on each micelle, the authors exposed the templates to oxygen plasma in a reactive ion etcher, which reduced the P2VP domain size and, thereby, the cluster size. The obtained substrates showed excellent SERS performance with enhancement factors of the order of 10^8, due to the high density of SERS hot spots in AuNP clusters, and the SERS signal intensities were found to systematically increase with increase in AuNP cluster size.

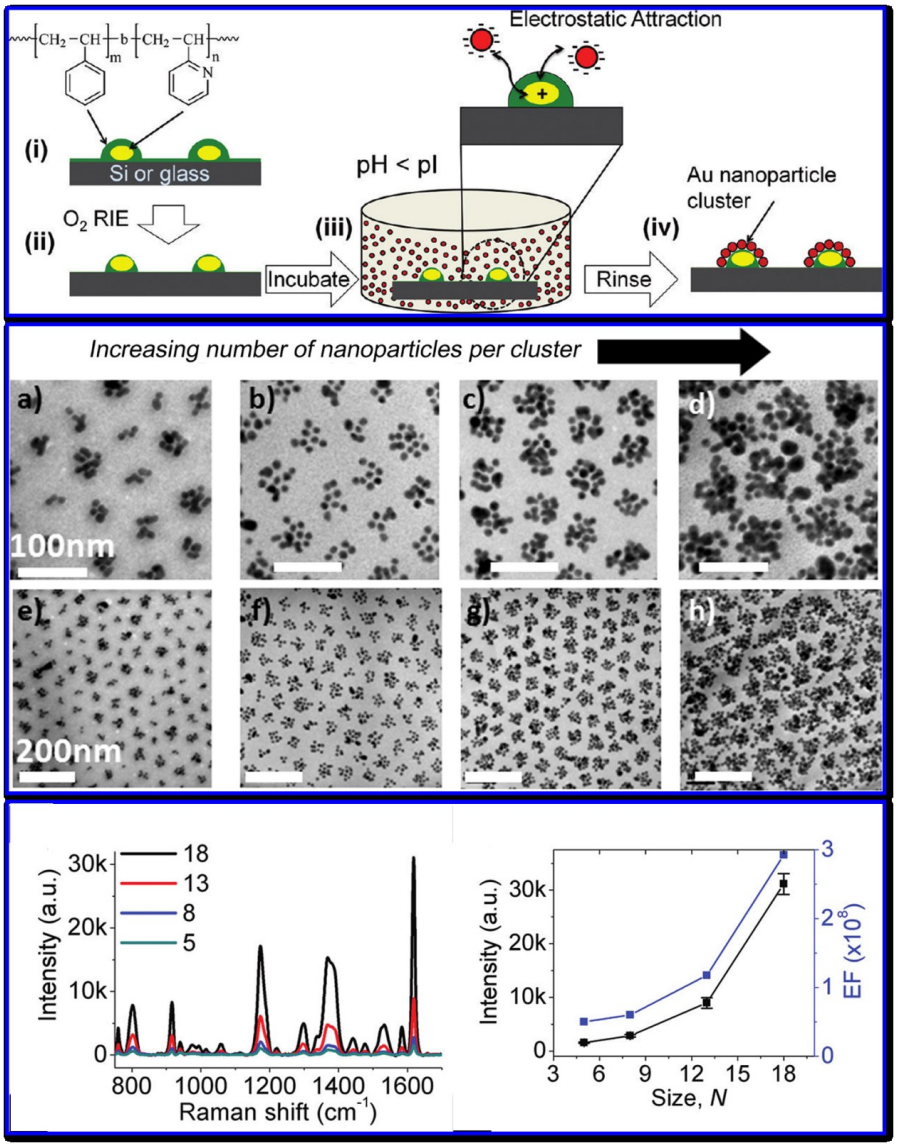

Figure 1.12. Top panel, schematic illustration of templating AuNP cluster arrays using PS-b-P2VP thin films: (i) spin-coating a BCP film; (ii) feature size reduction by oxygen plasma reactive ion etching; (iii) incubation in AuNP colloid at pH 5.8; (iv) formation of AuNP clusters of various sizes. Middle panel, plain-view TEM images of high (a, b, c and d) and low (e, f, g and h) magnifications showing AuNP clusters with systematically increasing number of AuNPs per cluster. Bottom panel, SERS spectra of crystal violet measured on AuNP cluster arrays of increasing cluster size (left) and the most intense peak and the calculated enhancement factors as a function of cluster size (right). Reproduced with permission from Ref. 137. Copyright (2012), American Chemical Society.

Although the overall arrangement of AuNP clusters is ordered, the arrangement and spacing of the AuNPs in each cluster are uncontrolled. To control order on the single AuNP level, there must be a one-to-one registry between each AuNP and the BCP domains. This was shown by Lee *et al*. who used PS-b-P4VP that forms P4VP cylinders in a PS matrix to prepare thin films by spin-coating and solvent annealing so that the cylinders aligned perpendicular to the substrate (Figure 1.13).[73] Thus, the film had a surface pattern of hexagonal P4VP circular domains with a diameter of 20 nm. In order to achieve one-to-one registration, it was found necessary to crosslink the P4VP domains first by treating the film with a 1,4-dibromobutane vapour and also use gold nanospheres slightly larger than the P4VP domains. In order to obtain other AuNP sizes without having to change the BCP characteristics, the authors used seed-growth chemistry to enlarge the deposited nanoparticles. During the growth process, the gap between nanoparticles was systematically reduced, which allowed the LSPR wavelength to be tuned to maximize the SERS signal strength.

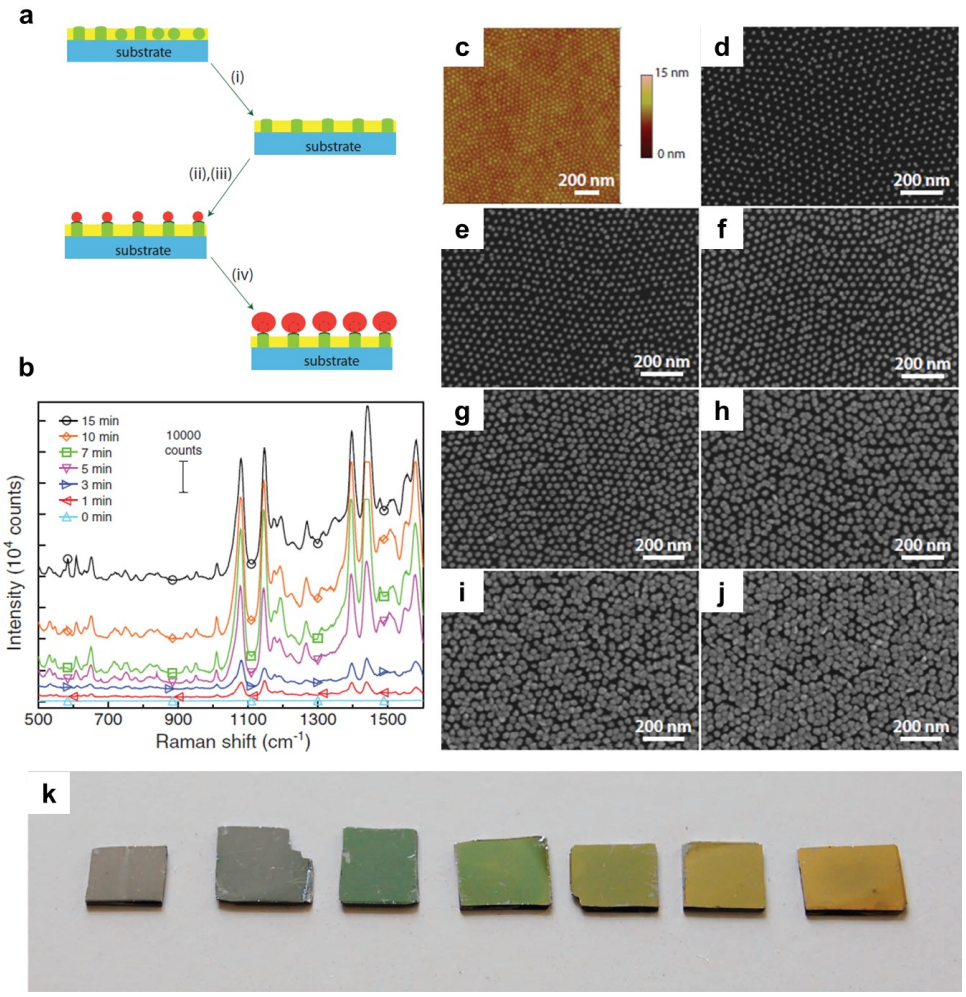

Figure 1.13. a, SERS substrate fabrication scheme: i) solvent annealing of spin-coated PS-b-P4VP film leading to vertically oriented P4VP cylinders in PS matrix; ii) crosslinking of P4VP domains; iii) AuNP colloidal adsorption (seed); iv) AuNP growth. b, SERS spectra of 4-aminobenzenethiol on the SERS substrates at different AuNP growth times. c, AFM height image of the PS-b-P4VP film. d-j, SEM images of AuNP arrays on the PS-b-P4VP films after different growth times: d) 0 min, e) 1 min, f) 3 min, g) 5 min, h) 7 min, i) 10 min and j) 15 min. k, Photographs of SERS substrates fabricated on Si with increasing AuNP growth time from left to right under white light illumination. Reproduced with permission from Ref. 73. Copyright (2011), John Wiley & Sons.

1.4.3.2 Back-filling

In the back-filling approach, the BCP film is first transformed into a nanoporous film by appropriate surface reconstruction and then nanoparticles are deposited into the pores (Figure 1.14).[132,135,141-144] The surface reconstruction can be achieved by treating the film with a solvent that is selective towards the block of which the nanostructure is composed. For example, Stamm *et al.* used ethanol to rinse PS-b-P4VP dip-coated thin films having P4VP cylindrical nanostructures and obtained hexagonally ordered pores from vertically aligned P4VP cylinders.[70,132] Palladium nanoparticles were back-filled into the pores and after the removal of the polymer film, ordered arrays of Pd nanoparticles were obtained on the surface. By the same token, they also achieved nanowires composed of palladium nanoparticles by using thin films with horizontally aligned cylinders and vertically aligned lamellae.[132]

For back-filling, nanoparticles of much smaller size than the BCP nanostructures have to be used, in order to fit into the pores. The NPs can be attracted into the pores through electrostatic interactions, but the process can also be driven by capillary force.[133,141] For example, Russell and co-workers have shown the assembly of sub-10 nm CdSe nanoparticles into porous PS-b-PMMA thin film templates by use of capillary forces.[141] The pores were created by UV irradiation of a PS-b-PMMA film with vertically aligned PMMA cylinders, followed by washing with acetic acid. By immersing the film in a dilute nanoparticle solution and slowly withdrawing it from the solution, capillary forces sequestered the nanoparticles into the pores. The efficiency of the deposition is affected by the size of the nanoparticles relative to the pore diameter, solution concentration, rate of removal, and solvent evaporation rate.[141]

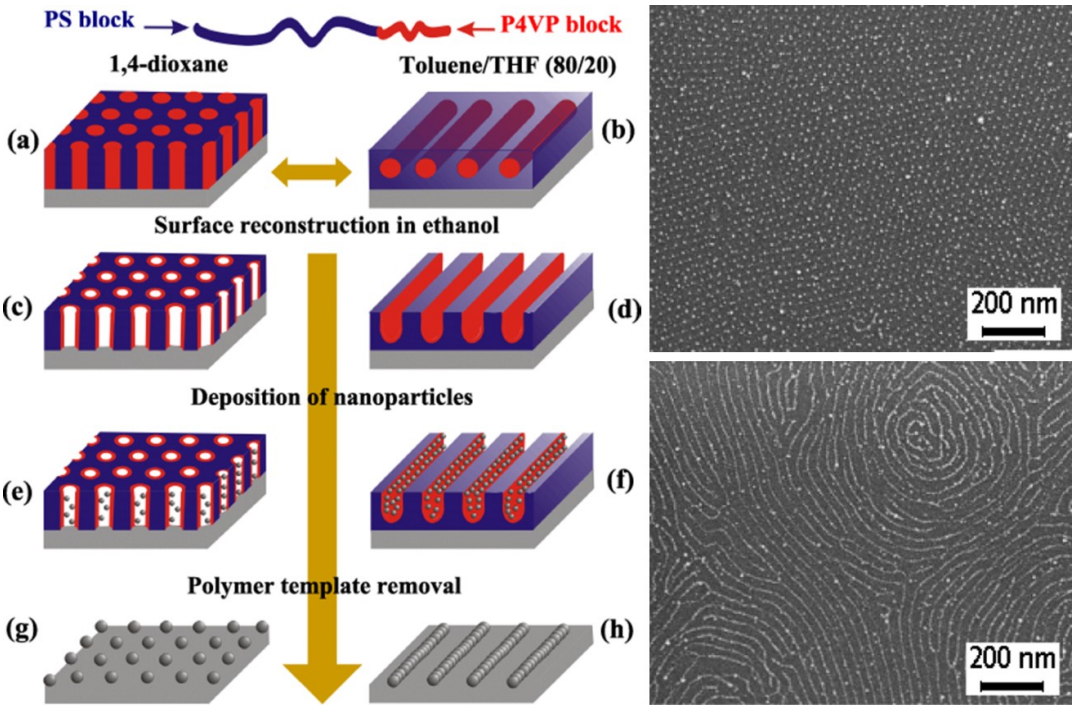

Figure 1.14. Left, schematic sketch of the back-filling fabrication process: solvent annealed block copolymer thin films are transformed into nanoporous films by exposure to ethanol leading to surface reconstruction, followed by the deposition of nanoparticles into the pores and then polymer removal. Right, HRSEM images of palladium nanodots and nanowires templated by block copolymer thin film back-filling process. Reproduced with permission from Ref. 132. Copyright (2009), IOP Publishing.

1.4.3.3 On-site synthesis of NPs in BCP films

Precursors of metal NPs in the form of metal ions can also be sequestered selectively in the spatially defined nanodomains of BCP thin films, and a subsequent metal reduction reaction leads to the on-site synthesis of NPs in the film and the formation of NP arrays on the surface.[75-76,145] The reduction occurs spontaneously between some semiconductor surfaces and metal ions through galvanic displacement upon contact, e.g. Ag on Ge(100), whereas additional reagents, such as HF, are required for other surfaces and metal ions. Cu, Au, Pt and Pd nanoparticle arrays have been patterned on semiconductor surfaces by Aizawa *et al.* (Figure 1.15).[76]

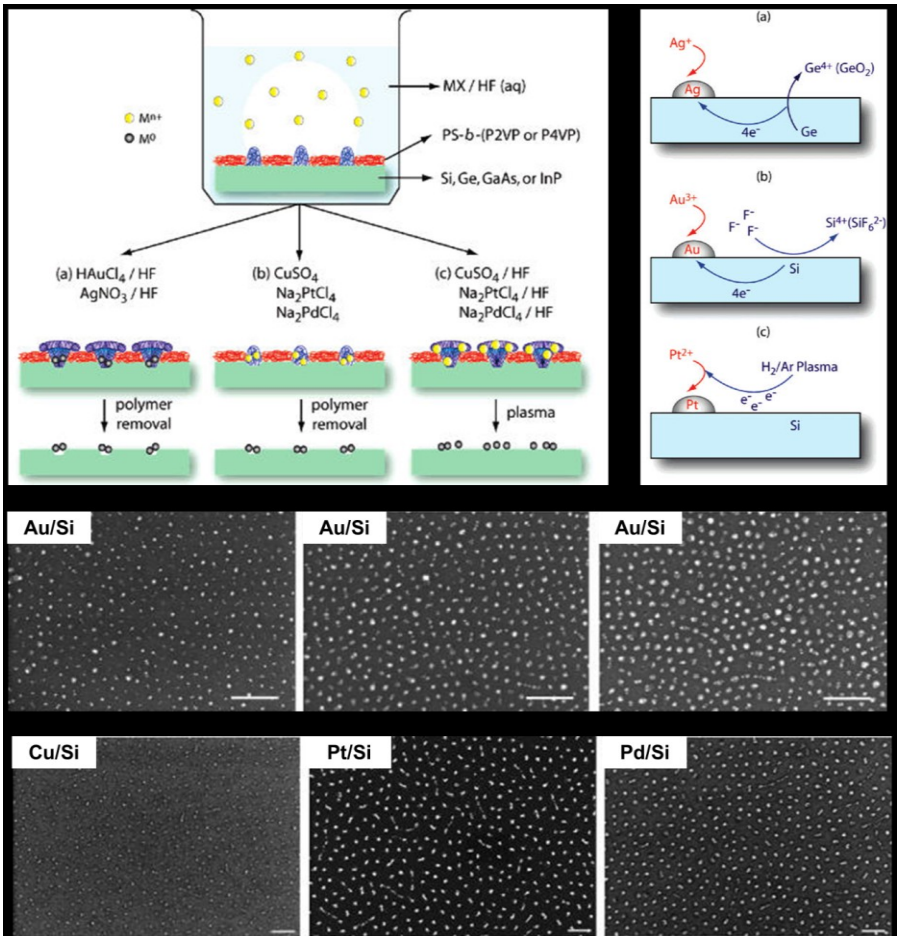

Figure 1.15. Top, scheme illustrating guided deposition of metal ions in BCP thin films and the galvanic displacement process to induce nanoparticle formation. Middle row, SEM images of AuNPs of different sizes and, bottom row, Cu, Pt and Pd nanoparticles on Si, all achieved by using the illustrated approach. Scale bars represent 200 nm in the middle images and 100 nm in the bottom images. Reproduced with permission from Ref. 76. Copyright (2007), American Chemical Society.

1.4.3.4 Preloading metal ions into micelles

The incubation of a BCP film in a precursor solution shown above often alters the BCP film, causing unwanted changes in the template or order disruption in the BCP patterns. To avoid this, metal ions can be incorporated into BCP micelles in solution before

film formation. For example, Spatz *et al.*[71] reported the fabrication of Au, Pt and Pd nanoparticle arrays on Si, where nanoparticle precursor salts were preloaded selectively into the P2VP cores of PS-b-P2VP micelles via electrostatic interactions, followed by dip-coating of a substrate into this solution, to obtain a film on the substrate. Highly hexagonally ordered monolayer arrays of micelles were obtained in the film, from which ordered arrays of nanoparticles were obtained by plasma reduction and polymer removal (Figure 1.16). The size of the clusters could be varied between 1 and 15 nm, depending on the concentration of the metal salt. The interparticle distance could be varied between 30 and 140 nm by using BCPs with different block lengths. Seed-growth chemistry can be used for NP enlargement.[71,73] It was found that NPs larger than 50 nm tend to lift off from the surface after the removal of the polymer template. However, partially preserving the BCP film by using short plasma treatment times was found to improve the immobilization of the NPs.[71] Alternatively, a silanol SAM can also be used for NP immobilization in the case of complete BCP film removal.[71]

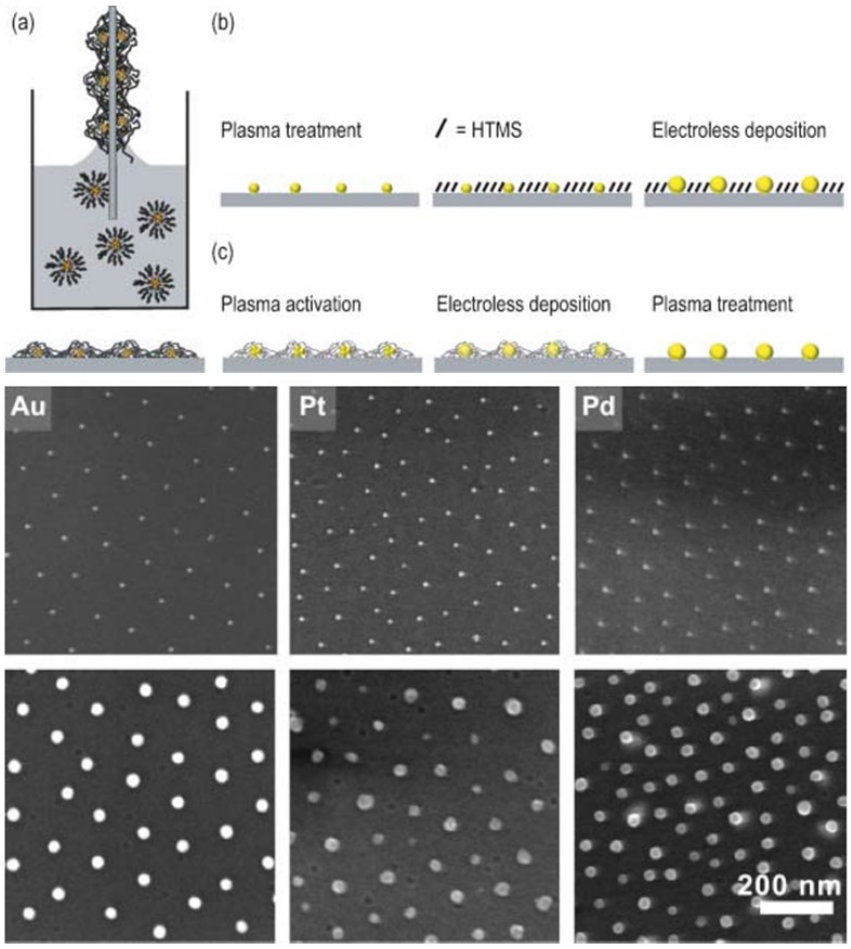

Figure 1.16. Top, schematic illustration of BCP templating: a, formation of a monolayer from preloaded micelles by dip-coating; b, the simultaneous formation of nanoparticles and complete removal of BCP film by plasma, followed by SAM surface derivatization and nanoparticle enlargement; c, partial BCP film removal by plasma and enlargement of nanoparticles, followed by complete BCP film removal. Bottom, SEM images of Au, Pt and Pd nanoparticles on glass cover slips before (top row) and after particle growth (bottom row). Reproduced with permission from Ref. 71. Copyright (2008), John Wiley & Sons.

1.5 Preparation of BCP thin films using dip-coating

BCP thin films can be prepared by both spin-coating and dip-coating techniques. Spin-coating is done by depositing drops of a BCP solution in a volatile organic solvent on

a spinning solid substrate and a film spreads by centrifugal forces coupled with rapid solvent evaporation. Spin-coating is suitable for substrates of uniform flatness, but not for curved substrates. Dip-coating is done simply by withdrawing a substrate from a polymer solution and can thus be done with non-flat substrates. In both techniques, the film thickness can be controlled through the substrate moving speed, the concentration of the block copolymer solution and the volatility of the solvent. Dip-coating offers many advantages over spin-coating such as simplicity of use, minimal loss of solution, and ability to coat irregular surfaces. For block copolymer films, it has the further advantage that it allows a variety of nanostructured films to be obtained directly (see below), whereas spin-coating generally requires thermal or solvent annealing to obtain a variety of nanostructured films.

1.5.1 "V" relationship in dip-coating

In dip-coating a film, surface tension (γ) and viscosity (η) play opposing roles in determining the film thickness, resulting in a balanced film thickness (h) that also depends on dip-coating rate (V), which has long been described by the Landau-Levich model, which is strictly applicable for Newtonian liquids,[146]

$$h = C\,(\eta V/\gamma)^{2/3} \qquad \textbf{1.5}$$

where C is a constant that takes into account the influence of gravity and the geometry of the substrate. The term in parentheses, $\eta V/\gamma$, is conveniently referred to as the capillary number in dip-coating.[147] It can be immediately seen that the film thickness increases with dip-coating rate. Recently, however, Grosso and co-workers discovered an opposite trend when dip-coating sol-gel films at unusually slow rates (typically 1-10 mm/s).[148-152] This has been explained by a capillarity feeding mechanism: the drying film induces a capillary force, on the condition that the drying line is not above the polymer solution meniscus which is met when the substrate withdrawal rate is slower than the solvent evaporation rate. Therefore, an overall "V"-shaped relationship between film thickness and dip-coating rate is observed for dip-coated films. Roland *et al.* were the first to confirm the "V" relationship for dip-coated BCP films involving various solvents.[89-90,94,153] The V shape results in a minimum film thickness on the curve that changes with changing solvents (Figure 1.17).[153]

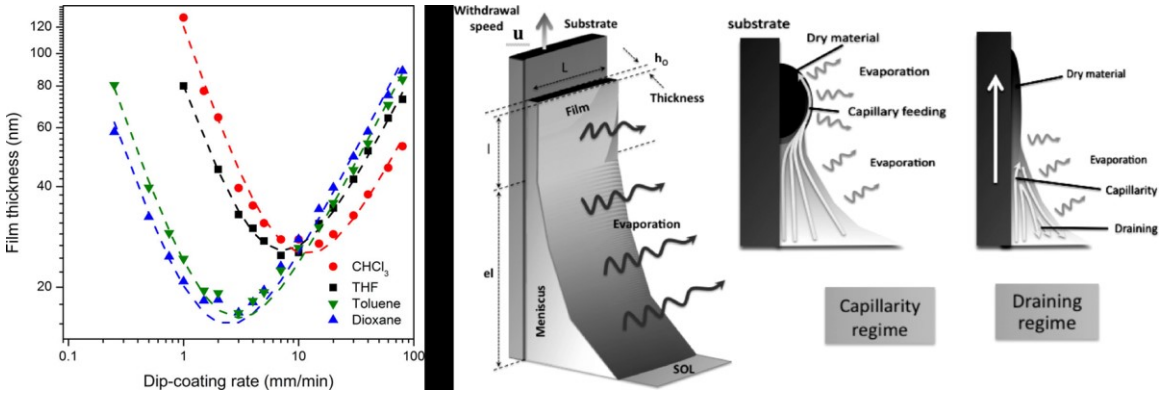

Figure 1.17. Left, Film thickness as a function of dip-coating rate from NCOOH-containing solutions of PS-b-P4VP (10 mg/mL BCP concentration, equimolar NCOOH:VP), where NCOOH is naphthoic acid. Reproduced with permission from Ref. 153. Copyright (2015), American Chemical Society. Right, Schematic illustration of the two different machenisms of film formation in the capillarity regime and draining regime during dip-coating. Reproduced with permission from Ref. 149. Copyright (2010), American Chemical Society.

1.5.2 Substrate curvature effect in dip-coating

When dip-coating a cylindrical substrate, the surface curvature is another factor that affects the film thickness, as found in various studies on fluid coatings on fibers.[147] Both the Landau-Levich-Derjaguin (LLD) model and the LLD model modified by White and Tallmadge (WT-LLD) describe a close to linear dependence of film thickness on the radius of the fiber (R) in the common capillary number range between 0.001 and 0.1. The WT-LLD model agreed fairly well with experimental data obtained by Ryck and Quere for fluid coatings on fibers for various wires and viscous silicone oils (Figure 1.18).[147] To our knowledge, this effect has never been studied for dip-coated BCP films, although it was mentioned in one publication that higher dip-coating velocities are needed to achieve the same film thickness on curved surfaces as on flat surfaces.[80]

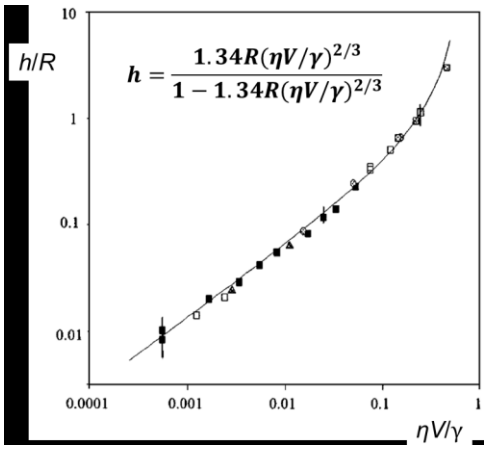

Figure 1.18. Relation between film thickness and capillary number for fibers of various radii and coating solutions of various viscosities (represented by the symbols). All the data obey the WT-LLD model (the inset equation and the solid curve) and show a near linear dependence between film thickness and capillary number in the capillary number range from 0.001 to 0.1. Reproduced with permission from Ref. 147. Copyright (1999), Annual review of fluid mechanics.

1.6 Adsorbed block copolymers

Amphiphilic block copolymers have remarkable ability to adsorb at liquid-solid interfaces, forming ultrathin films. One major achievement in this thesis is the finding that block copolymer adsorbed films are suitable templates for the deposition of NPs. Thus, this section introduces basic concepts related to the adsorption of block copolymers on surfaces. Certain aspects of adsorbed homopolymer films and end-grafted polymers are helpful in understanding adsorbed block copolymer films and some findings to be described in this thesis, and thus will be briefly described first.

1.6.1 Adsorbed homopolymer films

Polymer adsorption can apply to many polymers and surfaces via non-covalent interactions, such as electrostatic attraction, hydrogen bonding, polar-polar interactions, and hydrophobic interactions. A polymer chain adsorbs to a surface through its segments.

Because of the large number of segments or repeat units in a polymer chain, which allows multiple points of contact between the chain and the surface, the adsorption energy associated with polymer adsorption is high, resulting in strongly adsorbed polymer chains on surfaces even against good solvents.[154-155]

On the other hand, not all repeat units of the homopolymer make direct contact with the surface. In fact, Figure 1.19 shows a typical configuration of an isolated, linear, long, flexible homopolymer chain adsorbed on a flat surface.[156-157] The sections of the polymer chain that are in direct contact with the substrate are termed 'trains' and they are responsible for the immobilization of the polymer on the surface. Between the trains, there are 'loops', which are chain sections that are not in direct contact with the surface. Polymer chain ends that are dangling from the surface are called 'tails'. The proportions of each type of chain portions are determined by the molecular weight and flexibility of the polymer as well as the strength of the adsorption force and they, in turn, determine the thickness and stability of the polymer film.[156,158]

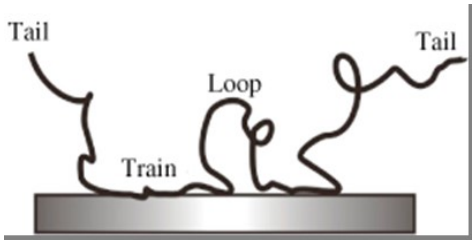

Figure 1.19. Homopolymer chain physically adsorbed on a surface, showing a configuration consisting of tails, loops and trains. Reproduced with permission from Ref. 157. Copyright (2008), IOP Publishing.

1.6.2 End-grafted polymer brush

End-grafted polymer chains are covalently attached to the surface by one end, leaving dangling chains.[159-165] An important aspect that affects the surface structure of such chains is their grafting density. According to a scaling theory describing this, which was first proposed by de Gennes,[161, 166] these chains can adopt three different structures

depending on grafting density. As shown in Figure. 1.20, at low grafting density, the distance between isolated chains is large compared to their radius of gyration. In this case, there is little interaction between adsorbed chains, and the chain structure is therefore determined by the affinity between the polymer segments and the substrate. While non-adsorbing polymer chains adopt a 'mushroom' conformation, adsorbing chains adopt a 'pancake' one. When the grafting density is sufficiently high, strong interchain repulsion and spatial restrictions cause the chains to adopt a more extended conformation, known as the 'brush' conformation.

Figure 1.20. Schematic picture of three limiting structures of chemically end-grafted polymer chains. Reproduced with permission from Ref. 157. Copyright (2008), IOP Publishing.

End-grafted polymer films are capable of producing distinct surface nanopatterns for templating as well as nanolithography.[167-172] The pattern is often achieved by controlling the solvent quality towards the polymer chains, in conjunction with the grafting density.[172] For example, Tebbe *et al.* presented a method termed homopolymer nanolithography, where they produced a variety of surface patterns in grafted PS homopolymer films on planar gold surfaces by controlling the surface grafting density and solvent quality.[172] As shown in Figure 1.21, the polymer chains were grafted on the surface in a good solvent. Thus, they initially adopt a brush conformation. Upon switching the solvent to a poor solvent, the chains collapse and form nanostructures that depend on grafting density, including spherical nanostructures at low grafting density, worm-like nanostructures at medium grafting density, and porous nanostructures at high grafting

density. By grafting different kinds of polymers in the same film, the incompatibility of those polymer chains can also lead to nanopatterns.[167-168,170]

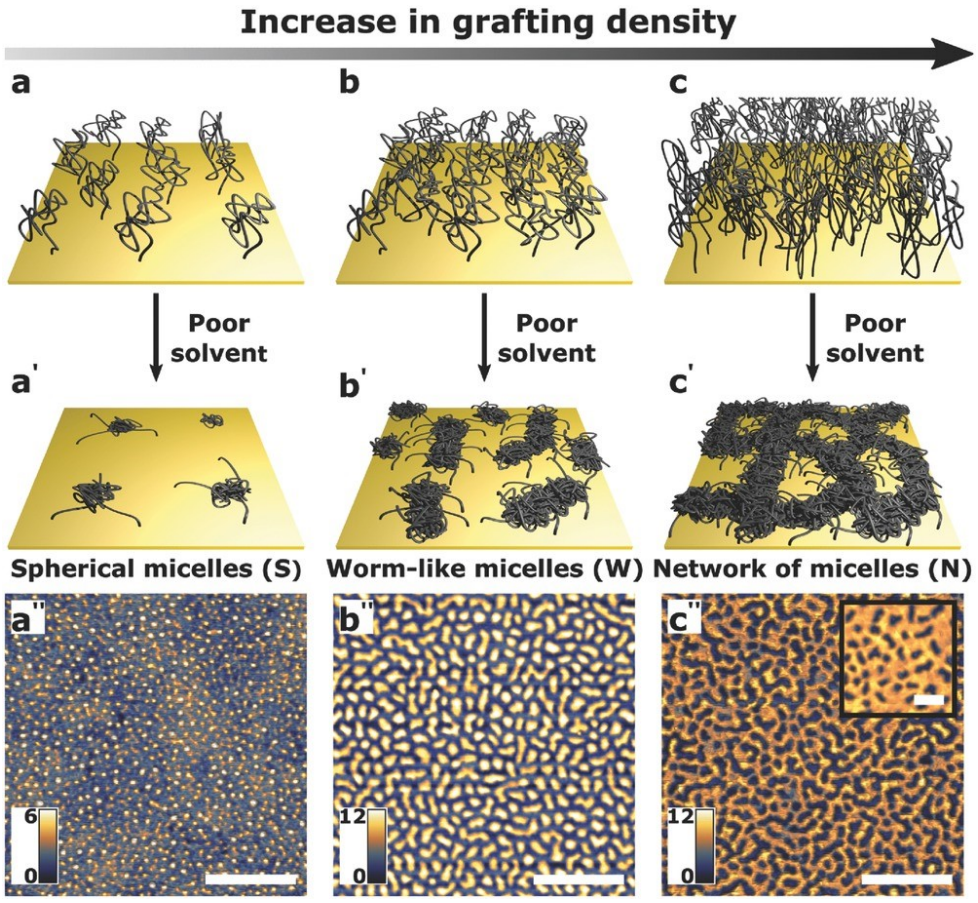

Figure 1.21. Nanopatterning in end-grafted homopolymer film. Top, Schematic of polymer end-grafted molecules in a good solvent at a) low, b) medium, and c) high grafting density. Middle, Schematic of polymer surface segregation in a poor solvent into a′) spherical, b′) worm-like, and c′) network nanostructures. Bottom, Representative AFM images end-grafted polymer films of PS-50K with surface patterns at different grafting densities. Scale bars in panels (a″)–(c″) are 300 nm. The inset in panel (c″) shows the porous structure. Scale bar is 100 nm. Reproduced with permission from Ref. 172. Copyright (2017), John Wiley & Sons.

1.6.3 Block copolymer adsorption

The amphiphilic nature of many block copolymers leads to different affinities of the blocks towards the substrate.[173-175] Consequently, adsorbed block copolymer chains adopt a configuration with one block (the anchor block) adsorbing on the surface with the pancake conformation and the other block (the buoy block) extending out from the surface with a mushroom or brush conformation depending on the density of adsorbed chains (Figure 1.22).[174-175] Therefore, adsorbed block copolymers resemble end-grafted polymers in many respects. However, a major difference for the mushroom and brush conformations is the extended size of the anchor block for block copolymers compared to a single anchor point for end-grafted polymers.

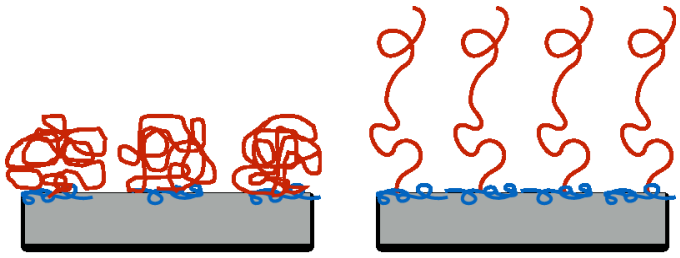

Figure 1.22. Schematic illustration of an adsorbed block copolymer in mushroom (left) and brush (right) conformations, where the blue lines represent the anchor block and the red lines the buoy block.

1.6.3.1 Two-stage adsorption process

The kinetics of block copolymer adsorption is a two-stage process.[176-180] In the first stage, the transport of polymer molecules to the surface is due to diffusion towards the surface and thus the adsorption rate is kinetically controlled in a diffusion-limited regime. The adsorbed amount of polymer as a function of time, $A(t)$, can be given as the integral of the flux of the material to the surface, j_s, with respect to time, t,

$$A(t) = \int_0^t j_s \, dt = (2/\pi^{1/2}) C_0 (Dt)^{1/2} \qquad \textbf{1.6}$$

where D is the diffusion coefficient of the adsorbing chains and C_0 their bulk concentration. In the second stage of adsorption, since all empty areas on the surface have been occupied by polymer chains, the adsorption of additional chains requires that they penetrate through the barrier created by the already adsorbed chains, which must undergo conformational readjustment. As a consequence, the adsorption rate decreases (brush-limited regime) and the adsorbed amount reaches a saturation value at the end of the second stage.

Motschmann *et al.* studied the adsorption kinetics of PS-b-PEO onto a silicon wafer from toluene solutions by using in situ ellipsometry to measure the adsorbed amount.[176] Toluene is a good solvent for both blocks and no micelles are present in the solution. The PS-b-PEO is anchored through the small PEO block on the Si surface, due to H-bonding between PEO and surface hydroxyl groups. The relationship between the adsorbed PS-b-PEO amount and adsorption time clearly shows a two-stage adsorption process (Figure 1.23). At short adsorption times, a fast adsorption rate was observed; the adsorbed amount grows linearly with square root of adsorption time, indicating the diffusion-limited regime. At long adsorption times, the adsorption rate drops significantly and the adsorbed amount slowly approaches a plateau, indicating the brush-limited regime.

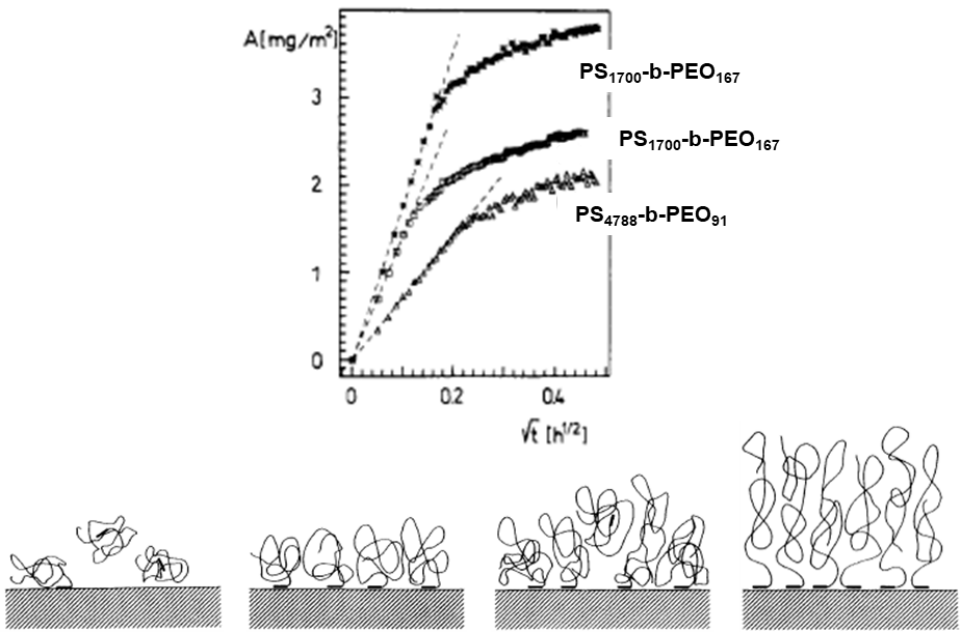

Figure 1.23. Top, adsorbed amount, A, of a series of PS_x-b-PEO_y (x and y indicate degree of polymerization) from 0.015 mg/mL toluene solutions onto Si as a function of adsorption time, t. Bottom, chain conformation of adsorbed PS-b-PEO evolving from the mushroom conformation in the first adsorption stage to the brush conformation in the second adsorption stage. Reproduced with permission from Ref. 175. Copyright (1991) American Chemical Society.

1.6.3.2 Effect of polymer solution concentration and micellization

Munch *et al.* studied the effect of polymer solution concentration on the adsorption kinetics of PS-b-PEO adsorbed onto sapphire from cyclopentane solutions.[177-178] The PS-b-PEO adsorbs to the sapphire surface by the small insoluble PEO block. Since cyclopentane is a selective solvent for the PS block, it forms micellar solutions above a critical micelle concentration (CMC). As shown in Figure 1.24, there are distinct differences in the curves below (Figure 1.24a) and above (Figure 1.24b) the CMC. In general, increasing the polymer solution concentration increases the adsorption rate in the diffusion-limited regime, but more strongly below the CMC than above the CMC with a pause in the vicinity of the CMC (Figure 1.24c).[178] On the other hand, the maximum adsorbed amount increases

sharply with increase in concentration below the CMC, and then rapidly decreases again just above the CMC to then increase a little with concentration (Figure 1.24d).[178] The net effect is that the maximum adsorbed amount is significantly lower above the CMC than just below the CMC, and also that a true plateau is reached at relatively short times for concentrations above the CMC whereas it tends to continue to rise slightly over the whole time period investigated for concentrations below the CMC.

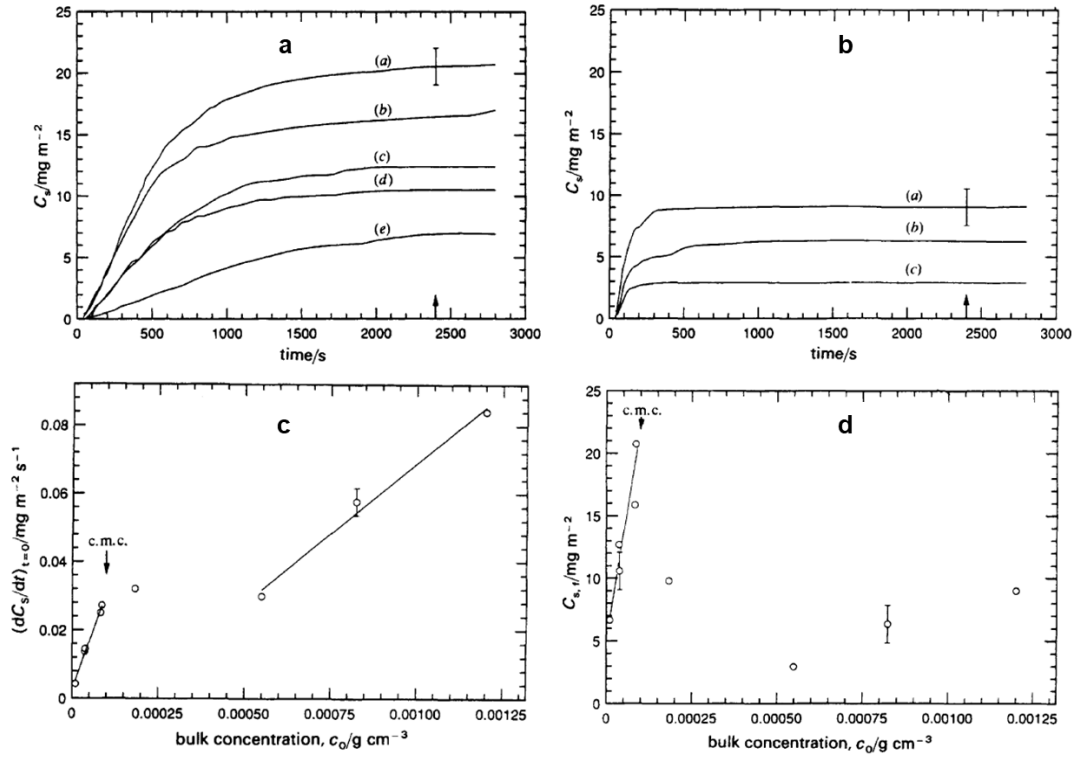

Figure 1.24. a, Plots of adsorbed amount of PS-b-PEO versus adsorption time for various bulk solution concentrations below CMC: (a) 8.7 x 10^{-5}, (b) 8.3 x 10^{-5}, (c) 3.8 x 10^{-5}, (d) 3.9 x 10^{-5} and (e) 1.0 x 10^{-5} g/mL. b, Plots of adsorbed amount of PS-b-PEO versus adsorption time for various bulk solution concentrations above CMC: (a) 1.2 x 10^{-3}, (b) 8.2 x 10^{-4}, and (c) 5.5 x 10^{-4} g/mL. c, Adsorption rate at the first adsorption stage as a function of polymer solution concentration. d, Maximum adsorbed amount as a function of polymer solution concentration. Reproduced with permission from Ref. 177. Copyright (1990) Royal Society of Chemistry.

1.7 Scope of the thesis

Incorporating AuNPs in nanofibers is a promising technique towards miniature SERS biosensors that have been employed by the Masson group for single cell studies. Optimal performance of the SERS nanofibers relies on the quality of the AuNP coating, as SERS is sensitive to irregularities in AuNP coatings. Among the best templates for making high-quality SERS chips is one based on block copolymers, owing to their self-assembled nanopatterns that can guide the ordered deposition of AuNPs on surfaces. However, so far, most studies on BCP-templated SERS substrates have been reported on flat surfaces and no research has been carried out on nanopipettes to the best of our knowledge. Therefore, a primary goal of this thesis is to implement the BCP film template technique on nanofibers in order to achieve dense and well-dispersed deposition of AuNPs on these nanopipettes, and thereby enable their use as SERS nanosensors.

Unlike flat substrates, the nanopipette is a unique type of substrate in that it is cylindrical in shape and has very high surface curvature due to its small radius. As a result, dip-coating is the most convenient technique by which to coat nanopipettes with a BCP film. Dip-coated BCP films (with added block-selective small molecules) on flat substrates have been investigated in detail by Sébastien Roland, a previous PhD student in the Bazuin group, and a good understanding has been established regarding the mechanism of film formation in dip-coating as well as the control on film thickness and morphology. Now, a fundamental problem arises as to how the substrate curvature associated with the small cylindrical geometry of the nanopipettes affects the dip-coated BCP thin films. It is known that, in pure fluid coatings, the substrate curvature significantly depresses the film thickness. Moreover, because of surface tension, cylindrical films tend to be unstable and break up into droplets, known as the Rayleigh or the Plateau-Rayleigh instability. However, these effects have not been studied in the context of dip-coated BCP thin films, which is a much more complex system that involves polymer solutions, solvent evaporation and the formation of a dry polymer film.

We will begin, in Chapter 2, by illustrating the high interest of using BCP coatings on nanofiber tips for obtaining a much improved nanosensor for neurotransmitters. In particular, it will be shown that, by first dip-coating a nanopipette from a PS-b-P4VP/THF

solution followed by an incubation process in a gold colloid, the BCP coating allows the deposition of dense and well-dispersed AuNPs on the nanofiber tips, thus establishing a simple bottom-up approach to the fabrication of SERS nanofibers. This will be shown to lead to an order of magnitude improvement in SERS performance (investigated by standard SERS tests of Raman-active molecules) and to a much improved *in vivo* detection of the co-release of neurotransmitter molecules secreted by single neurons.

Interestingly, the BCP coatings on the nanofiber tips in Chapter 2 were found to be uniform and only a few nanometers thick, differing from the thicker and patterned BCP films on flat surfaces. They were thus interpreted to be a nanothin adsorbed BCP brush, which, nonetheless, yield a high-quality AuNP monolayer that is superior in terms of uniformity and reproducibility to other nanofiber templates. These results indicate that the substrate curvature affects the BCP film thickness and, therefore, the film morphology. To better understand the physics of the phenomena observed and the factors that affect them, the next two chapters will focus on these brush layers and AuNP deposition on them, in comparison to thicker BCP layers. First, in Chapter 3, this will be done with flat substrates, since these are much more convenient to study, specifically using ellipsometry and AFM. Then in Chapter 4, with the knowledge gained in Chapter 3, the BCP dip-coated nanofibers will be studied in detail by varying different experimental parameters.

More specifically, in Chapter 3, we will vary the dip-coating PS-b-P4VP solution concentration to obtain a range of film thicknesses on flat silicon substrates, as well as several other parameters at concentrations giving only the brush layer, and use them for AuNP deposition. It will be shown that the brush layer, obtained with very dilute solutions, leads to dense and well-dispersed AuNP deposition, and that this is unaffected by the BCP coverage in the range investigated, studied in connection with the BCP adsorption kinetics. Thus, these adsorbed BCP brush layers prove to be stable templates for producing dense 2D arrays of nanoparticles of various sizes, superior to existing film templates such as SAMs or other polymer films, especially because surface nanoparticle aggregation is largely prevented. This constitutes a simple and robust bottom-up approach to the assembly of two-dimensional surface nanoparticles that promises many potential applications in optical coatings, plasmonic sensing, nanotemplating, nanocomposites and so on.

In Chapter 4, we investigate in detail the physicochemical phenomena related to the formation of these films on highly curved surfaces. We will demonstrate the substrate curvature effect on dip-coated PS-b-P4VP thin films on pulled glass fibers for diameters ranging from mm to submicron. A series of film morphologies associated with different curvatures were revealed by AFM and with the deposition of gold nanoparticles observed by SEM. The depressed film thickness caused by the increasing substrate curvature was shown to be at the origin of the changes in thin film morphology with curvature, constraining the films to be only adsorbed layers on highly curved surfaces. AuNP deposition on the adsorbed film was shown to be independent of polymer solution concentration and dip-coating rate, whereas nanoparticle density can be tuned by BCP molecular weight and composition. These findings are of particular value to bottom-up nanofabrications where coating of small cylindrical objects such as glass or carbon nanopipettes, optical fibers, free standing nanowires, and AFM tips with nanoparticles are desired.

Although dip-coating thick BCP films on nanofibers cannot be achieved, it might be possible by using two other methods based on drop-coating. This is the subject of Chapter 5. It is known from fluid coating theory that a spontaneous wetting film can spread around a fiber and that this film is ultrathin (typically within 1 nm) so that it is stabilized from Plateau-Rayleigh instability by long-range forces.[181] It will be shown that, by placing a small drop of polymer solution at the fiber taper, Au^{3+}-loaded BCP micelles can be transferred through the wetting film to form a uniform micellar coating down to sub-micron diameters on the fiber. Alternatively, a micellar film coating can also be achieved by a larger drop of polymer solution that flows down the fiber due to gravity. The former, but not the latter, requires the solvent to be a wetting solvent for the substrate.

The achievements in this thesis will not only find immediate application in fabricating SERS nanosensors and other nanosensors that desire the incorporation of nanoparticles on small cylindrical surfaces, such as nanowires and carbon nanotubes, but also provide knowledge on dip-coating block copolymer thin films on cylindrical surfaces, providing new insights and inspiring ideas in controlling the film thickness and the film

morphology. These aspects as well as future research subjects will be discussed in Chapter 6.

1.8 Structure of thesis

Chapters 2, 3 and 4 are manuscripts that have been submitted or are close to being submitted to recognized journals, as listed below. Chapter 5 will be completed by additional experiments and analysis before its completion as a manuscript to be submitted.

Chapter 2: Block Copolymer Brush Layer-Templated Gold Nanoparticles on Nanofibers for Surface-Enhanced Raman Scattering Optophysiology.

Published as a full paper paper in *ACS Applied Materials & Interfaces* **2019**, 11, 4373-4384.

Authors: Hu Zhu, Félix Lussier, Charles Ducrot, Marie-Josée Bourque, Joachim P. Spatz, Wenli Cui, Li Yu, Wei Peng, Louis-Éric Trudeau, C. Geraldine Bazuin, Jean-Francois Masson.

Description of content : The deposition of dense and well-dispersed gold nanoparticles (AuNPs) on glass nanofibres was achieved by using block copolymer ultrathin brush layer films as templates, giving rise to a surface-enhanced Raman scattering nanosensor that showed good stability, reproducibility and SERS performance in the in vitro detection of neurotransmitter molecules.

Role of coauthors: Part of the work was done under the supervision of J.P.S. in his laboratory. F.L. performed the SERS experiments, C.D. and M.-J.B. collected the dopaminergic neuron data under the supervion of L.-E.T., W.C., and L.Y. simulated the electric field on the nanofiber under the supervision of W.P.

Chapter 3: Monolayer Arrays of Nanoparticles on Block Copolymer Brush Films.

Revised manuscript submitted as a full paper in *Langmuir* **2019**.

Authors: Hu Zhu, Jean-Francois Masson, C. Geraldine Bazuin.

Description of content: Ultrathin block copolymer films in the form of an adsorbed brush-like layer on flat silicon substrates were obtained through dip-coating from very

dilute solutions. These were shown to be suitable templates for producing dense and well-dispersed AuNP arrays. This constitutes a simple and robust bottom-up approach to the assembly of two-dimensional surface nanoparticles that promises many potential applications in optical coatings, plasmonic sensing, nanotemplating, nanocomposites and so on. This study also helped in understanding the mechanism of block copolymer deposition on the highly curved surfaces.

Chapter 4: Templating Gold Nanoparticles on Nanofibers with Block Copolymer Brush Layers.

Close to submission as a full paper in *ACS Nano*.

Authors: Hu Zhu, Jean-Francois Masson, C. Geraldine Bazuin.

Description of content: Dip-coated block copolymer thin films on pulled nanofibers followed by AuNP deposition were investigated. The substrate curvature was found to strongly affect the film thickness and, thus, the film morphology. On highly curved substrates, the films are ultrathin and composed of only an adsorbed brush-like layer of block copolymer. The different film morphologies at different fiber diameters lead to different AuNP surface patterns depending on the degree of substrate curvature. We demonstrate that there is dense AuNP monolayer deposition at subnanometer diameters, making this range (i.e. the tip of pulled fibers) useful for bottom-up nanofabrication, such as for SERS nanosensors in optophysiology.

1.9 References

1. https://www.ibtimes.co.uk/romans-used-nanotechnology-turn-lycurgus-cup-green-red-1600-years-ago-1468746, **2014**.
2. Couture, M.; Zhao, S. S.; Masson, J.-F., *Phys. Chem. Chem. Phys*. **2013**, *15*, 11190-11216.
3. Petryayeva, E.; Krull, U. J., *Anal. Chimi. acta* **2011**, *706*, 8-24.
4. Willets, K. A.; Van Duyne, R. P., *Annu. Rev. Phys. Chem.* **2007**, *58*, 267-97.
5. Pérez-Juste, J.; Pastoriza-Santos, I.; Liz-Marzán, L. M.; Mulvaney, P., *Coordination Chemistry Reviews* **2005**, *249*, 1870-1901.
6. Kneipp, J.; Kneipp, H.; Kneipp, K., *Chem. Soc. Rev.* **2008**, *37*, 1052-1060.

7. Atkins, P., Physical chemistry 5th ed. Oxford University Press, Oxford: **1994**.
8. Bower, D. I., An introduction to polymer physics. Cambridge University Press: **2002**.
9. Hendra, P., *Analyst* **2016**, *141*, 4996-4999.
10. Fan, M.; Andrade, G. F.; Brolo, A. G., *Anal. Chimi. acta* **2011**, *693*, 7-25.
11. Jeanmaire, D. L.; Van Duyne, R. P., *J. Electroanal. Chem. Interfacial Electrochem.* **1977**, *84*, 1-20.
12. Albrecht, M. G.; Creighton, J. A., *J. Am. Chem. Soc.* **1977**, *99*, 5215-5217.
13. Van Duyne, R. P., *Chem. Biochem. Appl. Lasers* **1979**, *4*, 101.
14. McFarland, A. D.; Young, M. A.; Dieringer, J. A.; Van Duyne, R. P., *J. Phys. Chem. B* **2005**, *109*, 11279-11285.
15. Vo-Dinh, T.; Liu, Y.; Fales, A. M.; Ngo, H.; Wang, H. N.; Register, J. K.; Yuan, H.; Norton, S. J.; Griffin, G. D., *Wiley Interdiscip. Rev. Nanomed. Nanobiotechnol.* **2015**, *7*, 17-33.
16. Kneipp, J., In Surface-Enhanced Raman Scattering, Springer: **2006**; pp 335-349.
17. Kneipp, J.; Kneipp, H.; Wittig, B.; Kneipp, K., *Biology and Medicine* **2010**, *6*, 214-226.
18. Jin, D.; Bai, Y.; Chen, H.; Liu, S.; Chen, N.; Huang, J.; Huang, S.; Chen, Z., *Anal. Meth.* **2015**, *7*, 1307-1312.
19. Lu, G.; De Keersmaecker, H.; Su, L.; Kenens, B.; Rocha, S.; Fron, E.; Chen, C.; Van Dorpe, P.; Mizuno, H.; Hofkens, J.; Hutchison, J. A.; Uji-i, H., *Adv. Mater.* **2014**, *26*, 5124-5128.
20. Lussier, F.; Brule, T.; Vishwakarma, M.; Das, T.; Spatz, J. P.; Masson, J. F., *Nano Lett.* **2016**, *16*, 3866-3871.
21. Masson, J. F.; Breault-Turcot, J.; Faid, R.; Poirier-Richard, H. P.; Yockell-Lelievre, H.; Lussier, F.; Spatz, J. P., *Anal. Chem.* **2014**, *86*, 8998-9005.
22. Scaffidi, J. P.; Gregas, M. K.; Seewaldt, V.; Vo-Dinh, T., *Anal. Bioanal. Chem.* **2009**, *393*, 1135-1141.
23. Vitol, E. A.; Orynbayeva, Z.; Bouchard, M. J.; Azizkhan-Clifford, J.; Friedman, G.; Gogotsi, Y., *ACS Nano* **2009**, *3*, 3529-3536.

24. Xu, W.; Chen, Z.; Chen, N.; Zhang, H.; Liu, S.; Hu, X.; Wen, J.; Wang, T., *Sensors* **2017**, *17*, 467.

25. Singhal, R.; Orynbayeva, Z.; Kalyana Sundaram, R. V.; Niu, J. J.; Bhattacharyya, S.; Vitol, E. A.; Schrlau, M. G.; Papazoglou, E. S.; Friedman, G.; Gogotsi, Y., *Nat. Nanotechnol.* **2011**, *6*, 57-64.

26. Lv, J.; Qian, R.-C.; Hu, Y.-X.; Liu, S.-C.; Cao, Y.; Zheng, Y.-J.; Long, Y.-T., *Chem. Comm.* **2016**, *52*, 13909-13911.

27. Hanif, S.; Liu, H.-L.; Ahmed, S. A.; Yang, J.-M.; Zhou, Y.; Pang, J.; Ji, L.-N.; Xia, X.-H.; Wang, K., *Anal. Chem.* **2017**, *89*, 9911-9917.

28. Niu, J. J.; Schrlau, M. G.; Friedman, G.; Gogotsi, Y., *Small* **2011**, *7*, 540-545.

29. Bulbul, G.; Chaves, G.; Olivier, J.; Ozel, R. E.; Pourmand, N., *Cells* **2018**, *7*, 55.

30. Froede, E.; Rothenbergrer, M., Past, Present, and Future: Nanopipette Applications to Single Cell Analysis, **2011**.

31. Schrlau, M. G.; Dun, N. J.; Bau, H. H., *ACS Nano* **2009**, *3*, 563-568.

32. Kim, B. M.; Murray, T.; Bau, H. H., *Nanotechnology* **2005**, *16*, 1317-1320.

33. Schrlau, M. G.; Bau, H. H., *Jala* **2010**, *15*, 145-151.

34. Schrlau, M. G.; Falls, E. M.; Ziober, B. L.; Bau, H. H., *Nanotechnology* **2008**, *19*, 015101.

35. Liang, F.; Zhang, Y.; Hong, W.; Dong, Y.; Xie, Z.; Quan, Q., *Nano Lett.* **2016**.

36. Chen, X.; Kis, A.; Zettl, A.; Bertozzi, C. R., *Proc. Natl. Acad. Sci. U S A* **2007**, *104*, 8218-8222.

37. Zito, G.; Rusciano, G.; Vecchione, A.; Pesce, G.; Di Girolamo, R.; Malafronte, A.; Sasso, A., *Sci. Rep.* **2016**, *6*, 31113.

38. Ballarin, B.; Cassani, M. C.; Scavetta, E.; Tonelli, D., *Electrochimica Acta* **2008**, *53*, 8034-8044.

39. Bright, R. M.; Musick, M. D.; Natan, M. J., *Langmuir* **1998**, *14*, 5695-5701.

40. Freeman, R. G.; Grabar, K. C.; Allison, K. J.; Bright, R. M.; Davis, J. A.; Guthrie, A. P.; Hommer, M. B.; Jackson, M. A.; Smith, P. C.; Walter, D. G., *Science* **1995**, *267*, 1629-1632.

41. Grabar, K. C.; Freeman, R. G.; Hommer, M. B.; Natan, M. J., *Anal. Chem.* **1995**, *67*, 735-743.

42. Grabar, K. C.; Smith, P. C.; Musick, M. D.; Davis, J. A.; Walter, D. G.; Jackson, M. A.; Guthrie, A. P.; Natan, M. J., *J. Am. Chem. Soc.* **1996**, *118*, 1148-1153.
43. Zhu, M.; Lerum, M. Z.; Chen, W., *Langmuir* **2012**, *28*, 416-423.
44. Asenath Smith, E.; Chen, W., *Langmuir* **2008**, *24*, 12405-12409.
45. Malynych, S.; Luzinov, I.; Chumanov, G., *J. Phys. Chem. B* **2002**, *106*, 1280-1285.
46. Bhat, R. R.; Genzer, J.; Chaney, B. N.; Sugg, H. W.; Liebmann-Vinson, A., *Nanotechnology* **2003**, *14*, 1145-1152.
47. Malynych, S.; Chumanov, G., *J. Am. Chem. Soc.* **2003**, *125*, 2896-2898.
48. Tanaka, H.; Mitsuishi, M.; Miyashita, T., *Langmuir* **2003**, *19*, 3103-3105.
49. Jackson, J. B.; Halas, N. J., *Proc. Natl. Acad. Sci. U S A* **2004**, *101*, 17930-17935.
50. Theiss, J.; Pavaskar, P.,; Echternach, P.M.; Muller, R.E; Cronin, S.B., *Nano Lett.* **2010**, *10*, 2749-2754.
51. Li, Y.; Lu, Q.; Qian, X.; Zhu, Z.; Yin, J., *Appl. Surf. Sci.* **2004**, *233*, 299-306.
52. Tian, S.; Liu, J.; Zhu, T.; Knoll, W., *Chem. Mater.* **2004**, *16*, 4103-4108.
53. Tokareva, I.; Minko, S.; Fendler, J. H.; Hutter, E., *J. Am. Chem. Soc.* **2004**, *126*, 15950-15951.
54. Dong, H.; Fey, E.; Gandelman, A.; Jones, W. E., *Chem. Mater.* **2006**, *18*, 2008-2011.
55. Russell, L. E.; Galyean, A. A.; Notte, S. M.; Leopold, M. C., *Langmuir* **2007**, *23*, 7466-7471.
56. Sánchez-Delgado, R. A.; Machalaba, N., *Catal. Comm.* **2007**, *8*, 2115- 2118.
57. Gupta, S.; Agrawal, M.; Uhlmann, P.; Simon, F.; Oertel, U.; Stamm, M., *Macromolecules* **2008**, *41*, 8152-8158.
58. Gupta, S.; Uhlmann, P.; Agrawal, M.; Chapuis, S.; Oertel, U.; Stamm, M., *Macromolecules* **2008**, *41*, 2874-2879.
59. Gupta, S.; Uhlmann, P.; Agrawal, M.; Lesnyak, V.; Gaponik, N.; Simon, F.; Stamm, M.; Eychmüller, A., *J. Mater. Chem.* **2008**, *18*, 214-223.
60. McConnell, M. D.; Bassani, A. W.; Yang, S.; Composto, R. J., *Langmuir* **2009**, *25*, 11014-11020.
61. McConnell, M. D.; Yang, S.; Composto, R. J., *Macromolecules* **2009**, *42*, 517-523.
62. Kinnan, M. K.; Chumanov, G., *J. Phys. Chem. C* **2010**, *114*, 7496-7501.

63. Christau, S.; Moller, T.; Yenice, Z.; Genzer, J.; von Klitzing, R., *Langmuir* **2014**, *30*, 13033-13041.

64. Cho, W. J.; Kim, Y.; Kim, J. K., *ACS Nano* **2011**, *6*, 249-255.

65. Wang, Y.; Becker, M.; Wang, L.; Liu, J.; Scholz, R.; Peng, J.; Gösele, U.; Christiansen, S.; Kim, D. H.; Steinhart, M., *Nano Lett.* **2009**, *9*, 2384-2389.

66. Mistark, P. A.; Park, S.; Yalcin, S. E.; Lee, D. H.; Yavuzcetin, O.; Tuominen, M. T.; Russell, T. P.; Achermann, M., *ACS Nano* **2009**, *3*, 3987-3992.

67. Haryono, A.; Binder, W. H., *Small* **2006**, *2*, 600-611.

68. Gowd, E. B.; Nandan, B.; Bigall, N. C.; Eychmüller, A.; Formanek, P.; Stamm, M., *Polymer* **2010**, *51*, 2661-2667.

69. Bhoje Gowd, E.; Nandan, B.; Vyas, M. K.; Bigall, N. C.; Eychmuller, A.; Schlorb, H.; Stamm, M., *Nanotechnology* **2009**, *20*, 415302.

70. Nandan, B.; Gowd, E. B.; Bigall, N. C.; Eychmüller, A.; Formanek, P.; Simon, P.; Stamm, M., *Adv. Func. Mater.* **2009**, *19*, 2805-2811.

71. Lohmueller, T.; Bock, E.; Spatz, J. P., Advanced Materials 2008, 20, 2297-2302.

72. Yun, S.-H.; Yoo, S. I.; Jung, J. C.; Zin, W.-C.; Sohn, B.-H., *Chem. Mater.* **2006**, *18*, 5646-5548.

73. Lee, W.; Lee, S. Y.; Briber, R. M.; Rabin, O., *Adv. Func. Mater.* **2011**, *21*, 3424-3429.

74. Lee, W.; Lee, S. Y.; Zhang, X.; Rabin, O.; Briber, R. M., *Nanotechnology* **2013**, *24*, 045305.

75. Aizawa, M.; Buriak, J. M., Block copolymer-templated chemistry on Si, Ge, InP, and GaAs surfaces. *J. Am. Chem. Soc.* **2005**, *127*, 8932-8933.

76. Aizawa, M.; Buriak, J. M., *Chem. Mater.* **2007**, *19*, 5090-9101.

77. Glass, R.; M ller, M.; Spatz, J. P., *Nanotechnology* **2003**, *14*, 1153-1160.

78. Spatz, J. P.; Roescher, A.; Sheiko, S.; Krausch, G.; Möller, M., *Adv. Mater.* **1995**, *7*, 731-735.

79. Jahn, S.; Lechner, S. J.; Freichels, H.; Moller, M.; Spatz, J. P., *Sci. Rep.* **2016**, *6*, 20536.

80. Kruss, S.; Erpenbeck, L.; Schon, M. P.; Spatz, J. P., Lab Chip 2012, 12, 3285-3289.

81. Hamley, I. W., *Prog. Poly. Sci.* **2009**, *34*, 1161-1210.

82. Hamley, I., *Nanotechnology* **2003**, *14*, R39.

83. Bates, C. M.; Maher, M. J.; Janes, D. W.; Ellison, C. J.; Willson, C. G., *Macromolecules* **2013**, *47*, 2-12.

84. Fasolka, M. J.; Mayes, A. M., *Ann. Rev. Mater. Res.* **2001**, *31*, 323-355.

85. Lazzari, M.; López-Quintela, M. A., *Adv. Mater.* **2003**, *15*, 1583-1594.

86. Cummins, C.; Ghoshal, T.; Holmes, J. D.; Morris, M. A., *Adv. Mater.* **2016**, *28*, 5586-5618.

87. Hahm, J.; Sibener, S., *Langmuir* **2000**, *16*, 4766-4769.

88. Weng, C.-C.; Wei, K.-H., *Chem. Mater.* **2003**, *15*, 2936-2941.

89. Roland, S.; Pellerin, C.; Bazuin, C. G.; Prud'homme, R. E., *Macromolecules* **2012**, *45*, 7964-7972.

90. Roland, S.; Gaspard, D.; Prud'homme, R. E.; Bazuin, C. G., *Macromolecules* **2012**, *45*, 5463-5476.

91. Laforgue, A.; Bazuin, C. G.; Prud'homme, R. E., *Macromolecules* **2006**, *39*, 6473-6482.

92. Vapaavuori, J.; Bazuin, C. G.; Priimagi, A., *J. Mater. Chem. C* **2018**, *6*, 2168-2188.

93. Vapaavuori, J.; Grosrenaud, J.; Pellerin, C.; Bazuin, C. G., *ACS Macro Lett.* **2015**, *4*, 1158-1162.

94. Roland, S.; Prud'homme, R. E.; Bazuin, C. G., Morphology, *ACS Macro Lett.* **2012**, *1*, 973-976.

95. Deng, Y.; Yu, T.; Wan, Y.; Shi, Y.; Meng, Y.; Gu, D.; Zhang, L.; Huang, Y.; Liu, C.; Wu, X., *J. Am. Chem. Soc.* **2007**, *129*, 1690-1697.

96. Zhang, M.; Yang, L.; Yurt, S.; Misner, M. J.; Chen, J. T.; Coughlin, E. B.; Venkataraman, D.; Russell, T. P., *Adv. Mater.* **2007**, *19*, 1571-1576.

97. Park, S.; Kwon, K.; Cho, D.; Lee, B.; Ree, M.; Chang, T., *Macromolecules* **2003**, *36*, 4662-4666.

98. Heo, K.; Yoon, J.; Jin, S.; Kim, J.; Kim, K.-W.; Shin, T. J.; Chung, B.; Chang, T.; Ree, M., *J. Appl. Crystallography* **2008**, *41*, 281-291.

99. Chao, C.-C.; Ho, R.-M.; Georgopanos, P.; Avgeropoulos, A.; Thomas, E. L., *Soft Matter* **2010**, *6*, 3582-3587.

100. Park, S.; Kim, B.; Wang, J. Y.; Russell, T. P., *Adv. Mater.* **2008**, *20*, 681-685.

101. Smart, T.; Lomas, H.; Massignani, M.; Flores-Merino, M. V.; Perez, L. R.; Battaglia, G., *Nano Today* **2008**, *3*, 38-46.
102. Gu, X.; Gunkel, I.; Russell, T. P., *Phil. Trans. R. Soc. A* **2013**, *371*, 20120306.
103. Segalman, R. A., *Mater. Sci. Eng. R Rep.* **2005**, *48*, 191-226.
104. Bates, F. S.; Fredrickson, G. H., *Annu. Rev. Phys. Chem.* **1990**, *41*, 525-557.
105. Leibler, L., *Macromolecules* **1980**, *13*, 1602-1617.
106. Bates, F. S.; Fredrickson, G., *Physics Today* **2000**, *52*.
107. Darling, S., *Prog. Polym. Sci.* **2007**, *32*, 1152-1204.
108. Park, C.; Yoon, J.; Thomas, E. L., *Polymer* **2003**, *44*, 6725-6760.
109. Stoykovich, M. P.; Nealey, P. F., *Materials Today* **2006**, *9*, 20-29.
110. Li, M.; Ober, C. K., *Materials Today* **2006**, 9, 30-39.
111. Krishnamoorthy, S.; Hinderling, C.; Heinzelmann, H., *Materials Today* **2006**, *9*, 40-47.
112. Albert, J. N.; Epps III, T. H., *Materials Today* **2010**, *13*, 24-33.
113. Kim, H.-C.; Hinsberg, W. D., *J. Vac. Sci. Technol A: Vacuum, Surfaces, and Films* **2008**, *26*, 1369-1382.
114. Cheng, J. Y.; Ross, C. A.; Smith, H. I.; Thomas, E. L., *Adv. Mater.* **2006**, *18*, 2505-2521.
115. Xiao, S.; Yang, X.; Edwards, E. W.; La, Y.-H.; Nealey, P. F., *Nanotechnology* **2005**, *16*, S324.
116. Tseng, Y.-C.; Peng, Q.; Ocola, L. E.; Elam, J. W.; Darling, S. B., Enhanced block copolymer lithography using sequential infiltration synthesis. *J. Phys. Chem. C* **2011**, *115*, 17725-17729.
117. Ruiz, R.; Kang, H.; Detcheverry, F. A.; Dobisz, E.; Kercher, D. S.; Albrecht, T. R.; de Pablo, J. J.; Nealey, P. F., *Science* **2008**, *321*, 936-939.
118. Bita, I.; Yang, J. K.; Jung, Y. S.; Ross, C. A.; Thomas, E. L.; Berggren, K. K., *Science* **2008**, *321*, 939-943.
119. Stein, A.; Wright, G.; Yager, K. G.; Doerk, G. S.; Black, C. T., *Nat. Commu.* **2016**, *7*, 12366.
120. Albrecht, T. R.; Bedau, D.; Dobisz, E.; Gao, H.; Grobis, M.; Hellwig, O.; Kercher, D.; Lille, J.; Marinero, E.; Patel, K., *IEEE T Magn.* **2013**, *49*, 773-778.

121. Ross, C. A.; Berggren, K. K.; Cheng, J. Y.; Jung, Y. S.; Chang, J. B., *Adv. Mater.* **2014**, *26*, 4386-4396.

122. Tsai, H.; Pitera, J. W.; Miyazoe, H.; Bangsaruntip, S.; Engelmann, S. U.; Liu, C.-C.; Cheng, J. Y.; Bucchignano, J. J.; Klaus, D. P.; Joseph, E. A., *ACS Nano* **2014**, *8*, 5227-5232.

123. Hawker, C. J.; Russell, T. P., *MRS Bulletin* **2005**, *30*, 952-966.

124. van Zoelen, W.; Ten Brinke, G., *Soft Matter* **2009**, *5*, 1568-1582.

125. Erb, D. J.; Schlage, K.; Röhlsberger, R., *Sci. Adv.* **2015**, *1*, e1500751.

126. Park, W. I.; Choi, Y. J.; Yuk, J. M.; Seo, H. K.; Kim, K. H., *Polymer Journal* **2018**, *50*, 221.

127. Jung, Y. S.; Ross, C. A., *Nano Lett.* **2007**, *7*, 2046-2050.

128. Jung, Y. S.; Lee, J. H.; Lee, J. Y.; Ross, C., *Nano Lett.* **2010**, *10*, 3722-3726.

129. Borah, D.; Rassapa, S.; Shaw, M. T.; Hobbs, R. G.; Petkov, N.; Schmidt, M.; Holmes, J. D.; Morris, M. A., *J. Mater. Chem. C* **2013**, *1*, 1192-1196.

130. OukáKim, S., *J. Mater. Chem.* **2011**, *21*, 5856-5859.

131. Cheng, J. Y.; Ross, C.; Thomas, E.; Smith, H. I.; Vancso, G. J., *App. Phy. Lett.* **2002**, *81*, 3657-3659.

132. Gowd, E. B.; Nandan, B.; Vyas, M. K.; Bigall, N. C.; Eychmüller, A.; Schlörb, H.; Stamm, M., *Nanotechnology* **2009**, *20*, 415302.

133. Yin, Y.; Lu, Y.; Gates, B.; Xia, Y., *J. Am. Chem. Soc.* **2001**, *123*, 8718-8729.

134. Horechyy, A.; Zafeiropoulos, N. E.; Nandan, B.; Formanek, P.; Simon, F.; Kiriy, A.; Stamm, M., *J. Mater. Chem.* **2010**, *20*, 7734-7741.

135. Bigall, N. C.; Nandan, B.; Gowd, E. B.; Horechyy, A.; Eychmuller, A., *ACS Appl. Mater. Interfaces* **2015**, *7*, 12559-12569.

136. Chai, J.; Wang, D.; Fan, X.; Buriak, J. M., *Nat. Nanotechnol.* **2007**, *2*, 500-506.

137. Yap, F. L.; Thoniyot, P.; Krishnan, S.; Krishnamoorthy, S., *ACS Nano* **2012**, *6*, 2056-2070.

138. Chai, J.; Buriak, J. M., *ACS Nano* **2008**, *2*, 489-501.

139. Wagner, T.; Lazar, J.; Schnakenberg, U.; Böker, A., *ACS Appl. Mater. Interfaces* **2016**, *8*, 27282-27290.

140. Cho, W. J.; Kim, Y.; Kim, J. K., *ACS Nano* **2012**, *6*, 249-255.

141. Misner, M. J.; Skaff, H.; Emrick, T.; Russell, T. P., *Adv. Mater.* **2003**, *15*, 221-224.

142. Shin, K.; Leach, K. A.; Goldbach, J. T.; Kim, D. H.; Jho, J. Y.; Tuominen, M.; Hawker, C. J.; Russell, T. P., *Nano Lett.* **2002**, *2*, 933-936.

143. Zhang, Q.; Xu, T.; Butterfield, D.; Misner, M. J.; Ryu, D. Y.; Emrick, T.; Russell, T. P., *Nano Lett.* **2005**, *5*, 357-361.

144. Horechyy, A.; Nandan, B.; Zafeiropoulos, N. E.; Formanek, P.; Oertel, U.; Bigall, N. C.; Eychmüller, A.; Stamm, M., *Adv. Fun. Mater.* **2013**, *23*, 483-490.

145. Aizawa, M.; Buriak, J. M., *J. Am. Chem. Soc.* **2006**, *128*, 5877-5886.

146. L. Landau, B. L., *Acta Physicochimica U.R.S.S.* **1942**, *17*, 42-54.

147. Quere, D., *Annu. Rev. Fluid Mech.* **1999**, *31*, 347-384.

148. Grosso, D., *J. Mater. Chem.* **2011**, *21*, 17033.

149. Faustini, M.; Louis, B.; Albouy, P. A.; Kuemmel, M.; Grosso, D., *J. Phy. Chem. C* **2010**, *114*, 7637-7645.

150. Faustini, M.; Ceratti, D. R.; Louis, B.; Boudot, M.; Albouy, P. A.; Boissiere, C.; Grosso, D., *ACS Appl. Mater. Interfaces* **2014**, *6*, 17102-17110.

151. Faustini, M.; Boissière, C.; Nicole, L.; Grosso, D., *Chem. Mater.* **2014**, *26*, 709-723.

152. Faustini, M.; Capobianchi, A.; Varvaro, G.; Grosso, D., *Chem. Mater.* **2012**, *24*, 1072-1079.

153. Roland, S.; Gamys, C. G.; Grosrenaud, J.; Boissé, S.; Pellerin, C.; Prud'homme, R. E.; Bazuin, C. G., *Macromolecules* **2015**, *48*, 4823-4834.

154. Kawaguchi, M.; Hayakawa, K.; Takahashi, A., Macromolecules 1983, 16, 631-635.

155. Kawaguchi, M.; Takahashi, A., *Macromolecules* **1983**, *16*, 1465-1469.

156. Kawaguchi, M.; Takahashi, A., *Adv. Colloid and Interface Sci.* **1992**, *37*, 219-317.

157. Kleshchanok, D.; Tuinier, R.; Lang, P. R., *J. Phys. Condens. Matter.* **2008**, *20*, 073101.

158. Dobrynin, A. V.; Rubinstein, M., *Prog. Polym. Sci.* **2005**, *30*, 1049-1118.

159. Milner, S., Polymer brushes. *Science* **1991**, *251*, 905-914.

160. Zhao, B.; Brittain, W. J., *Prog. Polym. Sci.* **2000**, *25*, 677-710.

161. de Gennes, P., *Macromolecules* **1980**, *13*, 1069-1075.

162. Advincula, R. C., *Encyclopedia of Polymer Science and Technology* **2004**.

163. Kim, M.; Schmitt, S. K.; Choi, J. W.; Krutty, J. D.; Gopalan, P., *Polymers* **2015**, *7*, 1346-1378.
164. Ayres, N., *Polym. Chem.* **2010**, *1*, 769-777.
165. Edmondson, S.; Osborne, V. L.; Huck, W. T., *Chem. Soc. Rev.* **2004**, *33*, 14-22.
166. De Gennes, P., *Journal de Physique* **1976**, *37*, 1445-52.
167. Santer, S.; Kopyshev, A.; Donges, J.; Yang, H. K.; Ruhe, J., *Langmuir* **2006**, *22*, 4660-4667.
168. Santer, S.; Kopyshev, A.; Donges, J.; Yang, H. K.; Rühe, J., *Adv. Mater.* **2006**, *18*, 2359-2362.
169. Filimon, M.; Kopf, I.; Schmidt, D. A.; Brundermann, E.; Ruhe, J.; Santer, S.; Havenith, M., *Phys. Chem. Chem. Phys.* **2011**, *13*, 11620-11626.
170. Santer, S.; Kopyshev, A.; Yang, H.-K.; Rühe, J., *Macromolecules* **2006**, *39*, 3056-3064.
171. Schuh, C.; Santer, S.; Prucker, O.; Rühe, J., *Adv. Mater.* **2009**, *21*, 4706-4710.
172. Tebbe, M.; Galati, E.; Walker, G. C.; Kumacheva, E., *Small* **2017**, *13*, 1702043.
173. Hadjichristidis, N.; Pispas, S.; Floudas, G., *Physical Properties and Applications* **2002**, 232-54.
174. Halperin, A.; Tirrell, M.; Lodge, T., Springer: **1992**; pp 31-71.
175. Tirrell, M.; Patel, S.; Hadziioannou, G., *Proc. Natl. Acad. Sci. U S A* **1987**, *84*, 4725-4728.
176. Motschmann, H.; Stamm, M.; Toprakcioglu, C., *Macromolecules* **1991**, *24*, 3681-3688.
177. Munch, M. R.; Gast, A. P., *Macromolecules* **1990**, *23*, 2313-2320.
178. Munch, M. R.; Gast, A. P., *J. Chem. Soc. Faraday Trans.* **1990**, *86*, 1341-1348.
179. Tassin, J. F.; Siemens, R. L.; Tang, W. T.; Hadziioannou, G.; Swalen, J. D.; Smith, B. A., Kinetics of adsorption of block copolymers revealed by surface plasmons. *J. Phy. Chem.* **1989**, *93*, 2106-2111.
180. Toomey, R.; Mays, J.; Tirrell, M., *Macromolecules* **2004**, *37*, 905-911.
181. Quere, D.; di Meglio, J. M.; Brochard-Wyart, F., *Science* **1990**, *249*, 1256-1260.

Chapter 2

Block Copolymer Brush Layer-Templated Gold Nanoparticles on Nanofibers for Surface-Enhanced Raman Scattering Optophysiology*

2.1 Abstract

A nanothin block copolymer (BCP) brush-layer film adsorbed on glass nanofibers is shown to address the long-standing challenge of forming a template for the deposition of dense and well dispersed nanoparticles on highly curved surfaces, allowing the development of an improved nanosensor for neurotransmitters. We employed a polystyrene-block-poly(4-vinylpyridine) BCP and plasmonic gold nanoparticles (AuNPs) of 52 nm in diameter for the fabrication of the nanosensor on pulled fibers with diameters down to 200 nm. The method is simple, using only solution processes and a plasma cleaning step. The templating of the AuNPs on the nanofiber surprisingly gave rise to more than one order of magnitude improvement in the surface-enhanced Raman scattering (SERS) performance for 4-mercaptobenzoic acid compared to the same AuNPs aggregated on identical fibers without the use of a template. We hypothesize that a wavelength-scale lens formed by the nanofiber contributes to enhancing the SERS performance, to the extent that it can melt the glass nanofiber under moderate laser power. We then show the capability of this nanosensor to detect the co-release of the neurotransmitters dopamine and glutamate from living mouse brain dopaminergic neurons with a sensitivity one order of magnitude greater than with

*Published as a full paper paper in *ACS Applied Materials & Interfaces* **2019**, 11, 4373-4384: Zhu, H.; Lussier, F.; Ducrot, C.; Bourque, M.-J.; Spatz, J.P.; Cui, W.L.; Yu, L.; Peng, W.; Trudeau, L.-É.; Bazuin, C.G.; Masson, J.-F.

aggregated AuNPs. The simplicity of fabrication and the far superior performance of the BCP-templated nanofiber demonstrates the potential of this method to efficiently pattern nanoparticles on highly curved surfaces and its application as molecular nanosensors for cell physiology.

2.2 Introduction

The manufacturing of increasingly smaller devices has led to the development of the nanoelectronics, nano-optics and nanobiology fields with wide-ranging applications.1 For nearly all nanofabrication techniques, the substrate is patterned using a series of processes designed to form the nanostructures by milling material and curing resins1 or by printing and molding structures from a template.2 These top-down approaches have led to the fabrication of complex nanostructures for creating a suite of electronic or photonic devices. However, nanopatterning is almost exclusively performed on flat wafers as top-down approaches are ill-suited for other surface geometries.

Curved surfaces have wide-ranging applications in modern and upcoming technologies.3 Fiber optics and optical waveguides can serve in optical nanodevices imparting sensing capabilities to previously inaccessible locations. Decorating these fibers or waveguides with various types of nanoparticles (NPs) could enable the development of highly sensitive in situ or in vivo molecular sensors as well as enable local photothermal therapy.4-6 For example, we recently demonstrated a SERS optophysiology application based on nanofibers (pulled glass rods) decorated with aggregated AuNPs to monitor cellular metabolites or neurotransmitters.7,8 While these proof-of-principle experiments showed the potential of SERS optophysiology for measuring multiple metabolites in a single experiment, the use of aggregated nanoparticles led to significant sensor-to-sensor irreproducibility and large variance in the data. Increasing the SERS sensitivity would allow the detection of metabolites at lower concentrations as well as enhance the temporal resolution of the technique. A more dispersed, still dense, deposition of AuNPs on these SERS nanofibers would significantly improve their performance, but this currently remains a challenge.

A bottom-up method for converting surfaces into SERS sensors is by coating them with a nanopatterned block copolymer (BCP) template, such as in the form of micelles that guide the deposition of AuNPs into well-ordered arrays, investigated almost exclusively with flat and low-curvature substrates.9-13 One of the most facile methods for directly achieving a phase-separated BCP coating on a fiber is dip-coating, which consists of simply dipping the fiber into a BCP solution and then withdrawing it at a controlled rate.14,15 However, the dip-coated film thickness decreases with decrease in fiber diameter,16 resulting in incomplete micellar coverage on low-diameter fibers. This can be compensated up to a point by increasing the BCP solution concentration and the withdrawal speed of the fiber from the solution, as achieved for fiber diameters down to 25 □m.17 At the very small diameters necessary for SERS optophysiology, ideally less than 1 μm, the withdrawal speeds must be impracticably high. Thus, patterned BCP coatings allowing ordered AuNP deposition on such small fibers are essentially impossible to achieve.

2.3 Experimental

2.3.1 Methods

2.3.1.1 Materials

The polystyrene-b-poly(4-vinylpyridine) (PS-b-P4VP) diblock copolymer [M_n(PS) = 41 kg/mol, M_n(P4VP) = 20 kg/mol, M_w/M_n (total) = 1.18], PS-s-P4VP statistical copolymer (M_n = 93.9 kg/mol, M_w = 140.8 kg/mol, M_w/M_n = 1.5, P4VP content = 35 mol%) and P4VP homopolymer (M_n = 15 kg/mol, M_w = 19 kg/mol, M_w/M_n = 1.25) were purchased from Polymer Source (Dorval, QC, Canada). Tetrahydrofuran (THF, 99.99%) was obtained from VWR. Gold(III) chloride trihydrate ($HAuCl_4 \cdot 3H_2O$, 99.9%), trisodium citrate dihydrate (99%) and 4-mercaptobenzoic acid (4-MBA, 99%) were purchased from Sigma-Aldrich. All were used as received. Borosilicate glass rods of 1.1 mm diameter and 10 cm length were obtained from Sutter Instrument.

2.3.1.2 Nanofibers

The glass rods were pulled into nanofibers using a laser-based Sutter P-2000 pipette puller (Sutter Instrument, California) with the following two-line program, where the

parameters given are instrument specific: LINE 1) Heat: 280, Filament: 3, Velocity: 15, Delay: 145, Pull: 20; LINE 2) Heat: 500, Filament: 0, Velocity: 15, Delay: 128, Pull: 200. Nanofibers were cleaned by immersion in ethanol for 5 min, dried in air, then immersed in a piranha solution at 90 ºC for 60 min, rinsed with Milli-Q water, and finally dried under vacuum at room temperature for an hour.

2.3.2 Block copolymer solution preparation and dip-coating

A BCP stock solution of 5 mg/mL in THF was prepared by dissolving 50 mg of PS-b-P4VP in 10 mL of THF in scintillation vials. The solutions were capped, sealed with parafilm and stirred at 30–40 ºC overnight. They were then filtered successively through a 0.45 μm and a 0.2 μm PTFE filter (Chromspec). BCP solutions of 1 mg/mL, 0.1 mg/mL, and 0.05 mg/mL were prepared by dilution from the 5 mg/mL stock solution. Most of the experiments described were performed with the most dilute BCP solution, but no differences in the final AuNP arrays on the nanofibers were noted for the other concentrations. A P4VP homopolymer solution and a PS-s-P4VP statistical copolymer solution were prepared at a concentration of 0.05 mg/mL in THF/MeOH (1:1 vol:vol) and THF, respectively, noting that P4VP is not soluble in pure THF. Dip-coated films were obtained from the solutions under ambient conditions (~21 ºC), using the dip-coater of a KSV3000 Langmuir-Blodgett instrument. The substrates were immersed vertically in the solutions at a rate of 5 mm/min, followed by a pause of 2 min, and then were withdrawn at controlled rates between 0.1 and 80 mm/min for PS-b-P4VP, for which no significant differences in the final AuNP arrays were observed, and at 40 mm/min for P4VP and PS-s-P4VP. The films were left to dry in covered containers at room temperature for at least 30 min before AuNP deposition.

2.3.3 Gold nanoparticle (AuNP) synthesis and deposition

Monodisperse citrate-stabilized AuNPs were synthesized in 6 growth steps, using the kinetically controlled seeded growth method developed by Puntes and coworkers.[38] The average size of the AuNPs was determined to be 52 nm from a room temperature UV-visible spectrum[39] (Figure 2.S1, obtained using an Agilent Technologies Cary 500 UV−vis spectrophotometer), in good agreement with ref 1, and a little larger than the average size

of 46 nm indicated by scanning electron microscopy (Figure 2.S2). The AuNP suspension was stored at 4 ºC, protected from light, and used within a month.

For deposition, the AuNPs were first centrifuged from a volume of their original colloidal suspension and redispersed in Milli-Q water of the same volume. Then, the solution pH was adjusted to between 4.5 and 5.0 by adding an appropriate volume of 1 M hydrochloric acid aqueous solution. The nanofibers were immersed overnight in the AuNP suspension at room temperature and then they were immersed in Milli-Q water several times, and air dried. To remove the polymer coating, the samples were placed in an oxygen plasma chamber (Harrick Scientific PDC-32G plasma cleaner/sterilizer), and treated for 5 min at medium RF level and an O_2 flow rate of 13.4 mL/min controlled by a Praxair PRS FM4301-1 15-cm flow meter.

2.3.4 Scanning electron microscopy (FE-SEM)

The AuNP-coated nanofibers were examined using a JEOL JSM-7400F (JEOL Ltd, Tokyo, Japan) field-emission scanning electron microscope operated at 1.5 kV and 20 μA. The analysis of AuNP size and size distribution was made using ImageJ (http://imagej.nih.gov/ij/features.html).

2.3.5 Atomic force microscopy (AFM)

AFM images were obtained in tapping mode with a Multimode microscope and a Nanoscope III controller (Digital Instruments), operated under ambient atmosphere, using Bruker AFM probes (TESPA-V2 model, spring constant 42 N/m, oscillation frequency 320 kHz, tip radius ≤ 10 nm). The nanofiber was carefully put in contact with a double-sided tape prefixed on an AFM metal sample disk and then broken from the unpulled part of the nanofiber. The height variation associated with highly curved surfaces may cause contact between cantilever and the surface or even tip breaking. To minimize this issue and better show the surface topology, the nanofiber was adjusted to lie parallel to the scanning lines of AFM with the assistance of an optical microscope and the horizontal plane symmetry axis of the image was adjusted to be along the top line of the curved surface. To measure the film thickness, a small section of the film (500 nm x 2 μm) was erased by scanning for 20 min with an AFM tip in contact mode at a deflection setpoint of 0.6 V and a scan rate of 3

Hz. Then, a new AFM tip in tapping mode was used to scan an area of 2 μm x 8 μm around the exposed area, and the film thickness was determined from a topological line profile across the scratch.

2.3.6 Surface enhanced Raman spectroscopy (SERS)

SERS spectra (Figures 3 and 4) were collected from the surface of nanofibers with various coatings by using an InVia Raman spectrometer (Renishaw, Wotton-under-Edge, Gloucestershire, UK) coupled to an imaging microscope (Leica, Wetzlar, Hesse, Germany). An excitation wavelength of 633 nm (diode laser) and a 50× objective (NA = 0.55) were used. A laser power intensity of 43 μW (1.8 kW/cm^2) was measured at the exit of the objective. The diffraction grating had a density of 600 lines/mm.

For SERS, 4-MBA self-assembled monolayers (SAM) were formed on the AuNPs deposited on nanofibers by immersion of the oxygen plasma-cleaned nanofibers in 100 μM 4-MBA ethanolic solutions overnight. The samples were then removed from the solution, rinsed with ethanol, air dried and used for SERS measurements within several hours.

2.3.7 Finite element method simulations

The simulations were performed with commercial software (FDTD solutions, Lumerical Solutions) based on an FDTD algorithm to obtain the electric field distribution at the cross section of the AuNP-coated nanofiber. Perfectly matched layers are used in the x, y and z directions. The Yee cell size used in our calculations was set to be 0.5 x 0.5 x 0.5 nm^3, much smaller than the AuNP diameter. The optical constants for gold were obtained from the Drude-Lorentz model and the refractive index of the BK7 substrate is 1.513. We compared different meshing sizes to confirm that this parameter did not influence the calculations (Figures 2.S6 and 2.S7).

2.3.8 SERS optophysiology near dopaminergic neurons

2.3.8.1 Animals

Transgenic mice expressing the eGFP gene in monoaminergic neurons under control of the TH promoter (TH-eGFP) were used in this study.[38] Experimental protocols

were approved by the animal handling and ethics committee (CDEA) at the Université de Montréal. Housing was at a constant temperature (21°C) and humidity (60%), under a fixed 12 hours light/dark cycle, with free access to food and water.

2.3.8.2 Primary neuronal cultures

P0-P2 TH-GFP mice were used for culture of dopaminergic neurons from mesencephalon. Pups were cryoanesthetized and decapitated for tissue collection. Freshly dissociated cells from mesencephalon were prepared and then plated (250 000 cells/mL) on glass coverslips containing a monolayer of cortical astrocytes as described previously.[39] Cells were incubated in 5% CO_2 and then used after 10 days *in vitro* for SERS optophysiology experiments.

2.3.8.3 Immunostaining and images acquisitions

Cultures were fixed with a PBS solution containing 4% of paraformaldehyde for 30 min and then permeabilized for 20 min in PBS solution containing 0.1% Triton X-100 and 0.02% NaN_3. Nonspecific sites were blocked in the same solution supplemented with 5% goat serum and 1% bovine serum albumin. A chicken anti-GFP primary antibody (1:2000; Avès Lab #GFP-1020) and a Alexa 488 goat anti-chicken secondary antibody (1:500; Molecular Probes) used to detect it were incubated overnight and for one hour, respectively, at room temperature. Then, two or three dopaminergic neurons per cover slip were randomly selected and fluorescence images were acquired on a Nikon TE 200 fluorescence microscope (Tokyo, Japan) equipped with a Hamamatsu flash 4.0 v2 camera (Hamamatsu, Japan) and a 60x oil immersion objective. Image acquisition was controlled and processed with the Micromanager software.[40] Fluorescence data analysis was carried out with Fiji.[41]

2.3.8.4 SERS optophysiology measurements

SERS spectra were acquired by placing the nanofiber within approximately 10–20 μm of the axonal varicosities of the dopaminergic neurons. The laser was focused near the tip of the SERS nanofiber and maintained at that location throughout the experiment. SERS spectra were acquired with an integration time of 100 ms using a 635-nm diode laser (OZ

Optics, Ottawa, Canada) at a laser power intensity of 500 µW (53.4 kW/cm^2 power density). Raman measurements were performed using an Alpha300 AFM-optical microscope from Witec (Ulm, Germany) equipped with a 63x water immersion objective (NA = 1) from Zeiss (Oberkochen, Germany). A 250 µm multimode optical fiber was used to collect the Raman signal, which was dispersed by a 600 lines/mm grating of a Spectra2300i from Princeton Instrument (Acton, MA). The Raman spectra were acquired with a 1024 x 1024 DU343-BV imaging CCD camera from Andor Technology (Belfast, Northern Ireland). We modified the optical microscope by adding a reflection lens in the infinite optical pathway of the microscope on which a CMOS CCD camera AxioCam 503 from Zeiss (Oberkochen, Germany) was mounted to allow fluorescence imaging. Fluorescence images were acquired by using a Xe arc lamp Xcite from Lumen Dynamic (Mississauga, Canada) with a 474/27 nm Brightlight filter for excitation and a 498 nm RazorEdge filter for emission, both filters were acquired from Semrock (Rochester, NY). The nanofiber was mounted on a custom-made magnetic holder (machine shop of the Chemistry Department of Université de Montréal), similar to an AFM cantilever holder. The magnetic holder was then magnetically attached to a piezoelectric inertial drive mounted on a support above the microscope objective. The inertial drive is usually used to hold and manipulate an AFM cantilever. SERS measurements from neurons were performed in a custom-made Teflon fluidic cell (machine shop of the Chemistry Department of Université de Montréal) with a constant flux of physiological buffer provided by a Minipuls 2 peristaltic pump from Gilson (Middleton, WI). The buffer flux was 50 µL/s and the approximate total volume of the cell was 700 µL.

All measurements with neurons were performed in a normal saline physiological buffer composed of 140 mM NaCl, 5 mM KCl, 2 mM $MgCl_2$, 2 mM $CaCl_2$, 10 mM HEPES, 6 mM sucrose and 10 mM glucose. Dopamine and glutamate release was stimulated with a 40 mM KCl solution. The depolarisation buffer was composed of 105 mM NaCl, 40 mM KCl, 2 mM $MgCl_2$, 2 mM $CaCl_2$, 10 mM HEPES, 6 mM sucrose and 10 mM glucose. Both buffers were adjusted to pH 7.35 and to an osmolality between 305-310 mOsm.

Data analysis of the SERS optophysiology experiments was performed with a custom chemometric algorithm on MatLab 2015b (MathWorks, MA) available on GitHub

(https://github.com/SPRBiosensors/D-SERS-optophysiology). Adaptative iteratively reweighted penalized least squares (airPLS) was applied on each spectrum in order to evaluate the baseline (lambda = 1e+08; order = 2; p value = 0.05).[44] The baseline was not subtracted, but used to generate a curved threshold line in order to avoid discrimination of Raman bands due to a non-uniform background. This was an alternative to a background subtraction routine which may introduce unintended artefacts.[45] A scalar value was then added to the baseline (e.g. 0.025 times the median of the spectrum) leading to a curved threshold (Figure 2.S12). Following the evaluation of the threshold, a Savitzky-Golay (SG) noise filter was then applied to enhance spectral quality (polynomial order = 3, frame = 11). The second derivative of each spectrum was then determined to increase the precision of band frequencies.

Barcodes were extracted from every SERS spectrum using the built-in function, *findpeaks*, in MatLab. If the intensity of the detected peak was greater or equal to the value of the threshold, the corresponding frequency was a positive detection event, resulting in the presence of a bar in the barcode extracted for that spectrum. This process was repeated for all peaks detected, thus generating the complete barcode of each spectrum. A library of reference barcodes was generated from the SERS response of the nanofibers with pure solutions of the neurotransmitters. Barcodes extracted from the optophysiology data were sequentially compared to the library of reference barcodes. If bars between the experimental and the reference barcode matched, a binary response for this frequency was generated (1 = matched, 0 = unmatched). If the number of matches in an experimental spectrum from the optophysiology data equaled at least 60% of the total number of bars of a reference barcode, a positive event was counted for that neurotransmitter. This event was then graphically expressed as a vertical bar in the optophysiology trace for the corresponding standard (Figures 2.3C and 2.3D). ANOVA and Kruskal-Wallis one-way analysis of variance were then performed on GraphPad Prism 7.00 (GraphPad Software, Inc., CA).

2.4 Results and discussion

Here, we show that a patternless and nanothin BCP brush-like coating on fibers of sub-micrometer diameters is an effective template for the dense deposition of well-

dispersed gold nanoparticles (AuNPs). Our procedure, depicted schematically in Figure 2.1A, with details given in the Experimental Section, consists of dip-coating the nanofiber (pulled glass rod) in a tetrahydrofuran (THF) solution of polystyrene-block-poly(4-vinylpyridine) (PS-b-P4VP) for 2 min and then immersing it overnight in an aqueous colloidal suspension of AuNPs with an average diameter of 52 nm as determined from the UV-visible spectrum (Figure 2.S1; 46 nm according to scanning electron microscopy, Figure 2.S2, the small difference from the UV-vis determination arising from minor biases in both techniques). The resulting dense and well dispersed AuNP array obtained on the nanofibers is illustrated by the SEM images in Figure 2.1B at a fiber diameter of about 8 μm (with a histogram of the AuNP size distribution and a plot of the AuNP density at three fiber diameters) and in Figure 2.1C in the fiber tip region where the diameter is less than 1 μm. The AuNP density is approximately constant at about 90 AuNPs/μm^2 at the three fiber diameters analyzed, ranging from 600 nm to 12 μm. Obtaining these arrays is reproducible on the order of 75%, as indicated in Figure 2.S3, and is independent of the dip-coating solution concentration (0.05-1.0 mg/mL) and withdrawal rate (0.1-80 mm/min). Conversely, AuNP deposition on nanofibers coated with an analogous statistical copolymer or a P4VP homopolymer, while dense, is less uniform and shows more aggregation, particularly near the tip (Figure 2.1C; see Figure 2.S4 for the 8-μm diameter), whereas very few AuNPs adsorb onto bare nanofibers (Figure 2.1C).

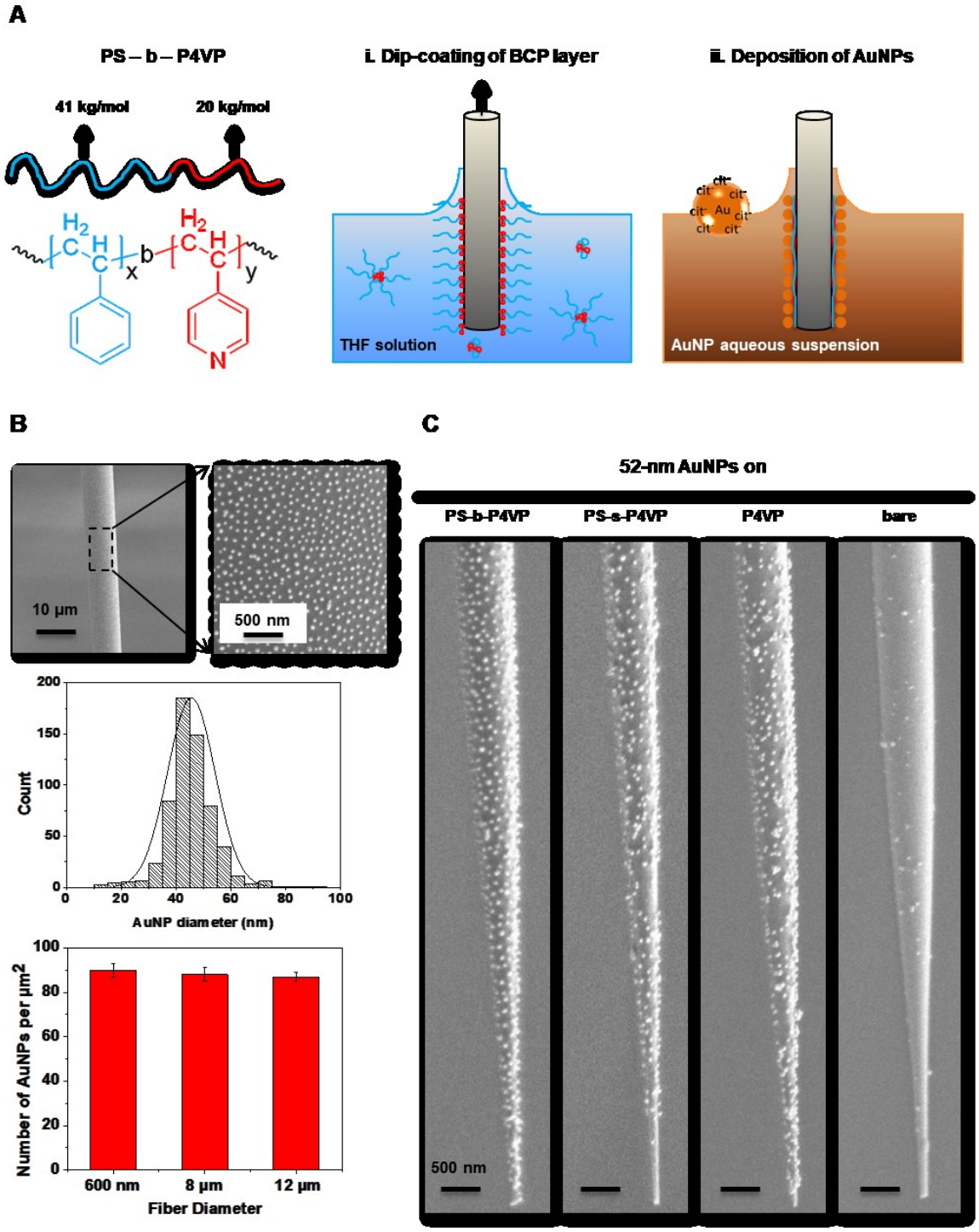

Figure 2.1. Block copolymer (BCP) brush-layer template for achieving dense and well-dispersed AuNP arrays on highly curved surfaces. (A) Structure and block molecular weights of the BCP used [polystyrene-b-poly(4-vinylpyridine), PS-b-P4VP] and schematic of the experimental procedure. The latter consists of dipping a glass nanofiber successively

in (i) a THF solution of PS-b-P4VP (0.05 mg/mL concentration, 40 mm/min withdrawal rate), resulting in only a nanothin brush layer adsorbed onto the nanofiber due to its very high curvature, and (ii) an aqueous suspension of citrate-capped AuNPs (52 nm in diameter according to UV-vis). The brush layer is highly stable due to multiple hydrogen bonds between the P4VP blocks (wetting underlayer) and the OH groups on the glass surface; the PS sublayer is exposed to the THF solution or to air). (B) and (C) show SEM images illustrating that a dense and well-dispersed array of AuNPs is deposited on the BCP brush layer, attributed to molecular reorganization exposing P4VP segments for electrostatic interactions with the AuNPs. The pattern is shown to be similar for nanofiber diameters around (B) 8 μm and (C) at the fiber tip with a taper from 1 μm to approximately 200 nm. (B) also shows the statistical polydispersity in AuNP diameter and the AuNP density at three fiber diameters. (C) also shows AuNP arrays on nanofibers coated by a statistical PS-s-P4VP (of similar P4VP content as the BCP), a P4VP homopolymer, and bare glass.

Several reasons lead us to conclude that the PS-b-P4VP coating on the nanofiber after immersion in the BCP solution is a brushlike layer of a few nanometers, where, as explained below, the P4VP block is adsorbed to the glass surface and covered by a layer formed by the PS block. For one, AFM images of a fiber dipped only in the BCP solution show no surface pattern and the surface roughnesses before and after dip-coating are comparable (Figure 2.2), consistent with the absence of the BCP micelles that are observed when dip-coating flat substrates in this solution.[14] Furthermore, erasure of the coating with an AFM tip indicates a dried film thickness of about 3 nm (Figure 2.2), in agreement with the thickness obtained for an adsorbed BCP dry brush layer on a flat surface,[18] whereas a layer of micelles for this BCP would lead to a thickness of at least 15 nm.[14] In the brush layer, given the polar nature of the silicon dioxide glass nanofiber and the block solubilities in THF (good for PS, poor for P4VP), the polar P4VP block acts as the wetting or anchoring sublayer in contact with the substrate and the hydrophobic PS block forms an overlayer of extended PS chains when in the THF solution and collapsed chains exposed to air when dried.[14,18] The multiple interactions per chain, in the form of hydrogen bonds

between P4VP and the polar (OH-functionalized) glass confers high stability to the adsorbed layer.[19,20]

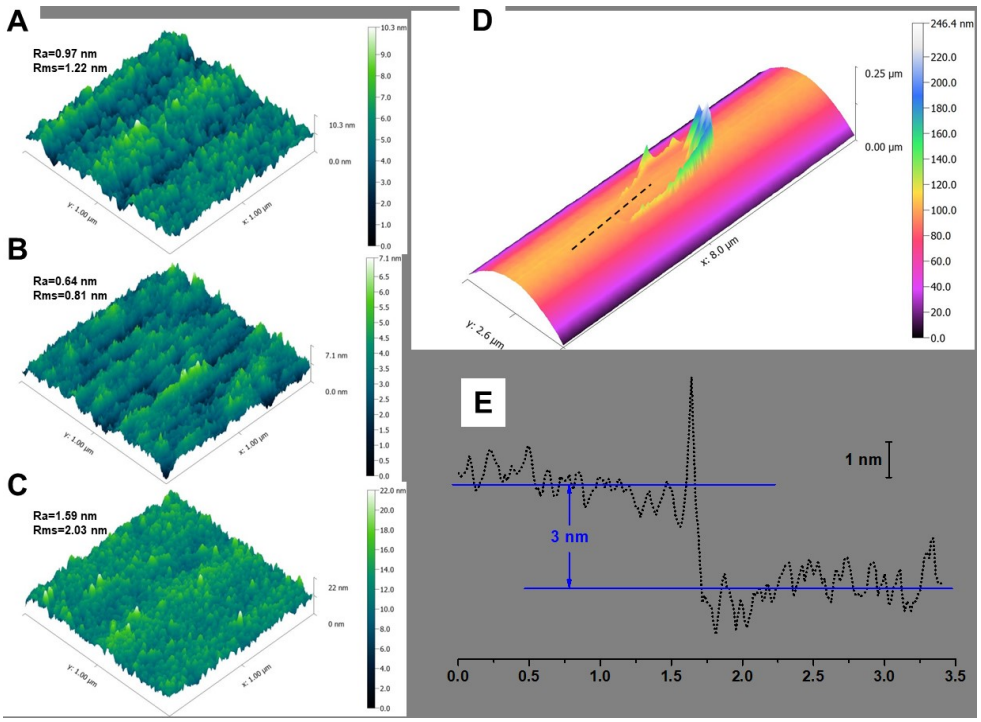

Figure 2.2. AFM analysis of the roughness and thickness of the PS-b-P4VP brush layer on nanofibers. 1 µm x 1 µm 3D AFM height images of the glass fiber surface at a diameter of about 8 µm before (A) and after (B) the PS-b-P4VP brush layer coating, and after overnight immersion of the BCP-coated fiber in a acidic aqueous solution (C). Ra and Rms stand for roughness and root mean square roughness, respectively, generated by Gwyddion. They indicate that the degree of roughness of the BCP-coated fiber is slightly lower than that of the bare surface and, in contrast, exposure to adidic solution results in increased roughness, consistent with molecular rearrangement of the PS sublayer exposing parts of the P4VP sublayer. (D) is 3D AFM height image of the BCP film after erasing a portion of the coating (approx. 0.5x2 μm^2) using an AFM tip in contact mode; (E) shows the height profile corresponding to the dashed line drawn in (D). The height profile indicates a BCP film thickness of approximately 3 nm.

Previous literature has indicated that a BCP brush-like layer is rapidly adsorbed onto solid substrates when immersed in BCP solutions, reaching maximum density within minutes.[21-23] Moreover, it was shown, for dip-coating of a flat mica substrate in a PS-b-P2VP toluene solution, that the brush layer is adsorbed during the immersion period, while any additional BCP material is deposited during withdrawal of the substrate from solution.[18,24] Thus, given the above-mentioned relation between the fluid film thickness on cylindrical surfaces and the substrate diameter, combined with the moderate dip-coating withdrawal rates used, it is likely that no additional material was deposited on the nanofibers during the withdrawal stage and that only the brush-like layer that was adsorbed during the immersion period is present. This would also explain why the AuNP pattern was unaffected by the dip-coating withdrawal rate.

When the BCP-coated nanofiber is immersed in the AuNP suspension, the burial of the P4VP anchoring layer by a PS protective layer might be expected to inhibit AuNP deposition on the brush, since interactions between the charged AuNPs and PS is energetically unfavorable and the PS constitutes a hydrophobic barrier to favorable P4VP-AuNP electrostatic interactions. Nevertheless, we observe dense AuNP coverage. This can be explained by some degree of molecular rearrangement in response to contact with the aqueous solution that exposes P4VP segments to AuNPs. The hydrophilic solvent itself could induce such a rearrangement, as has been shown to occur for nanostructured BCP films covered by a hydrophobic top layer.[25] It can also be driven by the solution acidity (pH 5) causing P4VP protonation and therefore even greater affinity with water and the negatively charged AuNPs, as discussed in ref 26 to explain the success in templating nanowires on nanostructured PS-b-P2VP thin films with buried P2VP in-plane cylinders. Molecular rearrangement is supported by the AFM images in Figure 2.2 (complemented by Figures 2.S5 and 2.S6), which indicate that the initially smooth brush-layer film became rougher after exposition to water and acidic buffers. Presumably, the brushlike PS chains that cover the P4VP underlayer following dip-coating in the BCP solution tend to aggregate into more mushroom-like arrangements when immersed in the aqueous AuNP solution, somewhat analogously to what is observed with end-grafted homopolymer chains exposed to a poor solvent,[27] thereby exposing the P4VP underlayer in the areas between the PS

agglomerations and allowing AuNP deposition, this without destabilizing the strong adsorption of the P4VP layer to the glass.

The observation that the AuNP deposition on the BCP adsorbed layer is dense and well-dispersed is striking. In contrast, the AuNP distribution on a P4VP homopolymer coating, on a statistical PS-s-P4VP copolymer coating (Figure 2.1C) and on an APTES coating[8] is less uniform and more aggregated. This suggests that the PS block plays a significant role in favoring well-dispersed AuNPs, probably by virtue of the covalent attachment of the PS chains to the P4VP chains that sterically inhibit AuNP aggregation. A P4VP homopolymer or APTES coating cannot provide this dispersion capability, and the results for the statistical copolymer suggest that (short) PS segments tethered at both ends by 4VP units that are randomly located within the chains likewise cannot play this role. Thus, the picture that can be formed of the AuNPs adsorbed to the dry BCP brush film is that the large AuNPs (52 nm) penetrate the PS collapsed brushlike overlayer (probably at least 2 nm in thickness) in order to contact the P4VP wetting layer (likely 1 nm or less in thickness), while the PS in the vicinity of the AuNPs forms a quasi-2D corona around the peripheries of the AuNPs.

To summarize, we propose the following AuNP nanotemplating mechanism on the nanofiber: a nanothin BCP brush layer is adsorbed through P4VP H-bonding onto the glass surface during immersion of the nanofibers in the BCP dip-coating solution, and molecular rearrangement of the PS chains occurs in the aqueous AuNP solution to expose P4VP, which then electrostatically adsorbs AuNPs, with the PS layer likely creating a corona around the AuNPs to minimize aggregate formation. With this BCP brush-layer nanotemplating method, dense arrays of well-dispersed AuNPs were thus obtained near the nanofiber tip, essential for SERS optophysiology.

Next, the optical properties of the AuNPs on the nanofibers were characterized by *in vitro* SERS experiments. The optical appearance of the nanofibers was altered from white for bare and BCP-coated nanofibers to yellowish after AuNP coating, due to the extinction of light by AuNPs (Figure 2.3A). To test the SERS performance of the nanofiber, the AuNP surface was derivatized with a self-assembly monolayer (SAM) of 4-mercaptobenzoic acid (4-MBA). To that end, the AuNP-coated nanofiber was first cleaned

by O_2 plasma for 5 min and then incubated in a 100 μM 4-MBA ethanolic solution overnight. The AuNP coating was robust vis-à-vis the plasma treatment and the surface functionalization, as indicated by the optical appearance (Figure 2.3A) and by SEM images (Figure 2.3B) that show identical AuNP coating before and after the treatments. The immobilization of the AuNPs after plasma treatment indicates that the polymer template was only partly removed, due to the shadowing effect from the AuNPs. Next, SERS spectra were collected from the nanofibers. As shown in Figure 2.3C, no SERS bands were observed on the spectrum of a bare nanofiber or a PS-P4VP-coated nanofiber. In contrast, the AuNP-coated nanofiber showed multiple sharp peaks with relatively high intensity, which are due to the citrate-capped AuNPs (Table 2.S1). There are no clear Raman bands observed for PS-b-P4VP, probably due to lack of SERS enhancement on the thin film template left underneath the AuNPs.[28] The background signal of citrate ligands was completely removed by the plasma treatment, as evidenced by the disappearance of SERS peaks from the spectrum after this treatment. However, we suspect that the polymer coating mostly survives the plasma cleaning process, as the particles are still stable on the surface thereafter. Finally, the SERS spectrum for the 4-MBA-modified nanofiber shows the characteristic peaks of 4-MBA at 1071 cm^{-1} and 1571 cm^{-1} with high intensity and a relatively weak mode at 1179 cm^{-1} (Table 2.S1).

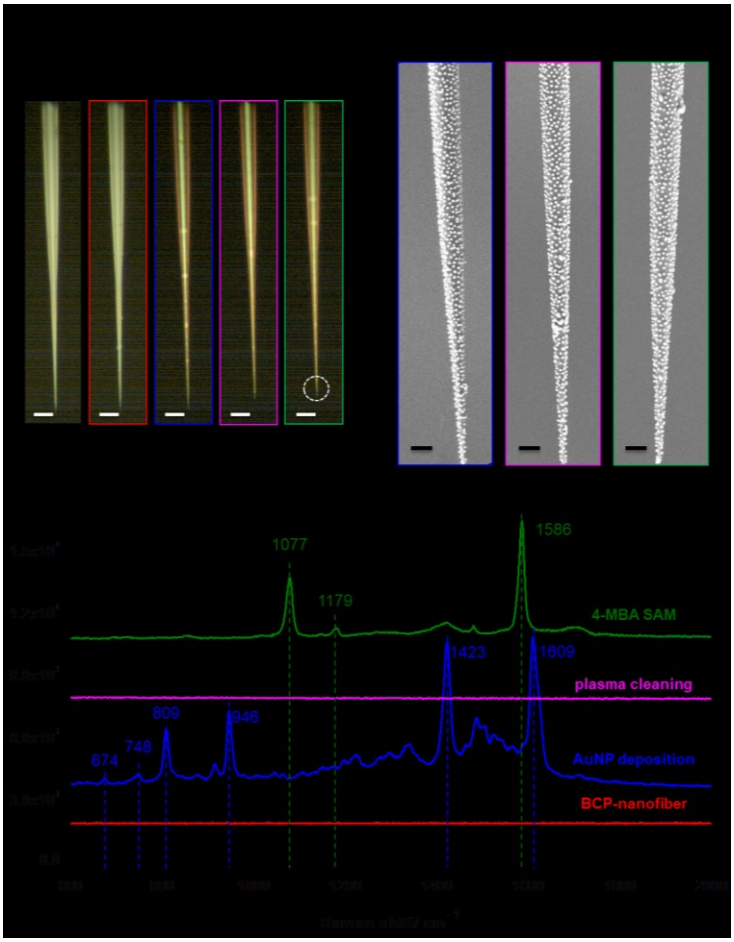

Figure 2.3. Optical characterization of SERS nanofibers. (A) Optical microscopic images of, from left to right, a bare nanofiber (black outline), after BCP film coating (red outline), after 54-nm AuNP deposition (blue outline), after plasma treatment (purple outline) and after 4-MBA SAM surface derivatization of the AuNPs (green outline). Scale bars represent 10 μm. The presence of AuNPs gives fibers a yellowish color, due to the extinction of light by the AuNPs. (B) SEM images indicate the uniformity of the AuNP coating at the fiber tip (leftmost image, outlined in blue) and their stability to plasma treatment (center image, outlined in purple) and 4-MBA SAM derivatization (rightmost image, outlined in green). Scale bars represent 500 nm. (C) SERS spectra with major SERS bands marked by dashed lines and their corresponding assignments given in Table 2.S1 collected from various nanofibers at the location indicated by a white dashed circle in (A).

We then compared the SERS response of 4-MBA on identically prepared AuNP arrays on flat silicon wafers (n = 20) and on the nanofibers (n = 10). Surprisingly, the response was more than 35 times greater with the nanofibers compared to the flat surfaces (Figure 2.4D). The Raman laser illuminates 2.5 times fewer AuNPs on the flat silicon wafer, as particles are irradiated only on one side of the flat silicon substrate (area of πr^2 where r is the radius) while the laser irradiates the AuNPs at the intersection of the laser beam and both sides of the nanofiber (approximated to an area of $8r^2$; half of a Steinmetz solid). Hence, there is an improvement in the SERS response of about an order of magnitude that is not accounted for by the number of particles on the nanofibers.

This enhanced response on the nanofiber seems attributable to the effect of the high curvature, as revealed by simulating the expected electric field of a nanofiber and a nanopipette (hollow core) using finite element method (FEM) calculations (Figure 2.4A-C). The simulations were performed on a commercial FDTD software (Lumerical solutions), as detailed in the Supporting Information. A strong electric field was predicted at the outlet of the nanofiber, which can be attributed to a lens effect (Figures 2.4C and 2.S7-S9), where the rays of the laser beam are focused on fewer nanoparticles. This was experimentally verified from the SERS intensity at different cross-sections of the nanofibers (Figure 2.4F), where the intensity of the Raman bands of 4-MBA at different heights (in the z-axis of the microscope) was used to probe the electric field on the nanofiber. We observed a stronger intensity of the Raman bands of 4-MBA at a smaller radius of 600 nm than at radii above 1 micron (Figure 2.4F). We hypothesize that a ring resonator effect can occur on the fiber, in addition to the plasmon enhancement. This is substantiated by the small shift in the Raman cross-section intensities at two different Raman shifts for a diameter of 600 nm. As these bands are shifted in scattering wavelength, we would anticipate that the enhancement would occur at different fiber diameters. Due to the taper of the fiber, this means that coupling of the light would be optimal at different cross-sections for different wavelengths.

FEM simulations predicted, and we observed experimentally, a Gaussian SERS intensity on nanofibers below 1 μm and a bimodal distribution on slightly larger diameters, corresponding to the two interfaces of the nanofibers (Figure 2.4F). In addition, the

simulations predict that the field is about twice stronger for a nanofiber than for a nanopipette (Figure 2.4B and C), improving on the nanopipettes that were used for the previous SERS experiments reported on these types of nanosensors.[7,8,29,30] Simulations were also carried out at different nanofiber radii. For a nanofiber radius around 100 nm, the field around the AuNPs is dipolar as expected for isolated particles (Figure 2.S8). As the radius of the nanofiber increases to at least 300 nm, FEM data show increasingly strong interparticle coupling, creating hotspots between particles despite the relatively large distance between them. At fiber diameters of a few microns, the field is no longer strongly concentrated at the outlet of the fiber. These pieces of evidence suggest that the nanofibers create a wavelength-scale lens which further improves the SERS signal of the nanofibers and optimal SERS should be expected by irradiating a nanofiber close to 1 μm in diameter. Hence, we thereafter focused the laser beam at a location slightly recessed from the tip, where the diameter is about 1 μm, to benefit from the higher SERS response.

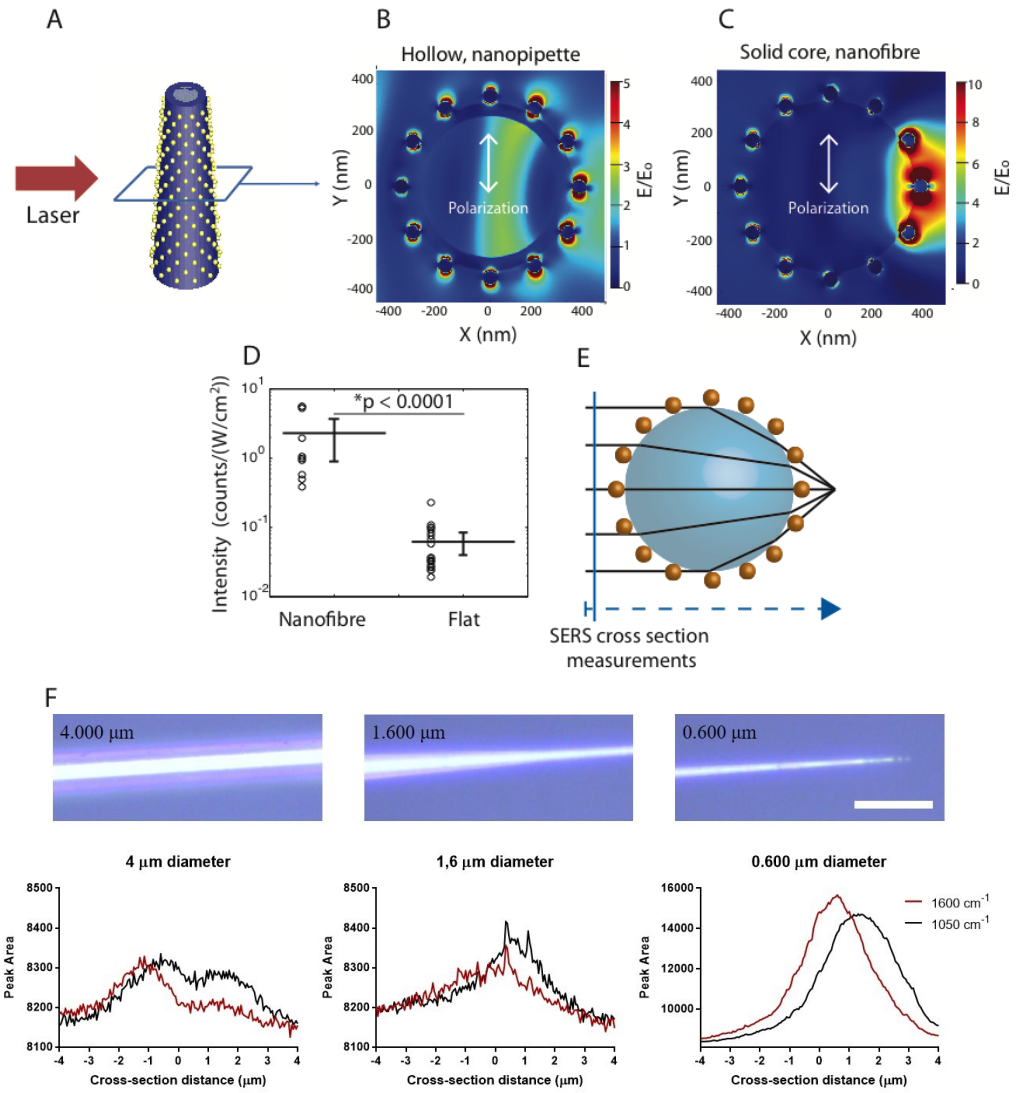

Figure 2.4. SERS performance of nanofibers modified with brush-layer templated AuNPs. A) Scheme representing the finite-element method (FEM) simulation methodology. Polarized light of 633 nm was oriented along the cross-section (parallel to the y-axis) as shown in panels B and C. Light traveled along the x-axis from left to right in the figures. The AuNPs (52 nm in diameter) are ordered in an hexagonal pattern with 70-nm spacing between neighboring AuNPs. Simulations were performed on a cross-section of 325-nm radius. B) and C) Normalized field intensity for a hollow nanopipette (B) and a solid core nanofiber (C). Fields of greater intensity are predicted at the outlet of the nanofiber. D) The SERS intensity of 4-mercaptobenzoic acid on the nanofiber (n = 10) was compared with a paired t-test on a series of AuNPs assembled on a flat silicon surface (n = 20). The SERS

intensity (normalized to the laser power density) was approximately 35 times greater on the nanofibers than on the flat surface. Identical arrays of AuNPs were formed on both surfaces. Raman parameters: Renishaw In Via Raman microscope, 633 nm laser excitation, 37.1 μW for the flat surfaces and 4.1 μW for the nanofiber, 100 X air objective (NA 0.85). E) Scheme depicting the ray convergence of a ball lens with AuNPs on the lens surface. This represents a cross-section of the nanofiber (panel C). The focal point of a ball lens is relatively close to the lens, for example a 650 nm diameter glass lens (conditions of panel C) would have a focal distance of 156 nm from the lens surface, concentrating the rays on fewer AuNPs and increasing the field intensity. F) Cross-section profiles of the SERS peak area at nearly 1600 cm^{-1} and 1050 cm^{-1} showing the presence of a single Gaussian peak for a smaller radius of 600 nm and two peaks for larger radii of 1.6 and 4 μm. These peaks are attributed to the two interfaces of the nanofiber. The Raman response was significantly greater for the smaller radius of 600 nm. The cross-section profiles were acquired with a Witec Alpha 300 with a 633 nm laser and a 50X air objective (NA 0.70), a laser power of 7.5 μW and an integration time of 500 ms.

The *in vitro* SERS response of the nanofibers was compared to that of heavily aggregated 52-nm AuNPs on otherwise identical pulled glass fibers that were APTES-coated in the same way as in previously published SERS optophysiology experiments.[7,8] For this, we used mouse dopaminergic neurons isolated from the mesencephalon of P0-P2 TH-GFP transgenic mice and cultured for 10-14 days to allow for the development of a large number of functional release sites. As this is the model we used in our previous publication, this allows for a direct comparison of the SERS nanosensors. The cell-wide expression of green fluorescent protein (GFP) in these neurons facilitated the positioning of the nanofibers in proximity to neurotransmitter release sites, the axonal varicosities (Figure 2.5A-C). Although the technique has the ability to monitor at least 5 different molecules,[29] we focused on monitoring dopamine (DA) and glutamate (Glu), both of which are released from subsets of mouse dopaminergic neurons.[31]

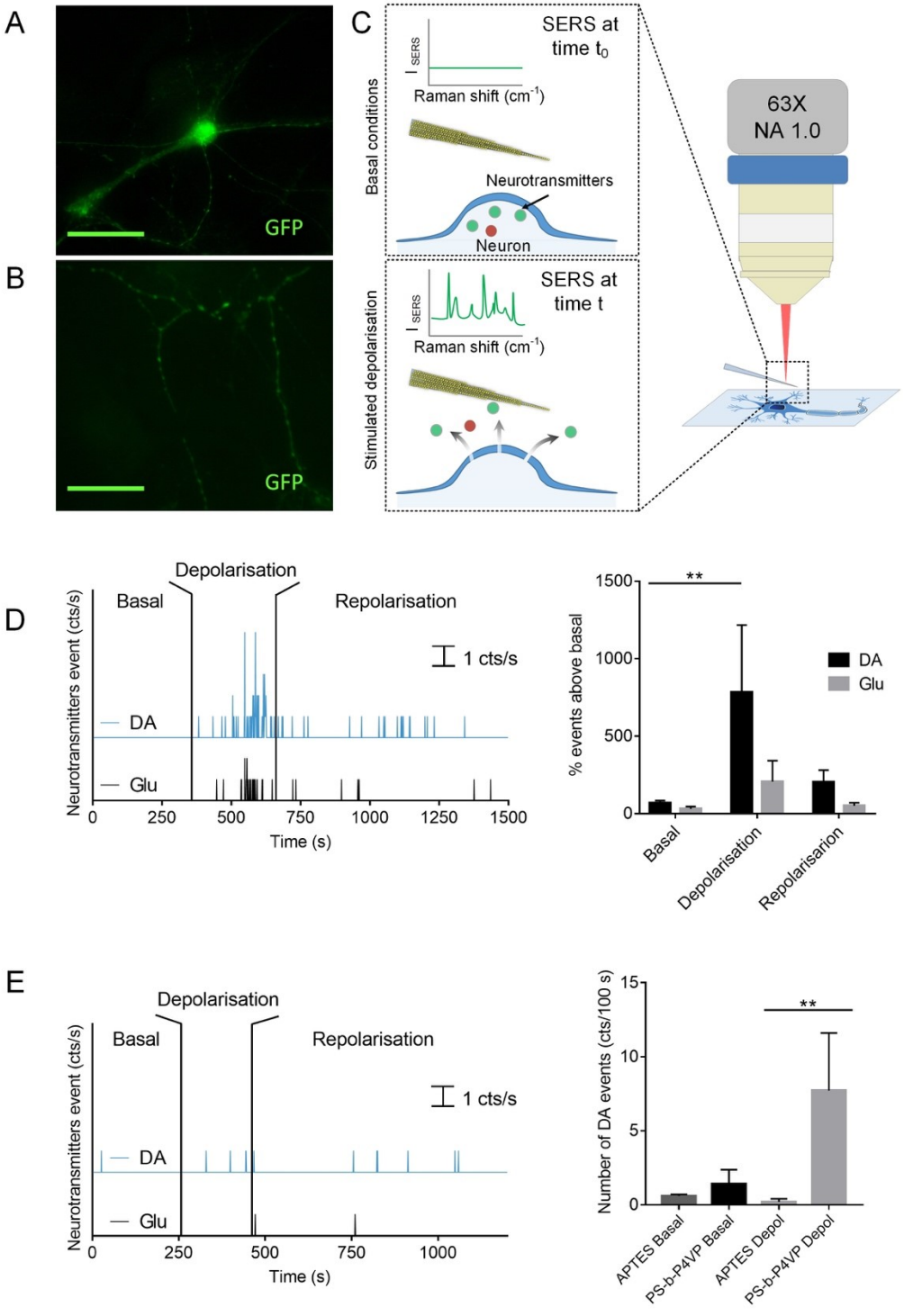

Figure 2.5. SERS optophysiology measurements of dopamine (DA) and glutamate (Glu) released by primary mouse dopaminergic neurons. A) Immunofluorescence image of a randomly selected eGFP-expressing dopaminergic neurons acquired using a TE 200

fluorescence microscope from Nikon. Neurons were immunolabelled with chicken anti-GFP primary antibody and detected with Alexa 488 goat anti-chicken secondary antibody to enhance the fluorescence intensity. B) Fluorescence images obtained with the optophysiology microscope (combination of a Fluorescence-Raman microscope with a piezoelectric stage to position the nanosensor, as described in Ref. 28) of axonal varicosities of a typical dopaminergic neuron expressing eGFP. Axonal varicosities are the main sites from which DA and other neurotransmitters such as Glu are released by the neurons. Scale bars, 20 μm. C) Representation of the SERS optophysiology measurement. The nanofiber was located approximately 10 μm above an area containing a high density of dopaminergic axonal varicosities. SERS spectra are obtained only for molecules diffusing on the AuNPs excited by the Raman laser. DA and Glu were identified from pre-calibrated SERS spectra. D) Left: SERS optophysiology traces of DA and Glu obtained with a BCP-templated AuNP nanofiber. Extracellular neurotransmitters were detected under basal conditions (Basal), followed by depolarisation of neurons with 40 mM KCl physiological buffer (Depolarisation) in order to enhance neurotransmitter secretion, and finally after returning to basal conditions with 4 mM KCl physiological buffer (Repolarisation). Vertical bars represent a positive event for the corresponding neurotransmitter. Right: Number of detected neurotransmitter events relative to basal conditions. The number of events was corrected according to the mean number of events detected near primary astrocytes without neurons. There is a statistically significant difference in the number of DA events detected during the stimulation compared to the basal level, and a tendency to decrease for repolarisation conditions (Kruskal-Wallis one-way analysis of variance, $^{**}P = 0.008$, $P = 0.27$), while the number of Glu events showed a tendency to increase ($P = 0.12$). The error bars correspond to the standard deviation of the mean ($n = 6$ independent measurements). E) Left: SERS optophysiology curves of a plasmonic nanofiber coated with heavily aggregated AuNPs (using an aminopropyltriethoxysilane (APTES) method) in otherwise identical conditions as panel D. Right: Number of events of DA in basal and depolarisation conditions. The number of events was corrected according to the average number of events near primary astrocytes under basal conditions. There is a statistically significant difference in the absolute number of DA events during the stimulation period (PS-b-P4VP Depol) compared to the basal condition (PS-b-P4VP Basal) (Kruskal-Wallis

one-way analysis of variance, $*P = 0.052$). There was also a statistically significant difference in the absolute number of DA events detected by the PS-b-P4VP nanofibers during the stimulation period (PS-b-P4VP Depol) compared to the number of DA events detected by the functionalized nanofiber APTES (APTES Depol) in the same physiological conditions (Kruskal-Wallis one-way analysis of variance, $**P = 0.0022$). The error bars correspond to the standard deviation from the mean ($n = 5$ for APTES and $n = 6$ for PS-b-P4VP independent measurements).

Rapid (100 ms) SERS spectra were acquired for a sufficient period of time to provide a temporal signature of the chemical composition near these neurons (Figure 2.5D). DA events were recorded using the vibrational signature in the SERS spectra collected on the nanofiber and processed with a barcode algorithm (details provided in the Supporting Information and Figure 2.S10 for examples of SERS spectra). We observed a significant increase ($*P = 0.0022$) of nearly one order of magnitude of signal intensity with the ordered AuNPs on the nanofibers in the rate of DA detection compared to aggregated AuNPs on the nanofiber (Figure 2.5E, right). One would expect that the response of highly aggregated AuNPs be significantly higher due to the presence of strong hotspots with aggregated AuNPs. Therefore, this result is relatively surprising as the AuNPs are spaced nearly 70 nm apart on average using the BCP fabrication method and it has previously been assumed that aggregated nanoparticles with sub-10 nm gaps are amongst the best SERS substrates.[32] However, FEM data (Figure 2.S7) suggest that the lens effect creates hotspots between AuNPs despite their interparticle distance.

Conversely, the fact that we reached this high SERS intensity with a low laser power density of 53.4 kW/cm^2 is even more striking. This low laser power had to be used for the SERS studies with the ordered AuNP on the nanofibers, as higher laser power led to significant heating and damage to neurons. Increasing the laser power to 5 mW (about 500 kW/cm^2) for 1 s induced sufficient heating to melt the glass at the tip (Figure 2.S11). Interestingly, the AuNPs remained well-dispersed despite the significant heating. The large heating observed at higher laser power could potentially constitute an excellent platform for killing cells with the release of heat from the AuNPs (*i.e.* photothermal therapy[33]).

During the past decade, multiple classes of neurons characterized by their ability to release other neurotransmitters, such as DA, serotonin and norepinephrine, have been shown to express vesicular transporters VGLUT,[34] indicating that such neurons can co-release glutamate, stimulating the need for multiplexed sensing. Although the release of DA and Glu from dopaminergic neurons can be measured separately using electrophysiology[35] or electrochemistry,[36] here their co-release in a single experiment was measured for the first time. Our previous report with aggregated AuNPs did not lead to significant detection of glutamate, due to the lower sensitivity of the SERS nanosensor.[29] We stimulated the release of neurotransmitters using a technique of membrane depolarization triggered by a 40 mM KCl saline buffer. As expected, the frequency of detection for DA and Glu events near neurons was low under basal conditions. However, an important increase in DA events relative to the basal condition was observed (**P = 0.0079) with membrane depolarisation, characterized by an increase in frequency in the SERS optophysiological curves (Figure 2.5D, right) followed by a tendency for the number of events to decrease during the return to basal conditions in 4 mM KCl (*P = 0.27). We observed about 700% increase in the rate of Glu detection events during the depolarisation of neurons compared to basal levels. A tendency to increase was thus observed with Glu (P = 0.12), again with a tendency to decrease during repolarisation (P = 0.41), suggesting that the co-release of multiple neurotransmitters can be monitored with SERS optophysiology for DA and Glu. Sensors allowing detection of extracellular glutamate have been developed,[37] but these do not allow multiplex detection of multiple neurotransmitters. Our study therefore constitutes a significant advance in the development of a novel tool for the study of neuronal co-transmission studies, as shown here for DA and Glu.

2.5 Conclusions

In summary, we report that the formation of a nanothin BCP brush layer on a nanofiber is an effective and simple method to adsorb dense and well-dispersed AuNPs, and forms a robust template for the fabrication of SERS-based nanosensors. In this brush layer, the AuNPs electrostatically interact with the P4VP underlayer that is strongly adsorbed by multiple H-bonds to the Si surface. During immersion in the aqueous colloidal solution, they are exposed to the P4VP by local molecular rearrangement of the PS

overlayer that then forms quasi-2D coronae around the AuNPs, effectively dispersing them and thus inhibiting their aggregation. The optical properties of the SERS nanosensor thereby created is improved by at least one order of magnitude in comparison to other methods of forming SERS nanosensors. The superior performance led to the capability of sensing the co-release of DA and Glu from dopaminergic neurons, where previous generations of SERS nanosensors lacked the sensitivity to detect Glu. As SERS optophysiology sensors can be used for purposes other than to study neurotransmission, we also envisage that the nanofibers will be broadly applicable in biological sciences, physiology and neuroscience for monitoring chemical composition with high spatial and temporal resolution as shown here.

2.6 Supporting information

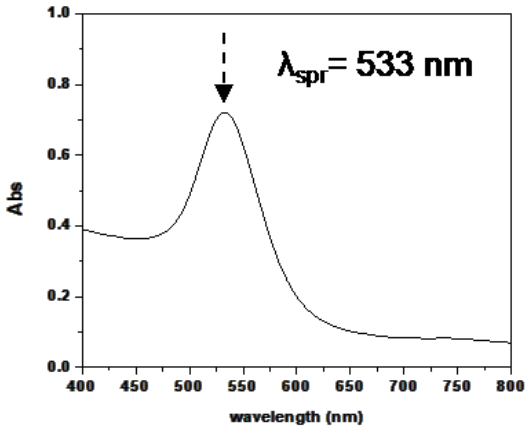

Figure 2.S1. UV-visible spectrum of the AuNP aqueous suspension used for the deposition of AuNPs on nanofibers. The average AuNP diameter was calculated from the peak wavelength, λ_{spr}, using the method of Haiss et al.[39] to be 52 nm.

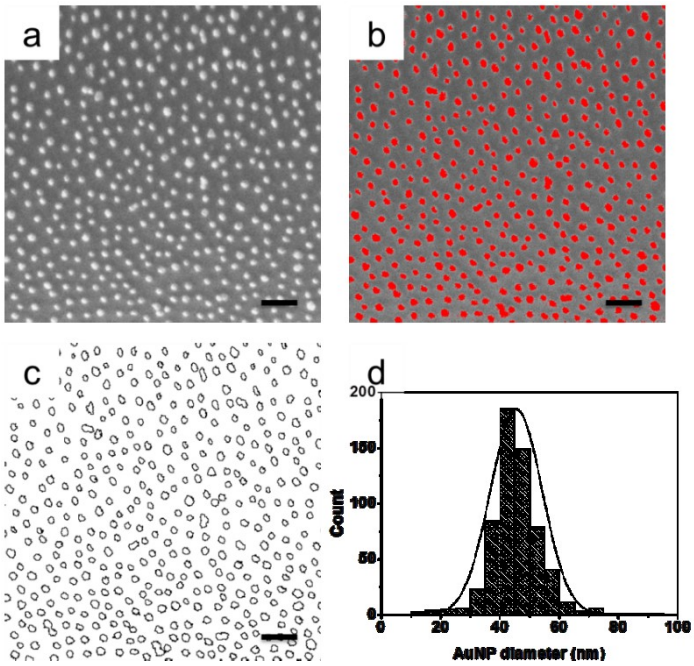

Figure 2.S2. a) SEM image of the AuNPs deposited on the BCP brush-coated nanofiber at a fiber diameter of 8 μm. Using ImageJ, the AuNPs are marked in red in (b) and their outlines in (c) in order to generate the size histogram distribution in (d). Scale bars represent 250 nm. The ImageJ auto-marking process generated an averaged AuNP size, from the maximum of the distribution curve shown, of 46 nm, which is a little smaller than the 52 nm obtained from UV-vis (Figure 2.S1).

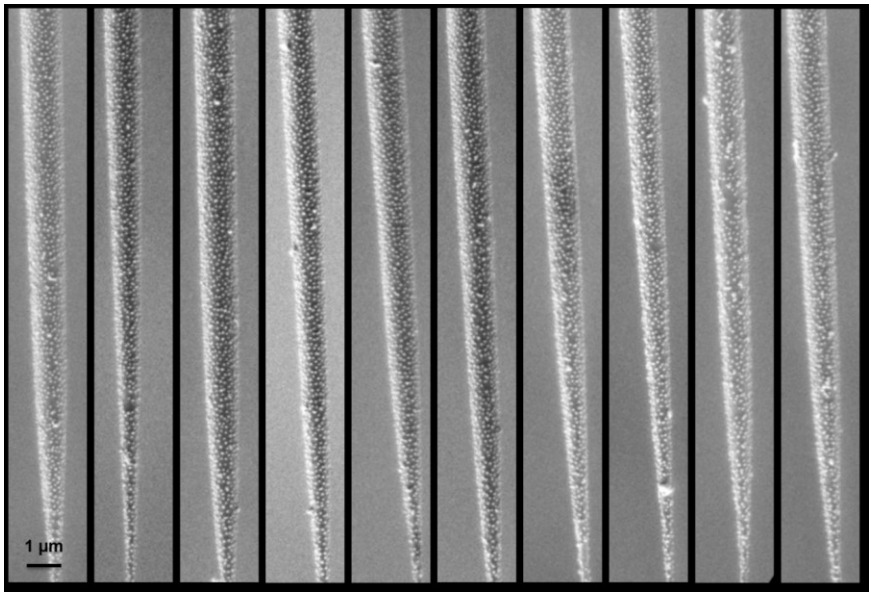

Figure 2.S3. SEM images of replicate PS-*b*-P4VP brush layer-coated nanofibers onto which 54-nm AuNPs were deposited. A total of 16 nanofibers were prepared in this set, of which 12 were successful; *i.e.* covered with a dense layer of well-dispersed AuNPs (10 shown), for a success rate on the order of 75%. In general, when sets of nanofibers were prepared, the success rate was 75 to 80%.

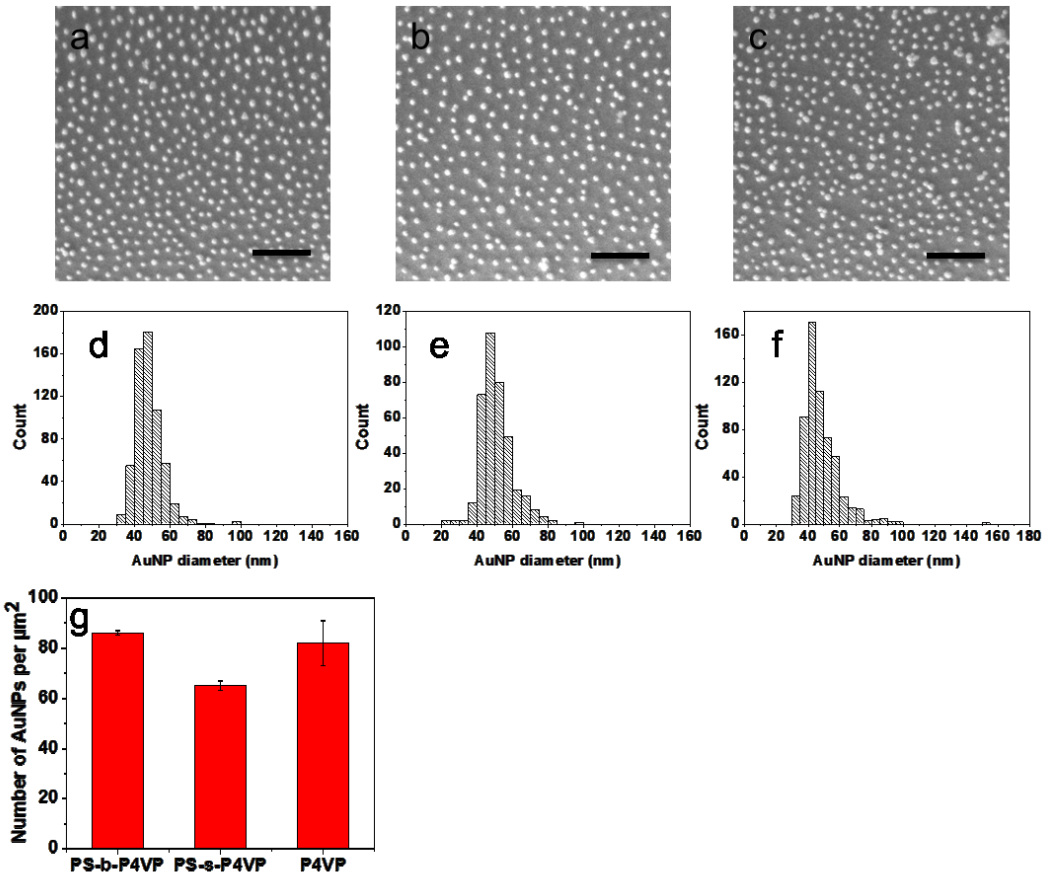

Figure 2.S4. SEM images of 54-nm diameter AuNPs deposited on nanofibers (shown at fiber diameters of about 8 µm), coated by a) a PS-b-P4VP block copolymer film template, b) a PS-s-P4VP statistical copolymer film template and c) a P4VP homopolymer film template. Scale bars represent 500 nm. Qualitatively, these images indicate that there are fewer AuNPs per unit area with a PS-s-P4VP film and less uniformity with a P4VP film. Panels d, e and f show the size distributions of the AuNPs on the surface of the nanofibers fabricated in panels a, b and c, respectively, showing longer tails at higher diameters due to greater aggregation for the PS-s-P4VP and P4VP films in comparison to the PS-b-P4VP film. g) Comparison of the surface nanoparticle density on the different polymer film templates, confirming the lower AuNP density on the PS-s-P4VP template, where the error bars are determined from 3 experiments per polymer type.

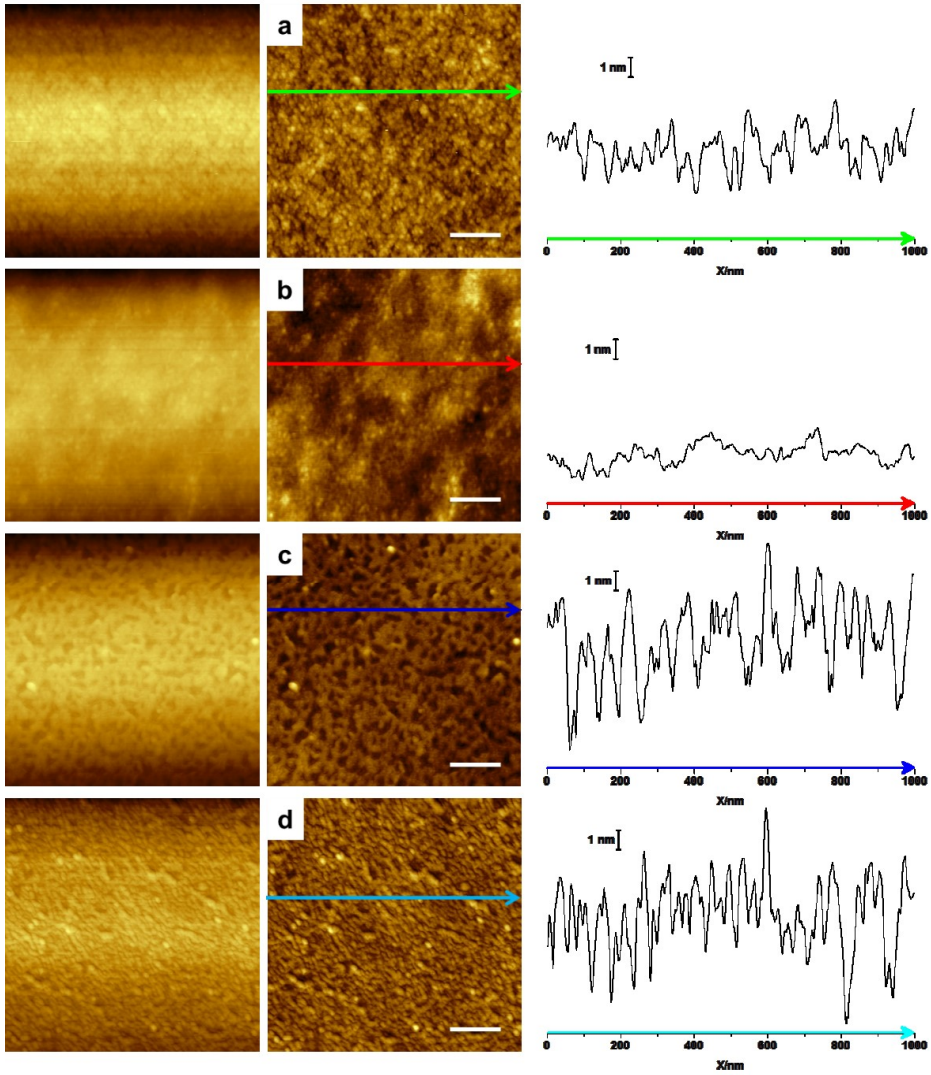

Figure 2.S5. AFM analysis of the roughness of the PS-b-P4VP coating on nanofibers. (a-d, center) Flattened AFM height images (1x1 μm^2, scale bars 100 nm, corresponding unflattened images shown on the left) of the nanofiber surface at a diameter of about 10 µm before (a) and after (b) dip-coating in the PS-b-P4VP THF solution, and after overnight immersion of the BCP-coated nanofibers in (c) neutral and (d) acidic (pH 5, citrate/citric acid buffer) aqueous solutions. To obtain the flattened images, those on the left were processed using four Gwyddion functions, namely, correct horizontal scans, correct lines by matching height median, level data to make facets point upward, and level data by mean plane subtraction, in that order. The height profiles on the right, all shown at identical

scales, correspond to the lines drawn in the flattened images. They indicate that the degree of roughness of the PS-b-P4VP coated nanofiber (b) is comparable to (even somewhat smoother than) that of the bare surface (a), supporting its assignment as a uniform brush-like layer. In contrast, exposure to aqueous solution, whether neutral (c) or acidic (d), results in significantly greater height variation, consistent with molecular rearrangement of the PS sublayer exposing parts of the P4VP sublayer.

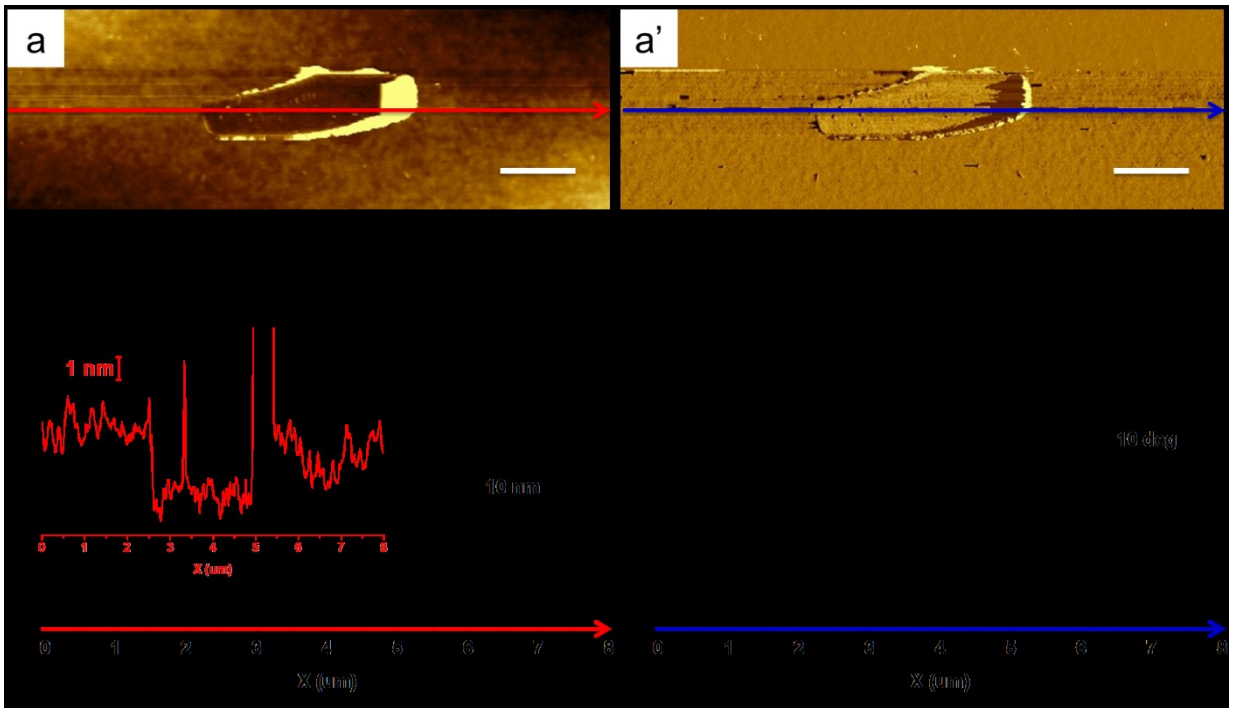

Figure 2.S6. AFM analysis of the thickness of the PS-b-P4VP coating on the nanofibers. AFM 2x8 μm^2 height (a) and phase (a') images, with 1 µm scale bars, of the BCP film at a fiber diameter of about 8 µm after erasing a portion of the coating (approx. 0.5x2 μm^2) using an AFM tip in contact mode; b and c show the height and phase profiles corresponding to the lines drawn in a and a', respectively. The height profile indicates a BCP film thickness of approximately 3 nm; the difference in phase angle (approximately 10 degrees) between the BCP-covered surface (below 2.5 and above 5.5 µm on the x-axis of the phase profile) and the erased section (between 2.7 and 4.7 µm on the x-axis) is consistent with a difference in mechanical hardness and/or chemical composition of the two parts.

Table 2.S1. Wavenumbers and band assignments of the main bands in the SERS spectra of Fig. 2.3 (green and blue lines).

Species	SERS mode /cm^{-1}	Assignment	SERS mode /cm^{-1}	Assignment
sodium citrate[a]	674	$\delta(CO_2)$	946	ν(C-C-O)
	748	$\rho(CH_2)$	1428	ν(C-O) + δ(O-H) + $\nu(CO_2)$, sym
	809	$\nu(C_4O)$, sym + $\rho(CH_2)$	1607	$\nu(CO_2)$, asym
4-MBA[b]	1077	ν(C-C)ring	1586	ν(CC)ring
	1179	δ(CH)		

[a]Assignments according to ref 47.[47] [b]Assignments according to ref 48.[48] Abbreviations: δ - in plane deformation, ν - stretching, ρ - rocking, sym - symmetric, asym – asymmetric, ring - ring breathing mode.

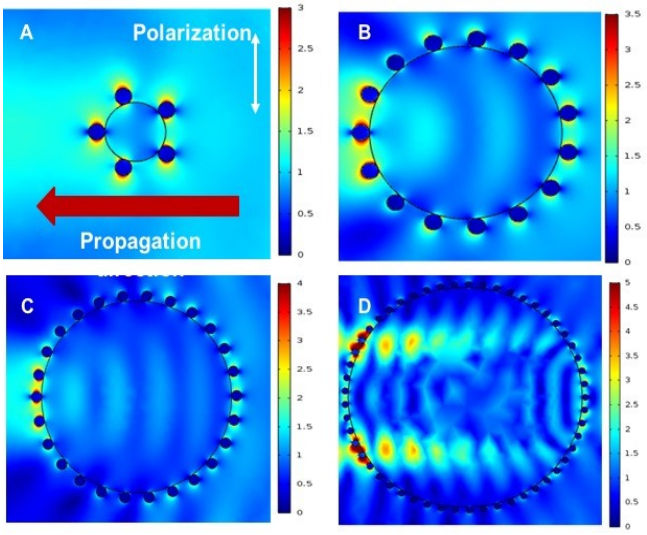

Figure 2.S7. Finite-element method (FEM) simulations, employing commercial software COMSOL Multiphysics, of the electric field distribution on a glass nanofiber of varying radii; A) 100 nm, B) 300 nm, C) 500 nm, and D) 1000 nm. The FEM calculations provide an indication of the SERS intensity, as SERS is proportional to $|E/E_0|^4$, corresponding to the incident electric field (E_0) and electric field close to the AuNPs (E). For these calculations, 54 nm AuNPs were placed around the circumference of the glass nanofiber at a constant spacing of 70 nm. Light was polarized in the vertical direction and propagated from right to left in each panel. The electric field near the AuNPs increased with the glass nanofiber diameter. At a nanofiber diameter of 100 nm, the field distribution for the AuNPs was dipolar and homogeneous; for diameters of 300 and 500 nm, it was dipolar and located at an angle of π; and for a diameter of 1000 nm, it was more intense in the interparticle gap and greater at angles of approximately 5/6 π and 7/6 π. The radius of the nanofiber is significantly smaller than the 633 nm wavelength of light, leading to little effect of the nanofiber on the optical properties of the AuNPs. A small convergence of the light rays was observed at radii of 300 and 500 nm, where the ball lens effect of the light led to a focal point near the surface of the exit point of the light. The larger diameter led to a focal point at a longer distance from the surface and stronger intensity of light outside the cone. This led to stronger intensity of the light at angles of 5/6 π and 7/6 π.

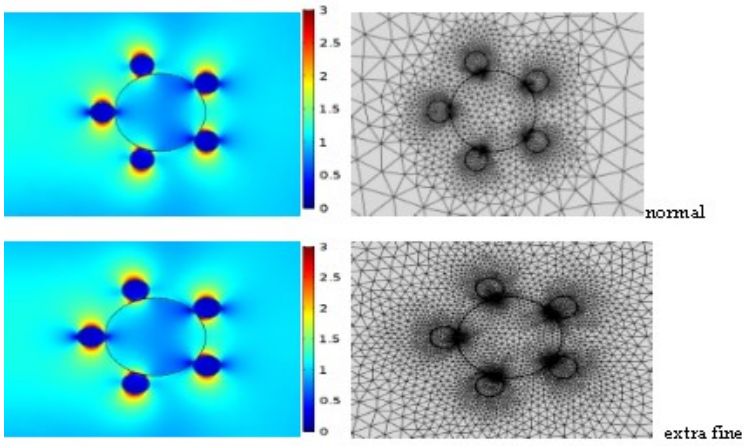

Figure 2.S8. FEM simulations of the electric field distribution on a glass nanofiber of 100 nm radius, with two different mesh sizes. No difference was observed in their electric field distribution.

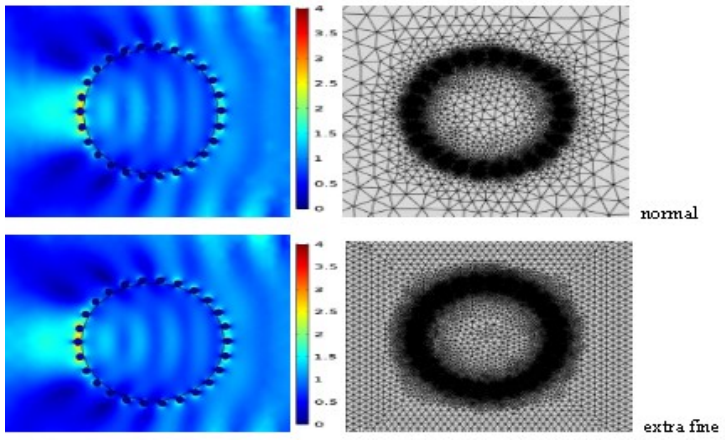

Figure 2.S9. FEM simulations of the electric field distribution on a glass nanofiber of 500 nm radius, with two different mesh sizes. No difference was observed in their electric field distribution.

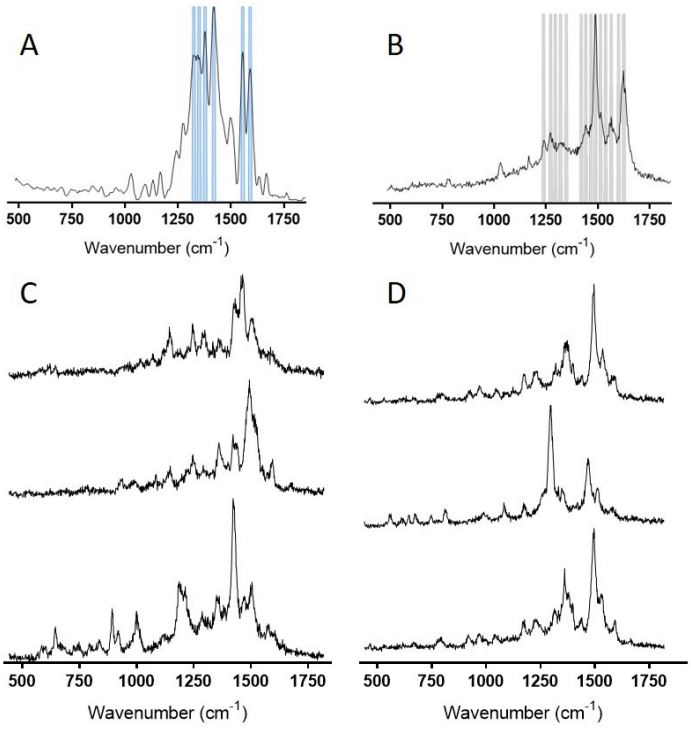

Figure 2.S10. Standard spectra of DA (A) and Glu (B) and their associated barcodes employed in the SERS optophysiology analysis. Typical SERS spectra associated with DA (C) and Glu (D) during the SERS optophysiology experiment near neurons during depolarization.

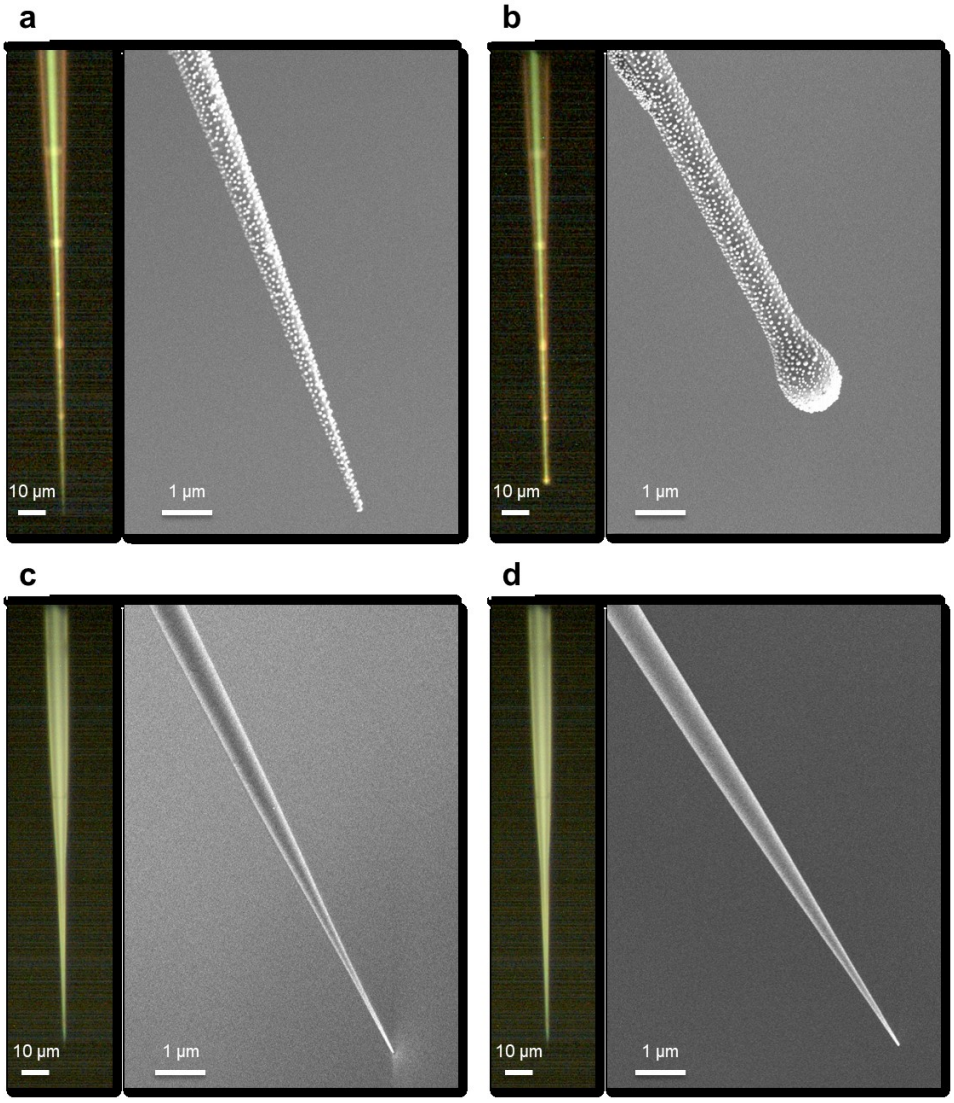

Figure 2.S11. Optical images (left) and SEM images (right) of a) an as-prepared AuNP-coated nanofiber and b) after laser exposure for 1 second by using a 633 nm laser of 5 mW focused on the nanofiber tip with a 50x lens. The photothermal effect of the AuNPs on the nanofibers generated heat that locally melted the small glass tip, leading to the formation of a small ball at the end of the nanofiber. SEM images show that the AuNP coating remained intact after laser exposure. c) and d) show a bare nanofiber before and after the laser exposure under identical conditions as a) and b). No change was observed on the nanofiber tip, confirming that the AuNPs were responsible for the local heating effect.

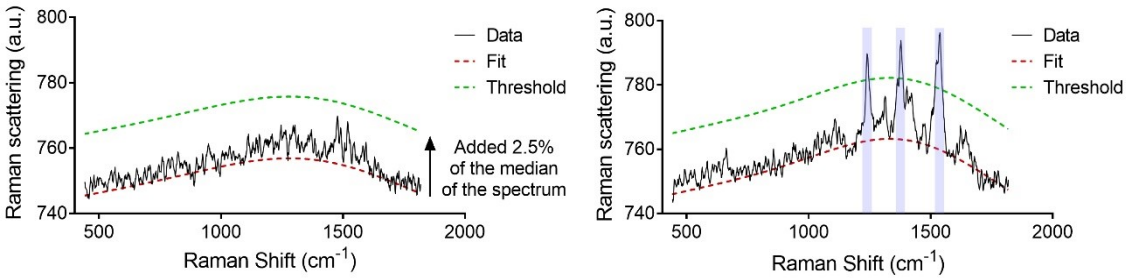

Figure 2.S12. Data pre-processing for SERS optophysiology. Left: SERS spectrum representing a blank spectrum where no Raman bands were detected. In a first step, the background was extracted with airPLS, represented by the red hatched line (Fit). 2.5% of the value of the median of the spectrum is added to the fit line to generate the threshold line corresponding to the green hatched line. If no Raman bands exceeded the threshold line, no bars were extracted in the following data processing. Right: SERS spectrum representing a positive spectrum where Raman bands were detected. The background and the threshold were also evaluated for the SERS spectrum. Three Raman bands exceeded the threshold line, leading to the extraction of 3 bars represented by the purple shaded areas. These bars composed the experimental barcode of this spectrum. This experimental barcode was then compared to the reference barcodes of our library. If the barcode matched a reference spectrum of a neurotransmitter, the experimental SERS spectra was assigned to the neurotransmitter.

2.7 References

1. Chen, Y.; Pepin, A. Electrophoresis 2001, 22, 187-207.
2. Gates, B. D.; Xu, Q.; Stewart, M.; Ryan, D.; Willson, C. G.; Whitesides, G. M. Chem. Rev. 2005, 105, 1171-1196.
3. Wang, X.-D.; Wolfbeis, O. S. Anal. Chem. 2013, 85, 487-508.
4. Huang, X. H.; El-Sayed, I. H.; Qian, W.; El-Sayed, M. A. J. Am. Chem. Soc. 2006, 128, 2115-2120.
5. Jain, P. K.; Huang, X.; El-Sayed, I. H.; El-Sayed, M. A. Acc. Chem. Res. 2008, 41, 1578-1586.

6. Vo-Dinh, T.; Fales, A. M.; Griffin, G. D.; Khoury, C. G.; Liu, Y.; Ngo, H.; Norton, S. J.; Register, J. K.; Wang, H.-N.; Yuan, H. Nanoscale 2013, 5, 10127-10140.
7. Vitol, E. A.; Orynbayeva, Z.; Bouchard, M. J.; Azizkhan-Clifford, J.; Friedman, G.; Gogotsi, Y. ACS Nano 2009, 3, 3529-36.
8. Lussier, F.; Brule, T.; Vishwakarma, M.; Das, T.; Spatz, J. P.; Masson, J. F. Nano Lett. 2016, 16, 3866-71.
9. Onses, M. S.; Wan, L.; Liu, X.; Kiremitler, N. B.; Yılmaz, H.; Nealey, P. F. ACS Macro Lett. 2015, 4, 1356-1361.
10. Liu, Z.; Chang, T.; Huang, H.; He, T. RSC Adv. 2013, 3, 20464-20470.
11. Yap, F. L.; Thoniyot, P.; Krishnan, S.; Krishnamoorthy, S. ACS Nano 2012, 6, 2056-2070.
12. Aizawa, M.; Buriak, J. M. Chem. Mater. 2007, 19, 5090-5101.
13. Nandan, B.; Gowd, E. B.; Bigall, N. C.; Eychmüller, A.; Formanek, P.; Simon, P.; Stamm, M. Adv. Funct. Mater. 2009, 19, 2805-2811.
14. Roland, S.; Gamys, C. G.; Grosrenaud, J.; Boissé, S.; Pellerin, C.; Prud'homme, R. E.; Bazuin, C. G. Macromolecules 2015, 48, 4823-4834.
15. Tokarev, I.; Krenek, R.; Burkov, Y.; Schmeisser, D.; Sidorenko, A.; Minko, S.; Stamm, M. Macromolecules 2005, 38, 507-516.
16. Quéré, D. Annu. Rev. Fluid Mech. 1999, 31, 347-384.
17. Kruss, S.; Erpenbeck, L.; Schon, M. P.; Spatz, J. P. Lab Chip 2012, 12, 3285-3289.
18. Meiners, J.; Ritzi, A.; Rafailovich, M.; Sokolov, J.; Mlynek, J.; Krausch, G. Appl. Phys. A 1995, 61, 519-524.
19. Liu, Y.; Quinn, J.; Rafailvoich, M.; Sokolov, J.; Zhong, X.; Eisenberg, A. Macromolecules 1995, 28, 6347-6348.
20. Munch, M. R.; Gast, A. P. J. Chem. Soc., Faraday Trans. 1990, 86, 1341-1348.
21. Munch, M. R.; Gast, A. P. Macromolecules 1990, 23, 2313-2320.
22. Tassin, J. F.; Siemens, R. L.; Tang, W. T.; Hadziioannou, G.; Swalen, J. D.; Smith, B. A. J. Phys. Chem. 1989, 93, 2106-2111.
23. Toomey, R.; Mays, J.; Tirrell, M. Macromolecules 2004, 37, 905-911.
24. Meiners, J. C.; QuintelRitzi, A.; Mlynek, J.; Elbs, H.; Krausch, G. Macromolecules 1997, 30, 4945-4951.

25. Laforgue, A.; Bazuin, C. G.; Prud'homme, R. E. Macromolecules 2006, 39, 6473-6482.
26. Chai, J.; Wang, D.; Fan, X.; Buriak, J. M. Nature Nanotechnology 2007, 2, 500-506.
27. Tebbe, M.; Galati, E.; Walker, G. C.; Kumacheva, E. Small 2017, 13, 1702043.
28. Freeman, R. G.; Grabar, K. C.; Allison, K. J.; Bright, R. M.; Davis, J. A.; Guthrie, A. P.; Hommer, M. B.; Jackson, M. A.; Smith, P. C.; Walter, D. G.; Natan, M. J. Science 1995, 267, 1629-1632.
29. Lussier, F.; Brule, T.; Bourque, M.-J.; Ducrot, C.; Trudeau, L.-E.; Masson, J.-F. Faraday Discuss. 2017, 205, 387-407.
30. Masson, J.-F.; Breault-Turcot, J.; Faid, R.; Poirier-Richard, H.-P.; Yockell-Lelièvre, H.; Lussier, F.; Spatz, J. P. Anal. Chem. 2014, 86, 8998-9005.
31. Dal Bo, G.; St-Gelais, F.; Danik, M.; Williams, S.; Cotton, M.; Trudeau, L.-E. J. Neurochem. 2004, 88, 1398-1405.
32. Banholzer, M. J.; Millstone, J. E.; Qin, L.; Mirkin, C. A. Chem. Soc. Rev. 2008, 37, 885-897.
33. Huang, X.; Jain, P. K.; El-Sayed, I. H.; El-Sayed, M. A. Lasers in Medical Science 2007, 23, 217.
34. El Mestikawy, S.; Wallen-Mackenzie, A.; Fortin, G. M.; Descarries, L.; Trudeau, L. E. Nature Reviews Neuroscience 2011, 12, 204-216.
35. Tecuapetla, F.; Patel, J. C.; Xenias, H.; English, D.; Tadros, I.; Shah, F.; Berlin, J.; Deisseroth, K.; Rice, M. E.; Tepper, J. M.; Koos, T. J. Neurosci. 2010, 30, 7105-7110.
36. Fulton, S.; Thibault, D.; Mendez, J. A.; Lahaie, N.; Tirotta, E.; Borrelli, E.; Bouvier, M.; Tempel, B. L.; Trudeau, L.-E. J. Biol. Chem. 2011, 286, 9360-9372.
37. Burmeister, J. J.; Pomerleau, F.; Palmer, M.; Day, B. K.; Huettl, P.; Gerhardt, G. A. J. Neurosci. Methods 2002, 119, 163-171.
38. Bastus, N. G.; Comenge, J; Puntes, V. Langmuir 2011, 27, 11098-11105.
39. Haiss, W.; Thanh, N. T.; Aveyard, J.; Fernig, D. G. Anal. Chem. 2007, 79, 4215-21.
40. Matsushita, N.; Okada, H.; Yasoshima, Y.; Takahashi, K.; Kiuchi, K.; Kobayashi, K. J. Neurochem. 2002, 82, 295-304.

41. Fasano, C.; Thibault, D.; Trudeau, L. E. Curr. Protoc. Neurosci. 2008, Chapter 3, Unit 3 21.

42. Edelstein, A. D.; Tsuchida, M. A.; Amodaj, N.; Pinkard, H.; Vale, R. D.; Stuurman, N. J. Biol. Methods 2014, 1, 1-10.

43. Schindelin, J.; Arganda-Carreras, I.; Frise, E.; Kaynig, V.; Longair, M.; Pietzsch, T.; Preibisch, S.; Rueden, C.; Saalfeld, S.; Schmid, B. Nat. Methods 2012, 9, 676-682.

44. Zhang, Z.-M.; Chen, S.; Liang, Y.-Z. Analyst 2010, 135, 1138-1146.

45. Butler, H. J.; Ashton, L.; Bird, B.; Cinque, G.; Curtis, K.; Dorney, J.; Esmonde-White, K.; Fullwood, N. J.; Gardner, B.; Martin-Hirsch, P. L. Nat. Protoc. 2016, 11, 664-687.44. Vinogradova, E., Tlahuice-Flores, A., Velazquez-Salazar, J. J., Larios-Rodriguez, E.; Jose-Yacaman, M., J. Raman Spectrosc. 2014, 45, 730-735.

47. Vinogradova, E., Tlahuice-Flores, A., Velazquez-Salazar, J. J., Larios-Rodriguez, E.; Jose-Yacaman, M., J. Raman Spectrosc. 2014, 45, 730-735.

48. Orendorff, C. J., Gole, A., Sau, T. K.; Murphy, C. J., Anal. Chem. 2005, 77, 3261-3266.

Chapter 3

Monolayer Arrays of Nanoparticles on Block Copolymer Brush Films*

3.1 Abstract

Two-dimensional arrays of nanoparticles have widespread applications in optical coatings, plasmonic sensors, and nanocomposites. Current bottom-up approaches that use homogeneous NP templates, such as silane SAMs or homopolymers, are typically plagued by NP aggregation, whereas patterned block copolymer (BCP) films require specific compositions for specific NP distributions. Here, we show, using polystyrene-*b*-poly(4-vinylpyridine) (PS-*b*-P4VP) and AuNPs of various sizes, that a nanothin PS-*b*-P4VP brushlike coating (comprised of a P4VP wetting layer and a PS overlayer), which is adsorbed onto flat substrates during their immersion in very dilute PS-*b*-P4VP THF solutions, provides an excellent template for obtaining dense and well-dispersed AuNPs with little aggregation. These non-close-packed arrays have similar characteristics regardless of immersion time in solution (about 10-120 s studied), solution concentration below a critical value (0.1 and 0.05 mg/mL studied), and AuNP diameter (10-90 nm studied). Very dilute BCP solutions are necessary to avoid deposition, during substrate withdrawal, of additional material onto the adsorbed BCP layer, which typically leads to patterned surfaces. The PS brush coverage depends on immersion time (adsorption kinetics), but full coverage does not inhibit AuNP adsorption, which is attributed to PS

*Revised manuscript submitted as a full paper in *Langmuir* **2019**: Zhu, H.; Masson, J.-F.; Bazuin, C.G.

molecular rearrangement during exposure to the aqueous AuNP colloidal solution. The simplicity, versatility and robustness of the method will enable applications in material science requiring dense, unaggregated NP arrays.

3.2 Introduction

Two-dimensional monolayer arrays of nanoparticles (NPs) on solid substrates are of technological and scientific importance in applications ranging from optical coatings,[1-3] plasmonic sensing[4-6] and data storage[7-9] to surface nanoengineering such as nanolithography,[10] layer-by-layer nanocomposites[11-13] and nanotemplating.[14,15] Nowadays, it is possible to synthesize NPs of controlled size, shape and chemical composition, spurring research activity toward their assembly into functional structures at the nano, micro and macro scales. Owing to the charges that are naturally incorporated in synthesized colloids, a simple and scalable NP self-assembly method involves modifying the substrate surface with a film template that carries opposite charges to that of the NP, so that electrostatic interactions drive the spontaneous formation of 2D monolayer arrays of NPs.[16-18] Forming NP arrays that are both dense and unaggregated, or non-close-packed, is important for creating robust and sensitive sensing devices and for efficient energy harvesting in plasmonic photovoltaics, as well as various other applications.[19] As indicated in the next paragraphs, uniform dispersion with minimal aggregation using simple strategies remains an issue that invites significant improvement.

SAMs (self-assembled monolayers) of functionalized alkoxysilanes, such as 3-aminopropyltrimethoxysilane (APTES), are commonly used as film templates to assemble gold and silver NPs on SiO_2 surfaces.[17,18,20-24] SAMs are nanothin and have very good stability due to covalent binding between the organic film and the substrate. However, they often suffer from poor uniformity, where, for example, low packing density and packing defects cause incomplete NP coverage or where self-polymerization of alkoxysilanes leads to NP aggregation.[20-23] In addition, SAM derivatization of a surface is a relatively complicated procedure that involves prolonged chemical reaction and thermal treatment.

Homopolymer thin films, such as poly(4-vinylpyridine) (P4VP), have also been used as film templates for NP adsorption.[18,25-28] The multiple interactions between each polymer chain and the substrate surface lead to high stability and complete surface coverage by the polymer film despite the binding being non-covalent. Although dense NP deposition can be achieved on polymer thin films, they tend to aggregate during film drying due to unoccupied neighboring adsorption sites on the film surface, reduced electrostatic repulsion, and capillary forces.[18,19,26] Interestingly, non-close-packed NP arrays (on gold surfaces) were achieved by combining electrostatic repulsion between negatively charged silica NPs with surface roughness of the NPs to counteract capillary force aggregation.[19]

A unique type of film template can be formed from block copolymer (BCP) self-assembling thin films.[29-33] Microphase separation between immiscible blocks leads to morphologies (e.g. spherical, cylindrical, and lamellar) that give rise to 2D patterns at the film surface that can be used as scaffolds to direct NP adsorption. Because the type and dimensions of BCP nanostructures can be tailored by changing the BCP characteristics, these films are attractive templates for guiding various spatial arrangements of NPs or groups of NPs. For example, as illustrated schematically in Figure 3.1 (left), micellar films with a spherical morphology provide a surface pattern of dots, whose size can be tuned by choice of block molecular weights to adsorb one or several NPs per micelle.[32] In a variation of this approach, a multistep procedure involving a BCP mask allows the nanopatterning of a P2VP end-grafted brush and subsequent AuNP deposition on this brush in different patterns.[34] Although attractive and versatile, with the ability to yield precise, highly ordered arrays of NPs, the use of surface-patterned BCP layers with lateral phase separation is also somewhat restrictive and cumbersome due to the necessity of properly choosing the BCP characteristics and film preparation conditions, often including annealing, to achieve the desired array characteristics.

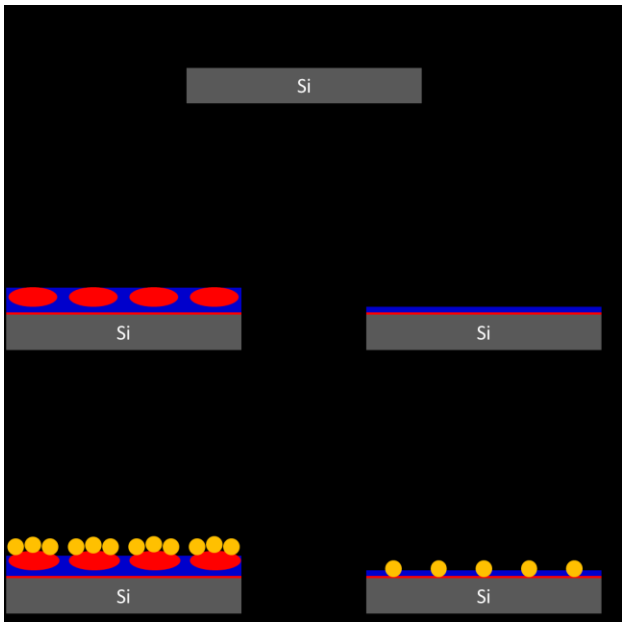

Figure 3.1 Two types of BCP thin film templates for the deposition of AuNPs, where the red and blue colors indicate the domains of two incompatible blocks. Left: thicker BCP film with microphase-separated domains that lead to ordered AuNP deposition, shown here in the form of AuNP clusters for AuNP sizes much smaller than the block domains (red) on which the AuNPs selectively deposit. Right: nanothin BCP brushlike film formed by adsorption on the substrate, which leads to dense monolayer arrays of well-dispersed AuNPs. These two types of films can be obtained by dipping the substrate in relatively concentrated (left) and very dilute (right) BCP solutions, respectively.

Herein, as depicted schematically in Figure 3.1 (right), we show that BCP films in the form of a nanothin adsorbed or brushlike layer are suitable templates for producing dense 2D non-close-packed arrays of AuNPs with little aggregation, and that they are obtained in two simple steps, namely dipping the substrate successively in a very dilute BCP solution and, after drying, in an AuNP suspension. This is illustrated using silicon substrates dip-coated in THF solutions of polystyrene-*block*-poly(4-vinylpyridine) (PS-*b*-P4VP) that are then immersed in an aqueous suspension of citrate-stabilized gold nanoparticles (AuNPs). The brushlike BCP layer is adsorbed to the substrate through multiple non-covalent bonds between SiOH and the P4VP block, which forms the wetting

underlayer, while the PS block forms a brushlike overlayer. The BCP solution must be sufficiently dilute to prevent deposition of additional BCP material (giving rise to partial or full coverage by the above-mentioned patterned BCP films) during substrate withdrawal. The AuNP arrays appear unaffected by the extent of PS overlayer coverage or by AuNP size, making the procedure universal in this sense and useful for applications where achieving dense but unaggregated or non-close-packed AuNP deposition is desired.

One such application, just published, is for the fabrication of improved surface-enhanced Raman scattering (SERS) nanosensors for localized neurotransmitter detection.[35] Due to the high curvature of the nanofibers used for this application, the dip-coating procedure allows only a BCP brush layer to be adsorbed, even with concentrated solutions. Nevertheless, AuNP deposition on this brush layer coating was found to be dense with little aggregation, thus leading to superior performance as a SERS nanosensor compared to APTES-coated nanofibers where AuNP aggregation occurs. In another application, we found that BCP brush-layer templated AuNPs on optical fibers likewise enhance their performance as LSPR (localized surface plasmon resonance) biosensors.[36] Since it is more difficult to investigate how different parameters might affect the AuNP deposition on the BCP brush layer of highly curved surfaces, we turned to flat substrates. This thus constitutes another major incentive for the present investigation.

3.3 Experimental

3.3.1 Materials

Polystyrene-*b*-poly(4-vinylpyridine) (PS-*b*-P4VP) [M_n(PS) = 41 kg/mol, M_n(P4VP) = 20 kg/mol, M_w/M_n (total) = 1.18] and P4VP (M_n = 15 kg/mol, M_w = 19 kg/mol, M_w/M_n = 1.25) were purchased from Polymer Source (Dorval, QC, Canada). Tetrahydrofuran (THF, 99.99%) and chloroform ($CHCl_3$, 99.99%) were purchased from VWR, gold(III) chloride trihydrate ($HAuCl_4 \cdot 3H_2O$, 99.9%) and trisodium citrate dihydrate (99%) from Sigma-Aldrich. All products were used as received. Rectangular flat silicon substrates of 10×15 mm^2 were cut from {1,0,0} silicon wafers (University Wafer, Pittsburgh). The substrates were cleaned by immersion in acetone for 15 min, dried under N_2 flow, then placed in a

piranha solution (*This solution is highly corrosive and should be handled with caution.*) at 90 ºC for 60 min, rinsed thoroughly with Milli-Q water, and dried under nitrogen flow.

3.3.2 Block copolymer solutions

BCP solutions of 1 and 5 mg/mL and a P4VP stock solution of 1 mg/mL were prepared by directly dissolving appropriate amounts of PS-*b*-P4VP in THF and P4VP in $CHCl_3$ (P4VP not being soluble in THF) in scintillation vials (VWR). The solutions were capped and sealed with parafilm, stirred at 30–40 ºC overnight, and then filtered successively through 0.45 and 0.2 μm PTFE filters (Chromspec). BCP solutions of 0.05 and 0.1 mg/mL and a P4VP solution of 0.05 mg/mL were prepared by dilution from the more concentrated solutions. For these dilute solutions, the vials were generally pre-exposed to solution that was then discarded, and the prepared solutions were used within an hour after preparation for a maximum of 11 films. These precautions were taken to minimize potential polymer solution concentration changes caused by the adsorption of block copolymer onto the inner wall of the vials and by removal of polymer onto the substrates. All four BCP solutions used are micellar according to dynamic light scattering (Malvern Zetasizer NanoZS).

3.3.3 Dip-coating

Dip-coated films (6-8 mm in height, 10 mm in width) were obtained from the solutions under ambient conditions (~21 ºC), using the dip-coater of a KSV3000 Langmuir-Blodgett instrument, enclosed in a plexiglass box (15x15x20 cm^3). To achieve this, the silicon substrates were vertically dipped into the solutions at an "immersion rate" of usually 40 mm/min (occasionally 5 mm/min), followed by a pause ("static immersion time") of 30 s unless otherwise noted, and then were withdrawn at a controlled rate ("withdrawal rate" or "dip-coating rate") of 40 mm/min, except when the effect of static immersion time or withdrawal rate was studied. The films were left to dry in covered containers at room temperature. No significant change was observed in film surface morphology up to at least one month after film preparation.

3.3.4 AuNP synthesis and deposition

Milli-Q water was used in all syntheses. All glassware and magnetic stir bars used were cleaned in aqua regia (HCl/HNO_3 3:1, v/v) and rinsed in Milli-Q water prior to use. *Aqua regia is highly corrosive and should be handled with caution.* Several batches of small (10-12 nm in diameter) citrate-stabilized AuNPs were synthesized using the Turkevich-Frens method.[37] The pH of the as-prepared solutions was measured to be around 6. A series of larger (20-90 nm in diameter) citrate-stabilized AuNPs were synthesized by using a kinetically controlled seeded growth method, starting with 10-nm seeds, following the recipe of Puntes and coworkers.[38] After the synthesized AuNPs were centrifuged and redispersed in Milli-Q water, the pH of the colloidal suspension, which was initially above 7, was adjusted to be between 4.5 and 5 (as measured by a pH meter, EcoMet P25, Istek) by dropwise addition of a 1M hydrochloric acid aqueous solution. The average diameters of the AuNP batches were determined from UV-visible spectra (Figure 3.S1a) obtained with an Agilent Technologies Cary 500 UV-vis spectrophotometer, following the method of Haiss *et al*.[39] All AuNPs were stored at 4 °C and used within a month. For AuNP deposition, the BCP-coated silicon wafers were incubated in the Au colloidal suspension for two hours. The substrates were then rinsed with Milli-Q water several times and dried with N_2 flow.

3.3.5 Atomic force microscopy (AFM)

AFM images were obtained in tapping mode with a Multimode microscope and a Nanoscope III controller (Digital Instruments), operated under ambient atmosphere, using Bruker AFM probes (TESPA-V2 model, spring constant 42 N/m, oscillation frequency 320 kHz, tip radius ≤10 nm). Typically, areas of 8x8 μm^2 were first scanned at three random locations within 2 mm of the film center to verify the uniformity, then a representative 2x2 μm^2 area was scanned and recorded. The images were treated in Gwyddion (http://gwyddion.net/download.php) by four functions, namely, correct horizontal scans, correct lines by matching height median, level data to make facets point upward, and level data by mean plane subtraction, in that order.

3.3.6 Spectroscopic ellipsometry

Film thicknesses were measured with a M-2000 V spectroscopic ellipsometer (J.A. Woollam) at an angle of 75°, using the Cauchy model to fit the data and taking into account the previously measured SiO_2 layer. Each sample was measured at three different locations to obtain an average.

3.3.7 Scanning electron microscopy (SEM)

The surface AuNPs were examined using a JEOL JSM-7400F (JEOL Ltd, Tokyo, Japan) field-emission scanning electron microscope operated at 1.5 kV and 20 μA, using the LEI detector. SEM examination was conducted at several random locations on the surface under various magnifications, with the images shown being representative of those surfaces. Deposited AuNP characteristics (size, size distribution, density, coverage) were obtained using ImageJ (http://imagej.nih.gov/ij/features.html), complemented by the Gwyddion software to obtain 2D FFTs (fast Fourier transforms) for center-to-center distances as well as by the Engineer's Toolbox (https://www.engineeringtoolbox.com/circles-within-rectangle-d_1905.html) to obtain center-to-center distances or densities.

3.3.8 Water contact angle measurements

Water contact angle measurements were performed under ambient conditions using an FTA200 contact angle analyzer (First Ten Angstroms), coupled with FTA32 video software for data analysis. In a typical measurement, a 2-μL drop of Milli-Q water was placed at the center of the film using a microsyringe and an image of the static drop was captured within 1-2 s and used to measure the water contact angle. Three parallel films were prepared for each measurement to obtain an average value. Selected films were exposed to Milli-Q water or 0.1 M pH 6 or pH 4.6 citrate-citric acid buffer overnight and dried with a N_2 flow before measurement.

3.4 Results and discussion

3.4.1 Effect of polymer solution concentration on BCP film pattern and AuNP distribution

It is known that the average thickness of dip-coated films at any given dip-coating rate decreases with decreasing polymer solution concentration.[40,41] For BCP films, we will show that this allows an investigation of the nanothin adsorbed layer and of its usefulness for templating NPs, in comparison with thicker dip-coated BCP films. Figure 3.2 illustrates the effect of BCP concentration on the surface pattern of PS-*b*-P4VP films dip-coated from THF solutions at a withdrawal rate of 2 mm/min (AFM height images) and the subsequent deposition of small AuNPs (10-12 nm in diameter) on these films (SEM images).

It can be observed immediately that there are distinct differences, both in the BCP film surface morphologies and, in parallel, in the adsorption pattern of the small AuNPs, that depend on the dip-coating solution concentration or, more precisely, film thickness. For the highest concentration investigated (5 mg/mL; thickest film, measured by ellipsometry to be 18.2±0.4 nm thick; Figure 3.2a), the surface morphology can be described as a close-packed quasi-hexagonal pattern of dots with an average intermicellar center-to-center spacing of 39 nm as indicated by the 2D FFT of the image. This concords with our previous studies showing that dip-coating from THF solutions having a concentration of 5 or 10 mg/mL PS-*b*-P4VP of approximately 30 wt % P4VP content (32.8 wt % in the present BCP) generally leads to films with a spherical micellar morphology.[42] The spherical micelles form in solution owing to the good solubility of PS and poor solubility of P4VP in THF for PS-*b*-P4VP of moderate and higher molecular weights, and are kinetically trapped in the dip-coated films.[42,43] (It should be noted, however, that in general the morphology of dip-coated films can evolve to other morphologies from that in solution.[42,43]) In the present case, since this pattern covers virtually the entire dip-coated surface, we term it the "full dot" pattern.

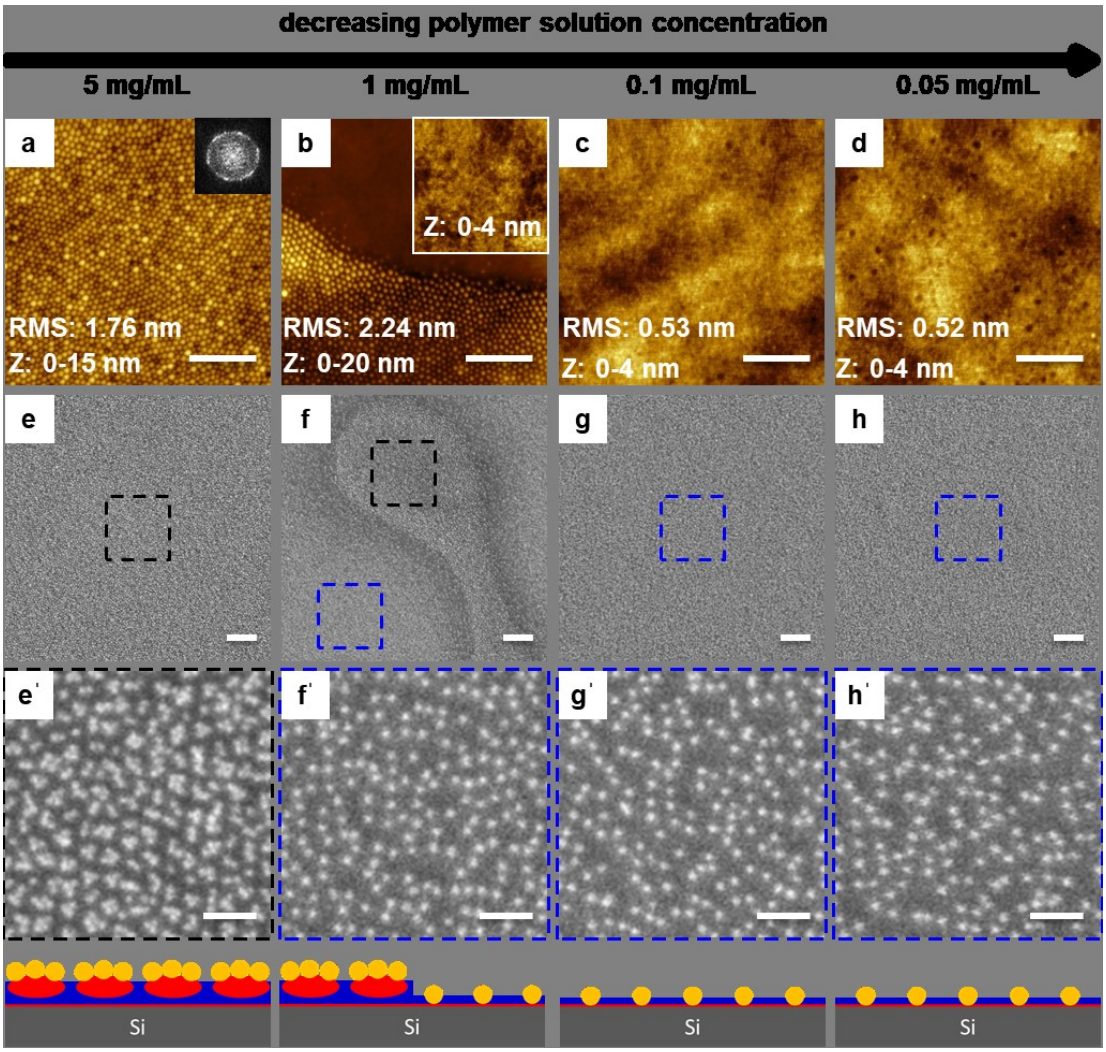

Figure 3.2 AFM height images of PS-*b*-P4VP thin films dip-coated on silicon substrates (immersion rate 40 mm/min, pause time 30 s, withdrawal rate 2 mm/min) from PS-*b*-P4VP/THF solutions of the concentrations indicated (1st row; Z indicates height scale; RMS indicates root-mean-square roughness; scale bars 500 nm; inset of a, 2D FFT image; inset of b, part of the dark region of b with same scale bar). Corresponding SEM images, after 10-12 nm AuNP deposition, at low resolution (2nd row; scale bar 500 nm) and at high resolution (3rd row, where the expanded areas are indicated by the dotted boxes in the 2nd row; the black box in f, not shown at high resolution, is very similar to e'; scale bar 100 nm). Schematic depiction of cross-sectional cuts through the film and Si wafer (4th row; P4VP in red, PS in blue, AuNPs as gold spheres).

After exposing this film to a 10-12 nm AuNP aqueous colloidal suspension, the AuNPs are deposited in distinctly visible groups or clusters of (mainly 2-4) AuNPs (Figure 3.2e,e'). These groups essentially reproduce the quasi-hexagonal pattern of P4VP dots, indicating that the AuNPs have adsorbed onto the P4VP micelles. This adsorption occurs through electrostatic interactions between the negatively charged citrate-stabilized AuNPs and the polar and positively charged P4VP that was (partly) protonated by the acidic aqueous milieu.[33,44] The charged AuNPs are not attracted to the nonpolar PS surface. Although the P4VP micelles in the dip-coated films were initially covered by an ultrathin layer of PS to minimize the interaction energy with air, this can be displaced by exposure to the aqueous milieu.[30,45] Several AuNPs deposit on each micelle due to the former being much smaller than the latter,[46] as shown also in ref 32 with spin-coated films of PS-*b*-P2VP.

The lower average thickness of the film dip-coated from the 1 mg/mL solution (measured to be 7.3±0.2 nm), in comparison to 5 mg/mL, manifests itself in the dual regions of the quasi-hexagonal dot pattern along with extended featureless areas (Figure 3.2b). Here, the average film thickness is too small to accommodate a complete spherical micellar layer, and therefore this layer "dewets", leading to partial coverage only.[42,47] We term this the "dewetted dot" pattern. As shown in Figure 3.2f,f', the micellar areas lead to the selective deposition of AuNP groups on the P4VP dots like in the full-dot films. In the featureless areas, the AuNPs are randomly distributed in the form of mainly unaggregated particles with no particular spatial order (Figure 3.2f,f').

The films obtained from the two most dilute solutions, 0.1 and 0.05 mg/mL, show a surface pattern that is featureless everywhere (termed "dot-free" pattern; Figure 3.2c,d) and the deposited AuNPs are generally unaggregated and randomly distributed all over (Figure 3.2g,g',h,h'). The average center-to-center AuNP spacing is approximately 40 nm (as calculated from the AuNP densities given in Figure 3.S2 for these two films; details given in the figure caption), thus similar to the intermicellar spacing of the dot-patterned film dip-coated from the 5 mg/mL solution. Almost no AuNPs deposit on bare Si (Figure 3.S3b), thus ruling out that the substrate in these areas is bare. Instead, film thicknesses of 3.4±0.1 and 3.0±0.1 nm for the 0.1 and 0.05 mg/mL concentrations, respectively, were measured by

ellipsometry. The root-mean-square roughness (RMS) determined from the AFM images is 0.52-0.53 nm, close to that of the bare Si surface (0.58; Figure 3.S3a), and thus indicative of a uniformly thick layer.

The featurelessness and thinness of the two films is consistent with their identification as a collapsed brushlike layer composed of a P4VP anchoring sublayer that "wets" the polar substrate through multiple hydrogen[48] or proton transfer[49] bonds per P4VP block with the OH-decorated Si surface, resulting in essentially irreversible adsorption with respect to the solvent,[48-50] and an overlying PS sublayer that reduces the interaction energy with air.[45,51-53] Past literature studies indicate that such a layer adsorbs onto polar solid substrates while they are immersed in an amphiphilic BCP solution. The anchoring block is considered to be spread out over the surface in a flattened conformation and the non-adsorbing block is more or less extended away from the surface when in solution to an extent that depends on parameters such as the solvent quality, relative block lengths, and surface density of the adsorbed chains.[50,54-62]

Moreover, in the context of dip-coating, it was shown, using micellar toluene solutions of PS-*b*-P2VP and a mica substrate, that film formation occurs in two steps: (a) the adsorption of the wetting/brush layer during the immersion period of the substrate in solution and (b) the deposition of additional BCP material as the substrate is withdrawn from solution, typically leading to thicker films characterized by surface patterns.[47,52,57,58] In the present case, this additional deposition gives rise to the full or dewetted micellar layer with the dot surface pattern, whereas, for the two least concentrated solutions used, only adsorption of a wetting/brush layer onto the substrate occurs in solution with no additional material deposited during substrate withdrawal. The relative smoothness of the surface indicates that the PS layer is quite uniform across the surface (contrasting with what is observed at shorter immersion times, described later). It may be mentioned here that we had previously obtained a cross-sectional TEM (transmission electron microscopy) image of a partial micellar film of a similar PS-*b*-P4VP as used here, which corroborates the presence of a P4VP wetting layer both below a single-layer micellar portion and a brush-layer portion of the film (see Figure 3.S4).[63]

The PS brush overlayer might be expected to be repulsive to the deposition of the charged citrate-stabilized AuNPs on the wetting/brush film. The fact that dense AuNP adsorption nevertheless occurs indicates that, like for the micellar films where the micelles are covered by ultrathin PS as mentioned above, the PS can be displaced sufficiently by exposure to the aqueous AuNP milieu, to permit electrostatic interactions between the citrate-stabilized AuNPs and the (partly) protonated P4VP, as also mentioned above for the patterned films. Such a displacement is supported by Table 3.1, showing a decrease in water contact angle from 87º for an as-prepared wetting/brush film (static immersion time of 110 s) to about 77º after overnight immersion in pure Milli-Q and pH 6 water and to 66º in pH 4.6 water (in comparison, PS and P4VP have water contact angles of 92º and 62º, respectively[45]).

Table 3.1. Water Contact Angles of Films Subjected to the Static Immersion Times Indicated.[a]

	Water Contact Angle (º)		
Static immersion time	10 s	20 s	110 s
As-prepared film	69±1	82±2	87±1
After immersion in pure water		77±2	76±2
After immersion in pH 6 buffer		78±1º	78±2º
After immersion in pH 4.6 buffer	61±2	61±3	66±3

[a] The films were dip-coated from a 0.05 mg/mL PS-b-P4VP/THF solution at immersion and withdrawal rates of 40 mm/min.

3.4.2 Relationship between dip-coating rate, polymer solution concentration, film thickness and film morphology

Another factor that influences dip-coated film thickness is the substrate withdrawal rate. It has been known for decades that the thickness increases with rate.[40] However, more recently, it was found that, for very slow dip-coating rates, the opposite holds, so that overall the thickness vs. rate dependence is V-shaped.[41,42] The fast side of the V-curve corresponds to the well-known "draining regime"[40] and the slow side to what has been termed the "capillarity regime", where the dip-coating rate is slower than the solvent evaporation rate, resulting in capillarity feeding of the depositing film.[41] For THF solutions of PS-*b*-P4VP, the minimum thickness in the V-curve lies at about 7-10 mm/min.[42,43] Thus, the films in Figure 3.2, obtained using a withdrawal rate of 2 mm/min, were dip-coated in the capillarity regime.

A range of other dip-coating rates covering the V minimum and the draining regime were also used to prepare films from the four solution concentrations. The measured average thicknesses of the various films are plotted in Figure 3.3 as a function of dip-coating rate. This figure demonstrates the decrease in film thickness as a function of decreasing BCP solution concentration at any given dip-coating withdrawal rate as well as the V-shaped thickness−withdrawal rate relationship. The latter becomes increasingly shallow as the solution concentration decreases, and is almost flat for the 0.1 and 0.05 mg/mL concentration, which is consistent with the brush layer becoming an increasingly greater fraction of the total film as the solution concentration decreases, to the extreme where the film is composed of only the brush layer for the two most dilute concentrations. (The slight V-shape that appears to persist for these two films, if not due to experimental uncertainty, could be rationalized by longer exposure to the solution due to slow immersion and/or withdrawal, as explained below).

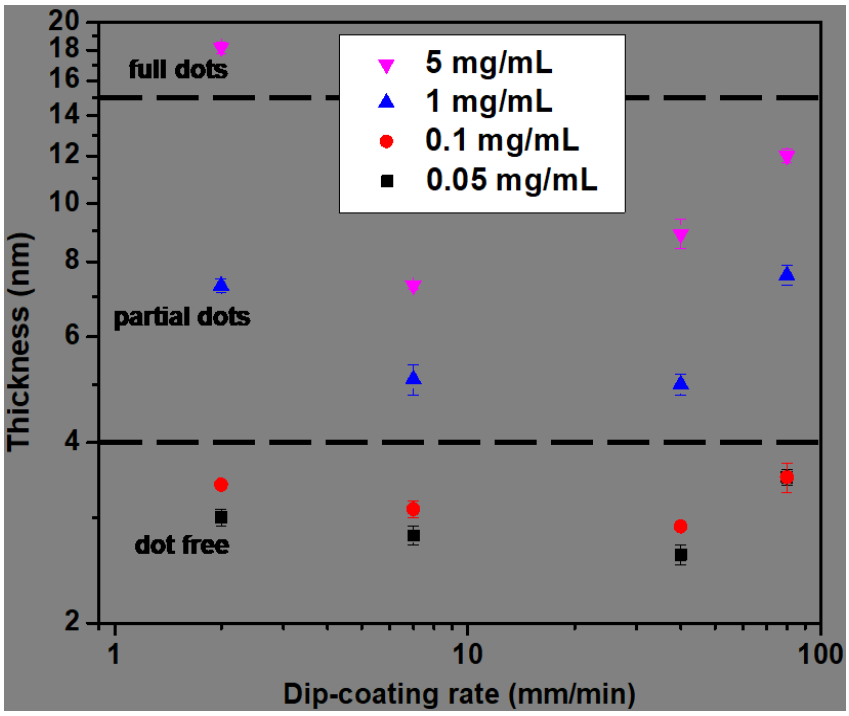

Figure 3.3 Log-log plot of average film thickness as a function of dip-coating rate for films dip-coated from PS-*b*-P4VP/THF solutions of various concentrations. The film thickness is divided into three regions by horizontal dashed lines according to the film surface morphologies.

The surface patterns on the films obtained at the various dip-coating rates are similar to those described above for 2 mm/min, taking into account the effect of dip-coating rate on the film thickness (see Figures 3.S5-S7, noting that these images were taken on separately prepared films compared to those used to measure film thicknesses). For example, the film obtained from the 5 mg/mL solution, which shows a full dot pattern at 2 mm/min, has a partial dot pattern at 7 mm/min near the thickness minimum (Figure 3.S5). The partial dot pattern is maintained for 40 and 80 mm/min withdrawal rates. The overall dependence of the surface pattern on film thickness is indicated by horizontal dashed lines in Figure 3.3: a full dot pattern is observed on the thickest film (18 nm), dewetted dots for film thicknesses between about 4 and 15±2 nm, and the featureless brush layer is obtained for thicknesses less than about 4 nm, in good agreement with adsorbed or brush layer thicknesses reported in the literature.[47,52,57,58,64] AuNP deposition onto these films follows

what was described above, namely in the form of small groups or clusters on the micelle (dot) regions and dense, mainly unaggregated and randomly distributed AuNPs on the brush regions.

3.4.3 Adsorbed block copolymer nanolayers for templating AuNPs

Studies of the adsorption of amphiphilic block copolymers from solution onto immersed polar solid surfaces in the form of a brushlike layer have led to the understanding that it is basically a two-stage process, consisting of (a) an initial fast diffusion- or transport-limited stage where individual chains (or micelles[50,54,61]) occupy bare surface, which can lead to essentially full coverage within seconds or minutes depending on factors such as solution concentration, presence or not of micelles, and block molecular weight and composition, and (b) a much slower densification stage, termed the brush-limited stage, where additional chains seek to penetrate the existing monolayer while the non-adsorbing block becomes increasingly extended in the form of a brush, analogous to what is observed for polymers that are end-grafted to surfaces.[54-56,60-62,65] (In our case, this brush, upon solvent evaporation after removal of the substrate from solution, becomes a "collapsed brush".) The kinetics curve in terms of adsorbed amount as a function of time thus shows a rapid initial rise, accounting for the major fraction of the final film (as much as 80-90%), followed by a rapidly decreasing rate of adsorption and finally a plateau, particularly in the case of micellar solutions.[50,54] A theoretical analysis of adsorption from micellar solutions indicates that micelles cannot adsorb directly onto the surface due to repulsive forces, but influence the adsorption kinetics by contributing free chains via re-equilibration between the micelles and free chains in solution to compensate for the loss of free chains to adsorption that creates a depletion zone near the surface.[65]

To learn about the specific adsorption kinetics of the adsorbed layer for our system and how the extent of BCP adsorption might affect the subsequent AuNP deposition on this layer, we conducted an experiment where a series of films were dip-coated at 40 mm/min from a 0.05 mg/mL solution for various static immersion times (pause times) and where their average thicknesses, which reflect the amount of adsorbed material, were measured. As shown in Figure 3.4, a film that is 1.8 nm thick has already developed within 10 s. The thickness increases by about 1 nm in the next 80 s, reaching a plateau or pseudo-plateau at

2.8 nm after about 90 s of immersion, signifying that the substrate is fully covered by a BCP monolayer. The appearance of a (pseudo-)plateau is consistent with the solution being micellar and with literature indicating that a micellar system tends to reach a true plateau more quickly than a non-micellar system.[50,54] Thus, we presume that brush coverage and therefore brush-layer thickness is near its maximum by about 90 s.

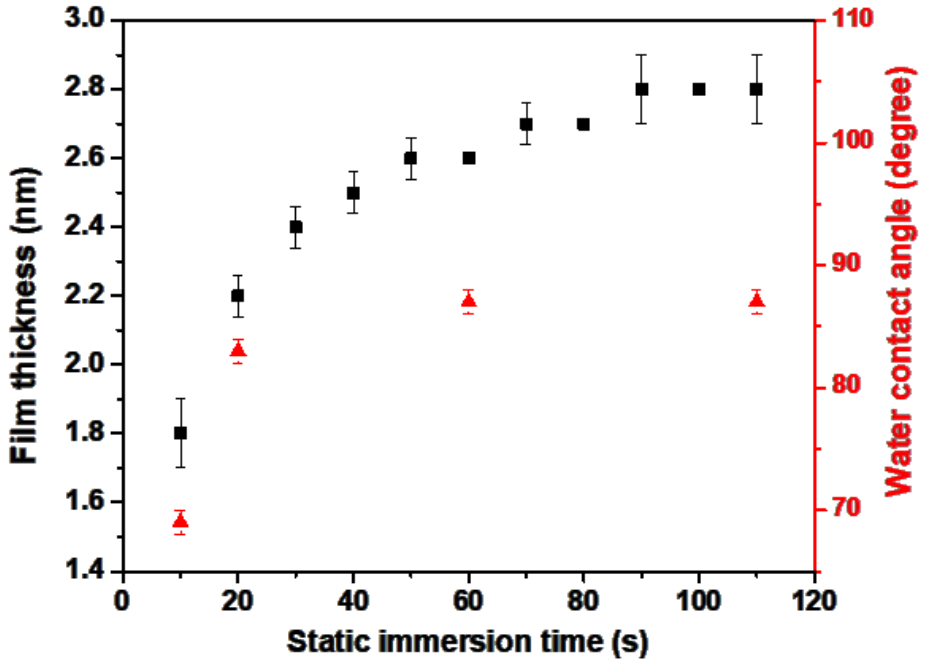

Figure 3.4 Average thickness (black squares) of films dip-coated at 40 mm/min immersion and withdrawal rates from a 0.05 mg/mL PS-*b*-P4VP/THF solution as a function of static immersion time (i.e. pause time between the end of immersion and beginning of withdrawal), along with water contact angles (red triangles) measured on representative films.

The quality of the adsorbed layer in terms of uniformity is indicated by the AFM images in Figure 3.5 for varying static immersion times, covering a range of 10 to 110 s (see also Figure 3.6 for immersion times of 3 and 10 min), at constant immersion and

withdrawal rates of 40 mm/min. Corresponding height profiles for the lefthand images are included. The 10-s film shows shows a pattern that can be described as a random network of ridges and grooves that have similar widths (about 100 nm, not considering the convolution of the 15-nm radius AFM tip) and a height difference of about 1.5 nm. On increasing the static immersion time, the ridges gradually grow together, closing the grooves into isolated holes by 30 s, while the depth of the holes appears constant at 1.5 nm. The holes continue to fill in at immersion times of 50 and 60 s and are no longer visible by about 70 s, as indicated by the much more uniform surface of the latter films. This sequence corresponds well to the adsorption kinetics in Figure 3.4, and shows that the adsorbed layer is indeed essentially uniform by the time the quasi-plateau has been reached.

The thickness trend in Figure 3.4 combined with Figure 3.5 suggest that the P4VP wetting layer is partially exposed at short immersion times (in the grooves and holes) and becomes increasingly covered by the PS overlayer up to full coverage with increasing exposure time to the solution. This is supported by the water contact angle measurements shown in Figure 4, which rise from 69º for a pause time of 10 s to 87º for 110 s. The evolution in the surface pattern is somewhat analogous to what can be observed for end-grafted homopolymers with increasing grafting density in poor solvent conditions.[66,67] For convenience in what follows, we will consider the PS layer as "saturated", even if not necessarily strictly true in terms of the maximum brush density, for exposure times of about 90 s and more.

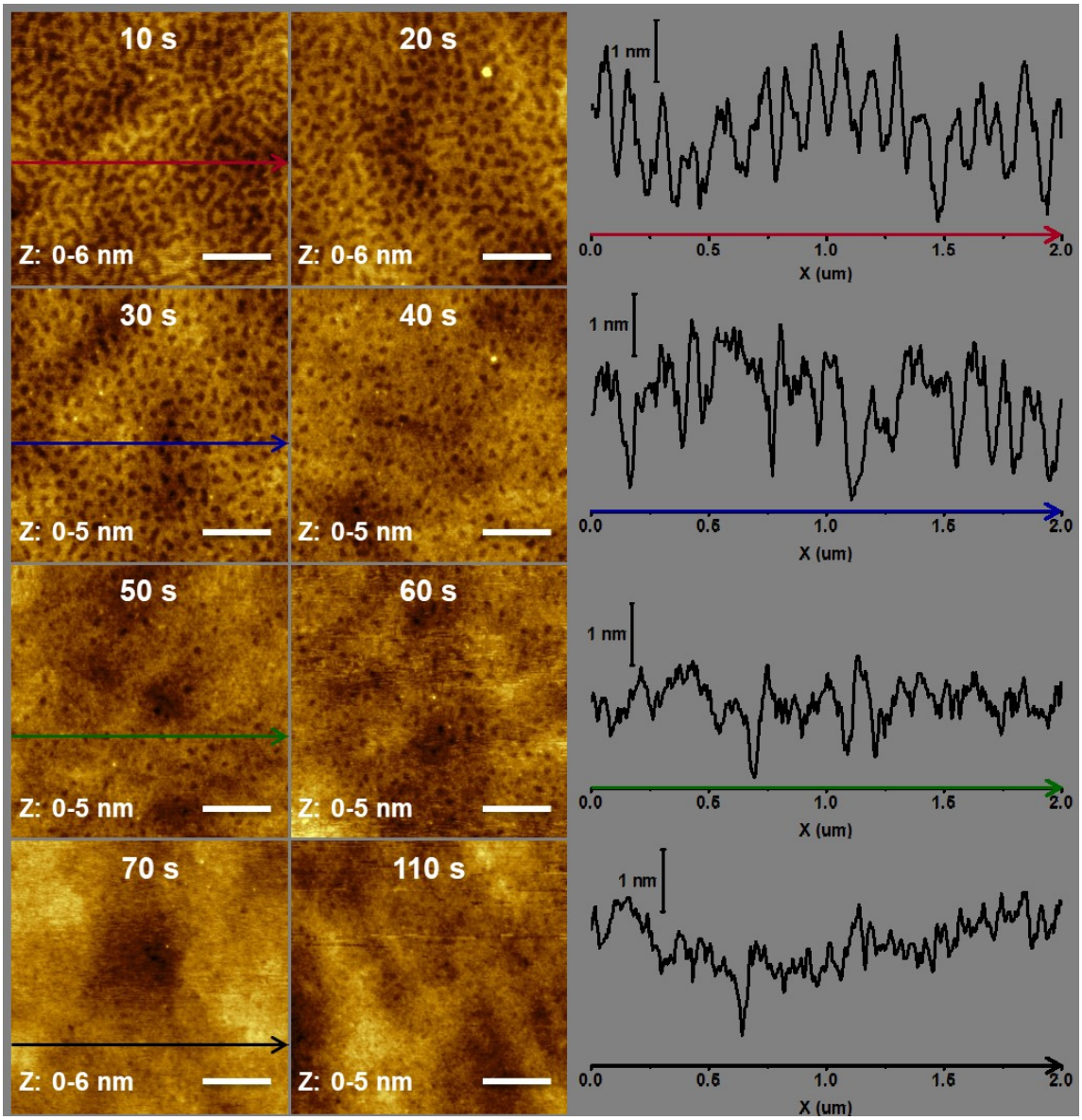

Figure 3.5 AFM height images (2x2 μm^2) of films dip-coated at 40 mm/min from a 0.05 mg/mL PS-*b*-P4VP/THF solution for the static immersion times indicated, with corresponding height profiles along the lines drawn in the lefthand images.

It may now be questioned whether the adsorbed brush layer films obtained from the most dilute solutions in Figures 3.2, 3.3 and 3.S5-S7, for which the static immersion time (pause time) was only 30 s, were saturated. To evaluate this, the different times of exposure to solution during substrate immersion (usually 40 mm/min; 5 mm/min for withdrawals

done at 80 mm/min) and withdrawal (2-80 mm/min) must also be taken into account. This analysis is given in Table 3.S1 and the accompanying text, and the results suggest that the adsorbed layer is at or near saturation for the films in Figure 3.3 obtained at withdrawal rates of 2 and 80 mm/min, but not for those obtained at 40 mm/min withdrawal and not quite for those obtained at 7 mm/min withdrawal. Indeed, it may be noted that the AFM image in Figure 3.S6 of the film withdrawn at 40 mm/min from the most dilute solution resembles those in Figure 3.5 for 30-40 s pause times, as would be expected from the exposure time analysis. The differences in effective adsorption times, which affect the average film thicknesses of the adsorbed brush layer when not saturated, also rationalize the apparent residual V-shape for the two lowest solution concentrations in Figure 3.3.

A verification of this was made by dip-coating a film from the 0.05 mg/mL concentration solution withdrawn at 80 mm/min at the same immersion rate (40 mm/min) as for the other withdrawal rates (same pause time at 30 s). This film was indeed thinner (2.5±0.1 nm), such that the thickness as a function of withdrawal rate for the films obtained from this solution (for identical immersion rate and pause time) decreases monotonically due to the decreasing exposure to solution with increasing withdrawal rate in a range where the adsorption kinetics are at least partly in the unsaturated region. Furthermore, this analysis raises the question whether or not an evolution in the brush layer surface pattern from partial to full coverage is observable from top to bottom of a given dip-coated film. Such a gradient film was indeed achieved using a fast immersion rate (80 mm/min), a relatively slow withdrawal rate (5 mm/min) and zero pause time, as shown in Figure 3.S8, resulting in a total immersion time that varied from 0 s at the top of the film to 153 s at the bottom and leading to a morphology evolution similar to that in Figure 3.4.

Since AuNP deposition on the adsorbed layer is the primary interest of this contribution, the above results raise the question as to how this deposition might be influenced by an adsorbed BCP layer that covers the substrate with greater or lesser uniformity. This is illustrated in Figure 3.6, using 30-nm AuNPs. It indicates that, despite the differences in the adsorbed layer surfaces (particularly the partially covered one obtained after a 10-s pause time compared to the more uniform surfaces obtained at pause times longer than a minute), AuNP coverage on all of the films is similar, giving monolayer

arrays of random and well-dispersed AuNPs, all with a similar density of about 150 AuNPs/μm^2. This is consistent also with the results for the deposition of the smallest AuNPs (10-12 nm) on the various brush-layer films shown in Figure 3.2 (images f', g, g', h, h') and Figures 3.S5-S7, for which the AuNP patterns and densities are essentially indistinguishable (Figure 3.S2).

We postulate that the reason for the lack of significant difference in AuNP deposition regardless of the PS coverage is related to the need or not for sufficient P4VP exposure combined with the presence of the PS and with AuNP mutual repulsion[19,68] that may determine its maximum density on a surface in the absence of screening. Thus, for unsaturated films, less rearrangement of the PS brush may be necessary if sufficient P4VP is already exposed prior to AuNP incubation. This is supported by water contact angle measurements on an unsaturated film (Table 3.1, pause time 20 s) whose water contact angles after overnight exposure to pure and acidic water are very close to those of the saturated film (pause time 110 s, with an initially higher contact angle than the unsaturated film) that was exposed to the same conditions. Furthermore, the water contact angle of the film obtained with a pause time of 10 s (Table 3.1), which is already low initially, is reduced by only a few degrees, becoming the same or similar to those of the two other films, all after exposure to the pH 4.6 solution.

It should be mentioned that all of the experiments involving AuNP deposition were performed using an incubation time in the AuNP colloid of 2 h, given literature indications that this time is sufficient to have maximum or near-maximum AuNP density.[44,68] We verified that this was true by incubating, overnight (about 12 h) compared to 2 h, one example each of a non-saturated (20-s pause time) and saturated (120-s pause time) brush layer. The results are given in Figure 3.S9, which shows that, in both cases, there is no significant difference within experimental uncertainty in the AuNP density between the 2- and 12-h incubations (nor between unsaturated vs. saturated films, as discussed above).

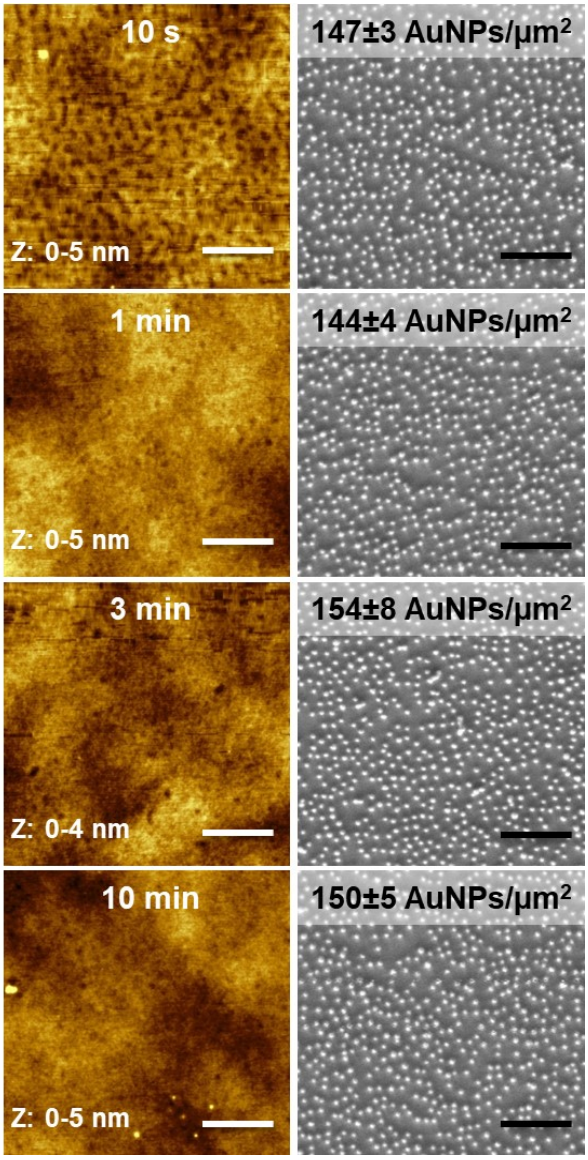

Figure 3.6 Left, AFM height images (2x2 μm^2) of films dip-coated at 40 mm/min from a 0.05 mg/mL PS-*b*-P4VP/THF solution for the static immersion times indicated. Right, SEM images showing 30-nm AuNPs deposited on BCP thin films. Scale bars represent 500 nm.

Since the AuNPs used for Figure 3.6 have a different diameter (30 nm) compared to those used for the earlier figures (10-12 nm), it was verified, as a last experiment, if AuNP size influences their deposition on the adsorbed BCP layer. This is illustrated in Figure 3.7, showing representative SEM images for a series of AuNP sizes ranging from 10 to almost

100 nm in diameter. In all cases, the surface pattern is of a dense monolayer array of well dispersed AuNPs and little aggregation (the microscale regions shown in Figure 3.7 extended over the entire films of ca. 1 cm^2, excluding the edges). They show good monodispersity, as indicated by relatively narrow size distribution curves peaking at values close to those calculated from the UV-visible spectra of the colloidal solutions (Figure 3.S1). Moreover, while the AuNP number density drops, as expected, with increase in AuNP diameter (from close to 1000 to about 20 AuNP/μm^2) (Figure 3.7a), the average gap size between neighboring AuNPs increases (from about 20-30 nm to approximately 130 nm; Figure 3.7b). (Details concerning the methods of determination of the values in Figure 3.7 are given in the Supporting Information.) Overall, the degree of surface coverage by the AuNPs lies at about 15±5% (Figure 3.7c), as shown also by the fit in Figure 3.7a. However, Method 2' suggests that there is a tendency towards an increase in surface coverage as AuNP diameter increases up to 50-60 nm. Both methods indicate that the surface coverage decreases for the 92-nm AuNPs, possibly due to their greater shape irregularity. It may be added that, despite the fact that the larger AuNPs have diameters that are much greater than the BCP adsorbed layer thicknesses, the deposited particles exhibit good stability against rinsing in water and ethanol.

It is noteworthy that the AuNP densities on the BCP brush are comparable to NP densities observed on organosilane SAMs and P4VP homopolymer templates.[16,18,68] However, the advantage of the BCP brush template is that there is little NP aggregation, in contrast to the organosilane SAMs and homopolymer templates. We verified this for a P4VP homopolymer-coated substrate, as shown in Figure 3.S9. The histograms in this figure clearly show that there is significantly more aggregation on the homopolymer films than on the BCP films, notably by the greater number of counts for larger than average diameters (i.e. the more intense and extended histogram tail), especially after overnight incubation in the AuNP colloid.

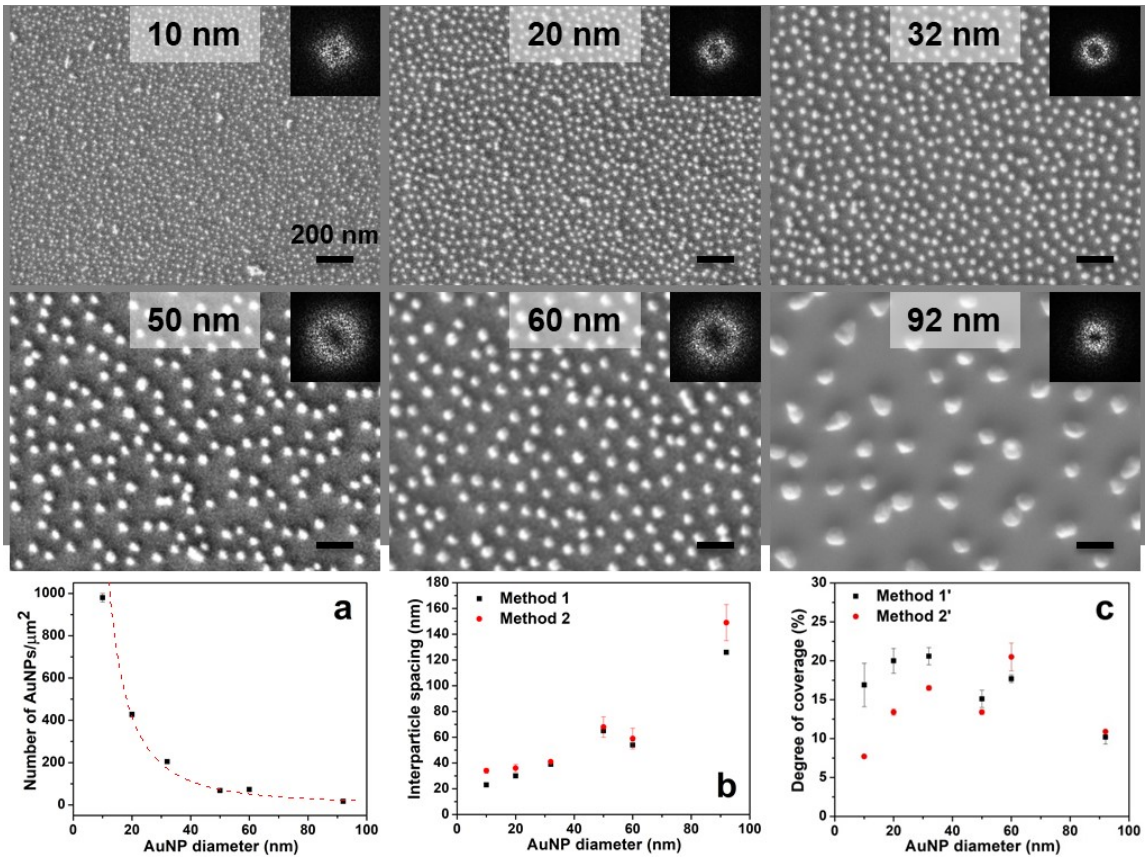

Figure 3.7 SEM images of AuNPs of the various diameters indicated (determined from UV-visible spectra) deposited on BCP brush-layer coated silicon wafers (dip-coated from a 0.05 mg/mL PS-*b*-P4VP/THF solution at immersion and withdrawal rates of 40 mm/min, pause time 30 s). Scale bars represent 200 nm. Bottom, from left to right, are plots, as a function of Au diameter, of (a) number density of the AuNPs, (b) average interparticle spacing (gap size between nearest-neighbor AuNPs) determined by two methods and (c) AuNP surface coverage (determined by two methods). Details of the methods are given in the Supporting Information. The dotted line in (a) indicates the density expected for a constant degree of coverage of 15%.

The low degree of aggregation on the BCP template can be rationalized by the presence of the PS, which acts as an effective corona around the site of each P4VP-adsorbed AuNP by virtue of the covalent connection between the PS and P4VP diblock chains. In this case, the PS segments behave as a 2D dispersant of the AuNPs on the

template surface. Thus, a reasonable if simplified picture of the AuNP-covered brush-layer BCP film, is that the negatively charged AuNPs, which are electrostatically adsorbed to the (partly) protonated P4VP, are each surrounded by a 2D corona of PS in the plane of the brush film, as shown schematically in Figure 3.1 (bottom right). In addition to molecular rearrangement of PS segments in at least the saturated brush-layer films to allow the electrostatic AuNP-P4VP contacts, it is possible that some rearrangement of the P4VP wetting layer also occurs to form a molecular barrier between the incompatible AuNPs and PS coronae. In line with ref 19, the non-close-packed nature of the arrays can be attributed to the initial electrostatic repulsion between the AuNPs as they deposit during the incubation process, while the 2D PS corona, which is repulsive to water, prevents the formation of a film of water, and therefore the development of strong capillarity forces during drying, between the AuNPs, thereby inhibiting AuNP aggregation.

Although our investigation concentrates on a single PS-*b*-P4VP block copolymer and citrate-capped AuNPs, benefiting from their convenient electrostatic interactions, the findings are applicable in principle to NPs of various shapes, compositions and functionalities, to other block copolymers, including those that adsorb NPs through other noncovalent interactions such as hydrogen bonds as well as through covalent interactions, and to substrates of different surface natures and geometries. The present investigation also helps understand how the dense and unaggregated AuNP deposition observed on the highly curved surfaces of nanofibers was possible.[35] It will be of interest to investigate if the interparticle NP spacing on the adsorbed polymer layers can be tuned by varying the characteristics of the BCPs or the solvent environment during adsorption, which are known to affect the adsorption of block copolymers on surfaces. Furthermore, as mentioned earlier, the exposure of the BCP brush layer to an aqueous milieu likely causes at least some molecular rearrangement in the PS layer to allow AuNP contact with P4VP segments, and possibly also in the P4VP layer. In future work, these aspects merit deeper investigation, in parallel with exploring if there are ways to influence the in situ surface patterning and vary the AuNP deposition pattern or density on BCP brush layers. What we have shown here are that the attributes of BCP adsorbed brushlike layers make them practical templates for surface incorporation of NPs and undoubtedly also other functional molecules.

3.5 Conclusions

We have exploited the fact that very dilute BCP dip-coating solutions allow the adsorption of a nanothin BCP brushlike layer onto substrates immersed in the solution, with no additional material deposited during withdrawal of the substrate from the solution. This was shown by investigating the effect of polymer solution concentration on film thickness, film surface morphology and AuNP patterning, determined by ellipsometry, AFM and SEM, respectively, supplemented by water contact angle measurements. While film formation and surface patterning are dominated by spherical micelles upon substrate withdrawal for high BCP solution concentrations (for the PS-*b*-P4VP and solvent utilized), there is only adsorption of the brushlike layer for low polymer concentrations. Correspondingly, with decreasing solution concentration, the film surface pattern transitions from P4VP dots in a PS matrix (a conventional BCP film template) to a featureless PS overlayer covering a P4VP wetting layer that is strongly adsorbed by multiple noncovalent bonds to the OH-decorated silicon substrate (BCP brushlike or adsorbed layer template). For small AuNPs, the two types of templates produce distinct patterns of AuNP arrays, dense in both cases, with the former producing AuNP clusters on the P4VP dots and the latter well-dispersed AuNPs with little aggregation. AuNP contact with the P4VP wetting layer can be explained by local molecular rearrangement in the PS brush layer upon exposure to the aqueous AuNP milieu. The lack of aggregation is attributed to the presence of PS. The time of immersion in the very dilute BCP solution, which determines whether the coverage by the PS brush is complete or not, and the size of the AuNPs have no observable effect on the AuNP pattern and density. Thus, we demonstrate that easy-to-fabricate brushlike BCP templates constitute a simple and effective strategy for assembling non-close-packed 2D monolayer arrays of nanoparticles on surfaces.

3.6 Supporting Information

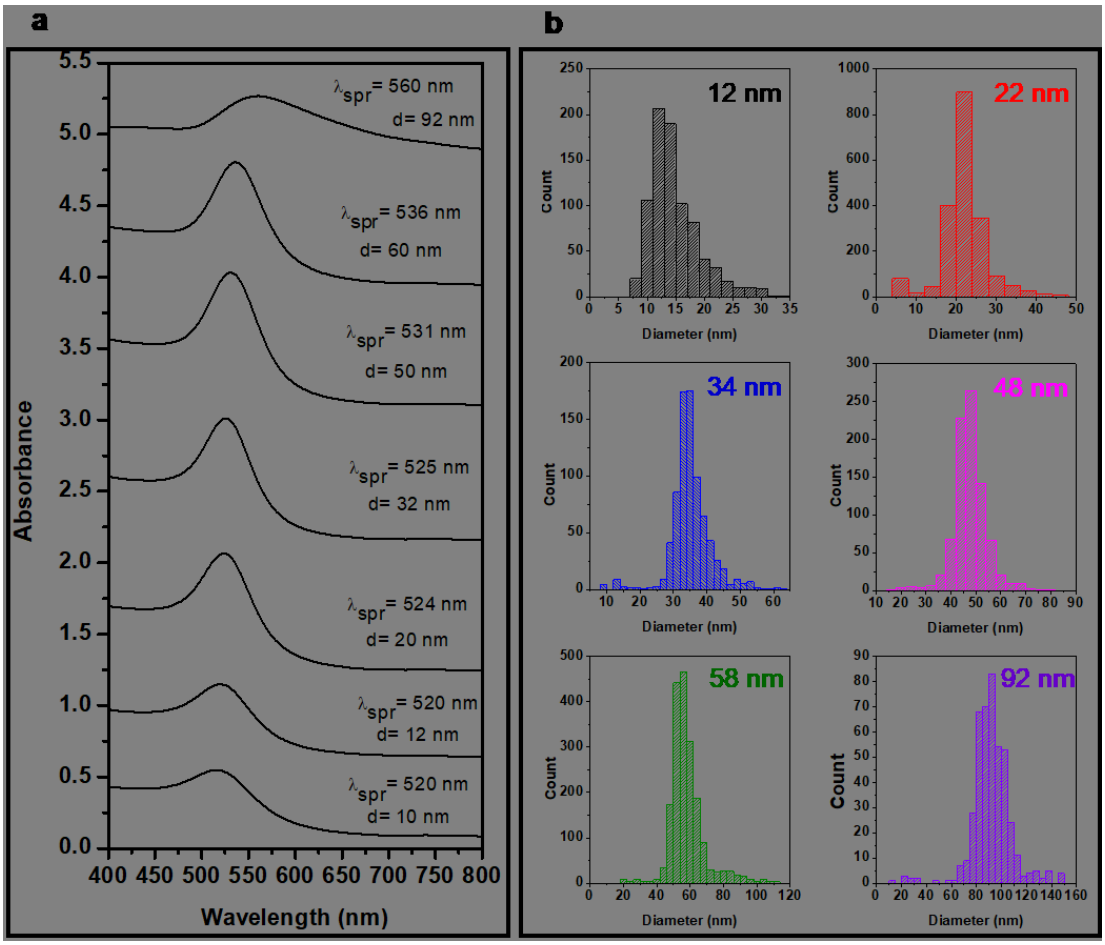

Figure 3.S1. a) UV-visible spectra of the AuNPs synthesized, with the measured surface plasmon resonance wavelengths, λ_{spr}, and the derived AuNP diameters, d, following Haiss et al. (ref 39 of main text). The batch, d=10 nm, served as seeds for the d=20-92 nm AuNPs. b) Diameter distribution of the AuNPs deposited on the block copolymer brush film templates, determined using ImageJ on the SEM images in Figure 3.7 in the main text, along with the average diameter indicated by the analysis (generally within 2 nm of the values obtained from UV-vis).

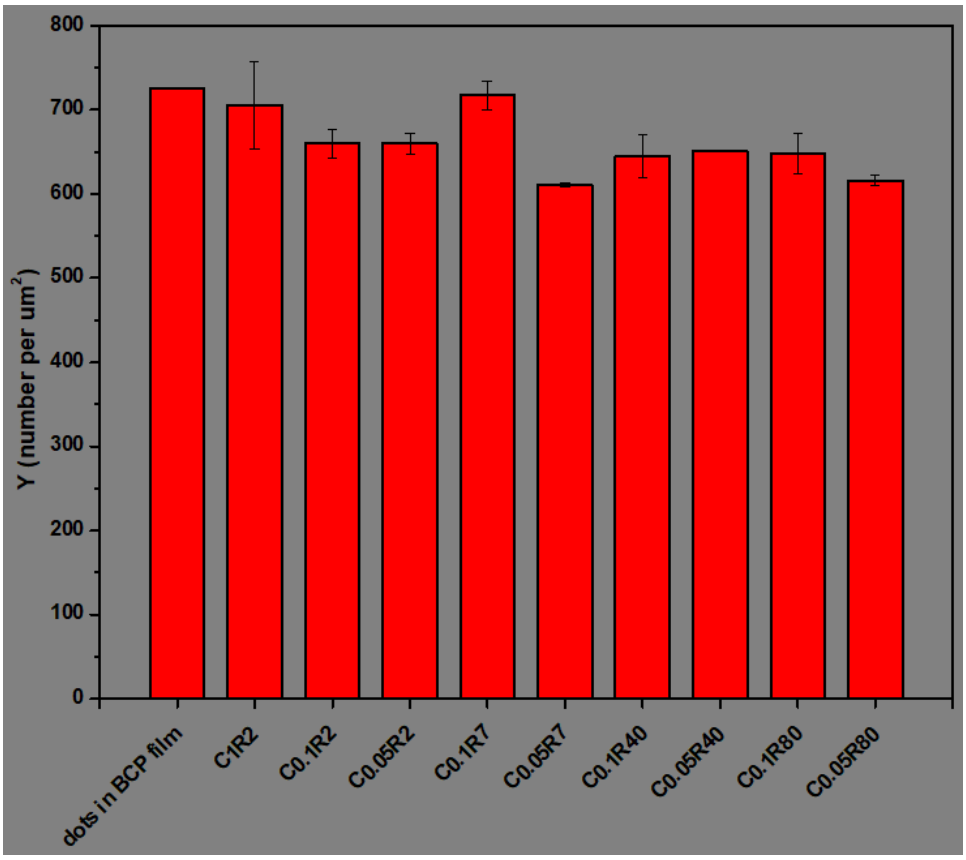

Figure 3.S2. Number densities of dots in the PS-*b*-P4VP full-dot film in Figure 3.2a (leftmost bar) and of the AuNPs (10-12 nm) on PS-*b*-P4VP templates obtained from various polymer solution concentrations (Cx, x in mg/mL) and using various dip-coating withdrawal rates (Ry, y in mm/min). The dot density of the BCP film was determined by using the center-to-center distance of the dots indicated by the 2D FFT and then applying the Engineer's Toolbox assuming 2D hexagonal (triangular) packing. The AuNP densities were determined from SEM images using ImageJ; error bars represent the standard deviation among three SEM images taken at different spots on the sample. An average center-to-center distance of 40 nm for the AuNPs deposited on the brush-layer films (solution concentrations of 0.1 and 0.05 mg/mL) was estimated using the Engineer's Toolbox, by inputting different integer values for the "space between circles" until the density, assuming hexagonal ("triangular") order, was close to the average density of the eight right-hand bars (651 AuNP/μm^2; a "space" of 29 nm for 11-nm diameter AuNPs gives a density of 658 AuNP/μm^2).

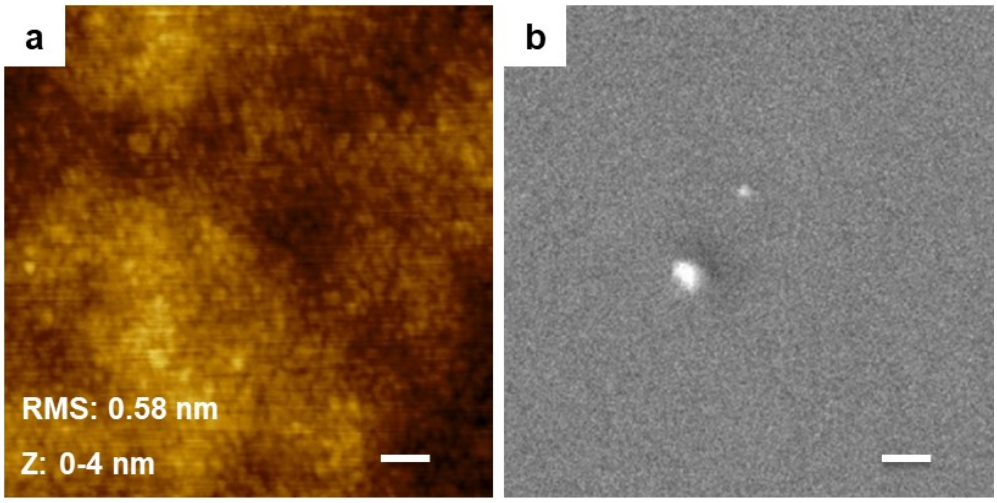

Figure 3.S3. a) AFM height image of a bare Si substrate (RMS is the root-mean-square roughness, Z is the height scale). b) SEM image of a bare Si substrate that was incubated in a 10-12 nm AuNP colloidal suspension. Scale bars represent 100 nm.

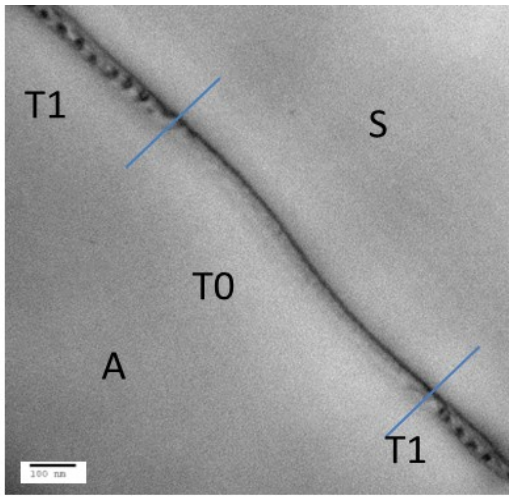

Figure 3.S4. Cross-sectional TEM (transmission electron microscope) image of a piece of thin film dip-coated at a withdrawal rate of 2 mm/min onto a silicon substrate from a THF solution of PS-b-P4VP (5 mg/mL) and equimolar naphthoic acid. The film was floated off the substrate, embedded in epoxy, microtomed, deposited on a TEM grid, and then stained with I_2 vapor, which selectively stains P4VP. T0 refers to the wetting/brush layer, T1 to the micellar monolayer, S and A to the substrate and air sides, respectively, of the film. The T0 section is consistent with P4VP acting as the wetting sublayer (extending also below the micellar T1 portions), with barely visible PS on the air side. Image extracted from ref 63 (Figure 9a) in the main text.

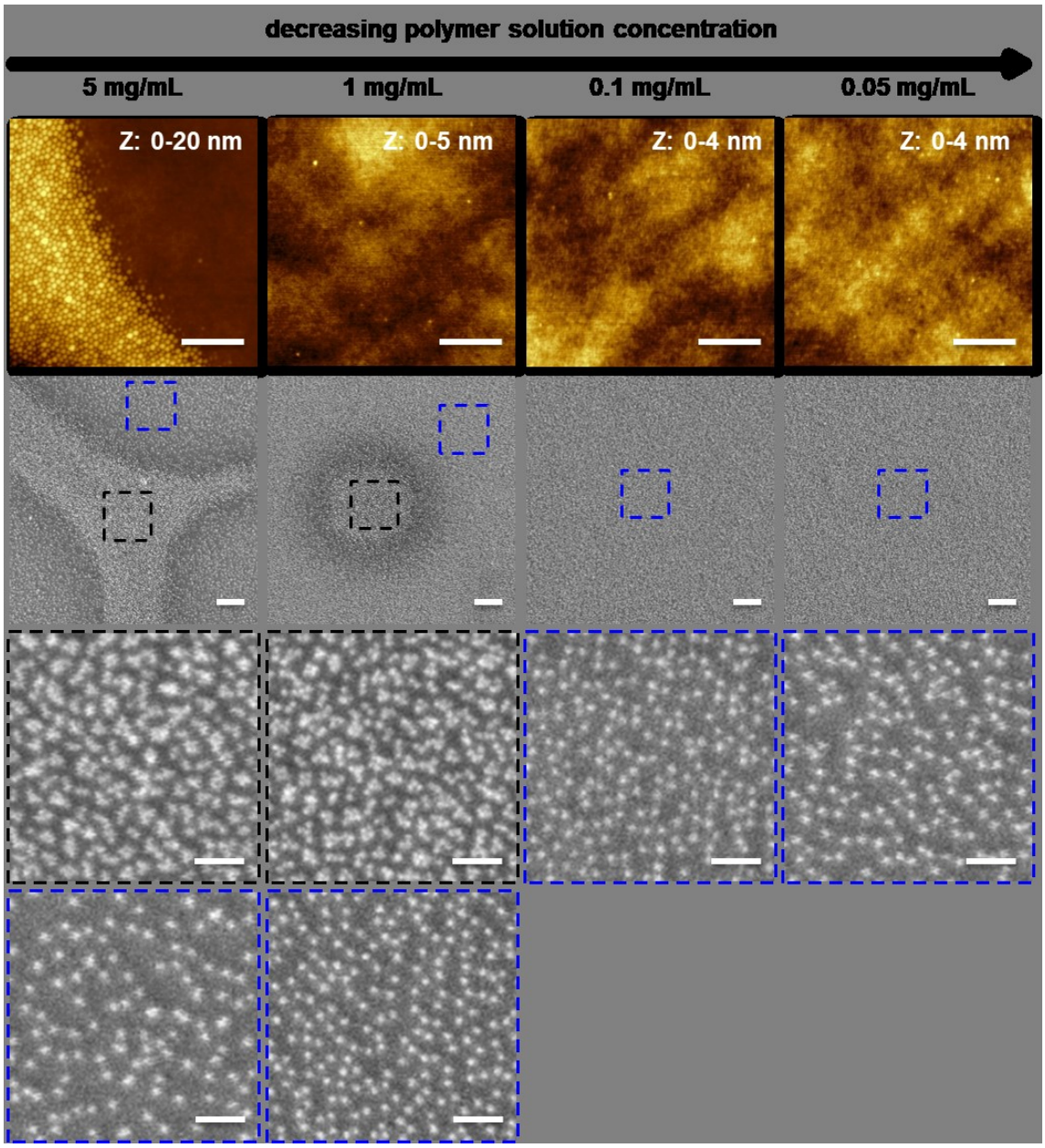

Figure 3.S5. AFM height images (1st row; Z indicates height scale; scale bars represent 500 nm) of films dip-coated on silicon substrates at 7 mm/min (immersion rate 40 mm/min; pause time 30 s) from PS-*b*-P4VP/THF solutions of various concentrations; corresponding SEM images of low resolution (2nd row; scale bars represent 500 nm) after the deposition of 10-12 nm AuNPs on these film templates; SEM images of high resolution (3rd and 4th rows; scale bars represent 100 nm; color of dotted outlines correspond to the regions indicated in the 2nd row images).

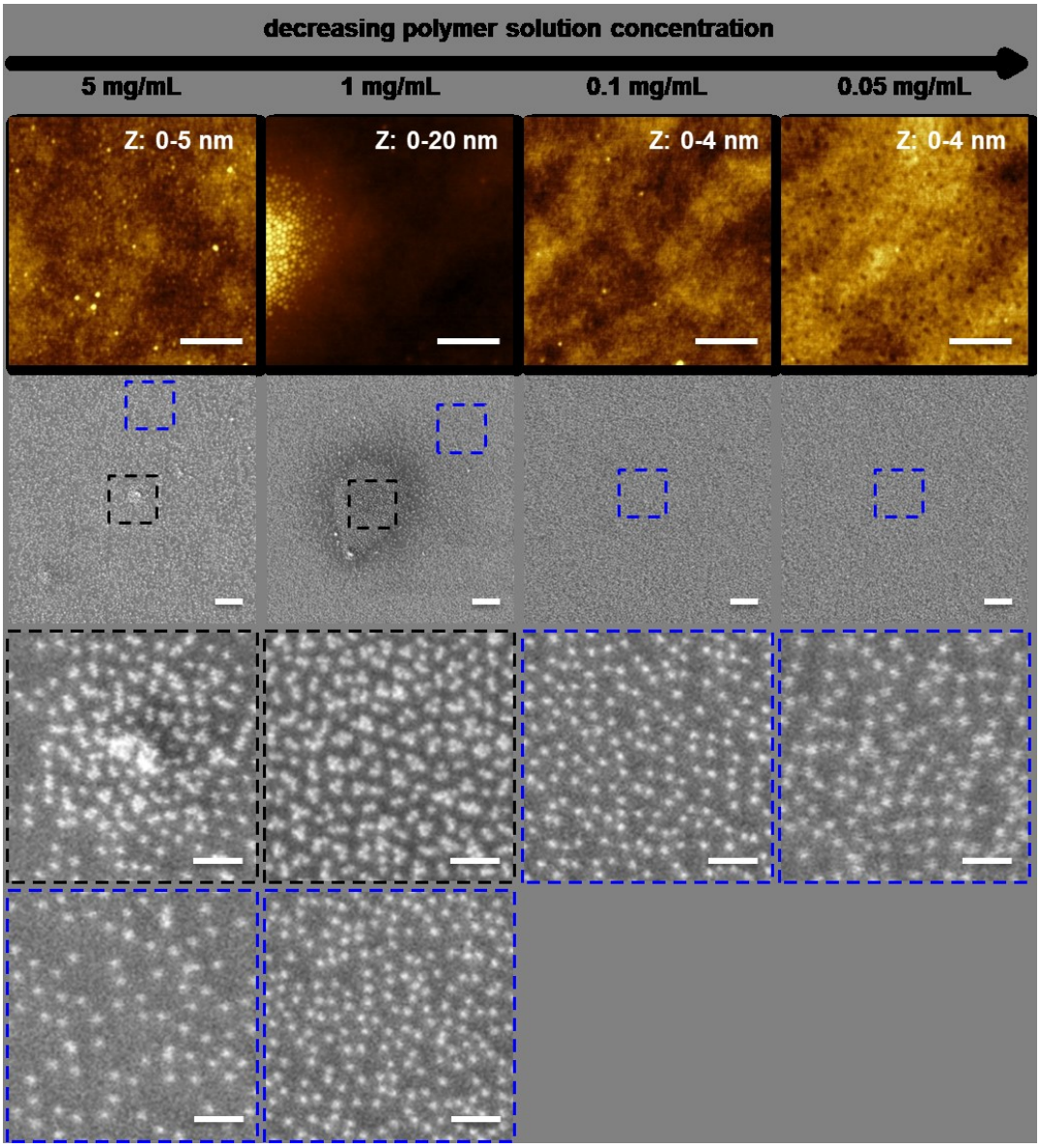

Figure 3.S6. AFM height images (1st row; Z indicates height scale; scale bars represent 500 nm) of films dip-coated on silicon substrates at 40 mm/min (immersion rate 40 mm/min; pause time 30 s) from PS-*b*-P4VP/THF solutions of various concentrations; corresponding SEM images of low resolution (2nd row; scale bars represent 500 nm) after the deposition of 10-12 nm AuNPs on these film templates; SEM images of high resolution (3rd and 4th rows; scale bars represent 100 nm; color of dotted outlines correspond to the regions indicated in the 2nd row images).

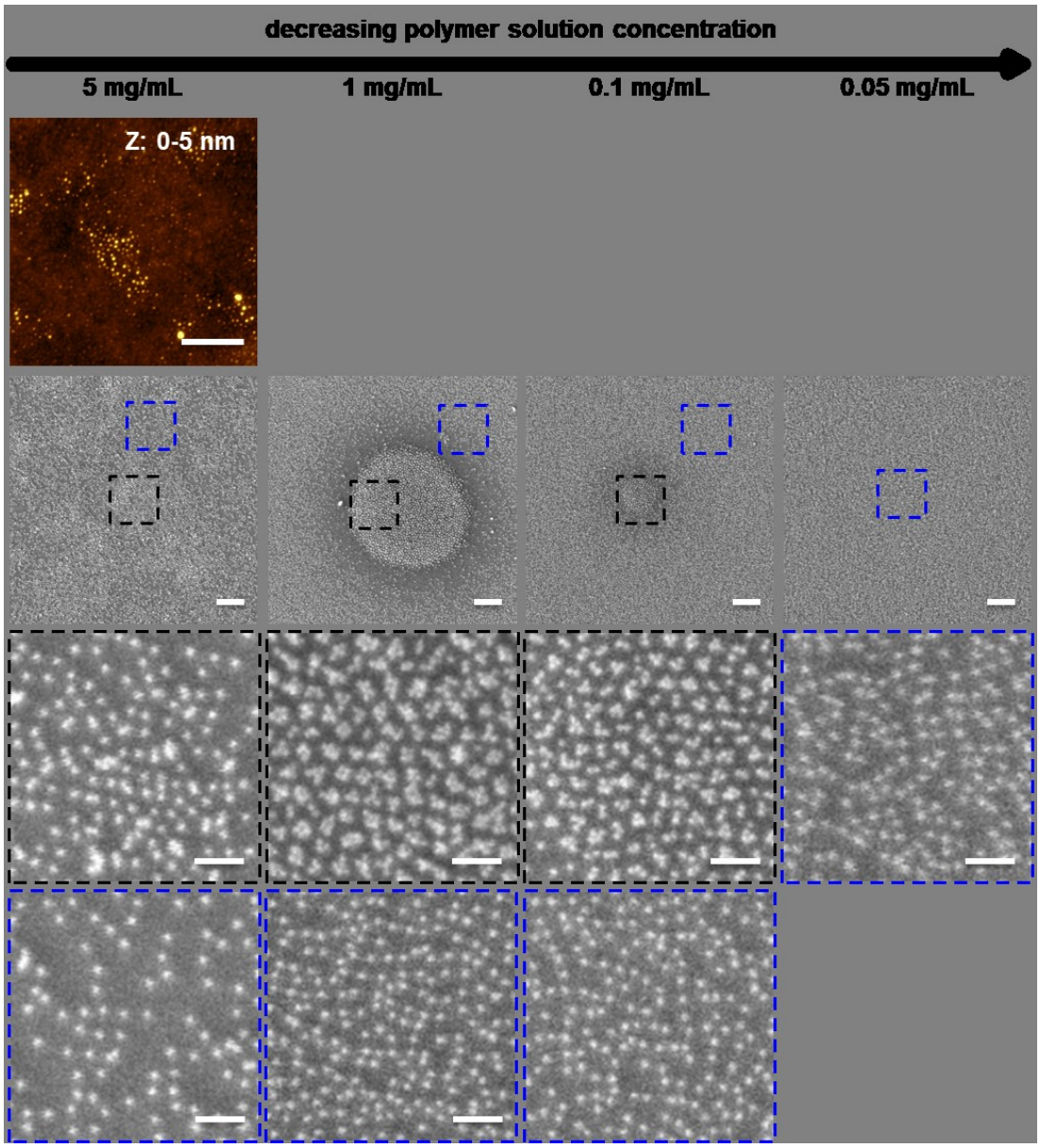

Figure 3.S7. AFM height image (1st row, only one concentration examined; Z indicates height scale; scale bar represents 500 nm) of thin films dip-coated on silicon substrates at 80 mm/min (immersion rate 5 mm/min; pause time 30 s) from PS-*b*-P4VP/THF solutions of various concentrations; corresponding SEM images of low resolution (2nd row; scale bars represent 500 nm) after the deposition of 10-12 nm AuNPs on these film templates; SEM images of high resolution (3rd and 4th rows; scale bars represent 100 nm; color of dotted outlines correspond to the regions indicated in the 2nd row images).

Table 3.S1 Detailed Analysis of Total Exposure Times of the Substrates to the BCP Solution, Relevant to the Thickness Data for the Brush-Layer (Dot-Free) Films Shown in Figure 3 of the Main Text. Left, schematic illustration of typical surface dimensions of the substrate (gray + blue) and area of the substrate exposed to solution (blue) in our experiments. The ellipsometric, AFM and SEM measurements were all performed within the white dotted box indicated. Right, estimated total adsorption times (time of substrate contact with the BCP solution), calculated for the location indicated by the horizontal white solid line drawn at the half-height (=0.5b) of the brush-layer film (blue area); R is followed by a number indicating the rate in mm/min of substrate immersion (R_{down}) or withdrawal (R_{up}).

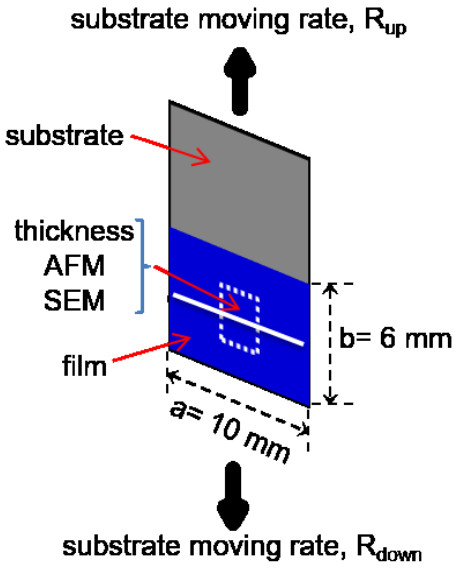

R	total immersion time[1]
$R_{down}40$ / $R_{up}2$	125 s
$R_{down}40$ / $R_{up}7$	60 s
$R_{down}40$ / $R_{up}40$	39 s
$R_{down}5$ / $R_{up}80$	70 s

[1] total immersion time at 0.5b = (0.5b/R_{down}) + (pause time = 30 s) + (0.5b/R_{up})

The brush-layer adsorption kinetics shown in Figure 3.4 indicate that the length of exposure to the BCP solution influences the brush-layer thickness until maximum adsorption is achieved. On the other hand, the substrate is exposed to solution not only during the static immersion time, but also during the immersion and withdrawal steps, for which the exposure time depends on the rates involved. Thus, to evaluate if the brush-layer (dot-free) thicknesses in Figure 3.3, as well as the corresponding films shown in Figures 3.2 and 3.S5-

S7, for which the withdrawal (and sometimes the immersion) rates vary, are for near-maximum adsorption or not, the total immersion time should be considered. For Figure 3.4 as the reference, 9 s (4.5 s each during substrate immersion and withdrawal, which were both done at 40 mm/min; calculated for the film half-height, i.e. at 0.5b, as shown by the white line in the schematic in Table 3.S1), which can be rounded up to 10 s, must be added to the static immersion times plotted there. Combined with Figure 3.5 (where 10 s must also be added to the static immersion times indicated), this implies that the brush-layer films are in the saturation region for total immersion times starting at approximately 80 s. It can be concluded that the film withdrawn at the very slow rate of 2 mm/min has a fully saturated brush layer and the one withdrawn at 80 mm/min (immersed at a much slower rate than the others; i.e. 5 vs. 40 mm/min) has a brushlike layer that is close to saturation, whereas the film withdrawn at 40 mm/min clearly has an unsaturated brush layer with an intermediate situation for the one withdrawn at 7 mm/min. As indicated in the main text, these values are relevant for the brushlike layer only, and thus particularly apply to the points in Figure 3.3 for polymer solution concentrations of 0.1 and 0.05 mg/mL (black and red symbols).

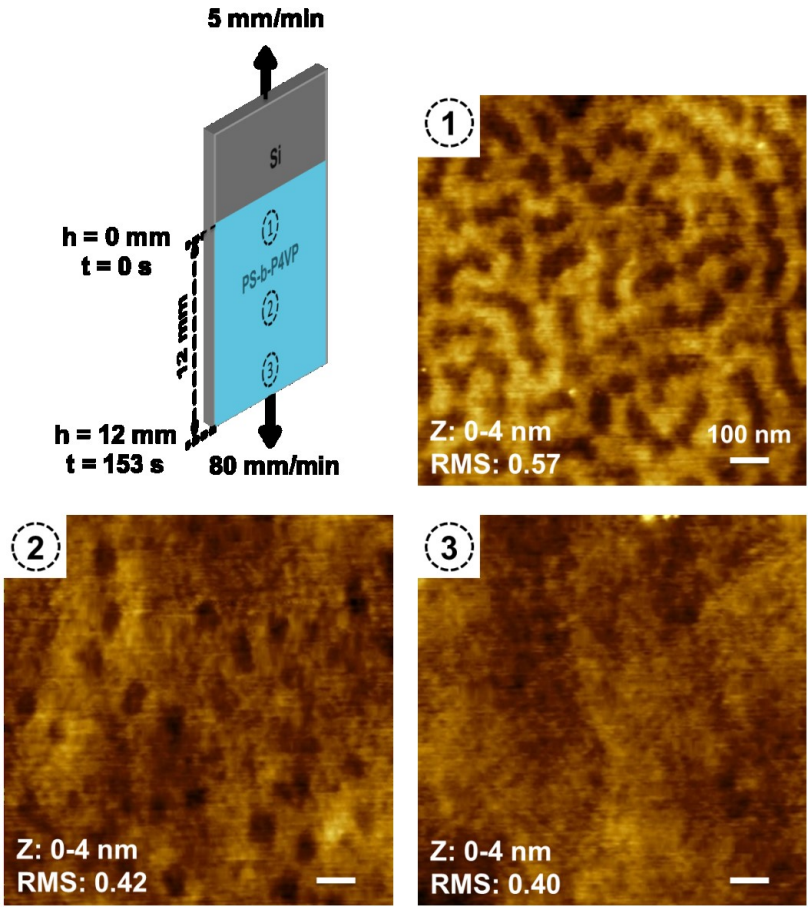

Figure 3.S8. AFM images of top, middle, and bottom areas (as indicated by the schematic) of a 12-mm high film (cyan) dip-coated on a silicon substrate (gray) from a 0.05 mg/mL PS-b-P4VP solution in THF at an immersion rate of 80 mm/min, 0 s of pause time and a withdrawal rate of 5 mm/min. This series illustrates the increasing coverage of the substrate by the PS brush layer with increasing exposure to the solution from 0 s at the very top of the film to 153 s at the very bottom.

Details regarding the values in Figures 7a, b, c

The AuNP densities, D, in Figure 3.7a were obtained by counting the number of AuNPs in three different areas of the SEM images using ImageJ and then manually adding the extra particles where there are aggregates (counted as one by ImageJ). The area sizes analyzed were 0.4x0.4 μm^2 for 10-nm AuNPs, 2x2 μm^2 for 20- and 32-nm AuNPs, and 4x4

μm^2 for 50-, 60- and 92-nm AuNPs. The decrease in density with increasing AuNP diameter is expected.

For Figure 3.7b, first, center-to-center distances (C-C distance) were determined by two different methods. In Method 1 (black squares), they were derived from the densities in Figure 7a with the help of the Engineer's Toolbox, as described in the caption of Figure S2. In Method 2 (red triangles), they were determined from the 2D FFT of the SEM images using the Gwyddion software, taking the average of the values obtained from eight cuts across the FFTs at different azimuthal angles. Then, the C-C distances were converted to interparticle spacings or gap distances between neighboring particles by substracting the AuNP diameters, d (from UV-vis). The two methods give similar values for each AuNP size.

The degrees of surface coverage, C, in Figure 3.7c were also estimated using two methods. In Method 1' (black squares), ImageJ was used, where the surface area of each AuNP is outlined; the outline is dependent on the quality of SEM images, the resolution of which is poorest for the smallest AuNPs. In Method 2' (red triangles), they were calculated from the nanoparticle densities in Figure 7a, assuming spherical AuNPs and uniform AuNP diameters, d (from UV-vis), as $C=D\pi(d/2)^2100$. The two methods give rather different values for the smallest AuNP's, with the difference decreasing with increase in AuNP size and becoming similar for sizes of 50 nm and higher. If the main source of the difference for the smaller AuNPs is the SEM resolution, then it appears that the total coverage of the AuNPs first increases with size to a maximum of about 20% and then decreases with size. If the coverage is constant at 15%, as modeled by the red dotted line in Figure 3.7a, then only the 10-nm AuNPs show significant deviation.

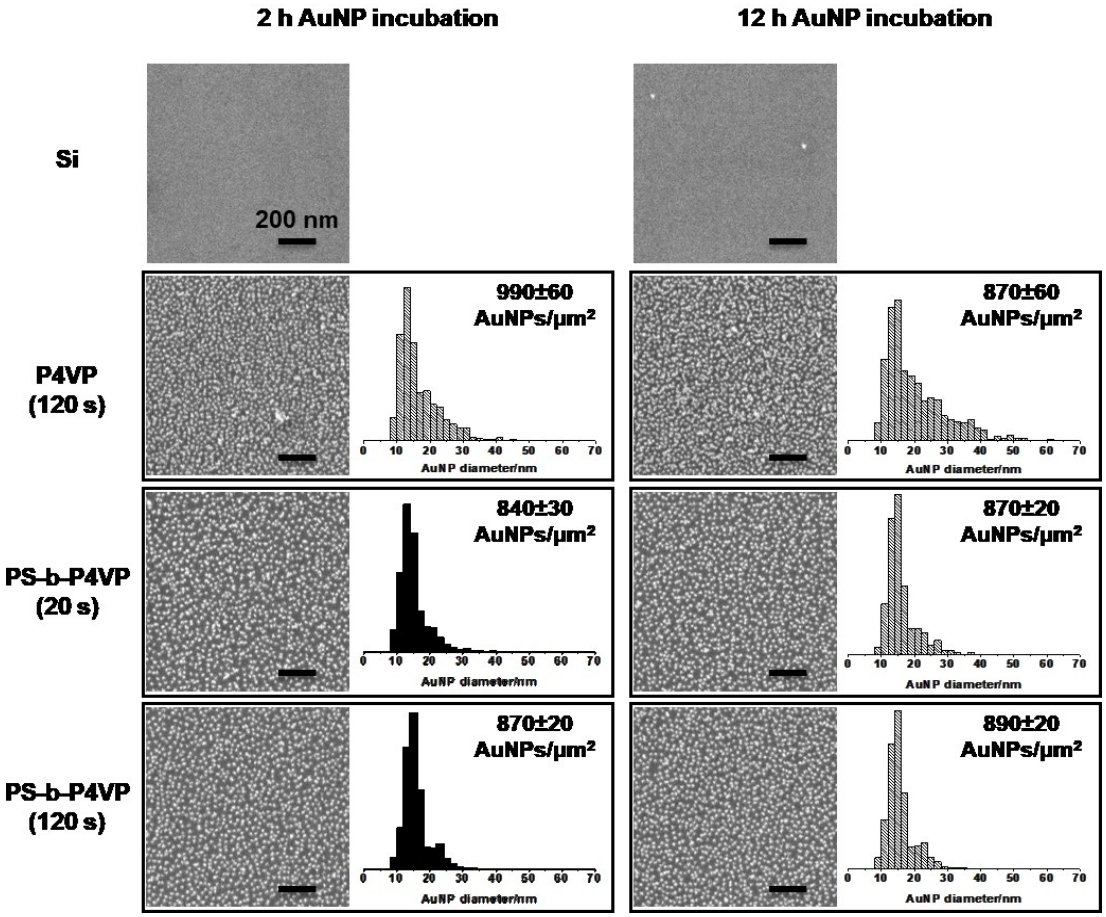

Figure 3.S9. SEM images and corresponding AuNP size distribution histograms of 10-12 nm AuNPs deposited on the surfaces indicated in the left column (along with the dip-coating pause times, 20 and 120 s for unsaturated and saturated BCP films) after 2 h and after overnight (12 h) incubation in the AuNP colloid. Scale bars 200 nm. The films were dip-coated from a 0.05 mg/mL BCP solution at immersion and withdrawal rates of 40 mm/min. The densities accompanying the histograms were determined by ImageJ without manual addition of NPs to account for those in aggregates seen by ImageJ as single (larger) particles. P4VP densities, in particular, are significantly affected by aggregation, as indicated by the longer and more intense tail corresponding to larger AuNPs.

3.7 References

1. Shankar, S. S.; Rai, A.; Ahmad, A.; Sastry, M. Chem. Mater. 2005, 17, 566-572.

2. Atwater, H. A.; Polman, A. Nat. Mater. 2010, 9, 205-213.
3. Wu, J. L.; Chen, F. C.; Hsiao, Y. S.; Chien, F. C.; Chen, P.; Kuo, C. H.; Huang, M. H.; Hsu, C. S. ACS Nano 2011, 5, 959-967.
4. Nath, N.; Chilkoti, A. Anal. Chem. 2002, 74, 504-509.
5. Lu, Y.; Liu, G. L.; Lee, L. P. Nano Lett. 2005, 5, 5-9.
6. Le, F.; Brandl, D. W.; Urzhumov, Y. A.; Wang, H.; Kundu, J.; Halas, N. J.; Aizpurua, J.; Nordlander, P. ACS Nano 2008, 2, 707-718.
7. Liu, X.; Fu, L.; Hong, S.; Dravid, V. P.; Mirkin, C. A. Adv. Mater. 2002, 14, 231-234.
8. Boyen, H. G.; Kästle, G.; Zürn, K.; Herzog, T.; Weigl, F.; Ziemann, P.; Mayer, O.; Jerome, C.; Möller, M.; Spatz, J. P.; Garnier, M. G.; Oelhafen, P. Adv. Funct. Mater. 2003, 13, 359-364.
9. Rybczynski, J.; Ebels, U.; Giersig, M. Large-scale, Colloids Surf., A 2003, 219, 1-6.
10. Wen, T.; Booth, R. A.; Majetich, S. A. Nano Lett. 2012, 12, 5873-5878.
11. Schmitt, J.; Decher, G.; Dressick, W. J.; Brandow, S. L.; Geer, R. E.; Shashidhar, R.; Calvert, J. M. Adv. Mater. 1997, 9, 61-65.
12. Sarathy, K. V.; Thomas, P. J.; Kulkarni, G. U.; Rao, C. N. R. J. Phys. Chem. B 1999, 103, 399-401.
13. Lee, D.; Rubner, M. F.; Cohen, R. E. Nano Lett. 2006, 6, 2305-2312.
14. Hannon, J. B.; Kodambaka, S.; Ross, F. M.; Tromp, R. M. Nature 2006, 440, 69-71.
15. Kang, S. J.; Kocabas, C.; Ozel, T.; Shim, M.; Pimparkar, N.; Alam, M. A.; Rotkin, S. V.; Rogers, J. A. Nat. Nanotechnol. 2007, 2, 230-236.
16. Grabar, K. C.; Freeman, R. G.; Hommer, M. B.; Natan, M. J. Anal. Chem. 1995, 67, 735-743.
17. Freeman, R. G.; Grabar, K. C.; Allison, K. J.; Bright, R. M.; Davis, J. A.; Guthrie, A. P.; Hommer, M. B.; Jackson, M. A.; Smith, P. C.; Walter, D. G. Science 1995, 267, 1629-1632.
18. Malynych, S.; Luzinov, I.; Chumanov, G. J. Phys. Chem. B 2002, 106, 1280-1285.
19. Schmudde, M.; Grunewald, C.; Goroncy, C.; Noufele, C. N.; Stein, B.; Risse, T.; Graf, C. ACS Nano 2016, 10, 3525-3535.

20. McIntire, T. M.; Smalley, S. R.; Newberg, J. T.; Lea, A. S.; Hemminger, J. C.; Finlayson-Pitts, B. J. Langmuir 2006, 22, 5617-5624.
21. Ballarin, B.; Cassani, M. C.; Scavetta, E.; Tonelli, D. Electrochim. Acta 2008, 53, 8034-8044.
22. Zhu, M.; Lerum, M. Z.; Chen, W. Langmuir 2012, 28, 416-423.
23. Ben Haddada, M.; Blanchard, J.; Casale, S.; Krafft, J.-M.; Vallée, A.; Méthivier, C.; Boujday, S. Gold Bull. 2013, 46, 335-341.
24. Ben Haddada, M.; Huebner, M.; Casale, S.; Knopp, D.; Niessner, R.; Salmain, M.; Boujday, S. J. Phys. Chem. C 2016, 120, 29302-29311.
25. Tian, S.; Liu, J.; Zhu, T.; Knoll, W. Chem. Mater. 2004, 16, 4103-4108.
26. Tokareva, I.; Minko, S.; Fendler, J. H.; Hutter, E. J. Am. Chem. Soc. 2004, 126, 15950-15951.
27. Vitol, E. A.; Orynbayeva, Z.; Bouchard, M. J.; Azizkhan-Clifford, J.; Friedman, G.; Gogotsi, Y. ACS Nano 2009, 3, 3529-3536.
28. Kim, K.; Ryoo, H.; Shin, K. S. Langmuir 2010, 26, 10827-10832.
29. Aizawa, M.; Buriak, J. M. J. Am. Chem. Soc. 2005, 127, 8932-8933.
30. Chai, J.; Wang, D.; Fan, X.; Buriak, J. M. Nat. Nanotechnol. 2007, 2, 500-506.
31. Lee, W.; Lee, S. Y.; Briber, R. M.; Rabin, O. Adv. Funct. Mater. 2011, 21, 3424-3429.
32. Yap, F. L.; Thoniyot, P.; Krishnan, S.; Krishnamoorthy, S. ACS Nano 2012, 6, 2056-2070.
33. Chen, X.; Perepichka, II; Bazuin, C. G. ACS Appl. Mater. Interfaces 2014, 6, 18360-18367.
34. Onses, M. S.; Wan, L.; Liu, X.; Kiremitler, N. B.; Yılmaz, H.; Nealey, P. F. ACS Macro Lett. 2015, 4, 1356-1361.
35. Zhu, H.; Lussier, F.; Ducrot, C.; Bourque, M. J.; Spatz, J. P.; Cui, W.; Yu, L.; Peng, W.; Trudeau, L. E.; Bazuin, C. G.; Masson, J. F. ACS Appl. Mater. Interfaces 2019, 11, 4373-4384.
36. Lu, M.; Zhu, H.; Bazuin, C. G.; Peng, W.; Masson, J.-F. J. A. s. ACS Sens. 2019. DOI: 10.1021/acssensors.8b01372.
37. Turkevich, J.; Stevenson, P. C.; Hillier, J. Discuss. Faraday Soc. 1951, 11, 55-74.

38. Bastús, N. G.; Comenge, J.; Puntes, V. Langmuir 2011, 27, 11098-11105.
39. Haiss, W.; Thanh, N. T.; Aveyard, J.; Fernig, D. G. Anal. Chem. 2007, 79, 4215-4221.
40. Landau, L.; Levich, B. Acta Phys.Chim. U. R. S. S. 1942, 17, 42-54.
41. Faustini, M.; Louis, B.; Albouy, P. A.; Kuemmel, M.; Grosso, D. J. Phys. Chem. C 2010, 114, 7637-7645.
42. Roland, S.; Prud'homme, R. E.; Bazuin, C. G. ACS Macro Lett. 2012, 1, 973-976.
43. Roland, S.; Gamys, C. G.; Grosrenaud, J.; Boissé, S.; Pellerin, C.; Prud'homme, R. E.; Bazuin, C. G. Macromolecules 2015, 48, 4823-4834.
44. Xu, H.; Hong, R.; Wang, X.; Arvizo, R.; You, C.; Samanta, B.; Patra, D.; Tuominen, M. T.; Rotello, V. M. Adv. Mater. 2007, 19, 1383-1386.
45. Laforgue, A.; Bazuin, C. G.; Prud'homme, R. E. Macromolecules 2006, 39, 6473-6482.
46. Zou, S.; Hong, R.; Emrick, T.; Walker, G. C. Langmuir 2007, 23, 1612-1614.
47. Spatz, J. P.; Roescher, A.; Sheiko, S.; Krausch, G.; Möller, M. Adv. Mater. 1995, 7, 731-735.
48. Liu, Y.; Quinn, J.; Rafailvoich, M. H.; Sokolov, J.; Zhong, X.; Eisenberg, A. Macromolecules 1995, 28, 6347-6348.
49. Spatz, J. P.; Möller, M.; Noeske, M.; Behm, R. J.; Pietralla, M. Macromolecules 1997, 30, 3874-3880.
50. Munch, M. R.; Gast, A. P. J. Chem. Soc., Faraday Trans. 1990, 86, 1341.
51. Green, P. F.; Christensen, T. M.; Russell, T. P.; Jerome, R. Macromolecules 1989, 22, 2189-2194.
52. Spatz, J. P.; Sheiko, S.; Moller, M. Macromolecules 1996, 29, 3220-3226.
53. Tokarev, I.; Krenek, R.; Burkov, Y.; Schmeisser, D.; Sidorenko, A.; Minko, S.; Stamm, M. Macromolecules 2005, 38, 507-516.
54. Munch, M. R.; Gast, A. P. Macromolecules 1990, 23, 2313-2320.
55. Motschmann, H.; Stamm, M.; Toprakcioglu, C. Macromolecules 1991, 24, 3681-3688.
56. Amiel, C.; Sikka, M.; Schneider Jr, J. W.; Tsao, Y.-H.; Tirrell, M.; Mays, J. W. Macromolecules 1995, 28, 3125-3134.

57. Meiners, J.; Ritzi, A.; Rafailovich, M.; Sokolov, J.; Mlynek, J.; Krausch, G. Appl. Phys. A 1995, 61, 519-524.

58. Meiners, J. C.; Quintel-Ritzi, A.; Mlynek, J.; Elbs, H.; Krausch, G. Macromolecules 1997, 30, 4945-4951.

59. Hershkovits, E.; Tannenbaum, A.; Tannenbaum, R. Macromolecules 2008, 41, 3190-3198.

60. Toomey, R.; Mays, J.; Tirrell, M. Macromolecules 2004, 37, 905-911.

61. Tassin, J. F.; Siemens, R. L.; Tang, W. T.; Hadziioannou, G.; Swalen, J. D.; Smith, B. A. J. Phys. Chem. 1989, 93, 2106-2111.

62. Parsonage, E.; Tirrell, M.; Watanabe, H.; Nuzzo, R. G. Macromolecules 1991, 24, 1987-1995.

63. Roland, S.; Gaspard, D.; Prud'homme, R. E.; Bazuin, C. G. Macromolecules 2012, 45, 5463-5476.

64. Spatz, J. P.; Sheiko, S.; Möller, M. Adv. Mater. 1996, 8, 513-517.

65. Johner, A.; Joanny, J. Macromolecules 1990, 23, 5299-5311.

66. Tebbe, M.; Galati, E.; Walker, G. C.; Kumacheva, E. Small 2017, 13.

67. Karim, A.; Tsukruk, V.; Douglas, J.; Satija, S.; Fetters, L.; Reneker, D.; Foster, M. J. Phys. II 1995, 5, 1441-1456.

68. Grabar, K. C.; Smith, P. C.; Musick, M. D.; Davis, J. A.; Walter, D. G.; Jackson, M. A.; Guthrie, A. P.; Natan, M. J. J. Am. Chem. Soc. 1996, 118, 1148-1153.

Chapter 4

Templating Gold Nanoparticles on Nanofibers with Block Copolymer Brush Layers*

4.1 Abstract

SERS endoscopy-based nanosensors that offer high spatial and temporal resolution as well as high sensitivity are promising for cellular studies. The fabrication of SERS endoscopic probes involves decorating glass nanofibers with gold nanoparticles (AuNPs), which is a challenge for highly curved nanofibers. We have shown that this challenge can be met with block copolymer (BCP) brush films, which permit the adsorption of dense and well-dispersed AuNPs on nanofibers, specifically using polystyrene-block-poly(4-vinylpyridine) (PS-*b*-P4VP). When dip-coating the fiber with the BCP solution, the effect of substrate curvature on the film thickness parallels that of decreasing polymer solution concentration on flat surfaces, giving rise to thicker dot-patterned films at low curvature and transitioning into the brush layer at high curvature. Exposure to an aqueous colloidal suspension of small AuNPs results in several AuNPs per BCP dot for the former and mainly isolated AuNPs for the latter. AuNP adsorption onto the brush layer is independent of BCP concentration and dip-coating rate and is effective for various AuNP diameters (10-100 nm studied). The average interparticle spacing of the AuNPs can be controlled by the P4VP weight content in the BCP.

*Will be submitted as a full paper: Zhu, H.; Masson, J.-F.; Bazuin, C.G.

4.2 Introduction

In cell endoscopy, small submicrometer probes such as glass pipettes, glass fibers, carbon nanopipettes, carbon nanotubes, nanowires, and atomic force microscopic tips are inserted into a cell non-invasively to perform various tasks such as intracellular sensing, delivery, plasmon phototherapy, electrochemistry and electrophysiology at different locations of the cell with high spatial resolution.[1-6] A particular cell endoscopy probe utilizes surface enhanced Raman spectroscopy (SERS), owing to its superb sensitivity for detection of biochemicals in and around cells.[7-11] As a proof of concept, Vitol *et al.* demonstrated that the positioning of the 150-nm tip of a glass pipette in the nucleus or cytoplasm of a HeLa cell can be clearly distinguished through the measured SERS signals.[8] Using a similar SERS nanopipette extracellularly, Lussier *et al.* showed that the metabolic process of a living Madin-Darby canine kidney epithelial cell can be monitored *in situ* through the SERS detection of several metabolites.[11] It is noteworthy that, unlike fluorescence-based sensing, SERS-based sensing is label-free, allowing studies of cells in their true native environments.

The fabrication of SERS endoscopic probes involves coating nanopipettes with gold nanoparticles (AuNPs). AuNPs do not readily deposit on the glass surface of nanopipettes and hence an adhesion layer is required. For this purpose, self-assembled monolayers of (3-aminopropyl)triethoxysilane[11] and poly(L-lysine) films[8] have been utilized. Although they both lead to a sufficiently dense coating of AuNPs for SERS, the surface pattern is not uniform and often coupled with severe surface nanoparticle aggregation (see Figure 1 in ref [11] and Figure 3 in ref [8]). Similar SERS nanoprobes have been constructed by decorating the surface of pulled nanofibers with a film of silver islands using sputtering[7] and by a method that utilizes corona discharge to synthesize nanoparticles locally on the tip of the fibers,[12] but they are uncontrolled processes and lead to irregular nanoparticle coatings. In SERS, such irregularities of the substrate are considered to be the major reason for poor data reproducibility and sensor stability.

Block copolymer (BCP) thin films are suitable templates for the ordered deposition of nanoparticles.[13-16] Their self-assembled nanostructures project a surface pattern that can be used as templates to guide the deposition of nanoparticles or their precursors in

particular patterns (Figure 4.1, left). However, while the BCP templating approach has been well established on flat surfaces, it remains a challenge on highly curved surfaces. In fluid coatings of these types of substrates, such as small fibers and wires, the substrate curvature significantly depresses the film thickness.[17] Spatz and coworkers have used block copolymer micelles to coat fibers and they achieved uniform coatings down to diameters as small as 25 μm, but this came at the price of increasingly high, and eventually impracticable, withdrawal speeds.[18] Even when such films form, they tend to be unstable and break up into droplets that can be related to what is known as the Plateau-Rayleigh instability.[19] For example, to achieve tip-enhanced Raman spectroscopy (TERS), Zito *et al.* dip-coated AFM tips with BCP micellar films, but only achieved islands of coating on the surface.[20]

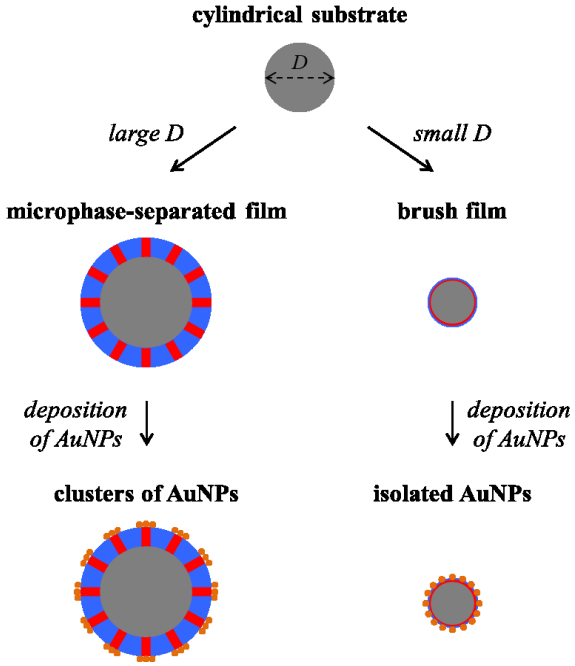

Figure 4.1. Two types of BCP thin film templates for the deposition of AuNPs on curved surfaces, where the red and blue colors indicate domains of two incompatible blocks. Left, thicker BCP film with microphase-separated domains can form on low-curvature surfaces, leading to a well-ordered deposition of AuNPs, shown here in the form of small clusters for AuNP sizes that are much smaller than the block domains (red) on which the AuNPs selectively deposit. Right, nanothin BCP brushlike film form by adsorption on high-curvature surfaces, leading to monolayer arrays of well-dispersed AuNPs.

We have recently demonstrated, using a polystyrene-*b*-poly(4-vinylpyridine) (PS-*b*-P4VP) diblock copolymer, that it is possible to obtain dense and well-dispersed deposition of citrate-stabilized AuNPs on glass nanofibers of diameters down to 200 nm using brushlike BCP films as templates (Figure 4.1, right), obtained simply by dipping the nanofiber in a THF solution of PS-*b*-P4VP.[21] Due to the high curvature, the BCP films do not show microphase-separated surface patterns as typically observed on flat surfaces for the solution concentrations employed, but instead are in the form of a nanothin BCP coating, where the P4VP block forms a stable wetting or anchoring sublayer on the substrate due to multiple noncovalent bonds with the OH groups on the glass surface and the PS block forms a brushlike overlayer. This brush template led to a one-order-of-magnitude improvement in the SERS performance for 4-mercaptobenzoic acid compared to the same AuNP-decorated nanofibers without the template. Furthermore, as a nanosensor, it could detect simultaneously the co-release of the neurotransmitters, dopamine and glutamate, from living mouse brain dopaminergic neurons with a one-order-of-magnitude greater sensitivity compared to APTES-coated nanofibers, on which the AuNPs are much more aggregated.[21] We also demonstrated that optical fibers with brush-layer templates for AuNP deposition have enhanced performance as LSPR (localized surface plasmon resonance) biosensors, specifically 3-fold better sensitivity compared to standard AuNP deposition methods using (3-aminopropyl)trimethoxysilane (APTMS) and polyelectrolytes.[22]

We subsequently investigated AuNP deposition on the BCP brush films on flat silicon substrates, where they can be obtained by dip-coating the substrates in very dilute BCP solutions. We found the same characteristics of dense, mainly unaggregated AuNP arrays – i.e. non-close-packed arrays – for a range of AuNP diameters extending from 10 to almost 100 nm.[23] These characteristics are, moreover, insensitive to the degree of PS coverage, which is controlled by the time of exposure to the BCP solution. This was attributed to PS block rearrangement during exposure to the aqueous AuNP colloid to the extent needed to allow electrostatic interactions between the negatively charged AuNPs and the (protonated) P4VP segments. BCP brush-layer templates thus provide a simple method for obtaining non-closed-packed NP arrays, which are useful for a variety of potential applications, as indicated in ref [24].

Here, we investigate in detail the physicochemical phenomena of the formation of these films on highly curved surfaces. We will demonstrate the substrate curvature effect on BCP thickness and surface morphology over a wide range of diameters on pulled glass fibers dip-coated in THF solutions of PS-*b*-P4VP and the consequences on AuNP deposition on these films after incubation in aqueous AuNP colloids. The influence of BCP solution concentration, AuNP size and block molecular weights on the brush-layer templates will also be studied, and a comparison with a P4VP homopolymer and an analogous random block copolymer will be made. The findings will be of particular value to bottom-up nanofabrication where coating small cylindrical objects such as glass or carbon nanopipettes, optical fibers, free standing nanowires, and AFM tips with nanoparticles is desired.

4.3 Experimental

4.3.1 Materials

The poly(styrene-*b*-4-vinylpyridine) (PS-*b*-P4VP) diblock copolymers of various molecular weights and block compositions (Table 4.1), a PS-*s*-P4VP statistical copolymer (M_n = 93.9 kg/mol, M_w = 140.8 kg/mol, M_w/M_n = 1.5, P4VP content = 35 mol%) and a P4VP homopolymer (M_n = 15 kg/mol, M_w = 19 kg/mol, M_w/M_n = 1.25) were purchased from Polymer Source (Dorval, QC). The block copolymers are denoted as PS_x-*b*-$P4VP_y$ where the subscripts x and y indicate the average molecular weights of the PS and P4VP blocks, respectively. Tetrahydrofuran (THF, 99.99%), methanol (MeOH, 99.99%) and chloroform (99.99%) were purchased from VWR. Gold(III) hydrochloride trihydrate ($HAuCl_4 \cdot 3H_2O$, 99.9%) and trisodium citrate dihydrate (99%) were purchased from Sigma-Aldrich. All were used as received. Borosilicate glass rods of 1.1 mm in diameter and 10 cm in length were obtained from Sutter Instrument. Silicon wafers {1,0,0} were obtained from University Wafer and cut into rectangular 15 × 10 mm^2 pieces for use as flat substrates.

Table 4.1 Molecular characteristics of the PS-*b*-P4VP block copolymers (BCPs) used and the density of 20-nm AuNPs deposited on the BCP coatings at a fiber diameter of about 10 μm.

PS_x-*b*-$P4VP_y$	PDI	average M_W (kg/mol)			P4VP (wt %)	AuNP density (100 NP/μm^2)
		total	PS	P4VP		
PS_{20}-*b*-$P4VP_{29}$	1.15	49.3	19.9	29.4	59.6	6.2 ± 0.2
PS_{41}-*b*-$P4VP_{20}$	1.18	61	41	20	32.8	6.0 ± 0.3
PS_{84}-*b*-$P4VP_{18}$	1.10	101.5	84	17.5	17.2	5.3 ± 0.3
PS_{72}-*b*-$P4VP_{35}$	1.09	107	72	35	32.7	6.0 ± 0.2
PS_{120}-*b*-$P4VP_{20}$	1.18	140	120	20	14.3	5.3 ± 0.2
PS_{252}-*b*-$P4VP_{43}$	1.09	295	252	43	14.6	5.7 ± 0.2

4.3.2 Glass fibers

The glass rods were pulled into nanofibers using a laser-based Sutter P-2000 pipette puller (Sutter Instrument) with the following two-line program, where the parameters given are instrument specific: LINE 1) Heat: 280, Filament: 3, Velocity: 15, Delay: 145, Pull: 20; LINE 2) Heat: 500, Filament: 0, Velocity: 15, Delay: 128, Pull: 200. They were cleaned with ethanol for 5 min, dried in air, then immersed in a piranha solution at 90 ºC for 60 min, rinsed well with Milli-Q water, and finally dried under vacuum at room temperature for an hour.

4.3.3 Block copolymer solution preparation and dip-coating

BCP solutions of 5 and 20 mg/mL were prepared by dissolving 50 and 200 mg of PS-*b*-P4VP, respectively, in 10 mL of THF in scintillation vials. The solutions were capped and sealed with parafilm and stirred at 30–40 ºC overnight. They were then filtered successively through a 0.45 µm and a 0.2 µm PTFE filter (Chromspec). BCP solutions of 1.0, 0.1, and 0.05 mg/mL were prepared by dilution from the 5 mg/mL stock solution. A P4VP homopolymer solution and a PS-*s*-P4VP statistical copolymer solution were prepared at 0.05 mg/mL concentration in THF/MeOH (1:1 v:v) and THF, respectively, noting that the P4VP used is not soluble in pure THF.

The substrates were dipped into these solutions by the dip-coating procedure under ambient conditions (~21 ºC), using the dip-coater of a KSV3000 Langmuir-Blodgett instrument. The dip-coater was enclosed in a plexiglass box (15x15 cm^2, 20 cm high) with holes at the top and bottom to accommodate the support. The dip-coating procedure consisted of vertically immersing the substrates into the solutions at a rate of 5 mm/min, followed by a pause of 2 min (except when the effect of immersion time was studied), and then withdrawal from the solution at controlled rates between 0.1 and 80 mm/min. The coated substrates were left to dry in covered containers at room temperature for at least 30 min before AuNP deposition.

4.3.4 AuNP synthesis and deposition

Several batches of citrate-stabilized gold nanoparticles (AuNPs) of 10-12 nm diameter were synthesized using the Turkevich-Frens method.[25,26] The same method with a doubled gold(III) chloride trihydrate to trisodium citrate dihydrate weight ratio produced AuNPs with an average diameter of 20 nm. The pH values of these colloidal suspensions were 5.5-6.0. Citrate-stabilized AuNPs of larger diameters were synthesized following the kinetically controlled seeded growth method developed by Puntes *et al.*, giving average diameters of 6, 32, 52, 78 and 94 nm at the 0^{th} (seeds), 3^{rd}, 6^{th}, 8^{th} and 10^{th} growth steps, respectively.[27] These larger AuNPs were centrifuged from desired volumes of the original colloidal suspensions and then were redispersed into Milli-Q water of the same volume. Since the pH of these suspensions was initially above 7, it was adjusted to be between 4.5

and 5.0 by dropwise addition of a 1 M hydrochloride acid aqueous solution. All average diameters were determined from UV-visible spectra using the method of Haiss *et al*. (Figure 4.S1).[28] The AuNP suspensions were stored at 4 ºC, protected from light, and used within a month.

AuNP deposition was accomplished by immersing the polymer-coated (and occasionally bare) glass fibers or silicon wafers in the desired AuNP colloidal suspension at room temperature for times between two hours and overnight (no difference was observed using the different times), followed by immersion in Milli-Q water several times and drying in air.

4.3.5 Scanning electron microscopy (SEM)

The AuNP-coated glass fibers were examined using a JEOL JSM-7400F (JEOL Ltd, Tokyo, Japan) field-emission scanning electron microscope operated at 1.5 kV and 20 μA. Analyses of the AuNP sizes, size distributions and densities were done using ImageJ (http://imagej.nih.gov/ij/features.html).

4.3.6 Atomic force microscopy (AFM)

AFM images were obtained in tapping mode with a Multimode microscope and a Nanoscope III controller (Digital Instruments), operated under ambient atmosphere, using Bruker AFM probes (TESPA-V2 model, spring constant 42 N/m, oscillation frequency 320 kHz, tip radius ≤ 10 nm).

4.4 Results and discussion

4.4.1 Effect of curvature on BCP coatings of pulled fibers

To demonstrate the effect of substrate curvature on BCP coatings obtained by the dip-coating procedure, pulled glass fibers serve as convenient substrates. The pulling process leads to a varying cylindrical substrate diameter ranging from millimeters to submicrons, while maintaining a relatively uniform and smooth glass surface with a root-mean-square roughness of about 0.9 nm (Figure 4.S2, slightly larger than the 0.6 nm measured for polished silicon wafers). Thus, dip-coating a single pulled glass fiber provides

a BCP coating associated with a wide range of substrate curvatures with this being the only variable.

Figure 4.2 illustrates what is observed by SEM after AuNP deposition on the BCP-coated pulled fiber at four different diameters. That at 1.1 mm corresponds to an unpulled region of the fiber where the curvature is the lowest, that at 50 μm is located in the neck region that developed during pulling, and the two at 20 and 7 μm are located in the region where the curvature is very high. For the BCP coating, the fiber was withdrawn at a rate of 0.5 mm/min (corresponding results for 80 and 10 mm/min are shown in Figures 4.S3 and 4.S4) from a 20 mg/mL THF solution of PS_{41}-*b*-$P4VP_{20}$. As will become clear in what follows, the use of small AuNPs (10-12 nm in diameter) facilitates the assessment of the underlying form of the BCP coating.

Starting with the largest diameter (Figure 4.2a), the SEM images show finite AuNP clusters dispersed in a quasi-hexagonal pattern. This pattern resembles what was observed on similarly treated flat surfaces, where the BCP itself forms a quasi-hexagonal surface pattern of P4VP dots within a PS matrix, reflecting a spherical film morphology,[15,29] and several AuNPs are deposited via electrostatic interactions on each P4VP dot because the size of the former is much smaller than the size of the latter.[23,30] The dot surface morphology of the BCP (without AuNP deposition) on this part of the fiber was confirmed by AFM, with an average micellar dot size of 25-30 nm in diameter (Figure 4.S5) that is much larger than the 10-12 nm AuNPs.

It is expected that the BCP film thickness at 1.1 mm is reduced compared to that on a flat surface dip-coated under the same conditions, given the known dependence of the thickness of fluid films on substrate curvature.[17,31] In its simplest form, this thickness decreases linearly with decreasing diameter (increasing curvature) of cylindrical surfaces. This implies that, for the solution concentration and withdrawal rate used for Figure 4.2 and considering that the average BCP film thickness on a flat surface under these conditions can be estimated to be about 250 nm, the thickness at the fiber diameter of 1.1 mm should be reduced to about 77 nm (See estimation in SI). This thickness on flat surfaces allows the formation of BCP films giving rise to surface patterns.[23,29]

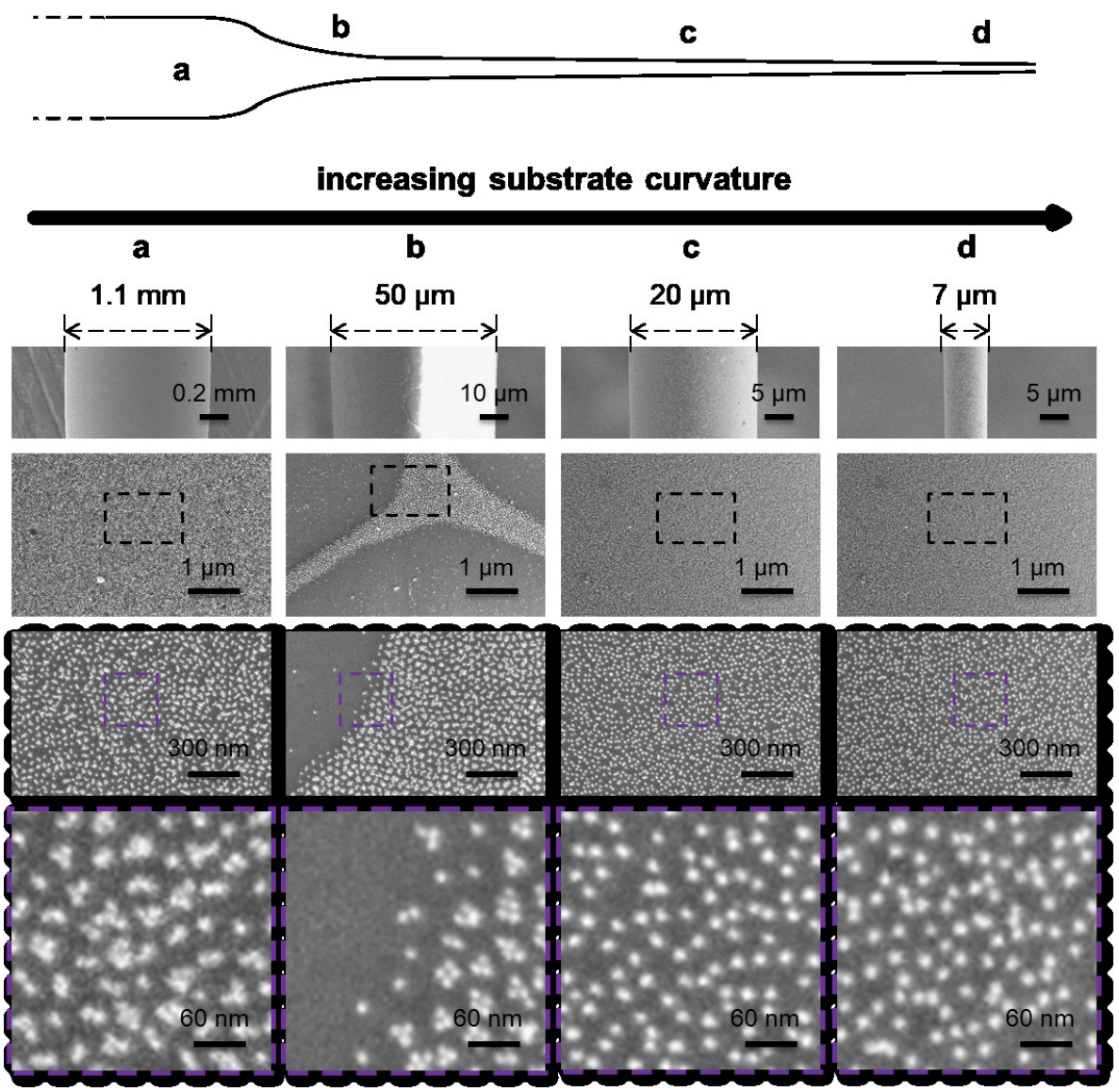

Figure 4.2. Curvature effect on AuNP deposition onto a nanofiber coated by PS_{41}-*b*-$P4VP_{20}$. SEM images of various magnifications, indicated by the scale bars, showing the AuNP patterns obtained, along with schematically modeled templated morphologies, at diameters corresponding to (a) the unpulled part of the fiber, (b) the neck region, and (c) and (d) the highly pulled fiber region. The fiber was imaged after the deposition of AuNPs of 10-12 nm in diameter on the BCP film template obtained by the dip-coating procedure using a withdrawal rate of 0.5 mm/min and a 20 mg/mL THF solution.

The dependence of film thickness on the curvature would explain what is observed in the neck region of the pulled fiber, which is illustrated in Figure 4.2b for diameters around 50 μm. Here, a region covered with AuNP clusters like at the 1.1-mm diameter appears as a dewetted film relative to regions where there are a few isolated AuNPs. This pattern is reminiscent of dewetted BCP thin films on flat surfaces, obtained when the average film thickness is insufficient for forming a full layer of BCP nanostructures.[29,32,33] The above calculation for the 50-μm diameter gives an estimated film thickness of about 3.5 nm (Figure 4.S6). This is within the range of thicknesses that, on flat surfaces for the same BCP, results in a partial dot pattern like is observed here, where the micellar layer dewets relative to the adsorbed layer.[23] Since dewetting by nature has a random component, it occurs on the nanofiber over a range of diameters, notably from about 100 to 40 μm for the system and dip-coating conditions used (Figures 4.S8 and 4.S9).

It is of interest to verify if the BCP solution concentration and the dip-coating withdrawal rate affect the diameter range of dewetting. As mentioned above, decreasing the BCP solution concentration decreases the film thickness. This effect should move the dewetting range to higher diameters. In practice, the random nature of dewetting, as well as the possibility of some downward flow of the dewetting regions that may be subject to Plateau-Rayleigh instabilities (a typical phenomenon for small-diameter fluid flow[19] and that we sometimes observed, as illustrated in Figure 4.S10), makes the demarcation of the upper and lower diameter limits of dewetting difficult to pinpoint. Thus, when comparing a BCP solution concentration of 5 mg/mL with the 20 mg/mL described above (0.5 mm/min withdrawal rate), only the lower-diameter limit was noted to increase as expected, to about 70 μm for the more dilute solution (Figure 4.S11) compared to 40 μm for the more concentrated solution (Figure 4.S9). When modifying the substrate withdrawal rate from the 20 mg/mL solution, a clear effect on the upper diameter limit could be observed (Figure 4.S8), changing from about 100 to 400 μm back to 110 μm for withdrawal rates of 0.5, 10 and 80 mm/min, respectively. This trend concurs with the V-shaped dependence of film thickness on withdrawal rate, established previously, and related to two different dip-coating regimes, the capillarity and draining regimes, for which the film thickness decreases and increases, respectively, with dip-coating withdrawal rate.[29,34]

At diameters below about 40 μm and extending to less than 100 nm at the fiber tip, dense and well-dispersed surface coverage by mainly isolated AuNPs is observed (Figures 4.2c, 4.2d, and 4.S9). At these diameters, the average film thickness is such that there is no possibility of micelle formation. Instead, as explained in our preceding papers,[21,23] the nanofiber is coated with just a nanothin brush-like layer, composed here of a P4VP wetting underlayer in contact with the substrate via multiple hydrogen-bonding interactions with the OH groups on the glass surface and a PS overlayer that reduces the interfacial energy with air.[29,35,36] In the dip-coating process, such a layer has been shown to adsorb onto the substrate during the period that it is immersed in the BCP solution, whereas additional material leading to patterned films is deposited on this layer as the substrate is being withdrawn from the solution.[32-34] Thus, for diameters below about 40 μm in the present case, dip-coating takes places without the deposition of additional material during withdrawal of the fiber from the BCP solution. This also implies that the brush layer, since it is adsorbed before substrate withdrawal, should be unaffected by the withdrawal rate. A film thickness of approximately 3 nm was measured at a fiber diameter of about 10 μm from an AFM height profile across a tiny region where the film was erased by an AFM tip in contact mode,[23] similar to dry brush layer thicknesses measured on flat surfaces.[23,32,33,36,37]

The effect of substrate curvature on the film thicknesses and patterns on BCP-coated pulled fibers parallels what we had found for the effect of solution concentration on BCP-coated flat substrates, for which the film thicknesses and surface morphologies could be conveniently measured by ellipsometry and AFM, respectively.[23] Specifically, sufficiently dilute BCP solutions led to the deposition of only the adsorbed layer, with no additional material deposited during substrate withdrawal. The subsequent deposition of 10-12-nm AuNPs follows the same trend with decreasing BCP solution concentration as observed in the present paper with decreasing fiber diameter, notably there are groups of finite AuNP clusters when the films are thick enough (greater than 15±2 nm) to allow the complete formation of BCP micelles and a dense array of mainly isolated AuNPs when only the brushlike BCP layer is present (for thicknesses below 4 nm), with a transition region of dewetted micellar films in between.

4.4.2 Investigation of parameters governing AuNP deposition on BCP brush-coated fibers

As mentioned in the Introduction, for potential applications such as nanobiosensors for SERS optophysiology, it is the small submicron diameters near the nanofiber tip that is most relevant.[21] The above results and analyses have shown that dipping of the pulled fibers in a BCP solution leaves only a nanothin coating of an adsorbed BCP layer at these diameters. They have also shown that the subsequent dipping of the nanofiber into an aqueous colloidal solution of small AuNPs gives a dense and well-dispersed monolayer array of the AuNPs on this adsorbed layer. In the following sections, we will concentrate on the range of diameters of interest where there is only the adsorbed BCP brushlike layer. These sections focus on whether or not the BCP solution concentration, the size of the AuNPs, and other block molecular weights influence the AuNP deposition on the adsorbed coating. These parameters are of potential use for fine-tuning the AuNP-decorated nanofiber in practical applications.

4.4.2.1 Effect of BCP solution concentration

Literature studies on adsorbed BCP layers on flat substrates indicate that their (equilibrium) thickness depends, among other parameters, on solution concentration.[38-40] Decreasing solution concentration leads to thinner films, and, eventually, partial coverage by the block exposed to air. Decreasing the adsorption time before equilibrium is reached has a similar effect.[38-40] Possibly, the thickness of the adsorbed film is affected as well by the surface curvature associated with the nanofiber diameter.[41-43] If so, the above data show no apparent effect of fiber diameter on the AuNP adsorption, which is the same along the whole fiber length of the brush-only region. Furthermore, we did not observe significant differences in the AuNP deposition density or pattern on the brush-only region when comparing solution concentrations between 0.1 and 5 mg/mL (Figure 4.S12) nor when comparing substrate immersion times between 30 and 120 s (Figure 4.S13). This concords with what we observed for flat substrates, for which we showed that equilibrium BCP brush-layer adsorption was reached by about 100 s of substrate immersion, but the AuNP deposition characteristics (using 30-nm diameter AuNPs) were the same for all immersion

times between 10 and 120 s.[23] This can be rationalized, when the PS overlayer fully covers the P4VP wetting layer, by its local displacement when exposed to the acidic aqueous AuNP suspension to allow the negatively charged citrate-stabilized AuNPs to interact electrostatically with the positively charged P4VP (partly protonated due to the acidic pH).[44,45] If the PS overlayer is not complete, then some P4VP is already locally exposed, and little or no displacement is necessary. The overall effect is the same whether or not the PS completely covers the P4VP after exposure to the BCP solution. From a practical perspective, the insensitivity of AuNP deposition to the details of the adsorbed layer, at least within the limits investigated, simplifies the fabrication of nanofibers for potential applications.

4.4.2.2 Effect of AuNP size

Besides the small 12-nm AuNPs used above, we showed that 52-nm AuNPs can similarly be deposited on BCP brush layer-coated nanofibers.[21] Figure 4.3 compares the deposition of AuNPs of several sizes, ranging from 20 to 94 nm in diameter, in the nanofiber tip region. For all except the largest, monolayer arrays of well-dispersed and dense AuNPs are obtained (Figure 4.3a-e). These patterns extend as well to higher nanofiber diameters, at least to about 30 μm, as illustrated in Figure 4.4 for 78-nm AuNPs at fiber diameters ranging from 8 to 25 μm and in Figures 4.S14-18 for the other AuNP sizes. The lower magnification SEM images indicate that the coating is uniform along the entire part of the fiber shown with no evidence of dewetting, partial coverage or Plateau-Rayleigh instability. The higher resolution SEM images clearly demonstrate that the AuNPs are well dispersed in a dense monolayer array. The accompanying AuNP size distribution histograms (in black), which are narrow and symmetric with no significant high-diameter tail, are indicative of the good dispersion of the AuNPs with little aggregation. In the case of the 94-nm AuNPs, although the AuNPs are well dispersed in dense arrays at higher fiber diameters (8-25 μm; Figure 4.S18), their coverage tends to be incomplete and irregular, even with some aggregation, near the nanofiber tip (Figure 4.3f), resulting in a low coating success rate of only 10-20 % (Figure 4.S19), as opposed to over 75% found for 52-nm AuNPs[21] (the reproducibility of the other sizes were not systematically determined).

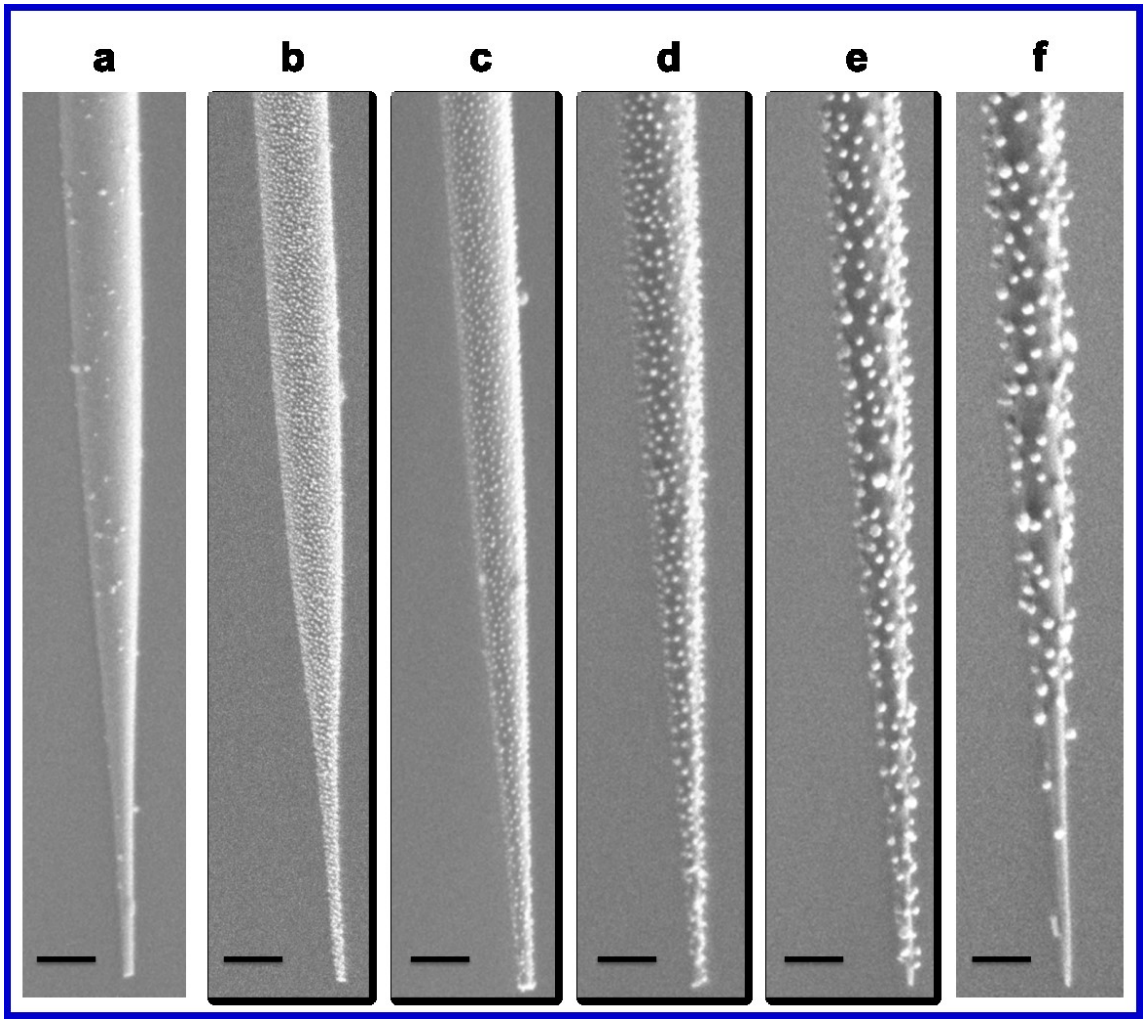

Figure 4.3. Monolayers of AuNPs on (a) a bare nanofiber and (b-f) nanofibers coated with PS41-b-P4VP20 brush-layer templates. SEM images of the nanofibers for deposited AuNPs of various diameters: b, 20 nm; a and c, 32 nm; d, 52 nm; e, 78 nm; f, 94 nm. Scale bars represent 500 nm. The brush-layer templates were dip-coated at 40 mm/min from a 0.05 mg/mL THF solution of the BCP.

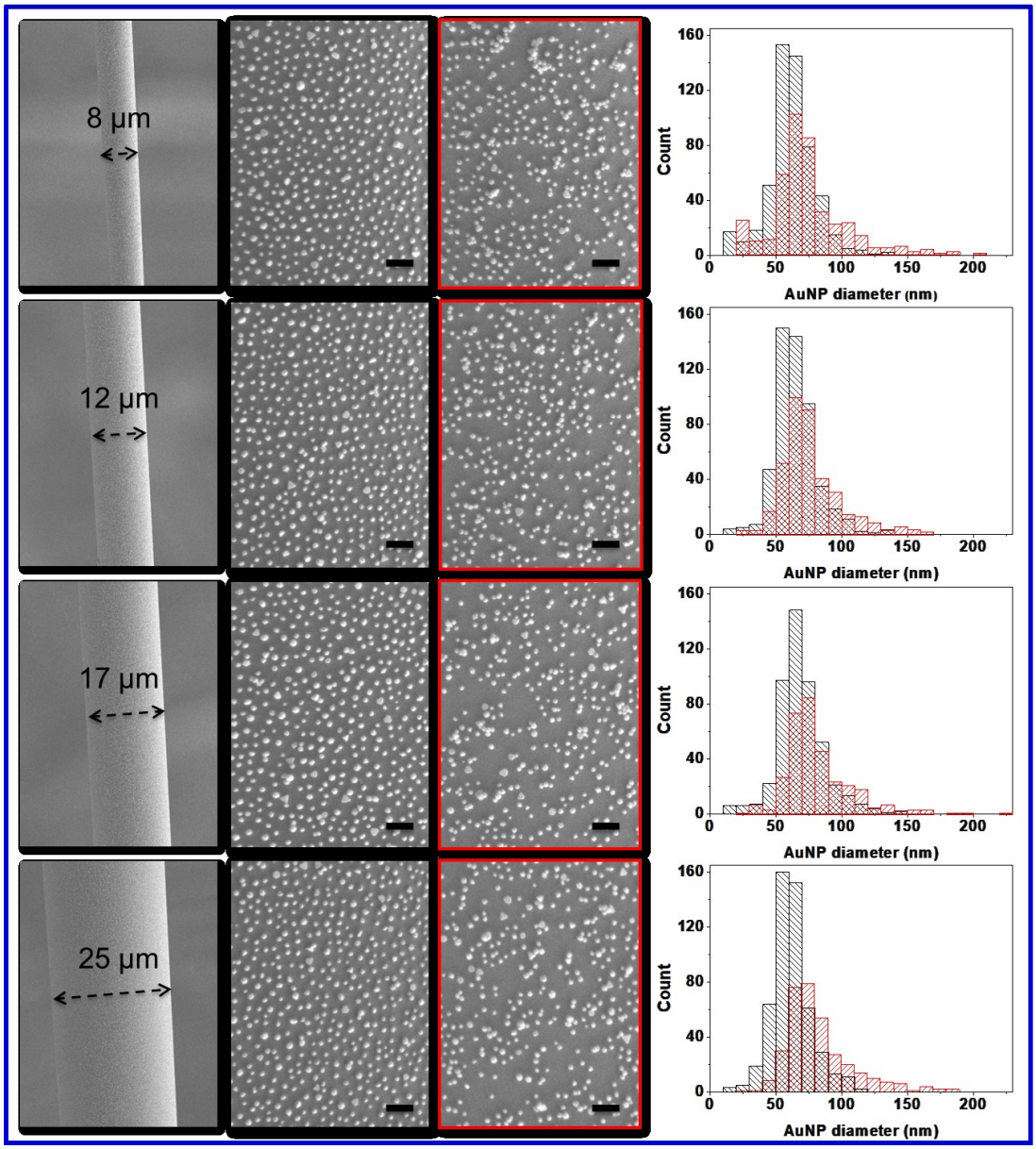

Figure 4.4. Deposition of 78-nm AuNPs on pulled fibers using PS_{41}-*b*-$P4VP_{20}$ and $P4VP_{20}$ film templates. 1st column (from left to right), low magnification SEM images showing macroscopically uniform coatings of AuNPs on the fibers at diameters from 8 to 25 µm; 2nd and 3rd columns, high magnification SEM images showing the AuNP pattern on BCP (2nd column) and homopolymer (3rd column) film templates, with scale bars of 200 nm; 4th column, AuNP size distribution histograms whose colors correspond to image outlines in the 2nd (black) and 3rd (red) columns.

Figure 4.5a shows that the surface AuNP density is constant with fiber diameter in the range between 7 and 25 μm for all AuNP sizes investigated. The density at lower fiber diameters seems to be the same qualitatively, but the highly curved surface makes a quantitative density evaluation difficult. Figure 4.5a also shows that changing the substrate withdrawal rate from the BCP solution (e.g., 0.5, 1, 10, 40 and 80 mm/min) or the polymer solution concentration (e.g., 20, 5 and 0.05 mg/mL) has no effect on the AuNP surface density for any of the AuNP diameters. The insensitivity to withdrawal rate is to be expected when only a brush layer adsorbed in solution is present, with no additional material deposited during withdrawal. The insensitivity to the solution concentration indicates that what was found above for the 12-nm AuNPs extends to the larger AuNP sizes. Furthermore, while the surface AuNP density drops drastically with increasing AuNP size (Figure 4.5b), the surface coverage (AuNP number density times AuNP circumferential area times 100%) is constant with size at 19±2% for all but the 94-nm AuNPs for which the coverage is a little lower at about 16% (Figure 4.5c). These values are somewhat better than the 10-15% observed with brush templates on flat silicon substrates.[21] The constancy of the AuNP surface coverage with AuNP size implies that the fractional PS coverage is also constant with AuNP size, which is as might be expected for a given PS-P4VP if the AuNP coverage is close to maximal in the presence of the PS and if there is no significant reorganization on the level of the P4VP sublayer. Possibly, the higher surface coverage on the highly curved surface reflects the likelihood that the PS brush is more splayed on this surface so that there is more room for the AuNPs to squeeze in.[41]

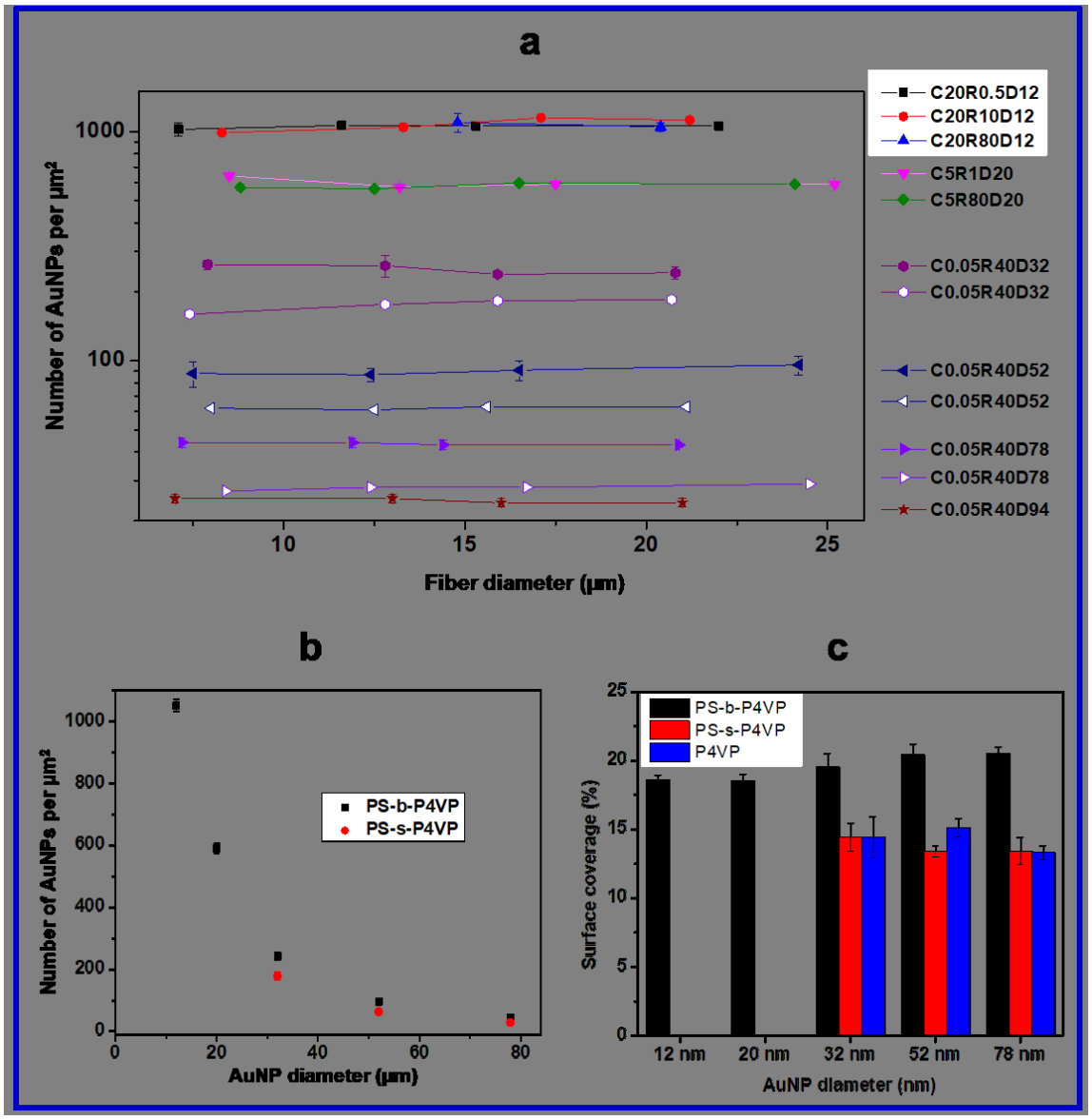

Figure 4.5. Dependency of surface nanoparticle density on AuNP size, fiber diameter, polymer solution concentration, dip-coating rate and copolymer type. a, surface AuNP density versus fiber diameter for AuNPs of various diameters (D, nm) deposited on fibers using PS_{41}-*b*-$P4VP_{20}$ (solid symbols) and PS-*s*-P4VP (open symbols) film templates dip-coated at various dip-coating rates (R, mm/min) from different polymer solution concentrations (C, mg/mL); b and c, plots of average AuNP density and AuNP surface area coverage, respectively, versus AuNP size.

4.4.2.3 Comparison with P4VP homopolymer and statistical PS-s-P4VP copolymer coatings

P4VP homopolymer coatings on flat substrates are also capable of adsorbing AuNPs.[21] Thus, their comparison with the BCP brush-coated nanofibers is of interest. Figure 4.6 shows the deposition of AuNPs of three different sizes near the nanofiber tips using a P4VP homopolymer that has a similar molecular weight to that of the P4VP block in the diblock copolymer used above. Although there is often dense deposition of the AuNPs, it tends to suffer severely from irregularities in the form of incomplete coverage and AuNP aggregation as well as from irreproducibility, at least for 52 and 78 nm AuNPs. Greater AuNP aggregation can also be observed in the higher diameter range of 8-25 μm, as shown in Figures 4.S15, 4.S16 and 4.4 for AuNP diameters of 32, 52 and 78 nm, respectively, as indicated also by the longer tail at higher AuNP sizes in the accompanying histograms and by the lower AuNP surface coverage compared to the PS-*b*-P4VP coating (Figure 4.5c). Smaller AuNPs (32 nm in the figures) show less of a difference between homopolymer and BCP coatings.

A random PS-*s*-P4VP copolymer of similar P4VP content to the block copolymer was also tested as a fiber coating for the deposition of several AuNP sizes (Figures 4.6, 4.S20-22). In this case, while the AuNP deposition near the nanofiber tip (Figure 4.6) suffered from incomplete coverage and aggregates like that with the homopolymer coating, at higher fiber diameters in the 8-25 μm range (Figures 4.S20-22) it showed improved coverage and uniformity compared to the homopolymer coating, and is largely free from AuNP aggregation with size distribution histograms similar to the those of the block copolymer template. On the other hand, the AuNP density on the statistical copolymer coating is less than on the BCP coating (Figures 4.5b and 4.5c).

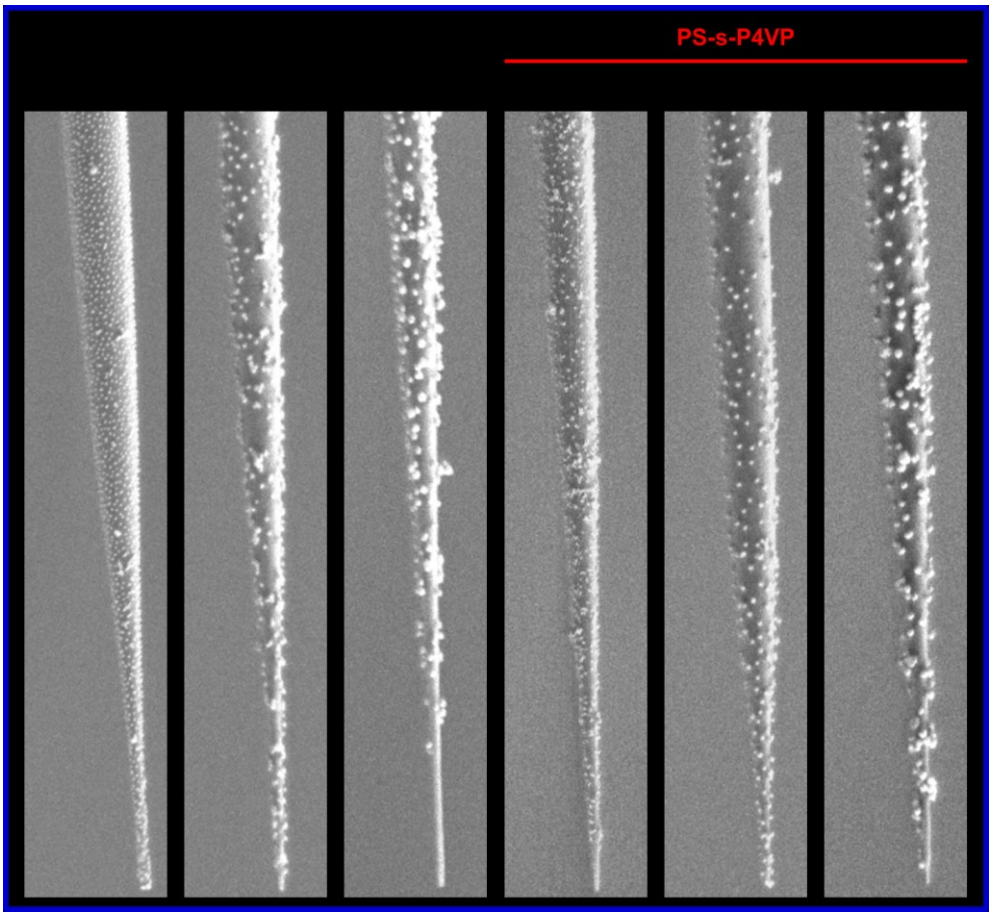

Figure 4.6. Deposition of AuNPs on nanofibers coated with P4VP homopolymer and PS-*s*-P4VP statistical copolymer. SEM images for AuNPs of the sizes indicated, where the coatings were adsorbed from 0.05 mg/mL THF/EtOH and THF solutions, respectively (dip-coating withdrawal rate 40 mm/min). Scale bars represent 500 nm.

4.4.2.4 Effect of block molecular weights

The absolute and relative block molecular weights are known to affect the adsorption of block copolymers at liquid-solid interfaces.[39,46,47] This raises the question as to whether AuNP deposition is affected by these factors. To investigate this, SEM images of AuNP deposition on pulled fibers coated by the six BCPs listed in Table 4.1 were examined and the AuNP densities determined. These block copolymers cover a wide range of total molecular weights from about 50 to 300 kg/mol and P4VP weight fractions from 14 to 60%. For all but one, P4VP is the minor block. The fibers were dip-coated from 5

mg/mL BCP solutions at withdrawal rates of 1 and 80 mm/min. AuNPs of 20 nm in diameter were deposited. In general, all six AuNP-decorated BCP coatings show dense deposition of well-dispersed AuNPs at the fiber diameters characterized by the brush layer (Figures 4.6 and 4.S22-S27). Again, no significant difference was noted between the two dip-coating rates tested (1 and 80 mm/min) nor at the different fiber diameters between 6 and 26 μm (Figure 4.S28). On the other hand, the AuNP densities range between about 530 and 630 AuNP/μm^2, depending on the particular block copolymer used. To verify if there is a dependence on a molecular weight-related parameter, the average density at several fiber diameters between 6 and 26 μm were plotted as a function of total BCP molecular weight, of the molecular weight of each block, of the P4VP weight percent, and of the P4VP/PS weight ratio (Figures 4.7 and 4.S29). Of these, the AuNP density was found to generally increase with increasing P4VP weight fraction (Figure 4.7), whereas no monotonic relationship with total molecular weight or absolute molecular weight of component blocks was apparent (Figure 4.S29a, b, and c). Thus, although PS_{41}-b-$P4VP_{20}$ and PS_{140}-b-$P4VP_{20}$ have the same absolute P4VP length, the much longer PS block in PS_{140}-b-$P4VP_{20}$ determines a much smaller P4VP weight fraction, and hence a smaller AuNP density. A possible reason for this is that the PS layer is thicker when the P4VP weight fraction or P4VP/PS ratio is lower, which could decrease local PS mobility during exposure to the AuNP colloidal suspension and thereby tend to diminish AuNP access to the P4VP.

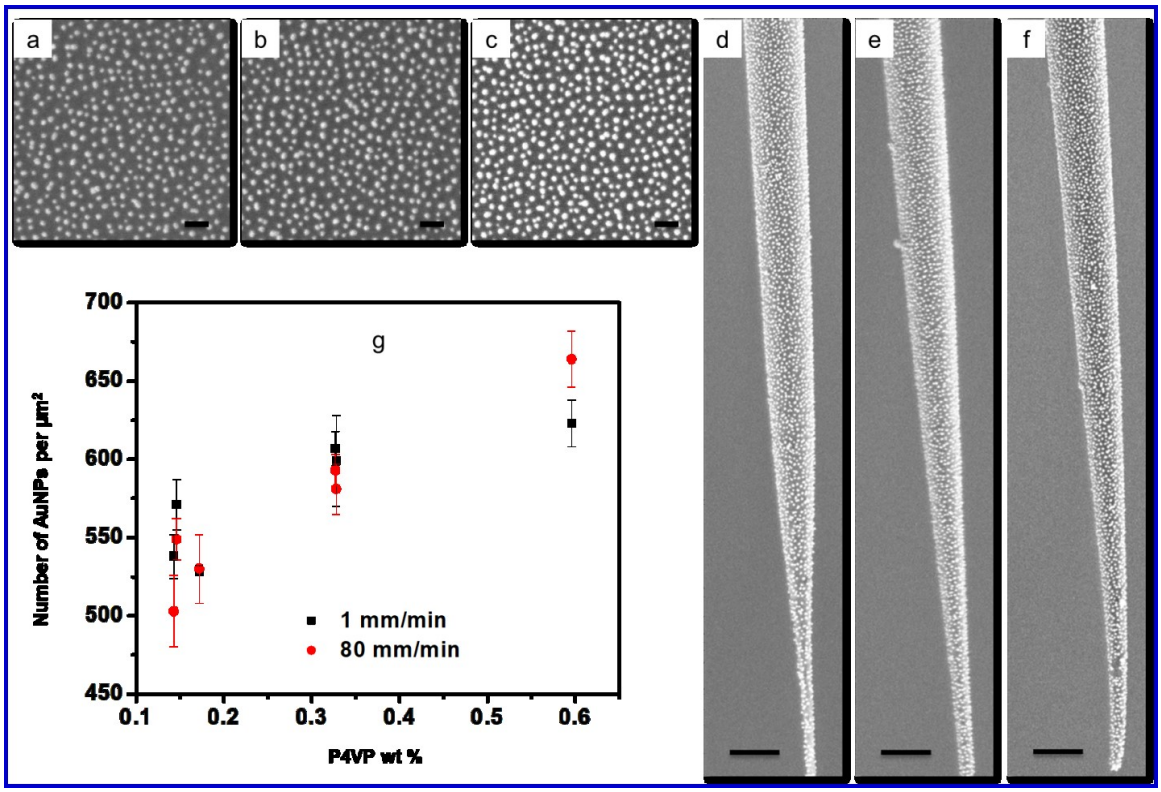

Figure 4.7. Dependence of surface nanoparticle density on P4VP weight fraction in the BCP. SEM images of 20-nm AuNP deposition on BCP-coated fibers at a fiber diameter of 8 µm (a, b and c) and at the fiber tip (d, e and f): PS_{120}-*b*-$P4VP_{20}$ (a and d), PS_{41}-*b*-$P4VP_{20}$ (b and e) and PS_{20}-*b*-$P4VP_{29}$ (c and f). Scale bars represent 100 nm in a, b and c and 500 nm in d, e and f. Average surface AuNP density versus P4VP weight fraction for various BCPs and two dip-coating rates (g).

4.5 Conclusions

Nanothin BCP films are suitable templates for the deposition of well-dispersed nanoparticles on nanofibers, thus constituting an efficient bottom-up approach for constructing SERS endoscopic probes. We showed, using THF solutions of PS-*b*-P4VP, that the substrate curvature strongly affects the film thickness of the dip-coated BCP films. At low curvature, BCP thin films with dot patterns of P4VP micelles in a PS matrix were obtained, leading to small clusters of AuNPs adsorbed onto the P4VP dots after immersion

of the BCP-coated fiber into a colloidal suspension of small citrate-stabilized AuNPs. At high curvature, only nanothin brush layer films were obtained by adsorption onto the glass substrate during immersion of the fiber in the BCP solution, where the P4VP is the wetting layer and PS a brushlike overlayer. When exposed to the AuNP suspension, dense and well dispersed AuNPs adsorb to the brush layer, where AuNP aggregation is prevented by the PS chains. Due to their formation mechanism by adsorption, the nanothin films are very robust against changing experimental conditions, such as polymer concentration, dip-coating rate and dipping time. The dense and uniform deposition of well-dispersed AuNPs onto the brush coating applies to a range of AuNP sizes (investigated for 10-100 nm in diameter). In contrast, on P4VP homopolymer and random PS-P4VP copolymer film templates, AuNP deposition suffered from greater aggregation and density variations, particularly for larger AuNP sizes. The average interparticle spacing of the AuNPs on the BCP brush layer showed a dependence on the P4VP weight content.

4.6 Supporting information

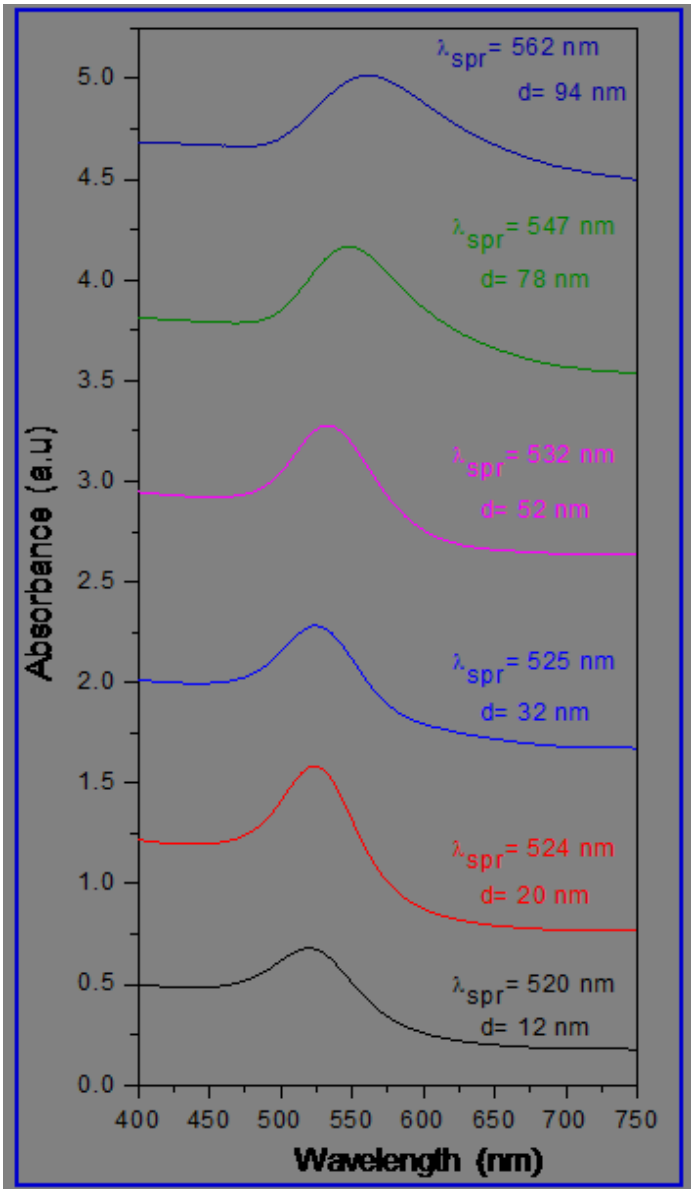

Figure 4.S1. Characteristics of the AuNPs synthesized. UV-visible spectra of the aqueous AuNP suspensions after pH adjustment, the peak or surface plasmon resonance wavelength, λ_{spr}, and the derived AuNP diameter, d.

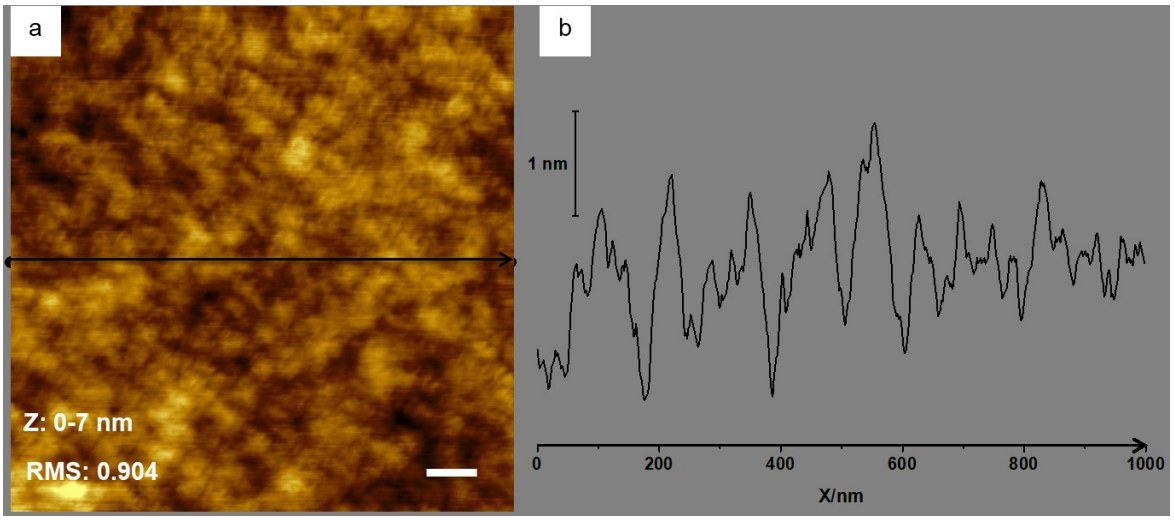

Figure 4.S2. Surface roughness of a glass fiber. a) AFM height image of the surface of a pulled glass fiber at a fiber diameter of about 10 µm. Z is the height scale, RMS is the root-mean-square roughness, and the scale bar represents 100 nm. b) Height profile corresponding to the line drawn in a. From the height profile, the surface has a global roughness within 2 nm and local roughness within 0.5 nm, resulting in a RMS of about 0.9 nm.

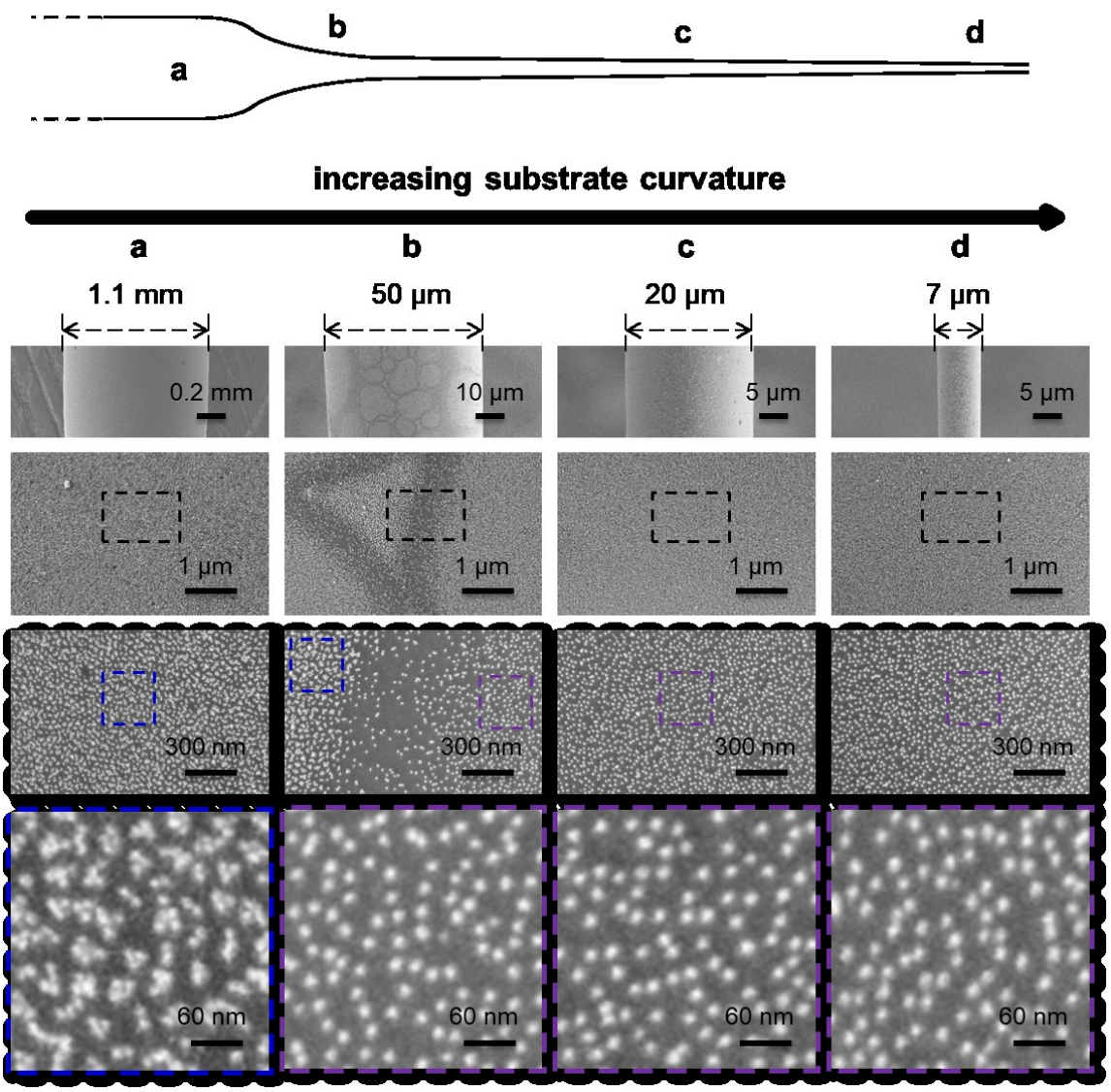

Figure 4.S3. SEM images of various magnifications, indicated by the scale bars, showing the AuNP patterns obtained at diameters corresponding to (a) the unpulled part of the fiber, (b) the neck region, and (c) and (d) the pulled fiber region. The fiber was imaged after the deposition of AuNPs of 10-12 nm in diameter on a PS_{41}-b-$P4VP_{20}$ film template obtained by the dip-coating procedure using a withdrawal rate of 80 mm/min and a 20 mg/mL THF solution.

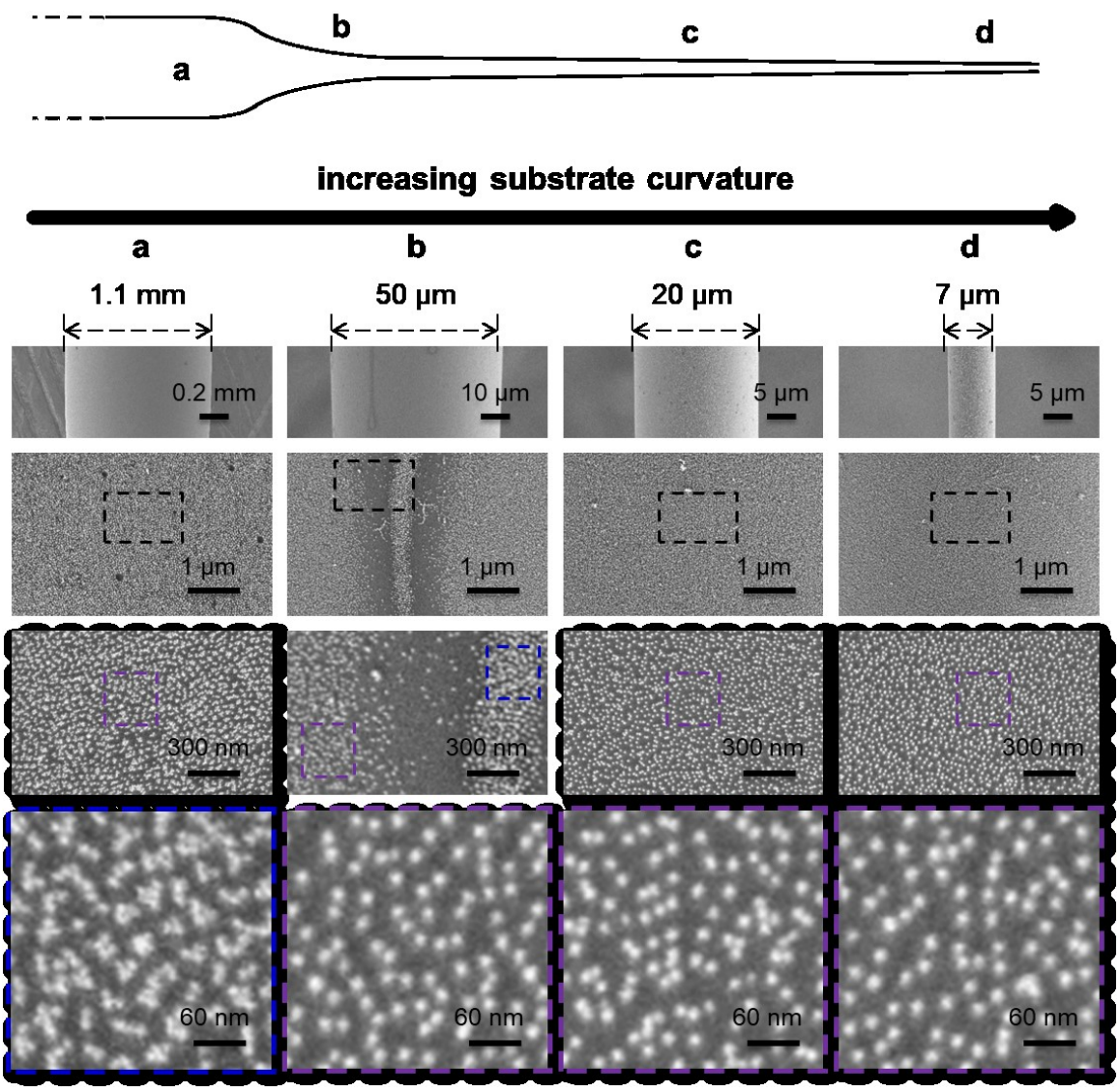

Figure 4.S4. SEM images of various magnifications, indicated by the scale bars, showing the AuNP patterns obtained at diameters corresponding to (a) the unpulled part of the fiber, (b) the neck region, and (c) and (d) the pulled fiber region. The fiber was imaged after the deposition of AuNPs of 10-12 nm in diameter on a PS_{41}-b-$P4VP_{20}$ film template obtained by the dip-coating procedure using a withdrawal rate of 10 mm/min and a 20 mg/mL THF solution.

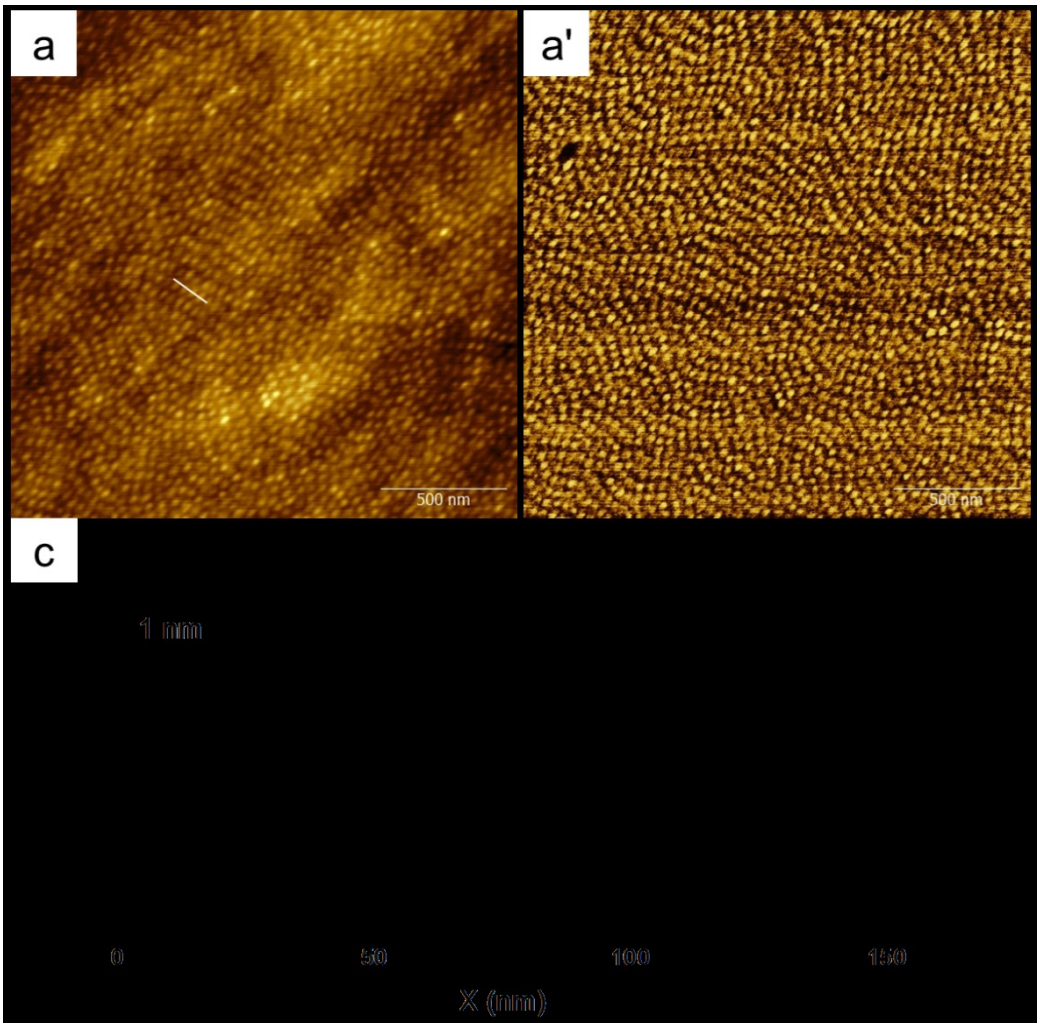

Figure 4.S5. AFM height (a) and phase (a') images of a BCP film on a glass fiber at a diameter of 1.1 mm. The film was dip-coated at a withdrawal rate of 0.5 mm/min from a 20 mg/mL PS_{41}-$P4VP_{20}$/THF solution. The height profile (c) along the line drawn in (a) indicates that the average center-to-center distance between dots is about 35 nm, from which a dot diameter of about 25-30 nm can be estimated.

Estimation of film thickness on fibers. In dip-coating, the film thickness, h, can be approximated as a function of the capillary number, Ca,

$$h \sim \mathrm{f}(Ca) \qquad \textbf{4.S1}$$

where Ca is defined as

$$Ca = \eta V/\gamma \qquad \textbf{4.S2}$$

with η and γ the liquid viscosity and surface tension, respectively, and V the coating velocity.

For dip-coated films on cylindrical substrates with radius, r, the Landau-Levich-Derjaguin (LLD) theory provides the following model for calculating the film thickness,[17]

$$h = 1.34r(Ca)^{2/3} \qquad \textbf{4.S3}$$

For a film dip-coated on the pulled fiber at 0.5 mm/min from a 20 mg/mL solution, Figure 4.2 in the main text shows that the film morphology transitions from a micellar film to a dewetted film (first transition), and then to a brush-only film (second transition) as the fiber diameter decreases. This indicates that the effect of substrate curvature on film thickness applies to these fibers, thereby justifying the use of the LLD theory. Figure 4.S6 shows that the fiber diameter for the second transition lies at about 43 μm. Assuming that the film thickness for the second transition is 3 nm (the thickness measured for the brush film), Ca is estimated to be on the order of 10^{-6}. Our study on flat substrates indicates that the film thickness for the first transition is about 15 nm, from which it can be estimated, using Eq. 4.S3, that the fiber diameter for this transition is about 215 μm. As shown in Figure 4.S6, the film indeed shows a dewetted pattern at this fiber diameter; however, the exact fiber diameter for the first transition can not be measured, due to the rapidly changing fiber diameter in its vicinity. By the same token, the film thickness at the original fiber diameter, 1.1 mm, is estimated to be about 77 nm, which is much smaller than the measured thickness on flat surfaces for 1 mm/min dip-coating rate (about 200 nm, Figure 4.S7), whereas it is still higher for 0.5 mm/min since the thickness increases with decreasing dip-coating rate in this region (capillarity region),[35] again indicating the curvature effect at this diameter.

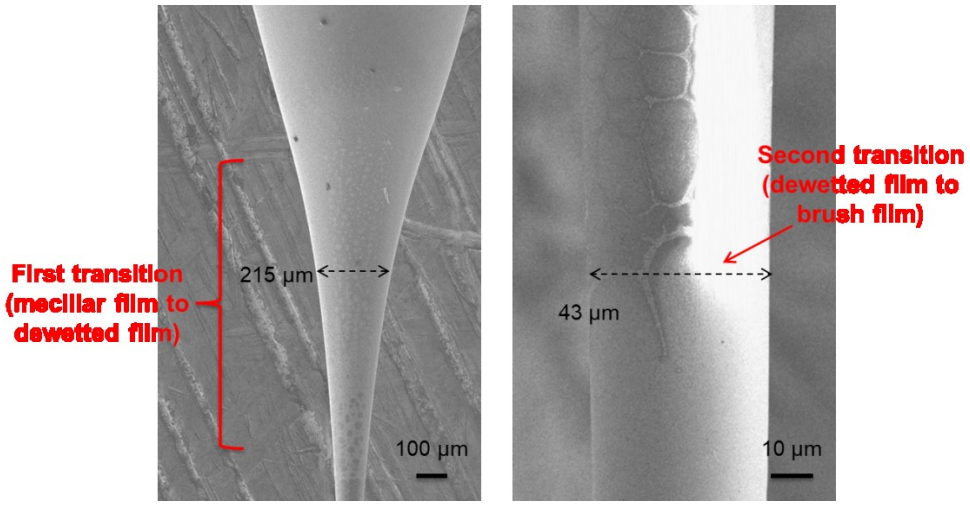

Figure 4.S6. SEM images of a glass fiber after coating with 12 nm AuNPs using a BCP film templated dip-coated at a withdrawal rate of 0.5 mm/min from a 20 mg/mL PS_{41}-$P4VP_{20}$/THF solution.

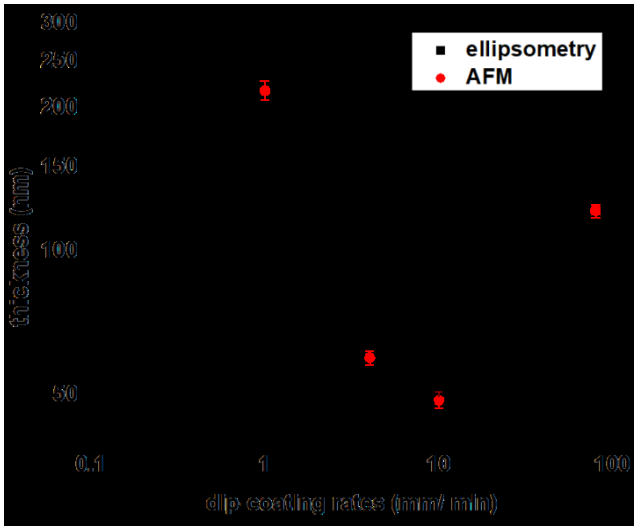

Figure 4.S7. Plot of film thickness, measured by using both AFM and ellipsometry, versus dip-coating rate for PS_{40}-*b*-$P4VP_{21}$ films dip-coated on flat substrates from a 20 mg/mL THF solution.

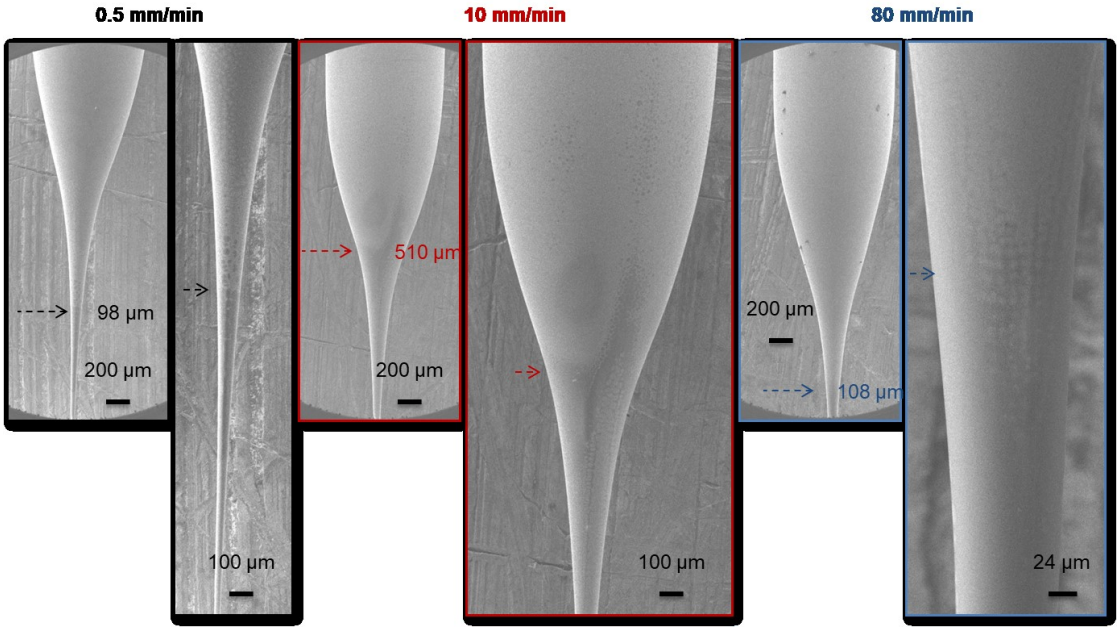

Figure 4.S8. Effect of dip-coating rate on substrate curvature induced film morphology transition from full micellar to dewetted micellar. SEM images of fibers after deposition of 12 nm-AuNPs using PS_{41}-$P4VP_{20}$ film templates dip-coated at three dip-coating rates from a solution of 20 mg/mL; dashed arrows indicate the fiber diameters at which the transition from "full micellar" BCP thin films with full coverage of hexagonal finite AuNPs clusters to dewetted films with islands AuNPs clusters.

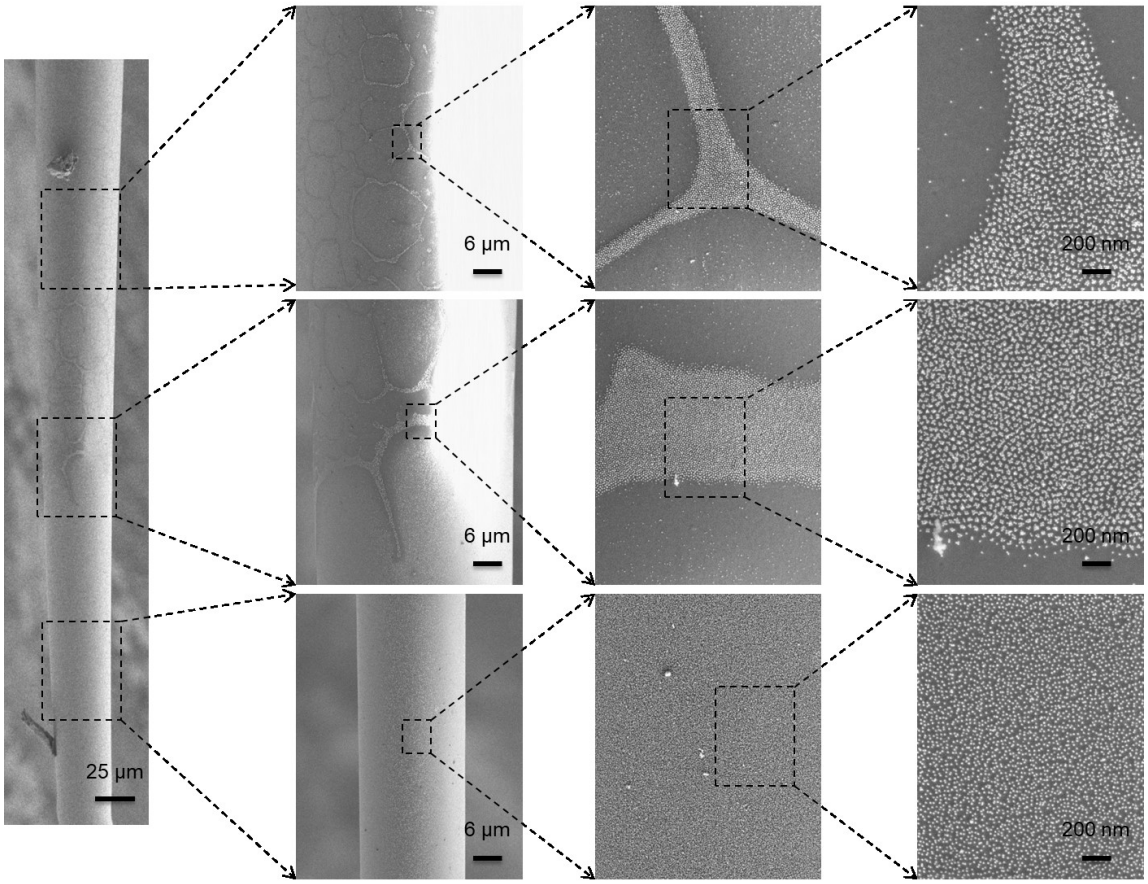

Figure 4.S9. Substrate curvature induced film morphology transition from dewetted micellar film to brush layer. SEM images of fibers after deposition of 12 nm-AuNPs using a PS_{41}-$P4VP_{20}$ film template dip-coated at 0.5 mm/min from a solution of 20 mg/mL, showing the transition from islands of AuNPs clusters to isolated AuNPs with decreasing substrate diameter.

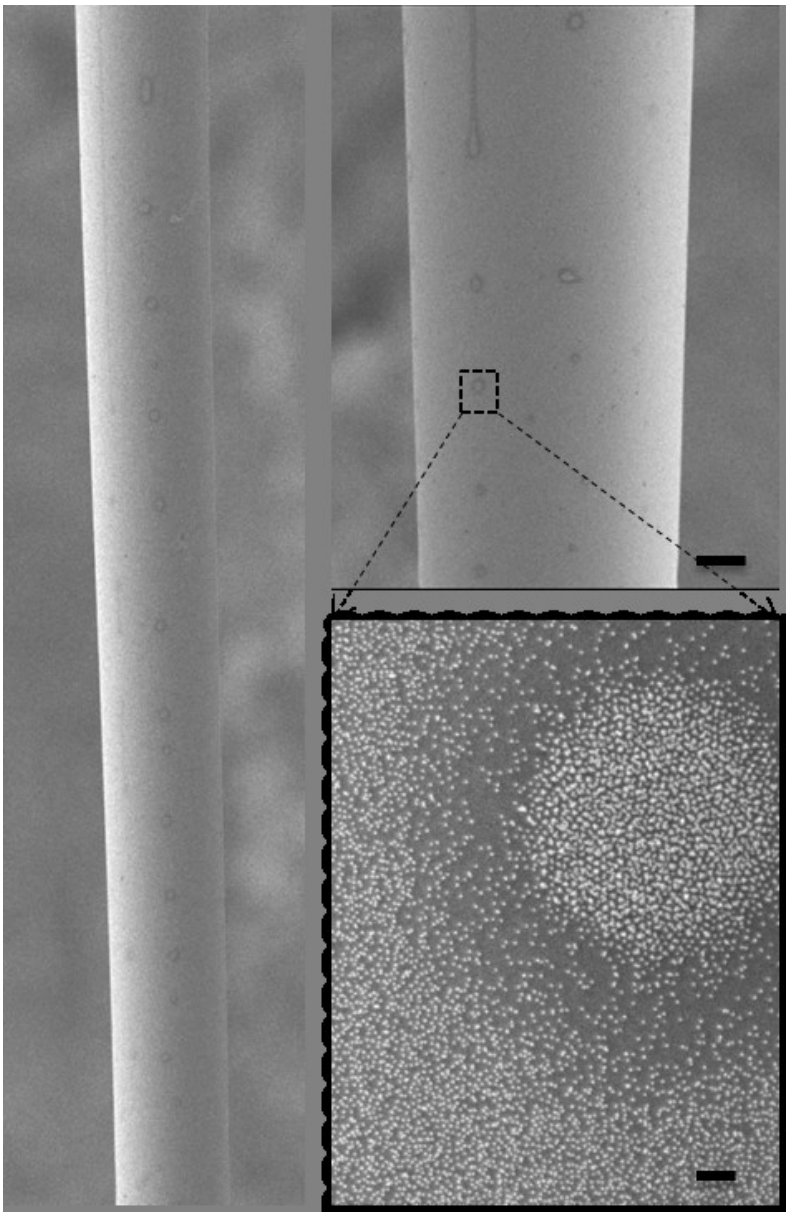

Figure 4.S10. Plateau-Rayleigh instability. SEM images of fibers after deposition of 12 nm-AuNPs using a PS_{41}-$P4VP_{20}$ film template dip-coated at 80 mm/min from a 20 mg/mL polymer solution. The narrow regions of dewetted micellar films break into droplets like regions of micellar films, due to Rayleigh instability.

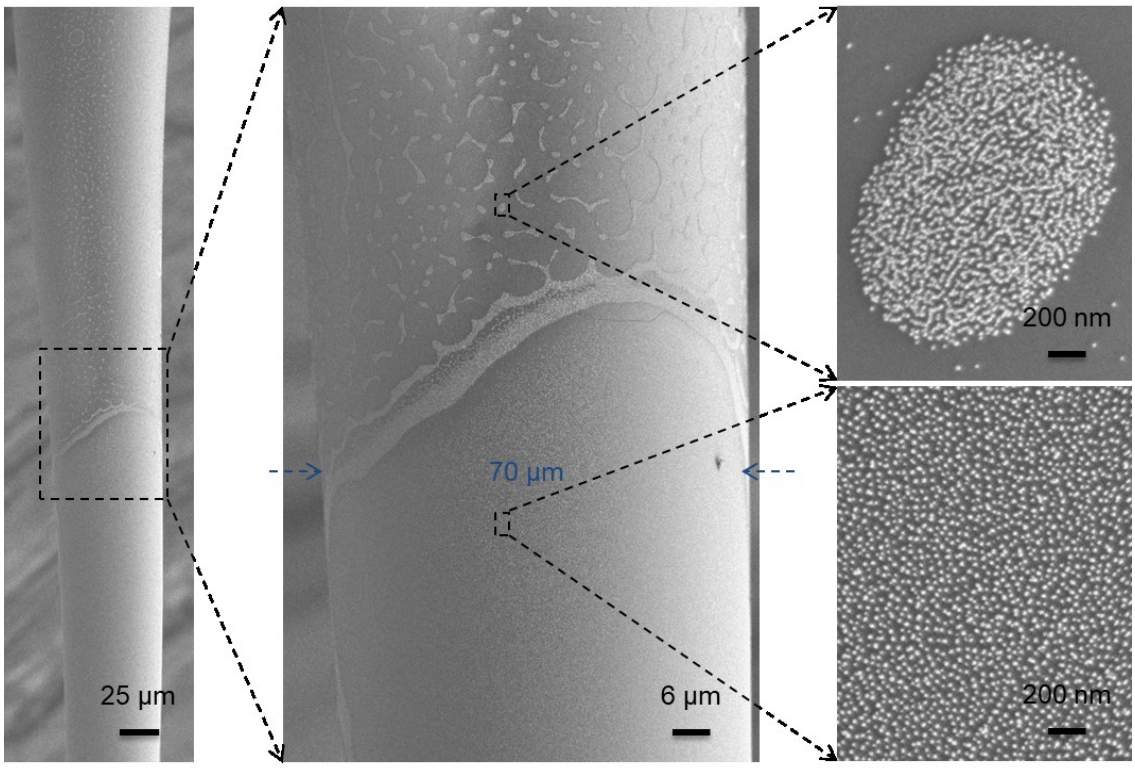

Figure 4.S11. Substrate curvature induced film morphology transition from dewetted micellar film to brush layer. SEM images of fibers after deposition of 12-nm AuNPs using a PS_{41}-$P4VP_{20}$ film template dip-coated at 0.5 mm/min from a solution of 5 mg/mL. In comparison to Figure S6, the lowered polymer concentration here changed the transition radius to wider fiber diameters.

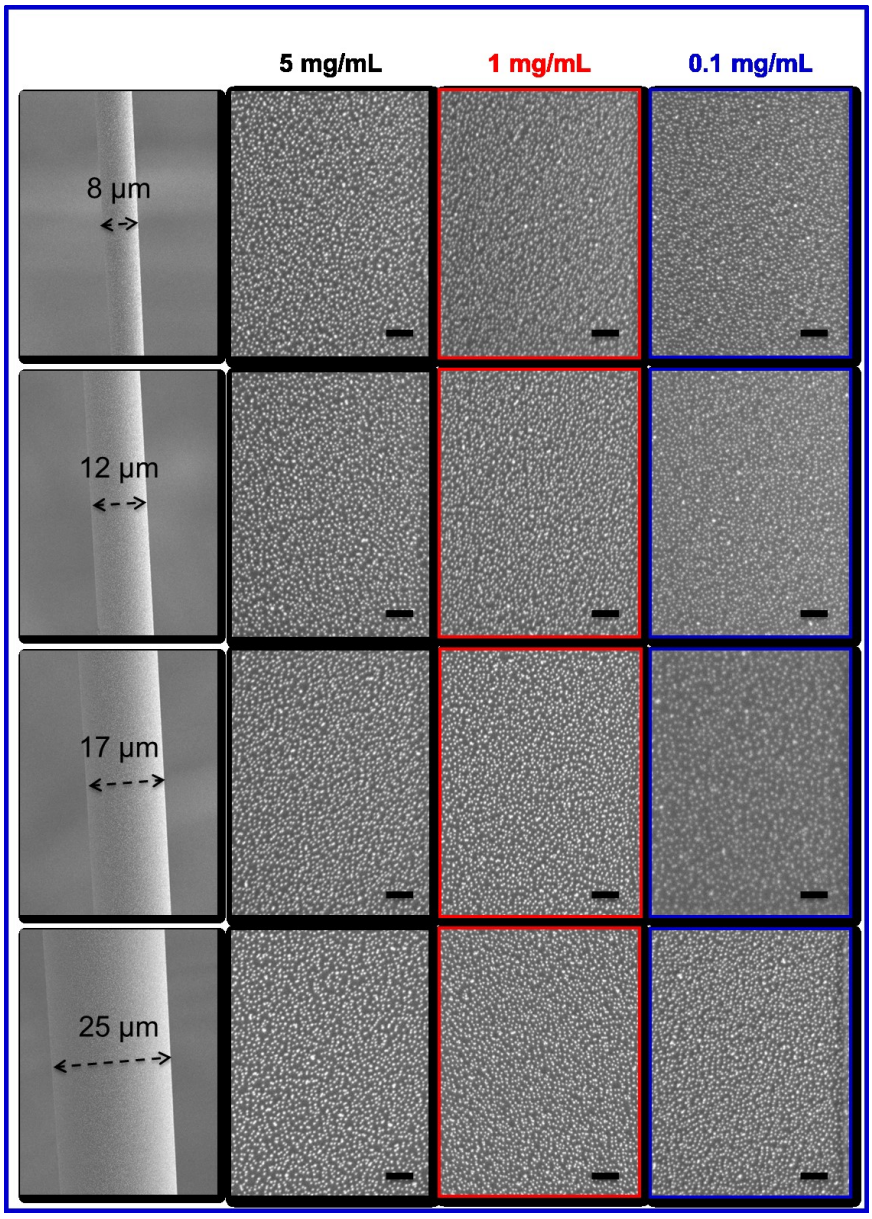

Figure 4.S12. Effect of polymer solution concentration on BCP film templates. SEM images of fibers at various fiber diameters (1st column) after deposition of 12-nm AuNPs using PS_{110}-$P2VP_{52}$ brush layer templates withdrawn at 40 mm/min from solutions of the BCP concentrations indicated. Scale bars represent 200 nm.

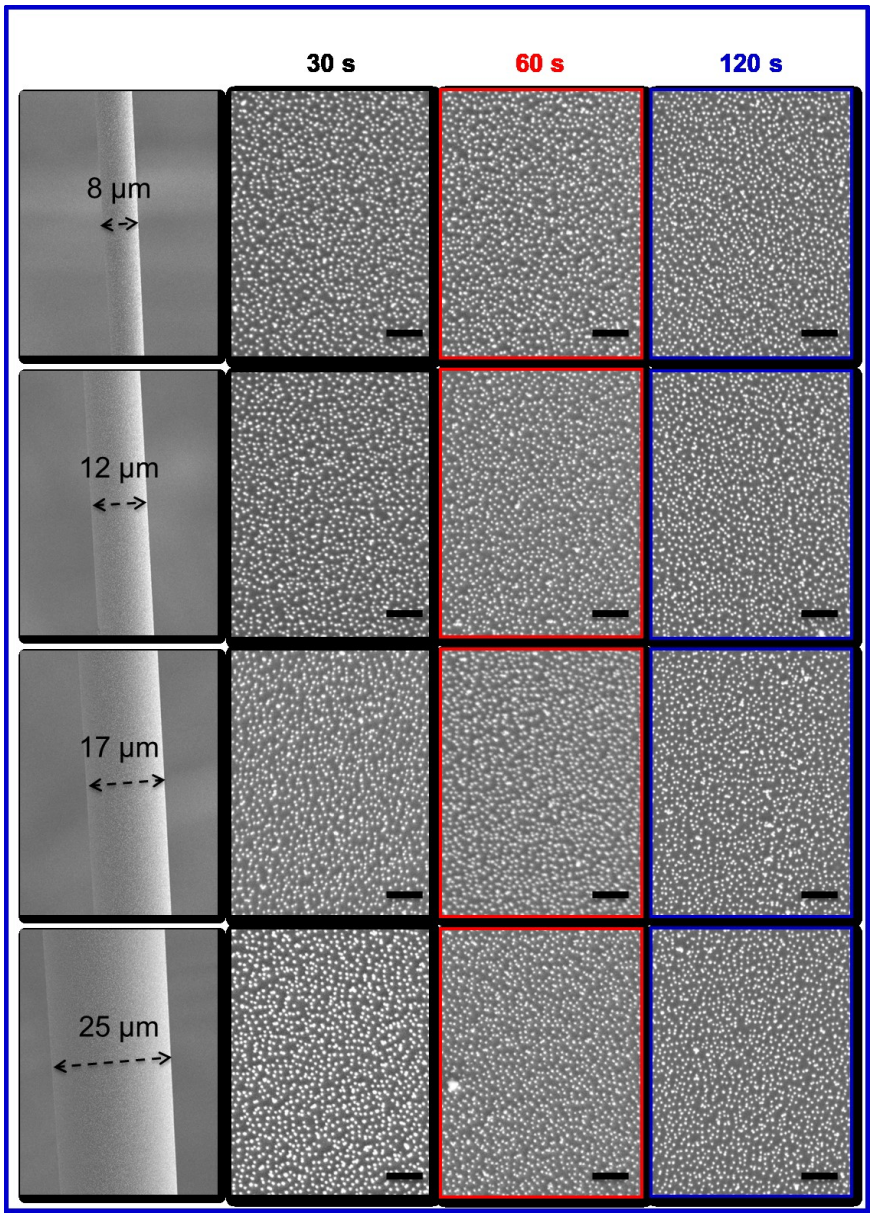

Figure 4.S13. Effect of dipping time on BCP film templates. SEM images of fibers at various fiber diameters (1st column) after deposition of 12 nm-AuNPs using PS_{110}- $P2VP_{52}$ film templates dip-coated at 40 mm/ min from a 0.1 mg/ mL solution with dipping time of 30 s (2nd column), 60 s (3rd column) and 120 s (4th column). Scale bars represent 200 nm.

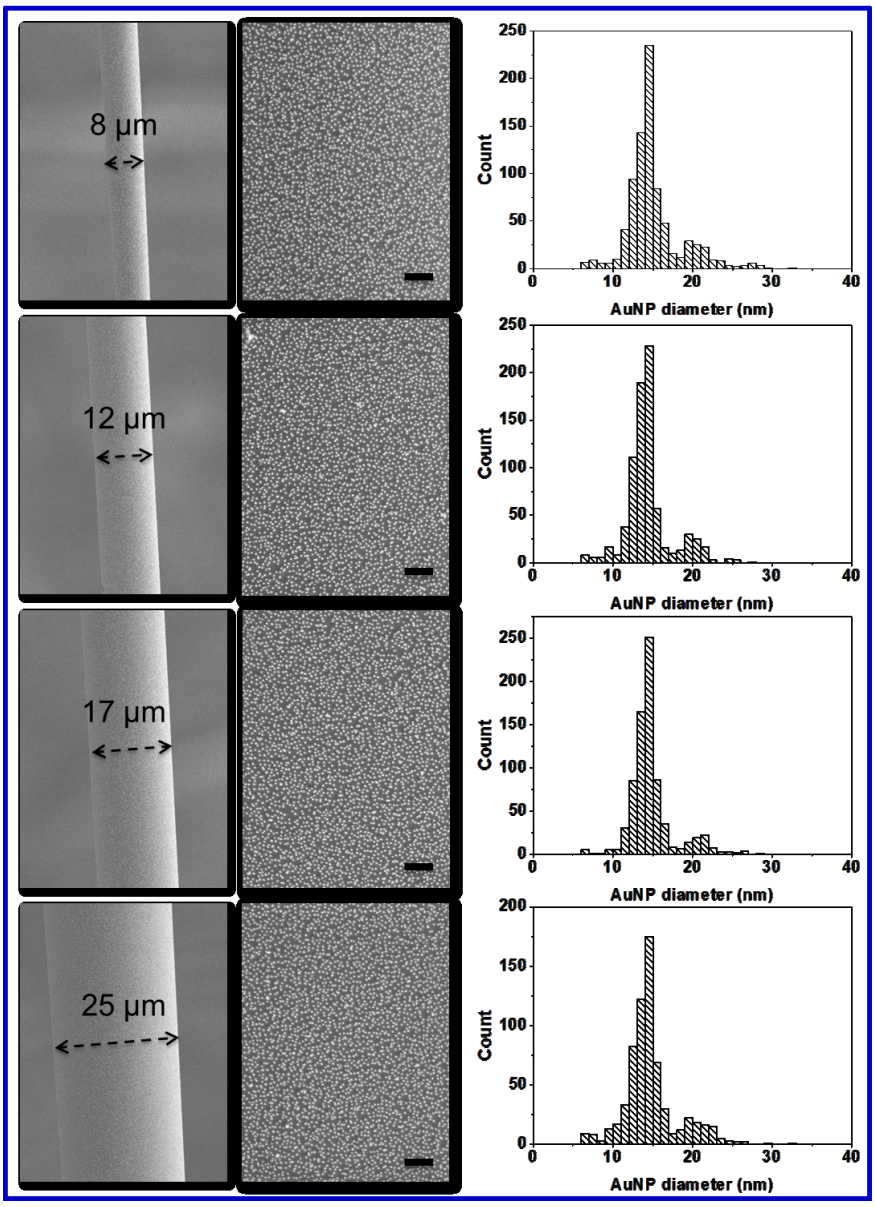

Figure 4.S14. Deposition of 12 nm-AuNPs using BCP film templates. SEM images of fibers at various fiber diameters (1st column) after deposition of 12 nm-AuNPs (2nd column) using a PS_{41}-$P4VP_{20}$ film template dip-coated at 0.5 mm/min from a 20 mg/mL solution. Scale bars represent 200 nm.

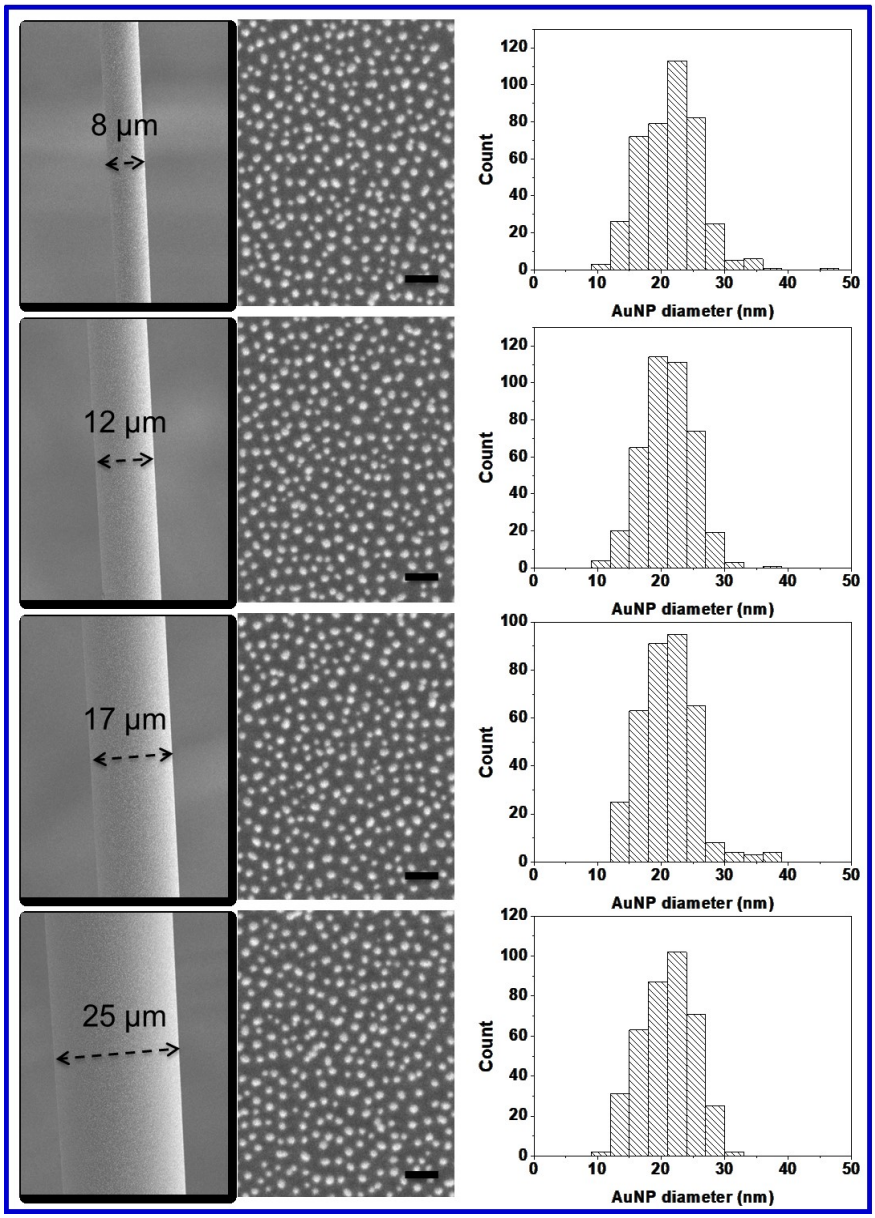

Figure 4.S15. Deposition of 20 nm-AuNPs using BCP film templates. SEM images of fibers at various fiber diameters (1st column) after deposition of 20 nm-AuNPs (2nd column) using a PS_{41}-$P4VP_{20}$ film template dip-coated at 80 mm/min from a 5 mg/mL solution. Scale bars represent 100 nm.

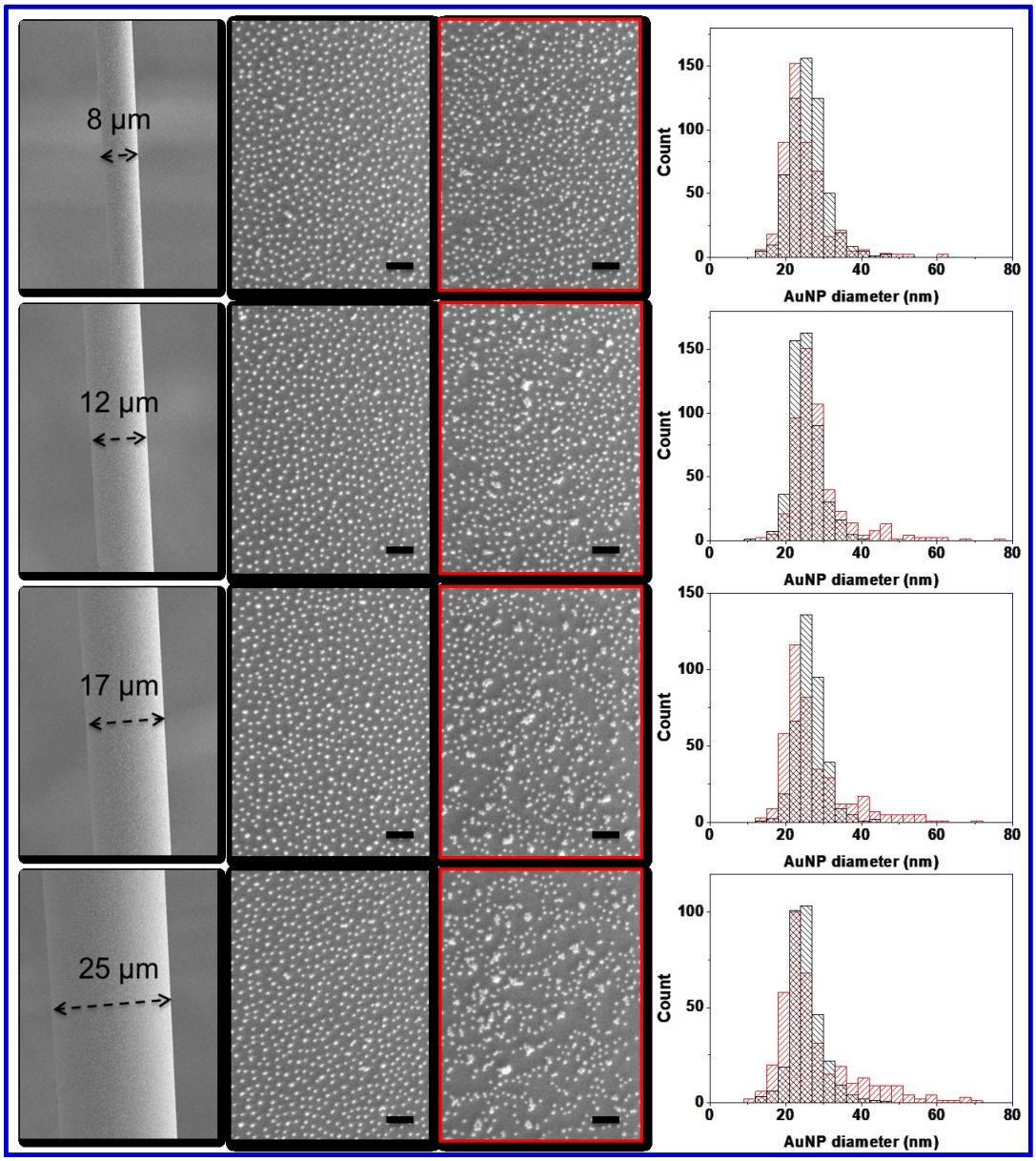

Figure 4.S16. Deposition of 32-nm AuNPs using both BCP and P4VP film templates. SEM images of fibers at various fiber diameters (1st column) after deposition of 32-nm AuNPs using a PS_{41}-$P4VP_{20}$ film template (2nd column) and a P4VP film template (3rd column). Scale bars represent 200 nm; 4th column, AuNP size distribution histograms color corresponding to images in second row (dark) and third row (red).

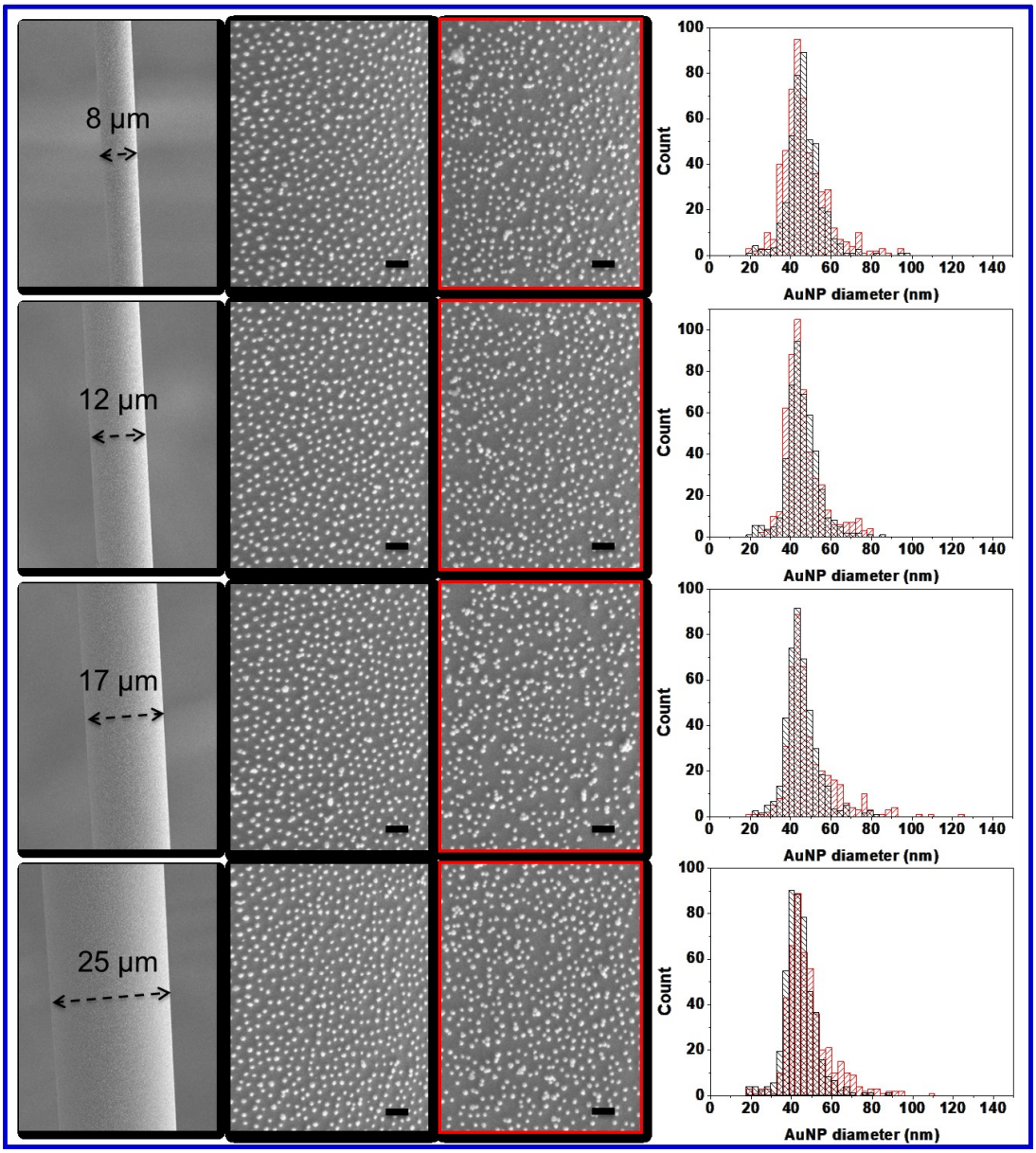

Figure 4.S17. Deposition of 52-nm AuNPs using both BCP and P4VP film templates. SEM images of fibers at various fiber diameters (1st column) after deposition of 52-nm AuNPs using a PS_{41}-$P4VP_{20}$ film template (2nd column) and a P4VP film template (3rd column). Scale bars represent 250 nm; 4th column, AuNP size distribution histograms color corresponding to images in second row (dark) and third row (red).

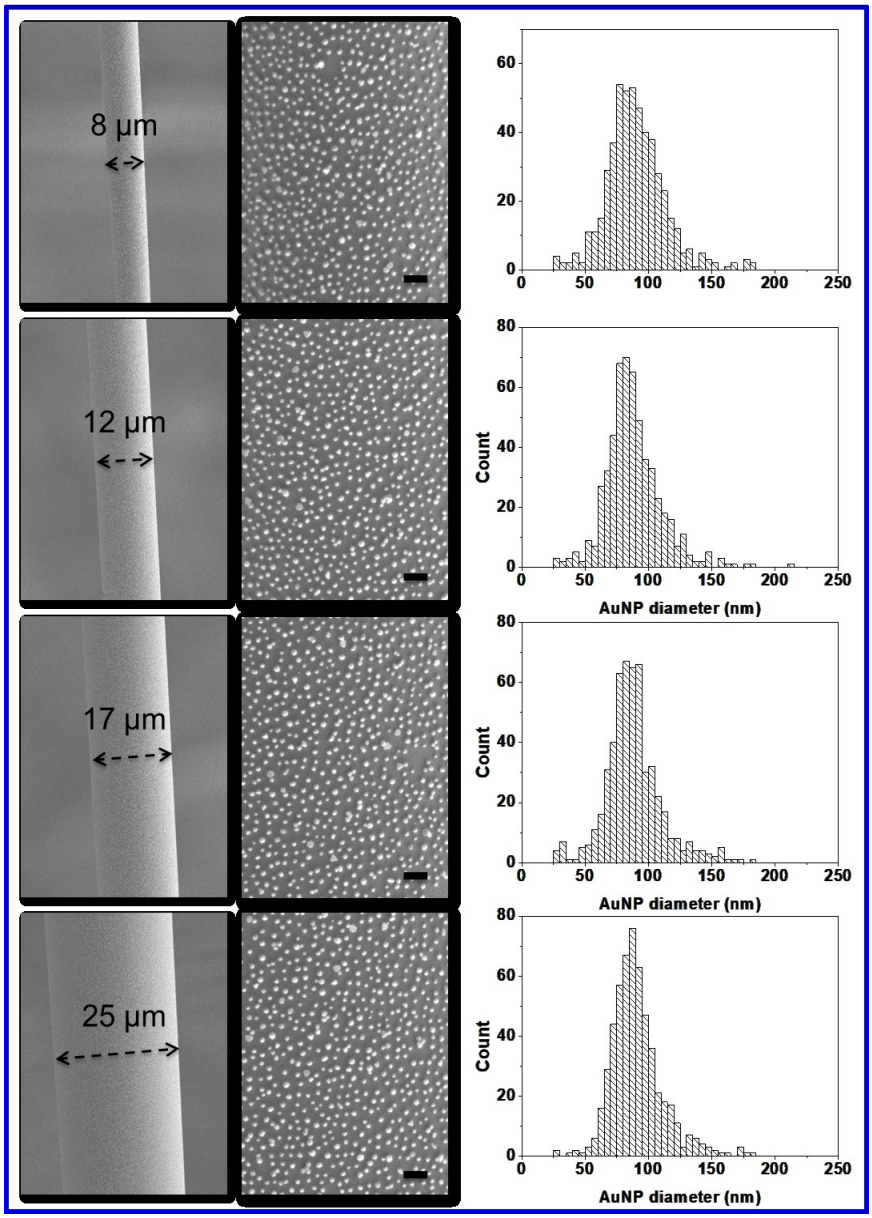

Figure 4.S18. Deposition of 94-nm AuNPs using BCP film templates. SEM images of fibers at various fiber diameters (1st column) after deposition of 94-nm AuNPs using a PS_{41}-$P4VP_{20}$ film template (2nd column). Scale bars represent 500 nm; 3rd column, AuNP size distribution histograms color corresponding to images in second row (dark) and third row (red).

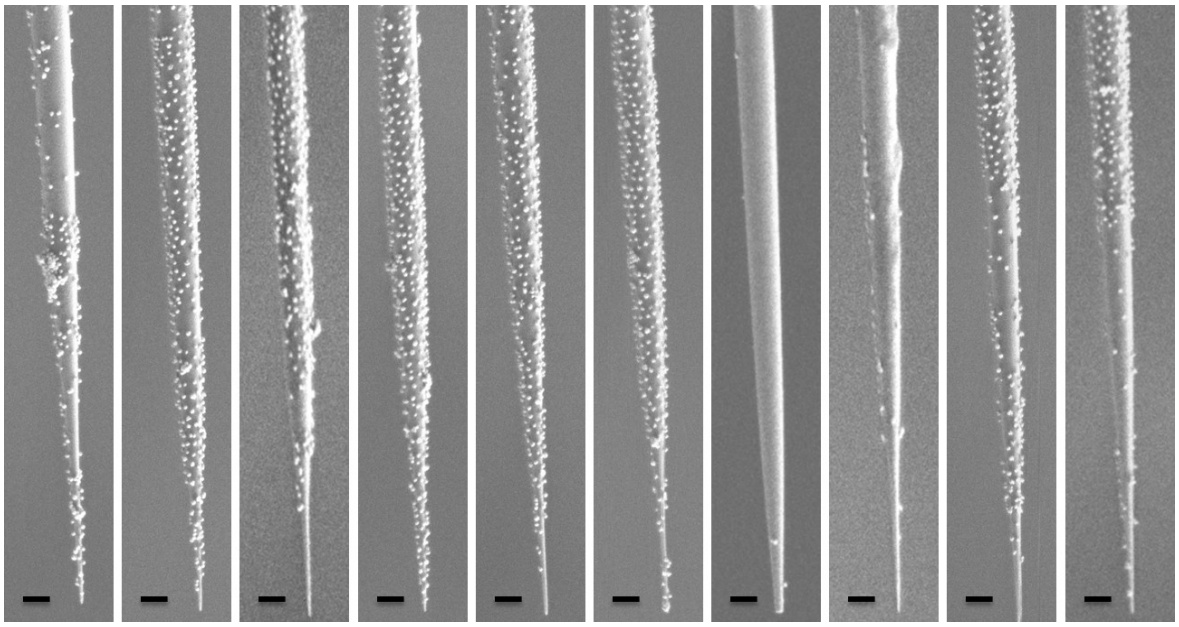

Figure 4.S19. SEM images of deposition of 94-nm AuNPs on fiber tips using PS_{41}-b-$P4VP_{20}$ film templates. Scale bars represent 500 nm.

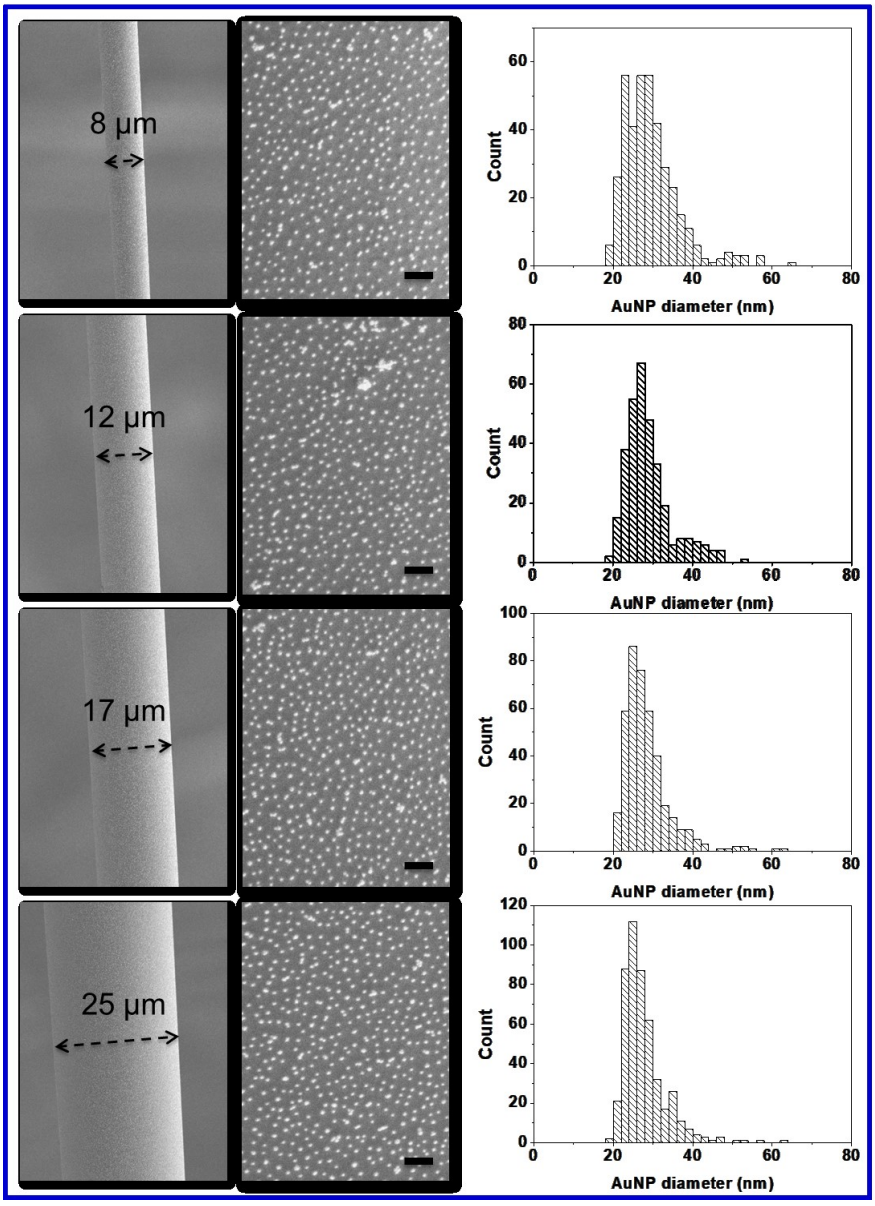

Figure 4.S20. Deposition of 32-nm AuNPs using random copolymer film templates. SEM images of fibers at various fiber diameters (1st column) after deposition of 32-nm AuNPs (2nd column) using a PS-s-P4VP random copolymer film template dip-coated at 80 mm/min from a 5 mg/mL solution. 3rd column, AuNP size distribution histograms corresponding to images in second row. Scale bars represent 200 nm.

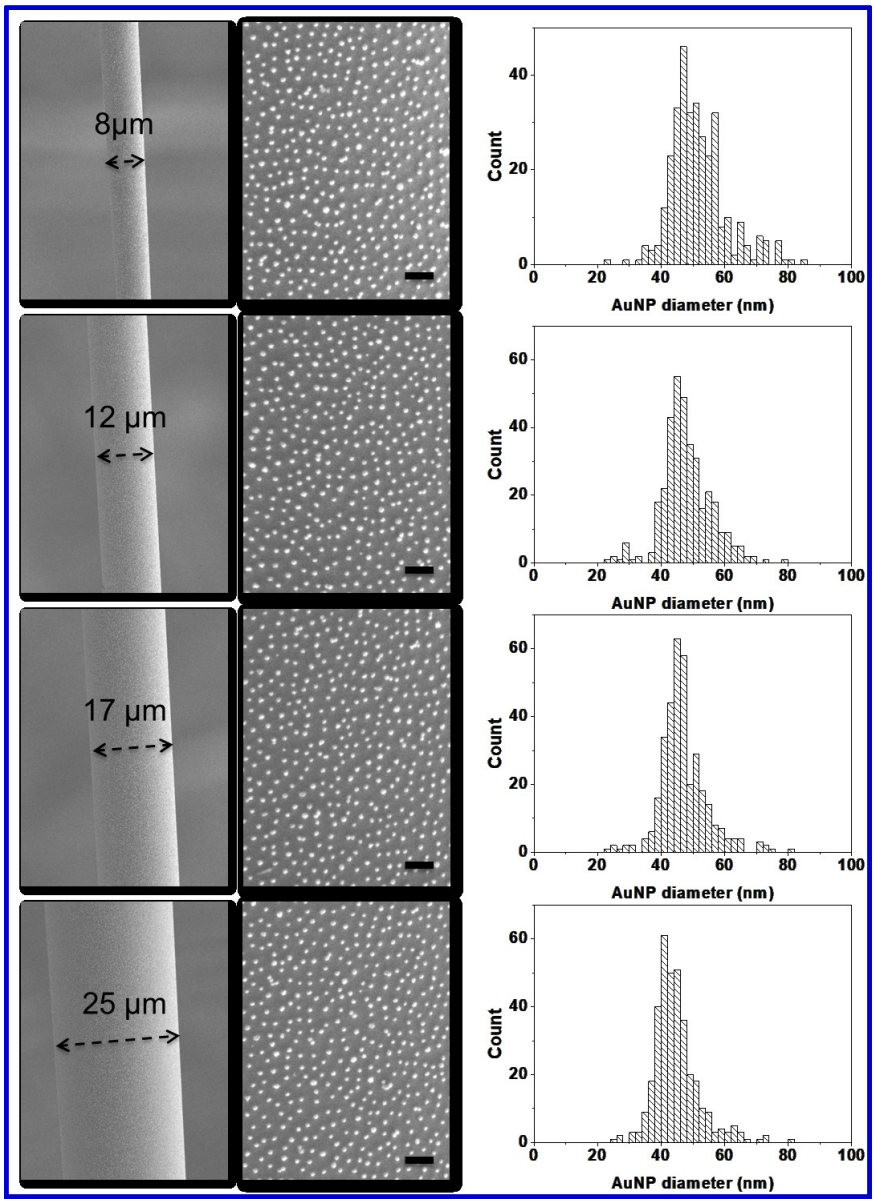

Figure 4.S21. Deposition of 52-nm AuNPs using random copolymer film templates. SEM images of fibers at various fiber diameters (1st column) after deposition of 52-nm AuNPs (2nd column) using a PS-s-P4VP random copolymer film template dip-coated at 80 mm/min from a 5 mg/mL solution. 3rd column, AuNP size distribution histograms corresponding to images in second row. Scale bars represent 300 nm.

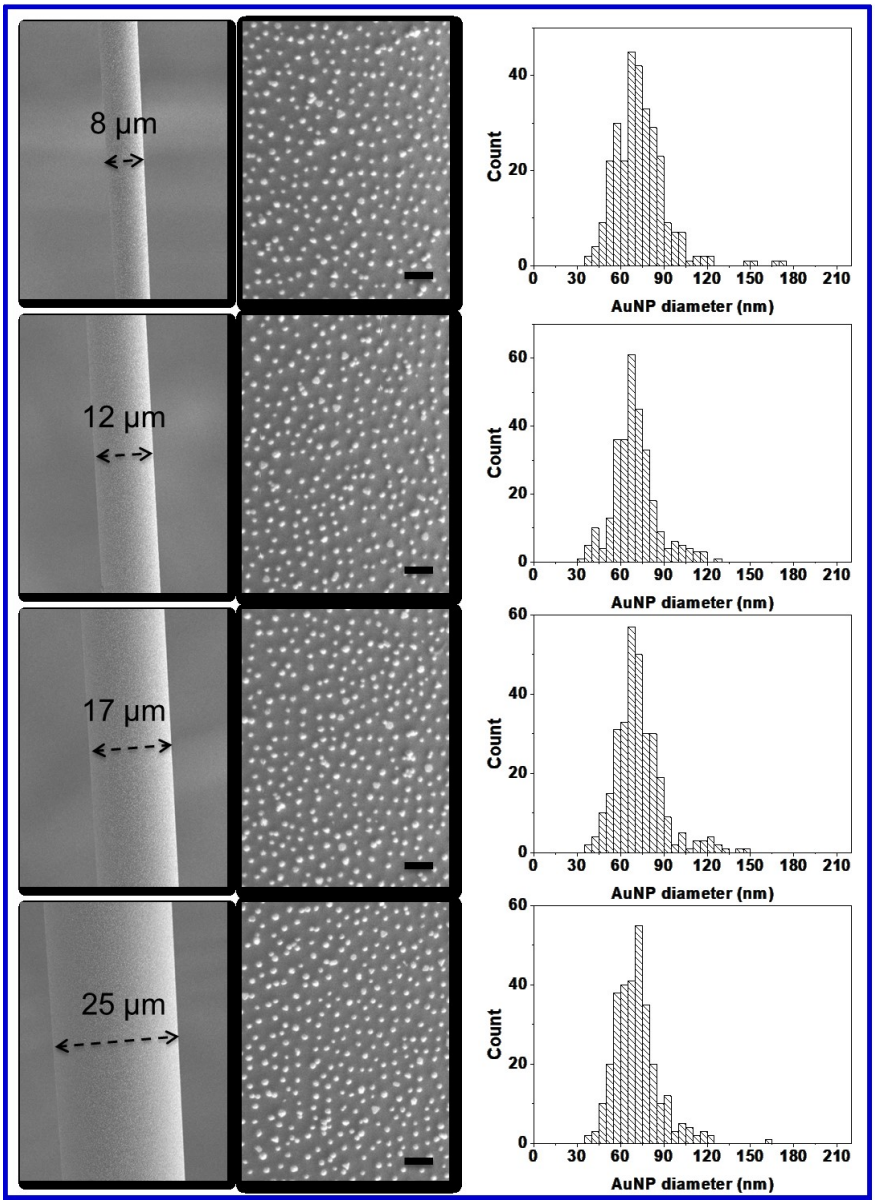

Figure 4.S22. Deposition of 78-nm AuNPs using random copolymer film templates. SEM images of fibers at various fiber diameters (1st column) after deposition of 78-nm AuNPs (2nd column) using a PS-s-P4VP random copolymer film template dip-coated at 80 mm/min from a 5 mg/mL solution. 3rd column, AuNP size distribution histograms corresponding to images in second row. Scale bars represent 400 nm.

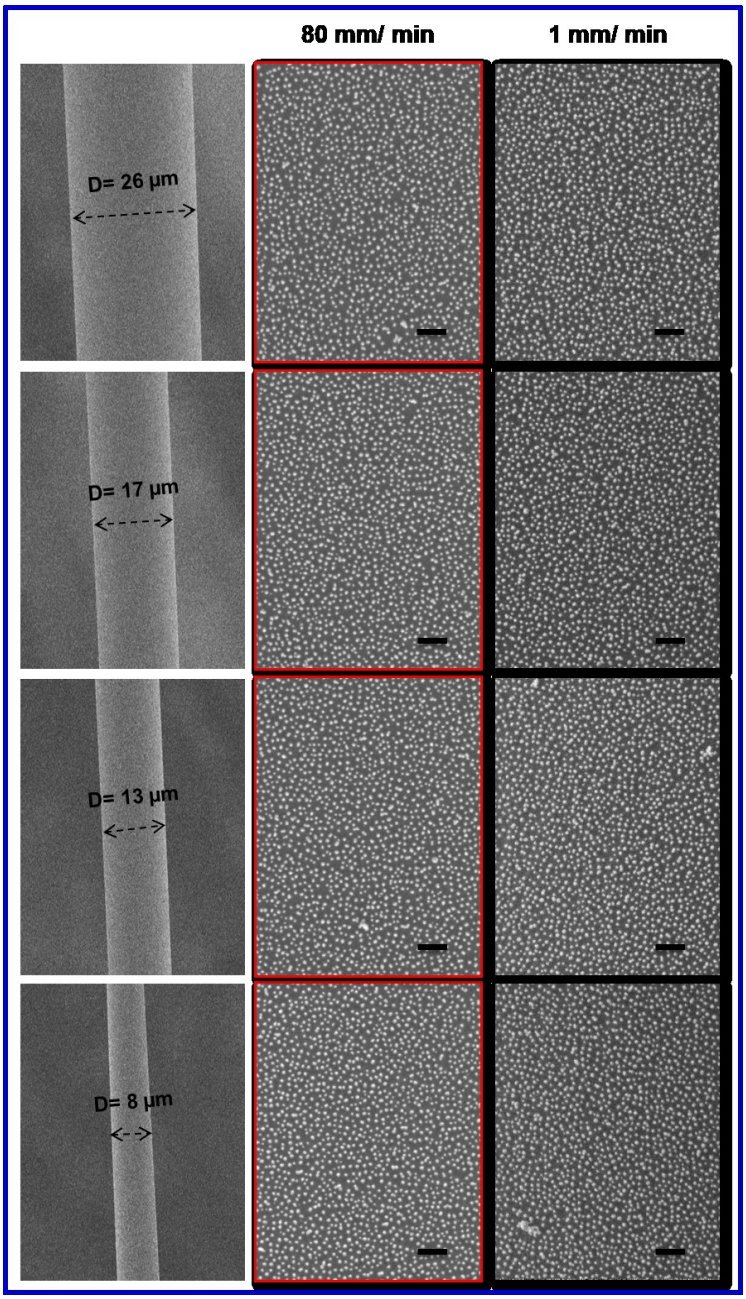

Figure 4.S23. Deposition of 20-nm AuNPs on PS_{252}-b-$P4VP_{43}$ brush films. SEM images of fibers at various fiber diameters (1st column) after deposition of 20 nm-AuNPs using PS_{252}-$P4VP_{43}$ film templates dip-coated at 80 mm/min (2nd column) and 1 mm/min (3rd column). Scale bars represent 200 nm.

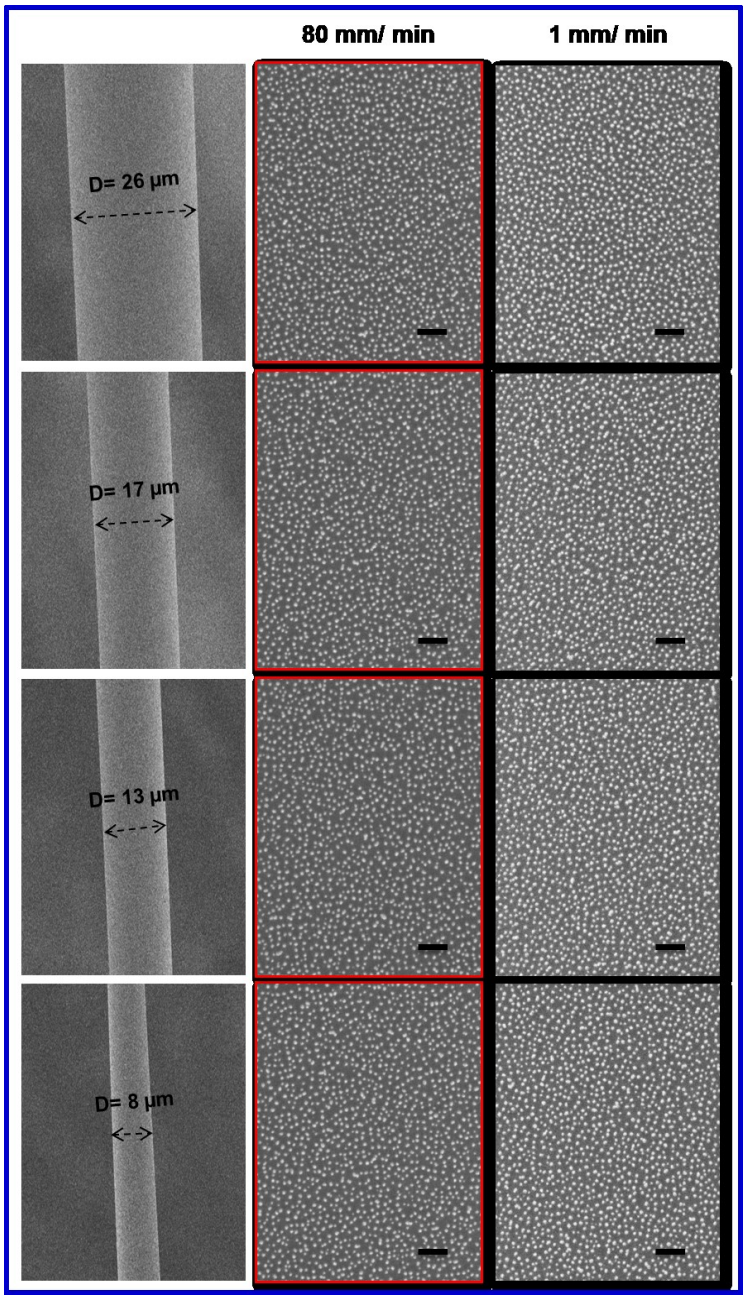

Figure 4.S24. Deposition of 20-nm AuNPs on PS_{120}-b-$P4VP_{20}$ brush films. SEM images of fibers at various fiber diameters (1st column) after deposition of 20 nm-AuNPs using PS_{120}-$P4VP_{20}$ film templates dip-coated at 80 mm/min (2nd column) and 1 mm/min (3rd column). Scale bars represent 200 nm.

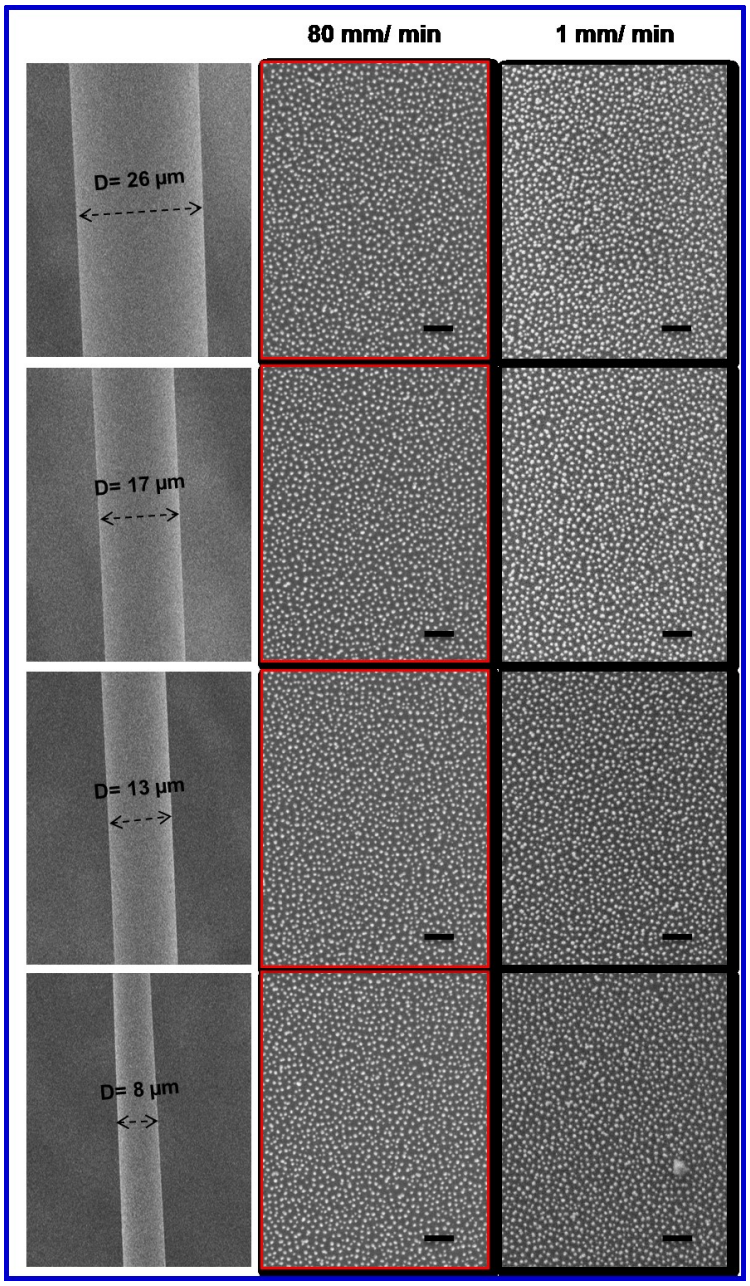

Figure 4.S25. Deposition of 20-nm AuNPs on PS_{41}-b-$P4VP_{20}$ brush films. SEM images of fibers at various fiber diameters (1st column) after deposition of 20 nm-AuNPs using PS_{41}-$P4VP_{20}$ film templates dip-coated at 80 mm/min (2nd column) and 1 mm/min (3rd column). Scale bars represent 200 nm.

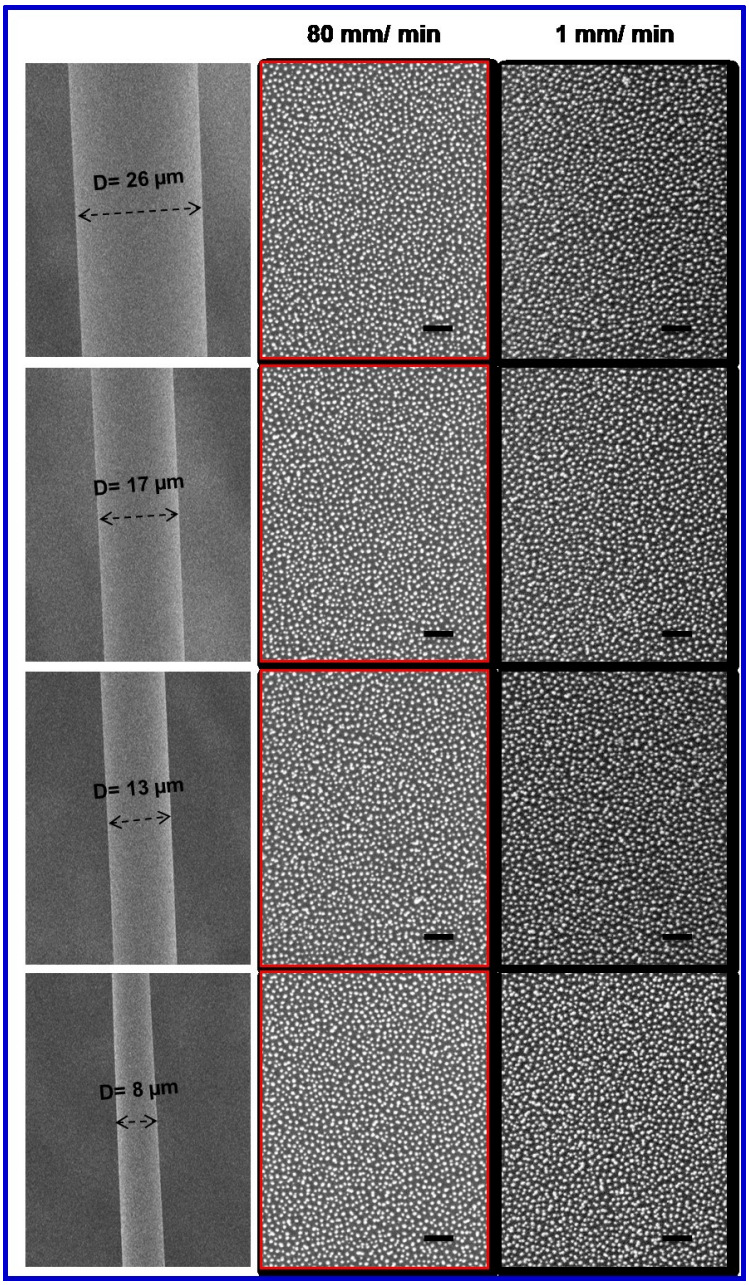

Figure 4.S26. Deposition of 20-nm AuNPs on PS_{20}-b-$P4VP_{29}$ brush films. SEM images of fibers at various fiber diameters (1st column) after deposition of 20 nm-AuNPs using PS_{20}-$P4VP_{29}$ film templates dip-coated at 80 mm/min (2nd column) and 1 mm/min (3rd column). Scale bars represent 200 nm.

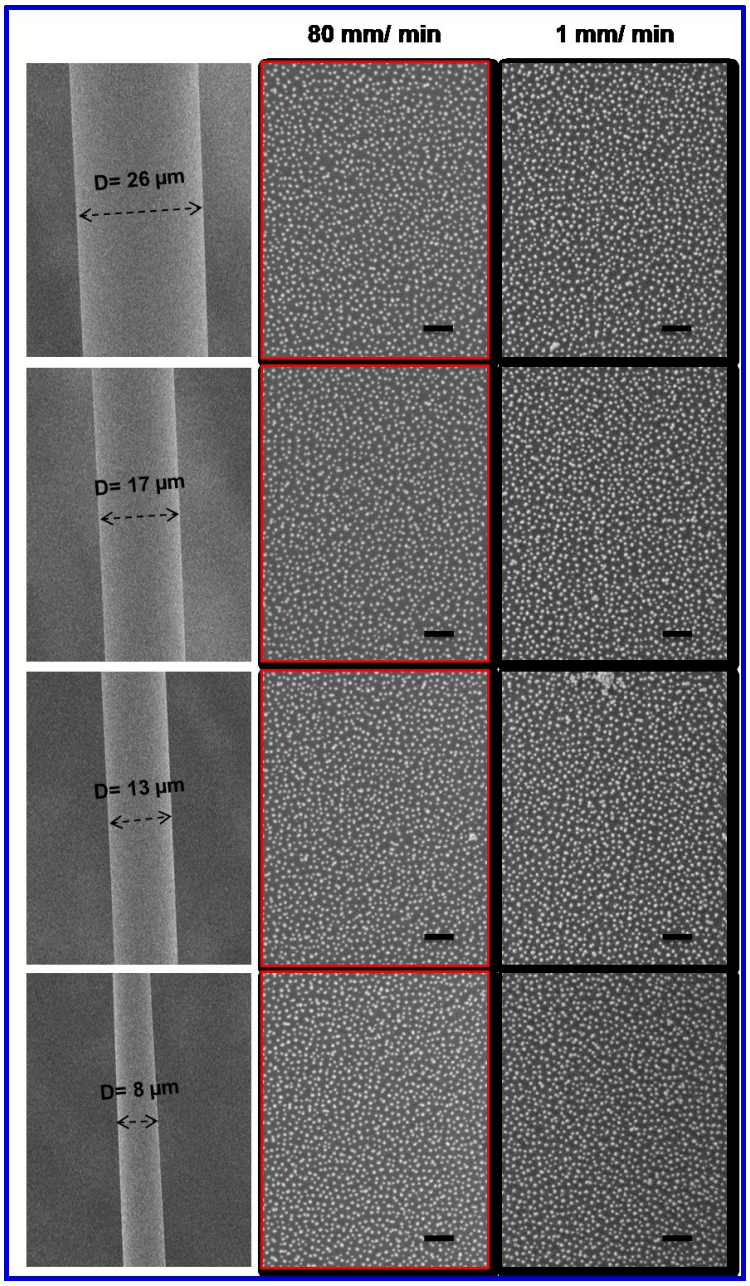

Figure 4.S27. Deposition of 20-nm AuNPs on PS_{84}-b-$P4VP_{18}$ brush films. SEM images of fibers at various fiber diameters (1st column) after deposition of 20 nm-AuNPs using PS_{84}-$P4VP_{18}$ film templates dip-coated at 80 mm/min (2nd column) and 1 mm/min (3rd column). Scale bars represent 200 nm.

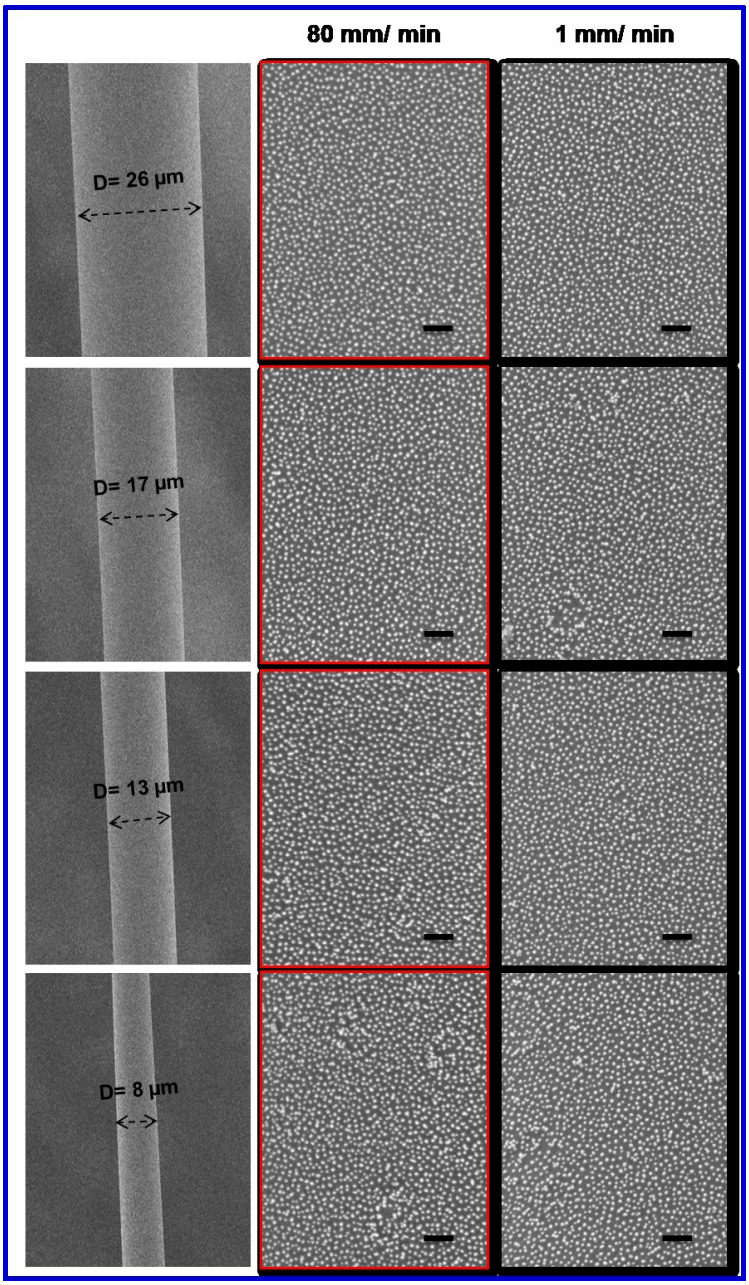

Figure 4.S28. Deposition of 20-nm AuNPs on PS_{72}-b-$P4VP_{35}$ brush films. SEM images of fibers at various fiber diameters (1st column) after deposition of 20 nm-AuNPs using PS_{72}-$P4VP_{35}$ film templates dip-coated at 80 mm/min (2nd column) and 1 mm/min (3rd column). Scale bars represent 200 nm.

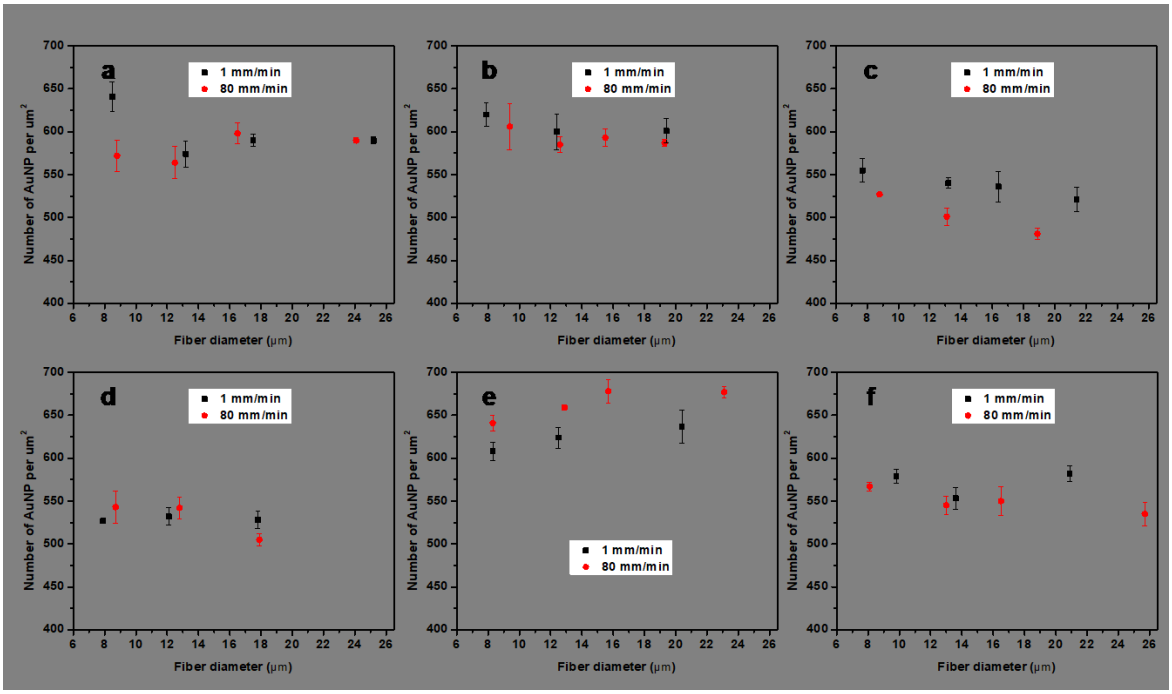

Figure 4.S29. Plot of surface nanoparticle density as a function of substrate diameter (6 μm to 26 μm) for the depositions of 20 nm AuNPs using six different BCP films dip-coated from both 1 mm/min and 80 mm/min from their 5 mg/mL THF solutions with and without the addition of small molecules of naphthol or naphthoic acid: a) PS(41 kg/mol)-P4VP(20 kg/mol), b) PS (72 kg/mol)-P4VP (35 kg/mol), c) PS (120 kg/mol)-P4VP (20 kg/mol), d) PS (84 kg/mol)-P4VP (17.5 kg/mol), e) PS (19.9 kg/mol)-P4VP (29.4 kg/mol), f) PS (252 kg/mol)-P4VP (43 kg/mol).

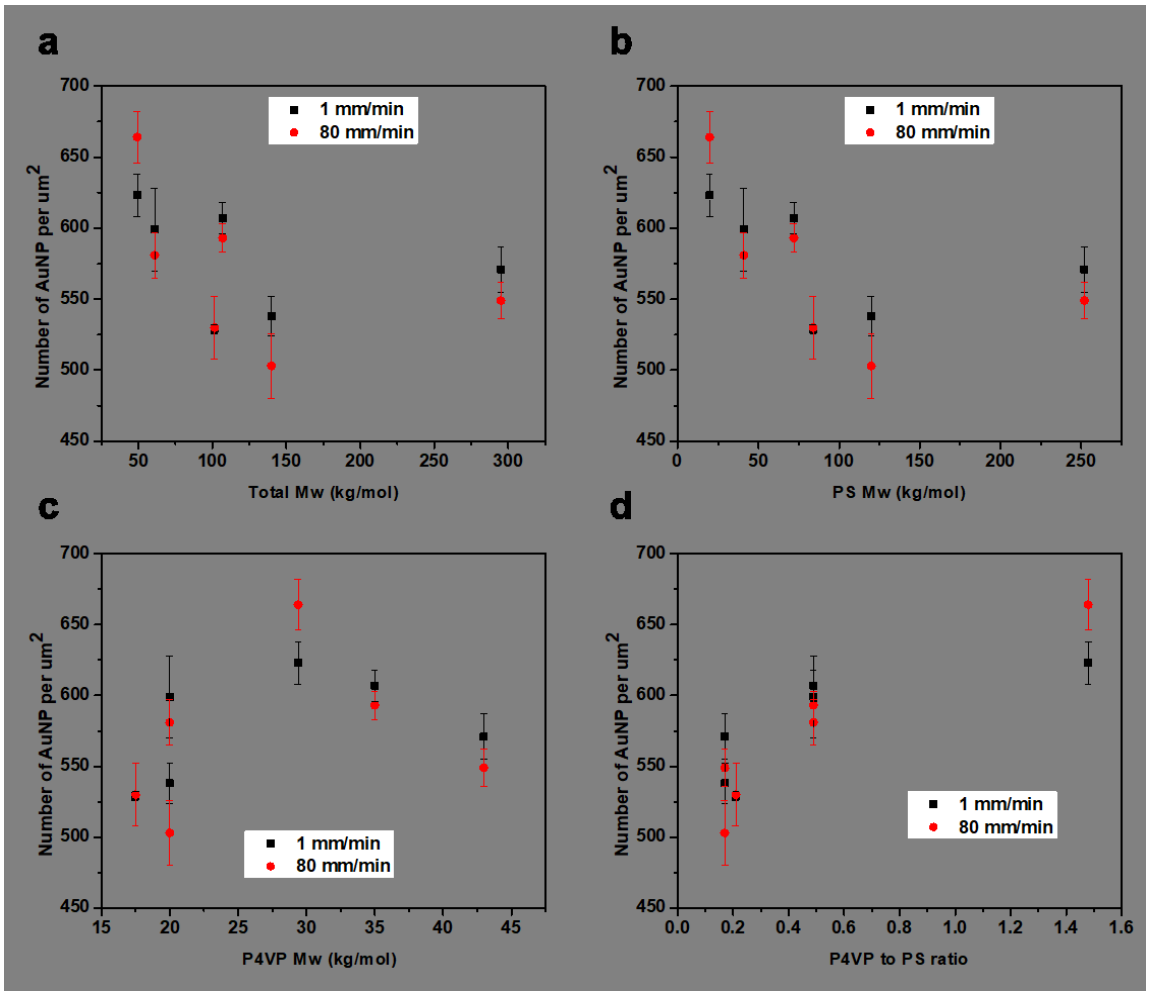

Figure 4.S30. Number of AuNP per μm^2 of 20-nm AuNPs deposited on fibers of diameters from 6 µm to 26 µm by using different PS-b-P4VP brush film templates plotted against a) total molecular weight, b) the molecular weight of PS, c) the molecular weight of P4VP, and d) the P4VP to PS block ratio.

4.7 References

1. Cheemalapati, S. V.; Winskas, J.; Wang, H.; Konnaiyan, K.; Zhdanov, A.; Roth, A.; Adapa, S. R.; Deonarine, A.; Noble, M.; Das, T.; Gatenby, R.; Westerheide, S. D.; Jiang, R. H. Y.; Pyayt, A. Sci. Rep. 2016, 6, 34400.

2. Lu, G.; De Keersmaecker, H.; Su, L.; Kenens, B.; Rocha, S.; Fron, E.; Chen, C.; Van Dorpe, P.; Mizuno, H.; Hofkens, J.; Hutchison, J. A.; Uji-i, H. Adv. Mater. 2014, 26, 5124-5128.
3. Shambat, G.; Kothapalli, S.-R.; Provine, J.; Sarmiento, T.; Harris, J.; Gambhir, S. S.; Vučković, J. Nano. Lett. 2013, 13, 4999-5005.
4. Singhal, R.; Orynbayeva, Z.; Kalyana Sundaram, R. V.; Niu, J. J.; Bhattacharyya, S.; Vitol, E. A.; Schrlau, M. G.; Papazoglou, E. S.; Friedman, G.; Gogotsi, Y. Nat. Nanotechnol. 2010, 6, 57.
5. Tan, W.; Shi, Z. Y.; Smith, S.; Birnbaum, D.; Kopelman, R. Science 1992, 258, 778-781.
6. Yan, R.; Park, J.-H.; Choi, Y.; Heo, C.-J.; Yang, S.-M.; Lee, L. P.; Yang, P. Nat. Nanotechnol. 2011, 7, 191.
7. Scaffidi, J. P.; Gregas, M. K.; Seewaldt, V.; Vo-Dinh, T. Anal. Bioanal. Chem. 2009, 393, 1135-1141.
8. Vitol, E. A.; Orynbayeva, Z.; Bouchard, M. J.; Azizkhan-Clifford, J.; Friedman, G.; Gogotsi, Y. ACS Nano 2009, 3, 3529-3536.
9. Masson, J.-F.; Breault-Turcot, J.; Faid, R.; Poirier-Richard, H.-P.; Yockell-Lelièvre, H.; Lussier, F.; Spatz, J. P. Anal. Chem. 2014, 86, 8998-9005.
10. Liang, F.; Zhang, Y.; Hong, W.; Dong, Y.; Xie, Z.; Quan, Q. Nano. Lett. 2016, 16, 3989-3994.
11. Lussier, F.; Brulé, T.; Vishwakarma, M.; Das, T.; Spatz, J. P.; Masson, J.-F. Nano. Lett. 2016, 16, 3866-3871.
12. Bhattacharyya, S.; Staack, D.; Vitol, E. A.; Singhal, R.; Fridman, A.; Friedman, G.; Gogotsi, Y. Adv. Mater. 2009, 21, 4039-4044.
13. Lee, W.; Lee, S. Y.; Briber, R. M.; Rabin, O. Adv. Funct. Mater. 2011, 21, 3424-3429.
14. Lohmueller, T.; Bock, E.; Spatz, J. P. Adv. Mater. 2008, 20, 2297-2302.
15. Aizawa, M.; Buriak, J. M. Chem. Mater. 2007, 19, 5090-5101.
16. Aizawa, M.; Buriak, J. M. J. Am. Chem. Soc. 2005, 127, 8932-8933.
17. Quere, D. Annu. Rev. Fluid. Mech. 1999, 31, 347-384.
18. Kruss, S.; Erpenbeck, L.; Schön, M. P.; Spatz, J. P. Lab Chip 2012, 12, 3285-3289.

19. Quere, D.; Dimeglio, J. M.; Brochardwyart, F. Science 1990, 249, 1256-1260.
20. Zito, G.; Rusciano, G.; Vecchione, A.; Pesce, G.; Di Girolamo, R.; Malafronte, A.; Sasso, A. Sci. Rep. 2016, 6, 31113.
21. Zhu, H.; Lussier, F.; Ducrot, C.; Bourque, M.-J.; Spatz, J. P.; Cui, W.; Yu, L.; Peng, W.; Trudeau, L.-É.; Bazuin, C. G.; Masson, J.-F. ACS Appl. Mater. Interfaces 2019, 11, 4373-4384.
22. Lu, M.; Zhu, H.; Bazuin, C. G.; Peng, W.; Masson, J.-F. J. A. s. ACS Sens. 2019. DOI: 10.1021/acssensors.8b01372.
23. Hu Zhu, J.-F. M., C. Geraldine Bazuin. Langmuir 2019, Revised version submitted Feb 2, 2019.
24. Schmudde, M.; Grunewald, C.; Goroncy, C.; Noufele, C. N.; Stein, B.; Risse, T.; Graf, C. ACS Nano 2016, 10, 3525-3535.
25. Turkevich, J.; Stevenson, P. C.; Hillier, J. Discuss. Faraday Soc. 1951, 11, 55-75.
26. Chen, X.; Perepichka, I. I.; Bazuin, C. G. ACS Appl. Mater. Interfaces 2014, 6, 18360-18367.
27. Bastús, N. G.; Comenge, J.; Puntes, V. Langmuir 2011, 27, 11098-11105.
28. Haiss, W.; Thanh, N. T. K.; Aveyard, J.; Fernig, D. G. Anal. Chem. 2007, 79, 4215-4221.
29. Roland, S.; Prud'homme, R. E.; Bazuin, C. G. ACS Macro Lett. 2012, 1, 973-976.
30. Yap, F. L.; Thoniyot, P.; Krishnan, S.; Krishnamoorthy, S. ACS Nano 2012, 6, 2056-2070.
31. Tallmadge, J. A.; Gutfinger, C. Ind. Eng. Chem. 1967, 59, 18-34.
32. Meiners, J. C.; Quintel-Ritzi, A.; Mlynek, J.; Elbs, H.; Krausch, G. Macromolecules 1997, 30, 4945-4951.
33. Spatz, J. P.; Roescher, A.; Sheiko, S.; Krausch, G.; Möller, M. Adv. Mater. 1995, 7, 731-735.
34. Grosso, D. J. Mater. Chem. 2011, 21, 17033-17038.
35. Roland, S.; Gamys, C. G.; Grosrenaud, J.; Boissé, S.; Pellerin, C.; Prud'homme, R. E.; Bazuin, C. G. Macromolecules 2015, 48, 4823-4834.
36. Meiners, J. C.; Ritzi, A.; Rafailovich, M. H.; Sokolov, J.; Mlynek, J.; Krausch, G. Appl. Phys. A 1995, 61, 519-524.

37. Spatz, J. P.; Sheiko, S.; Möller, M. Macromolecules 1996, 29, 3220-3226.
38. Tassin, J. F.; Siemens, R. L.; Tang, W. T.; Hadziioannou, G.; Swalen, J. D.; Smith, B. A. J. Phys. Chem. 1989, 93, 2106-2111.
39. Munch, M. R.; Gast, A. P. Macromolecules 1990, 23, 2313-2320.
40. Munch, M. R.; Gast, A. P. J. Chem. Soc., Faraday Trans. 1990, 86, 1341-1348.
41. Ligoure, C.; Leibler, L. Macromolecules 1990, 23, 5044-5046.
42. Galati, E.; Tebbe, M.; Querejeta-Fernández, A.; Xin, H. L.; Gang, O.; Zhulina, E. B.; Kumacheva, E. ACS Nano 2017, 11, 4995-5002.
43. Choueiri, R. M.; Galati, E.; Thérien-Aubin, H.; Klinkova, A.; Larin, E. M.; Querejeta-Fernández, A.; Han, L.; Xin, H. L.; Gang, O.; Zhulina, E. B.; Rubinstein, M.; Kumacheva, E. Nature 2016, 538, 79.
44. Chai, J.; Wang, D.; Fan, X.; Buriak, J. M. Nat. Nanotechnol. 2007, 2, 500.
45. Laforgue, A.; Bazuin, C. G.; Prud'homme, R. E. Macromolecules 2006, 39, 6473-6482.
46. Tassin, J. F.; Siemens, R. L.; Tang, W. T.; Hadziioannou, G.; Swalen, J. D.; Smith, B. A. J. Phys. Chem. 1989, 93, 2106-2111.
47. Toomey, R.; Mays, J.; Tirrell, M. Macromolecules 2004, 37, 905-911.

Chapter 5

Drop-Coating of Block Copolymer Self-Assembly Thin Films on Highly Curved Surfaces

5.1 Abstract

Block copolymer micelle nanolithography (BCML) can produce hexagonally ordered nanoparticle arrays on surfaces. However, BCML has not been achieved on nanofibers despite their usefulness for making SERS nanosensors, due to the effect of surface curvature on film thickness. Here, we show preliminary results obtained by two drop-coating methods that are potentially capable of coating nanofibers with gold nanoparticles using BCML. The first method utilizes the wetting film generated by a small static drop of the block copolymer solution placed on the fiber and that acts as a source for the coating. In the second method, the film is produced by a larger dynamic drop of the block copolymer solution that flows down the fiber. The coating of nanoparticles was found to be uniform on the nanofiber and free from Plateau-Rayleigh instability.

5.2 Introduction

Block copolymer micelle nanolithography (BCML) is an established bottom-up nanofabrication technique that can precisely pattern metal nanoparticles into hexagonal order on surfaces over large areas with wide controllability over the particle size and interparticle spacing.[1-10] BCML often involves the use of metal salts in the BCP solution to either load pre-existing BCP micelles (when block-selective solvents are used) or to induce micellization. Subsequently, the micelles are transferred onto a substrate by dip-coating or spin-coating to form a film with the micelles spontaneously arranged in hexagonal order. Then, plasma is used to reduce the metal ions into elemental state, causing the formation of

nanoparticles in the micelles with a one-to-one registration. Commonly used BCPs are polystyrene-*block*-poly(2-vinylpyridine), PS-*b*-P2VP,[4-6, 9, 11] and polystyrene-*block*-poly(4-vinylpyridine), PS-*b*-P4VP,[12-13] due to the ability of P2VP and P4VP to complex with metal salts.[14] The interparticle spacing can be controlled in BCML by changing the molecular weight of the PS block. While the initial size of metal nanoparticles is determined by the loading amount of the metal salt, the nanoparticles can be enlarged by seeding-growth chemistry *in situ* on the surface without disturbing the hexagonal order.[6]

BCML is an ideal method for preparing surface enhanced Raman scattering (SERS) substrates. However, it is not possible to use BCML on nanofibers to construct SERS nanosensors using dip-coating (spin-coating cannot be used on such curved substrates), due to the following two reasons. First, the high surface curvature associated with the nanofibers greatly depresses the film thickness during dip-coating, as shown in chapters 2 and 4, which effectively prevents the transfer of metal ion-loaded BCP micelles from solution onto the nanofiber. Secondly, it is known in fluid coatings that, because of surface tension, liquid film coating on fibers or the insides of capillary tubes are typically unstable and break up into droplets, due to the so-called Plateau-Rayleigh instability.[15-19] This renders a uniform BCP film coating on nanofibers impossible.

Here, we will use two simple methods for coating nanofibers with films composed of gold ions loaded in BCP micelles. Both methods involve using a drop of the BCP solution and rely on the unique geometry of the pulled glass fiber. In the first method, a small drop is placed at the taper part of the pulled glass fiber, where the diameter is large, from which a uniform BCP coating forms down to the tip part by spontaneous wetting. In the second method, a larger drop placed at the taper flows down by gravity from the taper, leaving behind a gold ion-loaded BCP film. Although the results obtained are preliminary, both drop-coating techniques comprise potentially simple and alternative methods for making nanosensors, compared to what has been described in the previous chapters.

5.3 Experimental

5.3.1 Materials

Poly(styrene-*b*-2-vinylpyridine) (PS-P2VP) with M_n(PS) = 110 kg/mol, M_n(P2VP) = 52 kg/mol and M_w/M_n (total) = 1.17 was purchased from Polymer Source (Dorval, QC, Canada). Tetrahydrofuran (THF, 99.99%) and toluene (99.99%) was purchased from VWR. Gold(III) hydrochloride trihydrate ($HAuCl_4 \cdot 3H_2O$, 99.9%) and trisodium citrate dihydrate (99%) were purchased from Sigma-Aldrich. All were used as received. Borosilicate glass rods of 1.1 mm in diameter and 10 cm in length were obtained from Sutter Instrument.

5.3.2 Glass fibers

The glass rods were pulled into nanofibers using a laser-based Sutter P-2000 pipette puller (Sutter Instrument, California) with the following two-line program, where the parameters given are instrument specific: LINE 1) Heat: 280, Filament: 3, Velocity: 15, Delay: 145, Pull: 20; LINE 2) Heat: 500, Filament: 0, Velocity: 15, Delay: 128, Pull: 200. They were cleaned with ethanol for 5 min, dried in air, then immersed in a piranha solution at 90 ºC for 60 min, rinsed well with Milli-Q water, and finally dried under vacuum at room temperature for an hour.

5.3.3 Block copolymer solution preparation

The deposition of AuNPs on glass fibers was realized by the BCML method established by Spatz and coworkers, as introduced in the introduction.[6, 9, 11] Polymer solutions of 3 mg/mL were prepared by dissolving 30 mg of PS-*b*-P2VP in 10 mL of THF or toluene in a scintillation vial. $HAuCl_4 \cdot 3H_2O$ was added into the solution with a loading of 0.3, defined by the molar ratios of $HAuCl_4 \cdot 3H_2O$ to the VP repeat units. The solutions were capped and sealed with parafilm and stirred at 30–40 ºC for at least 24 hours, in order to allow complete dissolution of the gold salt in the cores of the block copolymer micelles. They were then filtered successively through a 0.45 μm and a 0.2 μm PTFE filter (Chromspec) and stored in dark.

5.3.4 Drop coating

The dip-coater of a KSV3000 Langmuir-Blodgett instrument was used to move and hold the glass fibers. The pulled glass fibers were attached to the dip-coater with the tip pointing downwards and placed vertically inside a beaker half filled with the same solvent as that in the polymer solution. The glass fiber was suspended over the solvent reservoir with the fiber tip about 1 cm above the surface. The purpose of the beaker was to create a stable solvent vapor environment and stabilize it from sudden air flows. The beaker was placed in an oil bath on top of a heating instrument, with the temperature of the oil bath monitored by a thermometer.

For coating with a static drop, a small drop of about 4 μL of the BCP solution was placed on the taper part of the pulled fiber using a micropipette. Although not observable by eye, a spontaneous wetting film spread on the fiber. As the solvent evaporated, the drop gradually shrunk to its disappearance on the fiber, the time of which was dependent on the reservoir temperature. For a reservoir temperature of 28 ºC, the process took about 5 min to complete (for reservoir temperatures of 9 °C and 37 °C, the process took 3 and 15 min, respectively). For coating with a flowing drop, the drop volume was increased to >13 μL and the coating was done at room temperature. The drop was slowly transferred from the micropipette to the taper of the fiber, making sure the drop wrapped around the fiber during the entire time of transfer. Upon the drop detaching from the micropipette tip, it immediately flowed down the fiber, producing a film on the nanofiber that quickly dried. No visible residue of solution was found at the taper of the fiber. The coated fibers were removed from the beaker and kept in covered Petri dishes until use.

5.3.5 Scanning electron microscopy (SEM)

The coated glass fibers were examined using a JEOL JSM-7400F (JEOL Ltd, Tokyo, Japan) field-emission scanning electron microscope operated at 1.5 kV and 20 μA. Analyses of the AuNP size, size distribution and density were done using ImageJ (http://imagej.nih.gov/ij/features.html).

5.4 Results and discussion

5.4.1 Theory of static drop-coating

Whether a liquid drop deposited on a flat solid surface spreads or not is determined by the spreading parameter,

$$S = \gamma_{SG} - \gamma_{SL} - \gamma \qquad \textbf{5.1}$$

where γ_{SG}, γ_{SL}, and γ are the interfacial tension between solid and air, between solid and liquid, and between liquid and air, respectively.[20-24] As shown in Scheme 5.1, when S is negative, the drop wets the solid partially and forms an angle θ with the solid, as given by the Young-Laplace equation,

$$\cos\theta = 1 + {}^{S}/_{\gamma} \qquad \textbf{5.2}$$

When S is positive, the drop spreads out completely and forms a (liquid) film with a relatively high thickness.

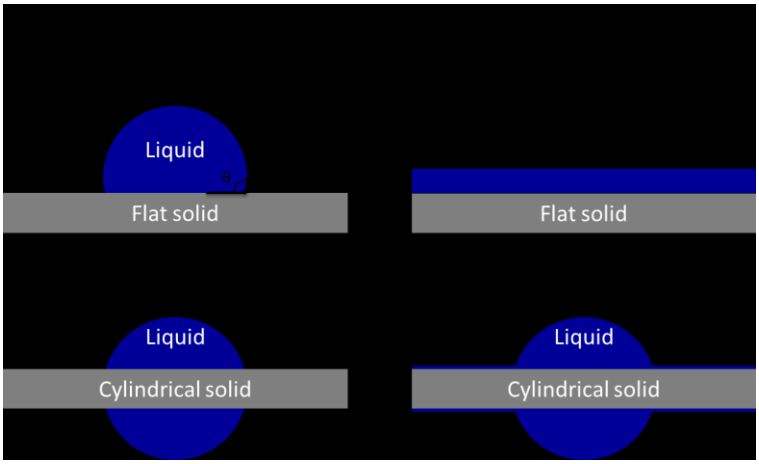

Scheme 5.1. Representation of partial wetting (left) and complete wetting (right) of a liquid drop on a flat substrate (top) and a cylindrical substrate (bottom).

However, when the solid is a small cylindrical solid, complete spreading of the liquid drop is prevented on the curved surfaces.[21] On the other hand, a film that is thicker than a critical film thickness, e_c, tends to break into droplets, due to the Rayleigh instability, where e_c is defined as

$$e_c = a^{1/2} b^{1/2} \qquad \textbf{5.3}$$

where b is the radius of the cylindrical solid and a is a length that is defined by

$$a = (-A/6\pi\gamma)^{1/2} \qquad \textbf{5.4}$$

where A is an effective Hamaker constant, on the order of a few $k_B T$ (where k_B is the Boltzmann constant and T is temperature).

Nonetheless, the liquid drop still spreads downwards along the fiber, resulting in what is termed a spontaneous wetting film that coexists with what remains in the drop.[21] This film is stabilized by long-range forces and has a thickness, e_0, smaller than e_c,

$$e_0 = a^{2/3} b^{1/3} \qquad \textbf{5.5}$$

The value for a here is substrate specific and typically on the order of a few Å, e.g., a is about 3 Å for a polymeric fiber/organic solvent system,[21] making the wetting film typically a few nanometers in thickness.

5.4.2 Coating with a static drop

The coating procedure using a static drop and relying on spontaneous wetting of the glass fiber below the drop down to submicron diameters is illustrated schematically in Scheme 5.2. The pulled glass fiber consists of a taper part and a narrow pulled part down to the tip that ranges in diameter from a few tens of microns to below 1 μm. A drop of the Au^{3+}-loaded BCP solution of a few μL in volume was placed at the taper part of the fiber, where the Laplace pressure gradients associated with the conical shape of the taper prevents the small drop of solution from flowing down the fiber.[25] A wetting film then spontaneously spreads below the drop to the lower fiber diameter region. After solvent

evaporation, what remains is a relatively thick film on the surface region that was covered by the drop (labeled region 1) and a much thinner film along the whole fiber below region 1 and extending to the fiber tip (labeled regions 2-5 in Scheme 5.2).

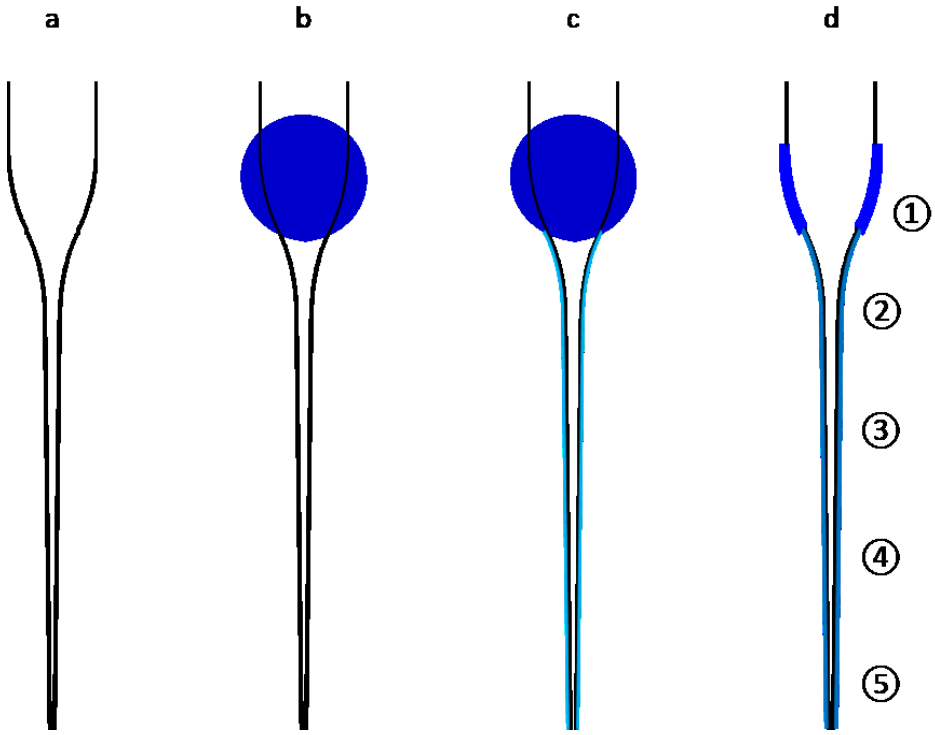

Scheme 5.2. Schematic illustration of the coating procedure: a) bare pulled glass fiber; b) a drop of Au^{3+}-loaded BCP solution (dark blue) placed at the taper of the fiber; c) spontaneous formation of a wetting film along the fiber below the original drop (light blue); d) Au^{3+}-loaded BCP thin film coating of the fiber after completion of the wetting process and solvent evaporation. The circled numbers refer to regions mentioned in the text.

SEM images of the coated fiber in regions 1-5 are shown in Figure 5.1. Region 1, where the thickest coating is, appears dark in the SEM image. In contrast, right next to this region, which corresponds to the upper part of region 2, appears bright. The sharp boundary between the two regions indicates that there was a three-phase contact line during spreading

of the drop and solvent evaporation, which characterizes the static drop situation. Zooming into region 2 (Figures 5.1 and 5.2), it was found that the coating shows a pattern of randomly distributed dots or circular nanoparticles whose radii are mainly between about 50 and 100 nm (Figure 5.2c). The size of these nanoparticles are similar to other Au^{3+} loaded BCP micelles reported in the literature, but their order is more random than hexagonal.[6, 12-13] The pattern extends over the entire length of the fiber below the original drop of solution (regions 3, 4 and 5 in Figure 5.1) and no sign of Plateau-Rayleigh instability was observed. Since these regions had no direct contact with the solution drop, this coating must be the result of the spontaneously formed wetting layer mentioned above.

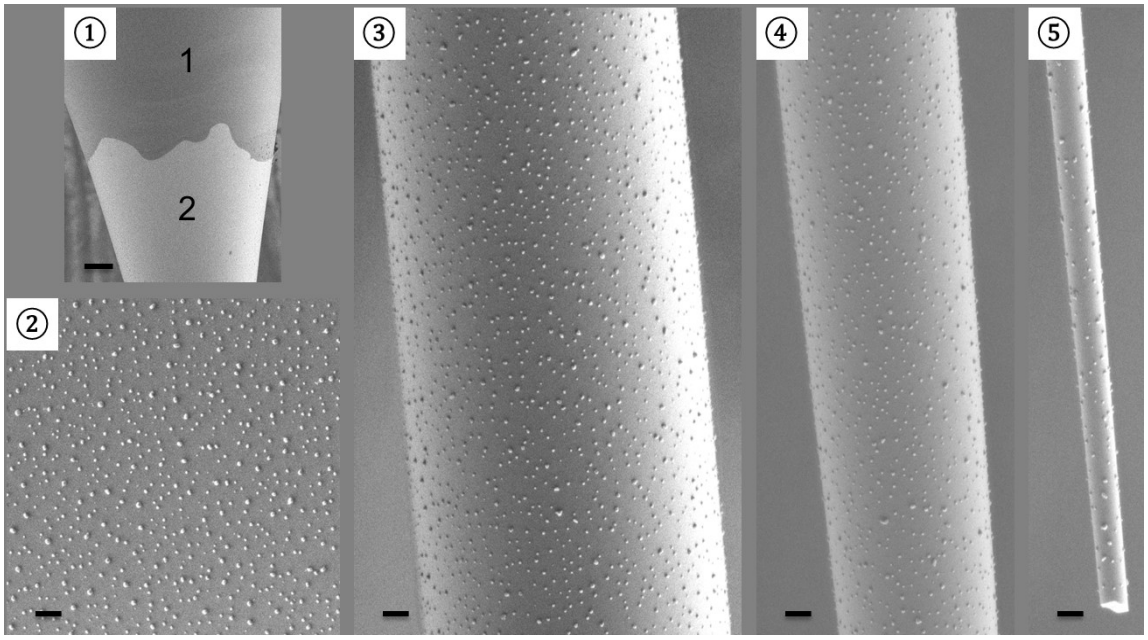

Figure 5.1. SEM images of the surface of an Au^{3+}-loaded BCP-coated pulled fiber (using a reservoir temperature of 28 ºC) at different diameters, where the numbers correspond to the regions identified in Scheme 5.2. Scale bars represent 50 μm in top-left image and 1 μm in the other images. The polymer solution consists of 3 mg/mL PS_{110}-b-$P2VP_{52}$ in THF with an Au^{3+} loading of 0.3.

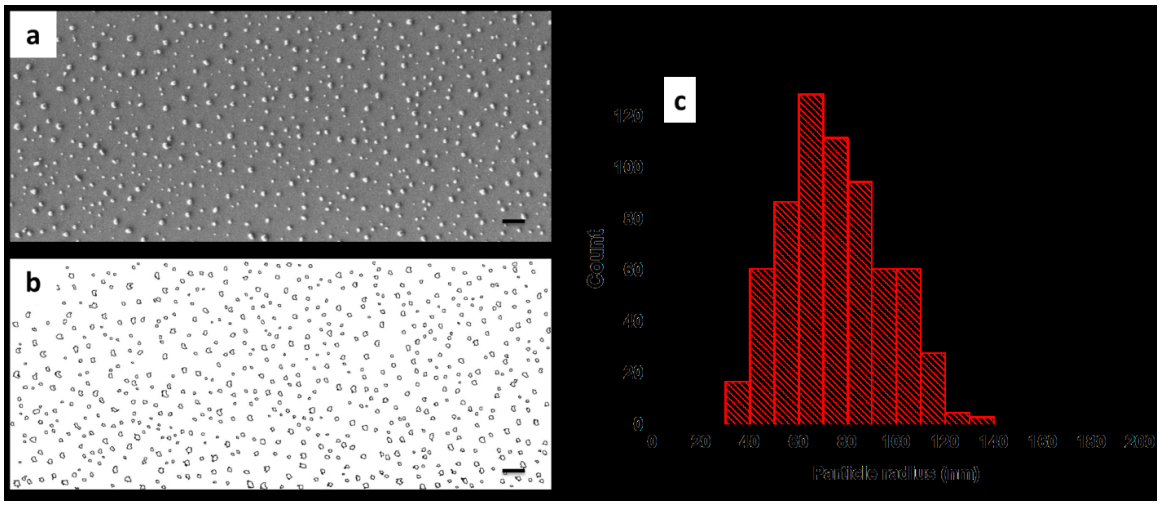

Figure 5.2. (a) SEM image of the surface nanoparticles corresponding region 2 in Figure 5.1. (b) outlines of the nanoparticles used to determine (c) the histogram plot of the nanoparticle radius distribution. Scale bars represent 1 μm.

As mentioned in the experimental part and indicated in Figure 5.3, the lower the reservoir temperature, the faster the completion of the process (as determined by the visual observation of drop volume stabilization). This is because there is less solvent in the atmosphere around the fiber for lower reservoir temperatures, which allows faster solvent evaporation from the drop on the fiber. Nonetheless, despite the different drying times, Figure 5.3 shows that similar coatings are obtained on the fiber down to the tip for all three reservoir temperatures. This indicates that the wetting layer forms quickly, certainly in less than a few minutes.

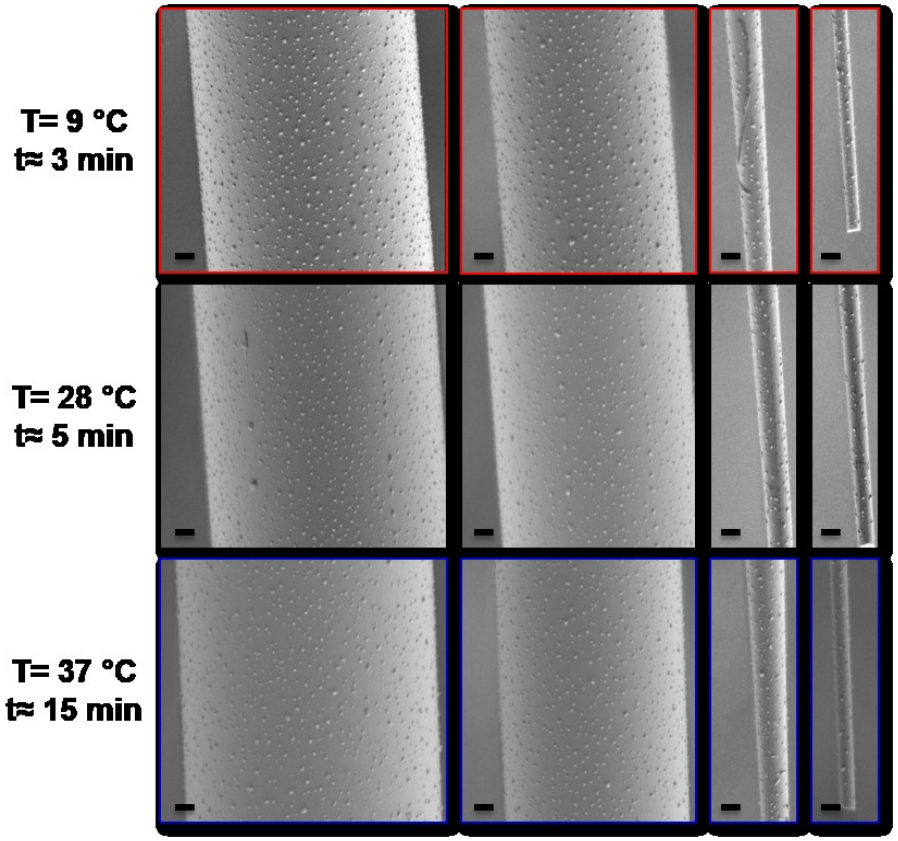

Figure 5.3. SEM images of the surface of Au^{3+}-loaded BCP-coated pulled fibers, taken at various diameters along the fiber. These coatings were formed from solution drops of 4 μL using the three different reservoir temperatures indicated (visual drying times, t, are also indicated). Scale bars represent 1 μm. The polymer solution consists of 3 mg/mL PS_{110}-b-$P2VP_{52}$ in THF with an Au^{3+} loading of 0.3.

It is noteworthy that the pulled glass fiber was subjected to a piranha bath prior to drop-coating, which is known to increase the OH functionality of the glass surface.[26] If a pulled fiber with no piranha treatment was used, it was poorly wet by the solution and the only coating achieved after solvent evaporation was at the location of the original drop. By the same token, when the solvent was changed from THF to toluene, spontaneous wetting did not occur. This indicates that, in order to achieve the film coating, it is critical that the fiber can be completely wetted by the solution. This condition is met when the glass fiber

surface is made hydrophilic by the piranha treatment and when using THF, which is a polar solvent, but not when using toluene, which does not wet a hydrophilic surface.

It is also probable that the BCP wets the hydrophilic surface through a P2VP wetting layer where multiple hydrogen bonds can form between the OH functions on the glass surface and the pyridine groups in the P2VP block,[27-28] as in the previous chapters for the P4VP block.[29-31] On the other hand, the presence of the Au^{3+} ions in the BCP solution means that these solutions are micellar, with P2VP cores protonated by $HAuCl_4$ in an acid−base reaction resulting in electrostatic binding with $AuCl_4^-$ ions[14] and PS coronae.[4, 6-7, 10, 13] It is likely that it is these Au^{3+}-loaded micelles that are observed as dots or nanoparticles in the SEM images in Figures 5.1 and 5.2, particularly since the $AuCl_4^-$ ions with their high electron density are probably responsible for the clarity of the dots/nanoparticles in SEM. The presence of micellar nanoparticles in the coating also implies that, during the spontaneous dewetting process, part of the P2VP is available (or frees itself from the micelles) to interact with the OH groups on the glass surface while another part remains in the micelles.

5.4.3 Coating with a flowing drop

A large enough polymer-solution drop experiences a gravitational force that can overcome the Laplace pressure at the taper, resulting in downward flow of the drop along the fiber. As it flows, it was found to leave behind a wet polymer film on the fiber that then dries. Using the same Au^{3+}-loaded BCP solution as that in the static-drop method above, a pulled fiber was coated by this flowing-drop method. Figures 5.4 and 5.5 shows SEM images of the resulting film at selected fiber diameters for large and sub-micron diameters, respectively. While the coating was observed at large fiber diameters, little coating was found below about 10 μm. In contrast to the static-drop method, the film resulting from the dynamic drop shows a surface morphology that varies with fiber diameter. A pattern featuring mostly chains of small nanoparticles was observed at a fiber diameter of 25 μm, with the chains having dimensions of about 40-60 nm in width, corresponding to the diameter of the composing nanoparticles, and 40-60 nm to over 1 μm in length, depending on the number of nanoparticles in the chain. There seems to be no preferential alignment along the direction of the drop flow indicated by an arrow on the image. The pattern

evolves into shorter chains of nanoparticles at 20 μm, mostly individual nanoparticles at 15 and 10 μm fiber diameters. At even lower diameters, such as 1 μm shown in Figure 5.5, little coating and thereby no pattern could be observed, although no other diameters in between were examined to pinpoint the lowest diameter limit for the coating. Nor have we checked diameters above 25 μm. Also in contrast to the static-drop method, when toluene solutions were used for the dynamic drop, patterned films were obtained. In this case, the patterns are in the form of mostly individual nanoparticles at all diameters down to at least 10 μm (Figure 5.4), with little coating observed at about 1 μm (Figure 5.5) (again, no other diameters were checked). These toluene nanoparticles have similar sizes to the THF nanoparticles shown above and they are close to the sizes of typical Au^{3+}-loaded BCP micelles of similar molecular weight and loading.[6, 13] It should be pointed out that, with both solvents, no evidence of the Plateau-Rayleigh instability was noted.

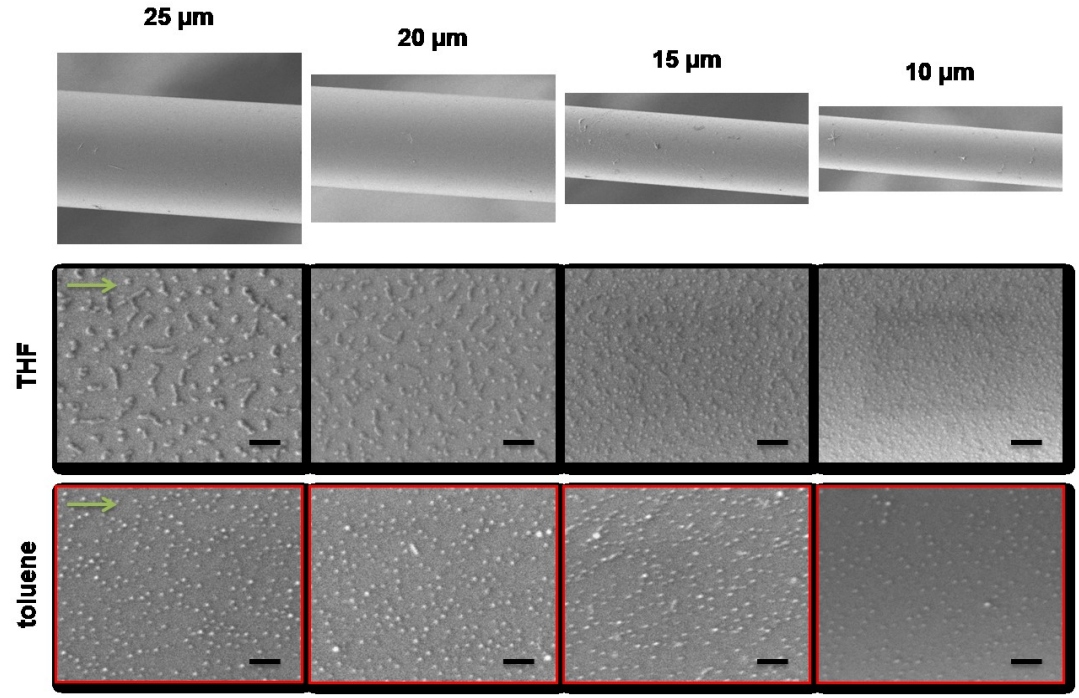

Figure 5.4. SEM images of Au^{3+}-loaded BCP-coated fibers at various fiber diameters. Scale bars represent 500 nm. The BCP coating formed as a large drop of BCP solution flowed down along the fiber. The green arrows indicate the flow direction. BCP solutions: 3 mg/mL PS_{110}-*b*-$P2VP_{52}$ in THF (middle row) and toluene (bottom row).

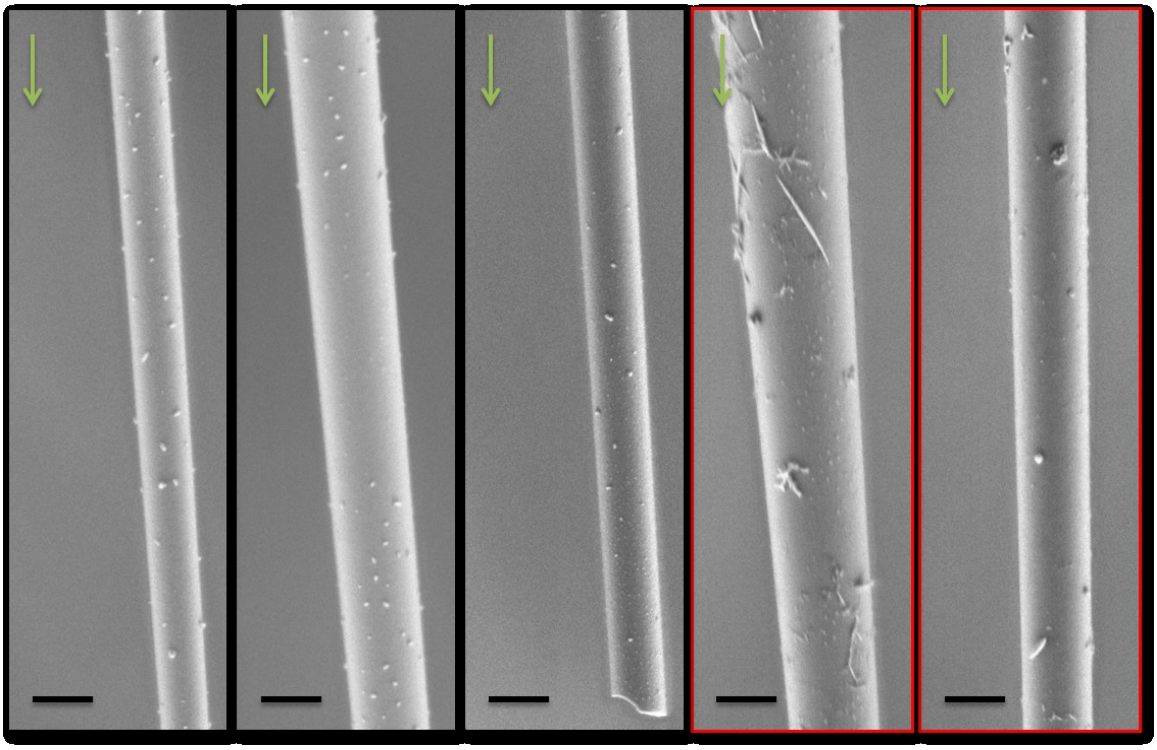

Figure 5.5. SEM images of Au^{3+}-loaded BCP-coated fibers at sub-micron fiber diameters. Scale bars represent 1 μm. The BCP coating formed as a large drop of BCP solution flowed down along the fiber. The green arrows indicate the flow direction. BCP solutions: 3 mg/mL PS_{110}-*b*-$P2VP_{52}$ in THF (black outline) and toluene (red outline).

Assuming that the nanoparticles are micelles with Au^{3+}-loaded P2VP cores and PS coronae, the difference in the films obtained with THF *vs*. toluene might be related to the harder nature of the micellar cores in toluene, given that toluene is a strongly selective solvent for PS in contrast to THF which, although better for PS, can also dissolve P2VP. Although the presence of the Au^{3+} ions causes some degree of immobilization in the micelle cores, these cores may be less mobile on a molecular level in toluene than in THF, which may prevent them from forming micelle chains with toluene whereas in the case of the THF solution, although individual nanoparticles could be recognized, they tend to arrange into short stripes, especially at large fiber diameters.

While these results are preliminary, they clearly merit further investigation to better understand the nature of the coatings and determine their dependence on various molecular

and experimental parameters, such as BCP solution concentration. It could be particularly informative to apply the two drop-coating techniques to pure BCP solutions (free of gold ions) and then expose the resulting coated nanofibers to AuNP colloids as in the preceding chapters. This could reveal whether the BCP coatings obtained are brush-layer coatings or if thicker BCP micelle layers are obtainable.

5.5 Conclusions

It is challenging to use block copolymer micelle lithography to pattern ordered nanoparticles on nanofibers, due to the depression of film thickness by surface curvature in dip-coating. The challenge can be met by two unique methods based on drop-coating. In the first method, a uniform film coating composed of Au^{3+}-loaded BCP micelles was obtained on the fiber by placing a drop of the polymer solution at the large taper part of the pulled glass fiber. While a wetting condition is critical for achieving such a coating, the coating is not affected by the environment temperature (or drying time). In the second method, similar coatings were obtained after a drop of polymer solution flew down the fiber by gravity. Although wetting condition is not a necessary requirement in the second method, different arrangements of nanoparticles were observed when different solvents were used. Both methods led to uniform coatings of nanoparticles without signs of Plateau-Rayleigh instability on fibers of down to submicron diameters.

5.6 References

1. Gadomska, K. M.; Lechner, S. J.; Spatz, J. P. *Part. Part. Sys. Char.* **2013**, *30*, 940-944.
2. Glass, R.; M ller, M.; Spatz, J. P. *Nanotechnology* **2003**, *14*, 1153-1160.
3. Jahn, S.; Lechner, S. J.; Freichels, H.; Moller, M.; Spatz, J. P. *Sci. Rep.* **2016**, *6*, 20536.
4. Kästle, G.; Boyen, H. G.; Weigl, F.; Lengl, G.; Herzog, T.; Ziemann, P.; Riethmüller, S.; Mayer, O.; Hartmann, C.; Spatz, J. P. *Adv. Funct. Mater.* **2003**, *13*, 853-861.
5. Kruss, S.; Erpenbeck, L.; Schon, M. P.; Spatz, J. P. *Lab Chip* **2012**, *12*, 3285-9.
6. Lohmueller, T.; Bock, E.; Spatz, J. P. *Adv. Mater.* **2008**, *20*, 2297-2302.

7. Möller, M.; Spatz, J. P.; Roescher, A. *Adv. Mater.* **1996**, *8*, 337-340.
8. Selvan, T.; Spatz, J. P.; Klok, H.-A.; Möller, M. *Adv. Mater.* **1998**, *10*, 132-134.
9. Spatz, J. P.; Mössmer, S.; Hartmann, C.; Möller, M.; Herzog, T.; Krieger, M.; Boyen, H.-G.; Ziemann, P.; Kabius, B. *Langmuir* **2000**, *16*, 407-415.
10. Wiedwald, U.; Han, L.; Biskupek, J.; Kaiser, U.; Ziemann, P. *Beilstein J. Nanotechnol.* **2010**, *1*, 24-47.
11. Spatz, J. P.; Mossmer, S.; Moller, M. *Chem-Eur J* **1996**, *2*, 1552-1555.
12. Aizawa, M.; Buriak, J. M. *J. Am. Chem. Soc.* **2005**, *127*, 8932-3.
13. Aizawa, M.; Buriak, J. M. *Chem. Mater.* **2007**, *19*, 5090-5101.
14. Antonietti, M.; Wenz, E.; Bronstein, L.; Seregina, M. *Adv. Mater.* **1995**, *7*, 1000-1005.
15. Brochard-Wyart, F.; di Meglio, J.-M.; Quéré, D. *Journal de Physique* **1990**, *51*, 293-306.
16. Quere, D. *Europhys. Lett.* **1990**, *13*, 721-726.
17. Quere, D.; di Meglio, J. M.; Brochard-Wyart, F. *Science* **1990**, *249*, 1256-60.
18. Tuteja, A.; Choi, W.; Ma, M.; Mabry, J. M.; Mazzella, S. A.; Rutledge, G. C.; McKinley, G. H.; Cohen, R. E. *Science* **2007**, *318*, 1618-22.
19. Quere, D. *Annu. Rev. Fluid. Mech.* **1999**, *31*, 347-384.
20. De Gennes, P.-G. *Rev. Mod. Phys.* **1985**, *57*, 827.
21. Quéré, D.; Di Meglio, J.-M.; Brochard-Wyart, F. *Science* **1990**, *249*, 1256-1260.
22. Bonn, D.; Eggers, J.; Indekeu, J.; Meunier, J.; Rolley, E. *Rev. Mod. Phys.* **2009**, *81*, 739.
23. Quéré, D. *Annu. Rev. Mater. Res.* **2008**, *38*, 71-99.
24. Adamson, A. W.; Gast, A. P. **1967**.
25. Zheng, Y.; Bai, H.; Huang, Z.; Tian, X.; Nie, F.-Q.; Zhao, Y.; Zhai, J.; Jiang, L. *Nature* **2010**, *463*, 640.
26. Zhu, M.; Lerum, M. Z.; Chen, W. *Langmuir* **2012**, *28*, 416-23.
27. Spatz, J. P.; Möller, M.; Noeske, M.; Behm, R. J.; Pietralla, M. *Macromolecules* **1997**, *30*, 3874-3880.
28. Spatz, J. P.; Sheiko, S.; Möller, M. *Adv. Mater.* **1996**, *8*, 513-517.

29. Motschmann, H.; Stamm, M.; Toprakcioglu, C. *Macromolecules* **1991**, *24*, 3681-3688.

30. Munch, M. R.; Gast, A. P. *J. Chem. Soc., Faraday Trans.* **1990**, *86*, 1341.

31. Tassin, J. F.; Siemens, R. L.; Tang, W. T.; Hadziioannou, G.; Swalen, J. D.; Smith, B. A. *J. Phys. Chem.* **1989**, *93*, 2106-2111.

Chapter 6

Conclusions and Perspectives

We set out to achieve the deposition of AuNPs on nanofibers by using BCP thin films as templates, in view of applications as SERS nanosensors. From this goal arises the investigation of dip-coated BCP thin films on small cylindrical substrates, which was poorly studied at the time. Over the course of the thesis work, we have not only successfully achieved the primary goal of coating nanofibers with AuNPs, but we have also gained new knowledge on dip-coated BCP thin films, used familiar adsorbed BCP thin films in new applications, and established more advantageous techniques for bottom-up nanofabrication. This chapter summarizes these achievements and points out some limitations of the study. As a final comment, we will propose several topics that require further research.

6.1 General conclusions

6.1.1 SERS optophysiology probes via BCP brush films

SERS endoscopic probes have been successfully fabricated by using BCP brush film templates, with improved SERS performance in the detection of 4-MBA and the *in vitro* detection of neurotransmitter molecules, as shown in Chapter 2. As illustrated in Scheme 6.1, we have found that PS-*b*-P4VP brush films, where P4VP forms a wetting layer adsorbed to the glass surface via multiple hydrogen bonds and PS forms a brush-like overlayer, are suitable templates for the deposition of negatively charged AuNPs of various sizes on nanofibers. The brush film is only a few nanometers thick, as measured by the AFM scratch method on a fiber (Chapter 2) and by ellipsometery on flat Si surfaces (Chapter 3); thus these studies are distinct from previous research that relied on thicker BCP films that have microphase-separated nanostructures with distinctive surface patterns

for guiding the deposition of phase-selective AuNPs. The method using BCP brush films shows much improved AuNP coatings compared to that using other methods,[1-3] in that the AuNP density is high and AuNP aggregation is largely prevented. In addition, while the lowest fiber diameter reported that has been coated with such a dense and uniform monolayer of AuNPs is 25 μm (using BCP templates),[4] we have extended the diameter range accessible to BCP patterning to the sub-micron scale down to the tip of pulled fibers (reaching 100 nm in diameter).

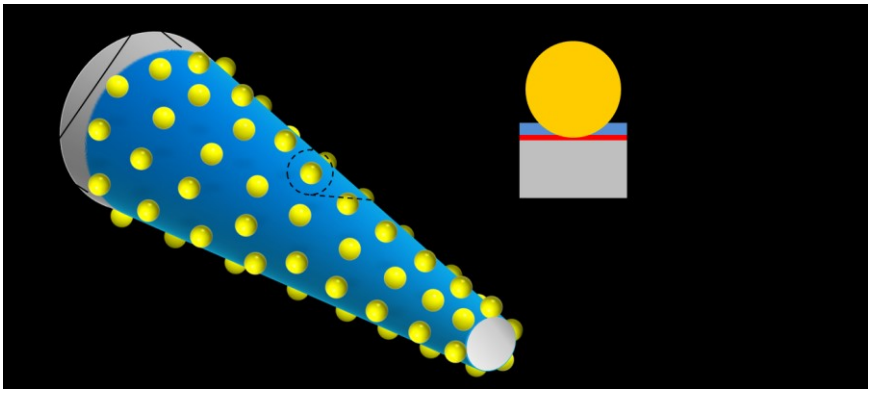

Scheme 6.1. Schematic illustration of an AuNP-decorated nanofiber at the sub-micron scale. The AuNP coating was achieved by using a PS-*b*-P4VP brush film template adsorbed on the glass surface of the fiber. The negatively charged AuNPs are deposited on the film through electrostatic interactions with the partly protonated P4VP blocks, while the PS blocks behave as a steric barrier to prevent AuNP aggregation on the surface.

The deposition of AuNPs on the BCP brush film is made possible because of surface reconstruction of the film during its exposure to the aqueous AuNP colloidal suspension, without which the PS top layer would protect the P4VP sublayer from interacting with AuNPs. The surface reconstruction of the BCP brush film, which involves local molecular displacement of PS segments to expose P4VP, was supported by the greater surface roughness observed by AFM in Chapter 2. Surface reconstruction is common in many other film patterning/templating systems, such as in patterned microphase-separated

BCP films[5] and in end-grafted polymer films.[6] The lack of AuNP aggregation on BCP brush films has been attributed to a steric barrier effect provided by the PS blocks in the BCP brush, given their covalent linkage to the stably bound P4VP wetting layer, since similarly adsorbed films using a P4VP homopolymer or PS-s-P4VP random copolymer, as discussed in Chapters 2 and 4, led to AuNP deposition that is often coupled with aggregates.

It is known that the brush films form by a fast adsorption process of BCP chains on surfaces.[7-10] Our study on the kinetics of BCP adsorption in Chapter 3 shows that the film thickness rapidly increases in the first two minutes of substrate exposure to the BCP solution and reaches a plateau thereafter, in good agreement with the two-stage adsorption process that has been established for amphiphilic BCP adsorption in solution.[7-13] From the same experiment, we also found that unsaturated BCP brush films, whose morphology is rougher in AFM images than fully developed BCP brush films, leads to the same AuNP deposition in terms of pattern and density as the fully developed BCP brush films. This is consistent with the idea of surface reconstruction upon exposure to the aqueous AuNP suspension, in that this reconstruction exposes part of the AuNP wetting layer, making the surface resemble that of unsaturated BCP film surfaces.

We conclude from the above that the nanofabrication process is simple and robust. It consists of two easy steps. The first is dipping the glass nanofiber into a polymer solution for a short period of time, during which BCP chains adsorb onto the nanofiber to form a brush film. The second is incubating the BCP brush-coated nanofiber in a slightly acidic AuNP colloidal suspension for about 2 hours, where the electrostatic self-assembly of AuNPs on the BCP brush film takes place, forming a monolayer of dense and well dispersed AuNPs. This is in contrast to the prolonged and complicated surface derivatization of SAMs, as was described in the introduction.[14-17]

6.1.2 Two distinct layers in dip-coated block copolymer films

Another important conclusion in this thesis is that, in order to obtain the brush films on flat surfaces by dip-coating, extremely low polymer solution concentrations have to be used. This is related to the two-stage process that takes place during BCP dip-coating of substrates, notably giving rise to the layer that is adsorbed when the substrate is immersed

in the BCP solution and the additional material that is deposited on this adsorbed layer as the substrate is being withdrawn from the solution, as illustrated in Scheme 6.2. The adsorbed layer forms the brush film; the additional material gives rise to thicker films that typically lead to nanostructured or patterned surfaces depending on the microphase-separated film morphology. This additional material accounts for the dependency of film thickness on polymer solution concentration and the withdrawal rate, for which a "V"-shaped relationship is observed.[18-21] For this reason, in Chapter 3, the thickness-rate “V” relationship was observed only at high polymer concentrations, whereas the film thickness was not affected by dip-coating rate at sufficiently low BCP solution concentrations, where only adsorbed films are formed. This observation has important consequences on the film morphology and, therefore, the pattern of AuNPs deposited on these films. Thus, while the (saturated) brush layer shows a featureless/smooth surface morphology in AFM, the additional material is responsible for a variety of film surface morphologies. These range from microphase separation-induced surface patterns, including those formed by frozen-in solution micelles, to "dewetted" patterns caused by an insufficient film thickness for full coverage of the adsorbed layer by the additional material. (This full coverage is achieved when the average film thickness is greater than the periodicity of the film morphology normal to the substrate.) It is noteworthy that BCP film templates used in past literature for nanoparticle deposition all correspond to the relatively thick films that contain the additional material, whereas the brush films used in this thesis constitute a novel template that gives rise to 2D dense and uniform monolayer arrays of well-dispersed AuNPs.

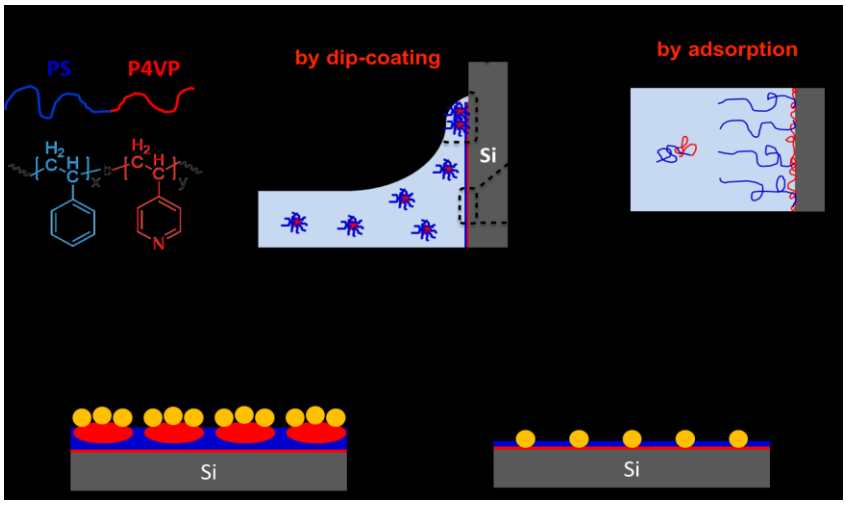

Scheme 6.2. Schematic illustrating the structure of a PS-*b*-P4VP dip-coated film and the deposition of small AuNPs on two types of films. The brush layer forms by adsorption during substrate exposure to the BCP solution, whereas the micellar layer forms during the withdrawal of the substrate from solution. In the case of PS-*b*-P4VP/THF solutions, the micellar layer, composed of P4VP cores in a PS matrix, is frozen in from the micellar solution. The micellar layer leads to clusters of AuNPs when the AuNP size is much smaller than the micelle size and the brush layer produces dense and well dispersed AuNPs with little aggregation.

6.1.3 Effect of substrate curvature on the thickness of dip-coated BCP thin films

Substrate curvature is known to affect the thickness of dip-coated fluids on fibers.[22] This effect has been verified in this thesis as well for dip-coated BCP films. This is especially interesting for the BCP films since film thickness plays a critical role in determining the film surface pattern. Indeed, by examining the dip-coated BCP films on a pulled fiber along its decreasing diameter, a series of morphologies in the film, as revealed by the pattern of deposited AuNPs, were observed in Chapter 4, ranging from films with a dot pattern due to PS-*b*-P4VP frozen-in micelles at low surface curvature, to dewetted films at intermediate curvature, and to the brush films at high curvature. The morphology evolution resembles that shown in Chapter 3, where the polymer solution concentration was

systematically decreased and where regimes of different film morphologies were clearly defined by film thickness. In addition, the approximate fiber diameters where the morphology undergoes a transition between full micellar and brush has been shown to change with changing polymer solution concentration and dip-coating rate. This is consistent with how these parameters affect the film thickness on flat surfaces.[18-21] Thus, as illustrated in Scheme 6.3, both decreasing polymer solution concentration and increasing substrate surface curvature can result in the transition from nanostructured films with specific surface patterns to brush-layer film templates. In fact, on the highly curved surfaces in the region of interest for nanopipette applications as SERS sensors, the BCP film is limited to the brush layer, and is independent of polymer concentration, as shown in Chapter 4. This template was shown to be effective for a wide range of AuNP sizes, emphasizing the potential usefulness of these AuNP-decorated nanofibers for potential applications.

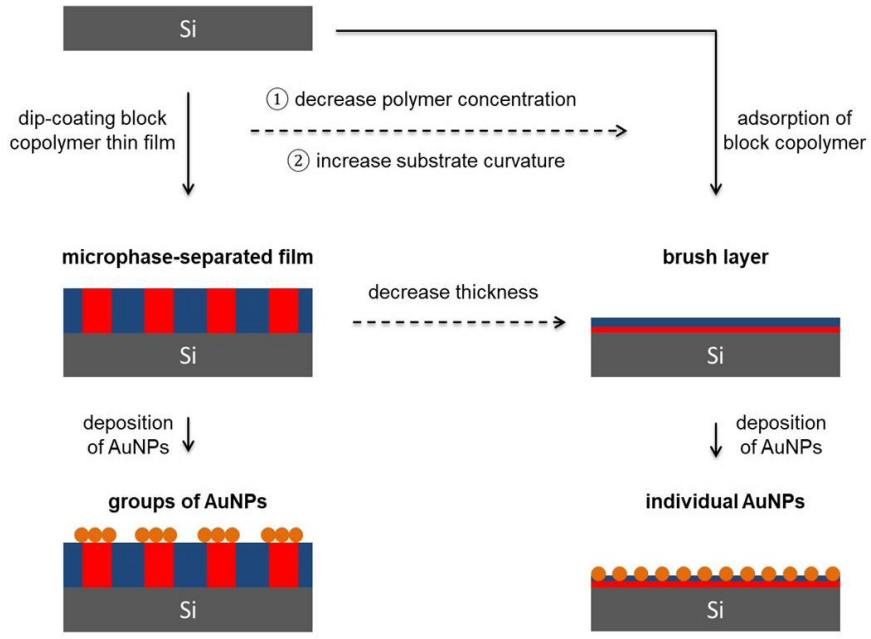

Scheme 6.3. Schematic illustration of the similar effect between decreasing polymer solution concentration and increasing substrate curvature on the thickness of dip-coated BCP films, the nature of the film, and the pattern of small AuNPs deposited on the film.

Nanostructured films are obtained at high polymer concentration or low substrate curvature, whereas brush films are obtained at low concentrations or high surface curvature.

6.1.4 Novel drop coating method for coating nanofibers

Knowing the curvature effect on film thickness, it remains a challenge to coat micro and nanofibers with polymer films of relatively large thicknesses. However, being able to do so can enable nanopatterning on these fibers using other BCP templates as mentioned in the introduction. In particular, block copolymer micelle lithography (BCML)[23] that can give rise to highly ordered nanoparticle arrays relies on films thicker than the dimension of micelles. However, it has been previously shown to be difficult to pattern highly curved surfaces.[4] The drop coating methods shown in Chapter 5 of this thesis are promising in addressing this challenge. Using a fluid wetting film that is unique to small cylindrical substrates, a drop of solution placed at larger fiber diameters results in coating BCP at small diameters. In a different approach, a drop quickly flowing over the fiber also results in a thicker film on the fiber. These films are uniform and contain Au^{3+} preloaded BCP micelles, indicating that we succeeded in overcoming of the Plateau-Rayleigh instability and the film thickness limit by substrate curvature.

6.2 Limitations

6.2.1 Thickness measurement on cylindrical surfaces

On flat substrates, the film thickness can be measured by ellipsometry, which allows us to study the effect of dip-coating rates and polymer solution concentration on film thickness. However, on cylindrical surfaces of glass fibers, it is difficult, if not impossible, to precisely measure the dry film thickness. Although this was done in one case by an AFM scratch method (Chapter 2), it was laborious, especially since the fiber is subject to movement during the measurement. As a result, we relied on the small-AuNP deposition pattern shown by SEM and on observations as a function of concentration on flat surfaces to indirectly deduce a qualitative picture of the relationship between substrate curvature and the thickness of dip-coated BCP thin films. Without the measurement of the film thickness

of films on small cylindrical surfaces, it limits the systematic study of the detailed effect of substrate curvature on film thickness.

6.2.2 Brush films on highly curved surfaces

We learned from flat surfaces that the AuNPs deposited on the brush film appear to be blind to potential nanofeatures in the film, as obtained for incomplete PS coverage. However, on the curved nanofiber surfaces, SEM was the technique primarily used and it did not provide information on such BCP nanofeatures. AFM, as was used on the flat surfaces, can be used to directly image those features but the difficulty in sample preparation, especially for small fibers, prevents us from extensively examining the brush films on highly curved surfaces. Nonetheless, there are potentially interesting phenomena in the brush films on highly curved surfaces. For example, because of the substrate curvature effect, brush films are obtained at both low and high polymer solution concentrations. Studies of BCP adsorption in solution indicate that these films have different thicknesses.[8, 12] However, how this plays out on highly curved surfaces has not been determined, although this should be possible by AFM. It cannot be studied for a wide concentration range on flat surfaces since very low polymer solution concentrations are necessary to obtain only the brush film. Similarly, we do not know how the substrate curvature affects the brush films, although there are indications in the literature that surface curvature can affect the grafting density of end-grafted polymers on nanoparticle surfaces.[24] Again, these questions would be more effectively answered if better techniques for measuring film thickness and surface morphologies on highly curved surfaces were used or available.

6.3 Perspectives

6.3.1 Solvents

As discussed in the introduction, solvent can affect the BCP brush films in many different ways, depending on the solubility of the solvent towards the two block components.[7-8, 25] In this work, we have restricted ourselves to THF for the preparation of BCP polymer solutions. THF is a good solvent for the PS block and a poor solvent for the

P4VP block, thus making THF solutions of PS-*b*-P4VP micellar (except for low molecular weights), although the micelles are relatively soft due to some swelling by THF.[19] Because P4VP is the anchor block for the adsorption of the BCP on the polar solid surface, the adsorption of the BCP on the surface is favored not only by the poor solubility of THF towards P4VP but also by the selectivity of the solvent for PS that directs the orientation of the PS block into the solution. This effect can be exaggerated by using a still more strongly selective solvent for PS, such as toluene, which is a worse solvent for P4VP than THF and which leads to micellar solutions with glassy cores.[18] On the other hand, we can also make the solvent less block-selective to the extent that it dissolves both blocks (e.g. chloroform) and even use a selective solvent for P4VP (e.g. ethanol or a mixture of ethanol and THF). It is worth pointing out that a wide range of solvent selectivities can be achieved by using mixed solvents.[26] Indeed, the case of using a P4VP-selective solvent is particularly attractive, as the solvent would compete with the surface for the P4VP block, which could dramatically affect the adsorption rate and the maximum adsorbed amount. Moreover, the quality of solvent is closely linked to the conformational state of the BCP blocks both in solution and on the substrate. We observed different surface patterns in adsorbed films from THF solutions as a function of adsorption time. Whether this is true for other solvents and, if so, whether we can control the pattern or other brush-layer characteristics sufficiently to achieve different AuNP deposition patterns are questions for future research. In preliminary work comparing the use of THF with chloroform, for example, Figure 6.1 indicates that the solvent used influences the brush layer thickness and adsorption kinetics. Possible characteristics that may affect AuNP adsorption onto the brush layer and that are likely to be influenced by the solvent used include the conformation of the P4VP wetting layer and the extent of its contact with the substrate, which in turn should influence the thickness of the P4VP layer (the greater the contact the thinner this layer). Greater P4VP contact with the substrate should likewise affect the thickness of the PS layer, since (for full coverage) it will adapt its spread (and therefore average thickness) to the spread of the P4VP layer. The selectivity of the solvent may also be expected to influence the P4VP/PS interface, where the two types of chains may undergo more or less interpenetration. For example, the greater selectivity of toluene compared to THF could lead to a narrower interfacial region with less interpenetration between the P4VP and PS sublayers, and this might possibly inhibit local

PS segmental rearrangement in the aqueous AuNP suspension and thereby inhibit AuNP adsorption to the brush layer.

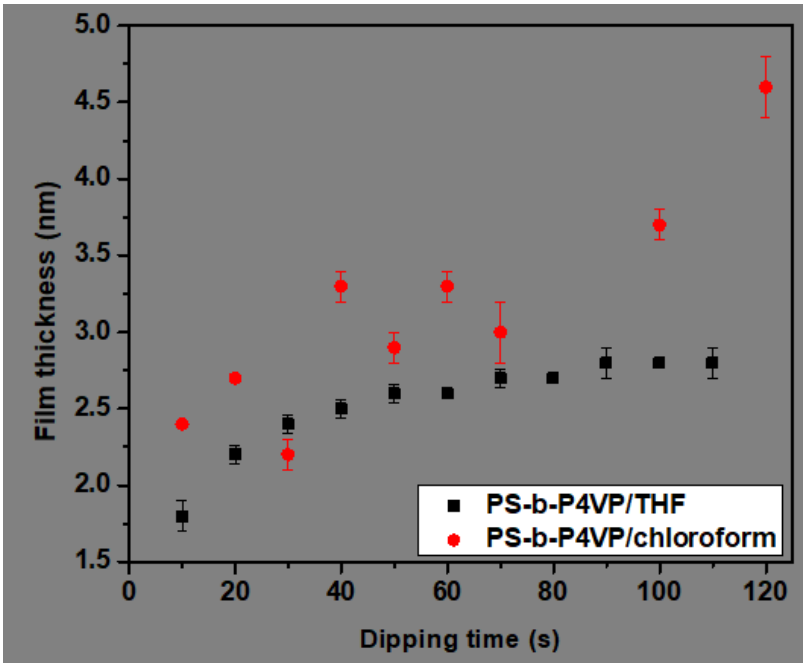

Figure 6.1. Film thickness against adsorption time for PS_{41}-*b*-$P4VP_{20}$ films adsorbed on flat substrates using dip-coating from THF and chloroform solutions with a BCP concentration of 0.05 mg/mL.

6.3.2 Molecular characteristics

In Chapter 4, we have shown that the deposition featuring monolayer arrays of well-dispersed AuNPs on nanofibers is preserved when BCP brush films of various molecular weights and compositions are used, but the AuNP density was found to increase with the P4VP content in the BCP. However, despite the fairly large range of P4VP contents studied, the change in AuNP density is small. It is of interest in future work to expand the P4VP content to further verify this dependence. It can be anticipated that a lower P4VP content limit will be reached where the deposition of AuNPs is impossible, and a higher P4VP content limit where AuNP aggregation appears, given that they are present in P4VP

homopolymer coatings. In addition, similar studies should also be carried out on flat surfaces, where the AuNP density was observed to be somewhat lower than on curved surfaces, to better understand this difference. The amount of work would dramatically increase if the effect of molecular characteristics were combined with that of solvent.

6.3.3 Applications

BCPs have been mostly used as dispersants in solution; occasionally, they are seen as dispersants for nanoparticles in polymer bulk to make nanocomposites. This thesis clearly shows that they are also capable, when in the form of brush films, of effectively dispersing nanoparticles on surfaces. In that sense, many applications that rely on well-dispersed surface nanoparticles, such as plasmonic sensing and optical coating for solar cells, could find the BCP brush films templates useful, noting that many types of NPs, not just the AuNPs used in this thesis, can, in principle, be templated in the same manner. An example in case is the deposition of quantum dots on pulled glass fibers via the BCP brush film template, as shown in Figure 6.2a. Going from simple to more complex nanofabrication and nanoengineering, BCP brush films are potential templates for the construction of multiple layers of nanoparticles and micro-contact printing. As an example, Figure 6.2b and c show a dot and a line pattern of micron/submicron size, respectively, composed of AuNPs that were written on a BCP brush film.

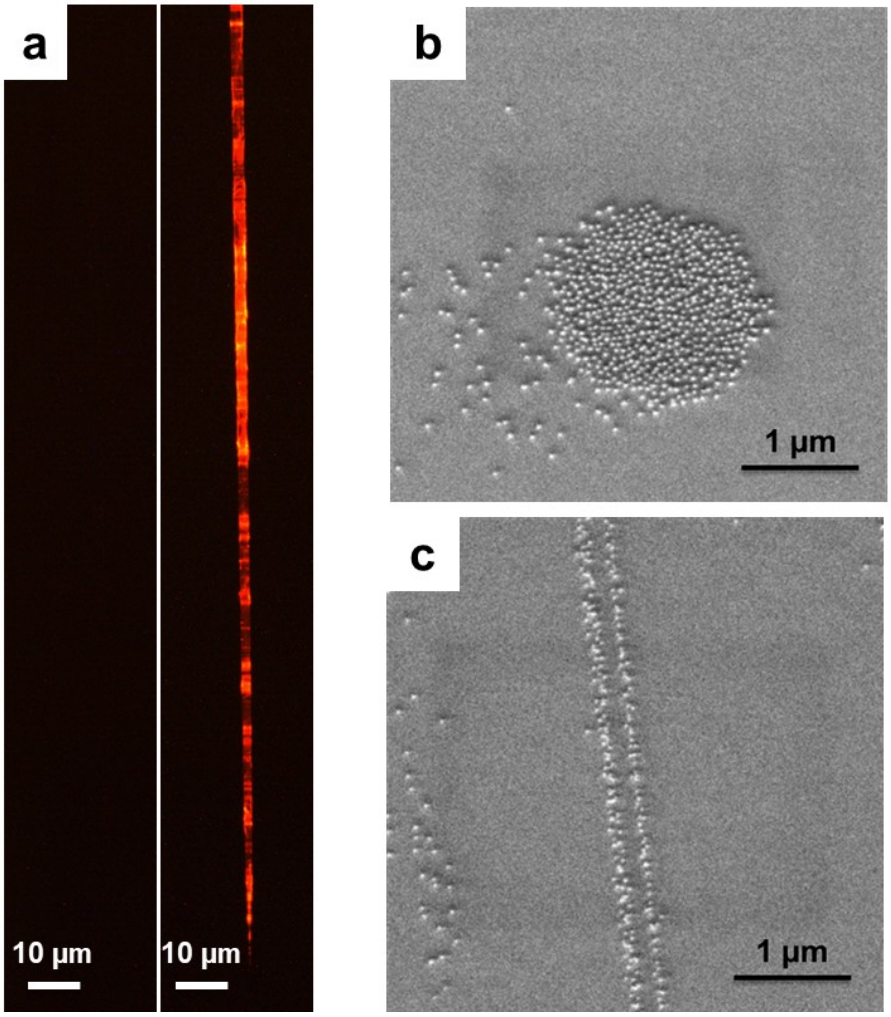

Figure 6.2. a, Fluorescent images of glass fibers after the deposition of quantum dots without (left) and with (right) a BCP brush film template. The brush film was a PS_{41}-b-$P4VP_{20}$ film dip-coated on the fiber at 80 mm/min from a 5 mg/mL PS-*b*-P4VP/THF solution. The quantum dots had glutathione ligands. The deposition was done at pH 6. b and c, Writing patterns on silicon surfaces by using the BCP brush film. SEM images of surface AuNP patterns on pre-defined templates in the form of (a) a dot and (b) a line pair. The writing was done by using a metal syringe needle prefilled with the 0.05 mg/mL PS-*b*-P4VP/THF solution. The dot was created by a quick touch of the needle tip on the surface and the line pair was created by drawing the needle across the surface at a normal writing speed.

6.4 References

1. Lussier, F.; Brule, T.; Vishwakarma, M.; Das, T.; Spatz, J. P.; Masson, J. F., *Nano Lett.* **2016**, *16*, 3866-3871.
2. Masson, J. F.; Breault-Turcot, J.; Faid, R.; Poirier-Richard, H. P.; Yockell-Lelievre, H.; Lussier, F.; Spatz, J. P., *Anal. Chem.* **2014**, *86*, 8998-9005.
3. Vitol, E. A.; Orynbayeva, Z.; Bouchard, M. J.; Azizkhan-Clifford, J.; Friedman, G.; Gogotsi, Y., *ACS Nano* **2009**, *3*, 3529-3536.
4. Kruss, S.; Erpenbeck, L.; Schon, M. P.; Spatz, J. P., *Lab Chip* **2012**, *12*, 3285-3289.
5. Chai, J.; Wang, D.; Fan, X.; Buriak, J. M., *Nat. Nanotechnol.* **2007**, *2*, 500-506.
6. Tebbe, M.; Galati, E.; Walker, G. C.; Kumacheva, E., *Small* **2017**, *13*, 1702043.
7. Motschmann, H.; Stamm, M.; Toprakcioglu, C., *Macromolecules* **1991**, *24*, 3681-3688.
8. Munch, M. R.; Gast, A. P., *Macromolecules* **1990**, *23* , 2313-2320.
9. Tirrell, M.; Patel, S.; Hadziioannou, G., *Proc. Natl. Acad. Sci. U S A* **1987**, *84* , 4725-4728.
10. Toomey, R.; Mays, J.; Tirrell, M., *Macromolecules* **2004**, *37*, 905-911.
11. Hadjichristidis, N.; Pispas, S.; Floudas, G., *Physical Properties and Applications* **2002**, 232-254.
12. Munch, M. R.; Gast, A. P., J. Chem. Soc. Faraday Trans. **1990**, 86, 1341-1348.
13. Tassin, J. F.; Siemens, R. L.; Tang, W. T.; Hadziioannou, G.; Swalen, J. D.; Smith, B. A., *J. Phys. Chem.* **1989**, *93*, 2106-2111.
14. Asenath Smith, E.; Chen, W., *Langmuir* **2008**, *24*, 12405-12409.
15. Zhu, M.; Lerum, M. Z.; Chen, W., *Langmuir* **2012**, *28*, 416-423.
16. Freeman, R. G.; Grabar, K. C.; Allison, K. J.; Bright, R. M.; Davis, J. A.; Guthrie, A. P.; Hommer, M. B.; Jackson, M. A.; Smith, P. C.; Walter, D. G., *Science* **1995**, *267*, 1629-1632.
17. Lyon, L. A.; Musick, M. D.; Natan, M. J., *Anal. Chem.* **1998**, *70*, 5177-5183.
18. Roland, S.; Gamys, C. G.; Grosrenaud, J.; Boissé, S.; Pellerin, C.; Prud'homme, R. E.; Bazuin, C. G., *Macromolecules* **2015**, *48*, 4823-4834.

19. Roland, S.; Gaspard, D.; Prud'homme, R. E.; Bazuin, C. G., *Macromolecules* **2012**, *45*, 5463-5476.
20. Roland, S.; Pellerin, C.; Bazuin, C. G.; Prud'homme, R. E., *Macromolecules* **2012**, *45*, 7964-7972.
21. Roland, S.; Prud'homme, R. E.; Bazuin, C. G., *ACS Macro Lett.* **2012**, *1*, 973-976.
22. Quere, D., *Annu. Rev. Mater. Res.* **1999**, 31, 347-384.
23. Lohmueller, T.; Bock, E.; Spatz, J. P., *Adv. Mater.* **2008**, *20*, 2297-2302.
24. Galati, E.; Tebbe, M.; Querejeta-Fernández, A.; Xin, H. L.; Gang, O.; Zhulina, E. B.; Kumacheva, E., *ACS Nano* **2017**, *11*, 4995-5002.
25. Toomey, R.; Mays, J.; Tirrell, M., *Macromolecules* **2004**, *37*, 905-911.
26. Park, S.-Y.; Sul, W.-H.; Chang, Y.-J., *Macromolecules* **2007**, *40*, 3757-3764.